X-RAY AND ELECTRON SPECTROMICROSCOPY OF CARBON NANOTUBE SYSTEMS

By

Ebrahim Najafi, M.Sc.

A Thesis

Submitted to the School of Graduate Studies

in Partial Fulfillment of the Requirements

for the Degree of

Doctor of Philosophy

McMaster University

DOCTOR OF PHILOSOPHY (2011)   McMaster University
(Chemistry and Chemical Biology)   Hamilton, Ontario

TITLE: X-Ray and Electron Spectromicroscopy of Carbon Nanotube
                Systems

AUTHOR: Ebrahim Najafi, M.Sc. (Gwangju Institute of Science and

                Technology)

SUPERVISOR: Professor Adam P. Hitchcock

NUMBER OF PAGES: XX, 246

List of publications

1- E. Najafi, D. Hernández Cruz, M. Obst, A. P. Hitchcock, B. Douhard, J. J. Pireaux, A. Felten, "**Polarization Dependence of the C 1s X-ray Absorption Spectra of Individual Multi-Walled Carbon Nanotubes**" *Small* 4,12 (**2008**) 2279.

2- E. Najafi, J. Wang, A. P. Hitchcock, J. Guan, S. De´nomme´e, B. Simard, "**Characterization of single-walled carbon nanotubes by scanning transmission x-ray spectromicroscopy: purification, order and dodecyl functionalization**" *J. Am. Chem. Soc.* 132 (**2010**) 9020.

3- A. Felten, X. Gillon, M. Gulas, J.-J. Pireaux,X. Ke, G. Van Tendeloo, C. Bittencourt, E. Najafi, A. P. Hitchcock, "**Measuring Point Defect Density in Individual Carbon Nanotubes Using Polarization-Dependent X-ray Microscopy**" *Nano 4* (**2010**) 4431.

4- E. Najafi, A. P. Hitchcock, D. Rossouw, G. Botton, "**Electron energy loss spectromicroscopy of multi walled carbon nanotubes**" *Ultramicroscopy* (to be submitted).

5- E. Najafi, A. P. Hitchcock, D. Rossouw, G. Botton, "**Mapping Defects in Multi-Walled Carbon Nanotubes Irradiated with Accelerated Particles**" *Nano. Lett.* (to be submitted)

ABSTRACT

This thesis presents studies of the X-ray linear dichroism (XLD) in individual single-walled (SW) and multi-walled (MW) carbon nanotubes (CNT) measured by a scanning transmission X-ray microscope (STXM). The C 1s spectra of CNT showed a large XLD at the C 1s→π* transition. The magnitude of the XLD was found to be related to the quality of CNT such that in high quality CNT, it was fairly large and as the quality lowered it decreased too. This dichroic effect was used to map defects along individual CNT. In addition, STXM was employed to map chemical components in pristine, purified, and dodecyl functionalized SWCNT bundles to investigate the changes occurring in them due to chemical functionalization.

STXM has limited spatial resolution. Thus, electron energy loss spectroscopy (EELS) in a transmission electron microscope (TEM) was used to obtain similar information about CNT, but at much higher spatial resolution. The measurements performed in the scanning transmission electron microscopy (STEM) mode produced signals analogous to the XLD when the orientation of the momentum transfer ($\mathbf{q}$) was resolved. This was achieved by displacing the EELS entrance aperture over the scattering pattern of CNT. TEM-EELS was then utilized to map defects in pristine and focused ion beam (FIB) modified CNT.

ACKNOWLEDGEMENTS

First and foremost I would like to offer my sincerest gratitude to my supervisor, Dr. Adam Hitchcock, for his excellent guidance, constant encouragement and endless support throughout my thesis research. It has been a pleasure and a precious experience to work for such a great scientist who is renowned for his passion for science, critical thinking, and scientific integrity. Furthermore, I would like to thank Ilona Hitchcock for hosting so many memorable summer and winter gatherings that brought the group closer together.

I am very grateful to my supervisory committee members, Dr. Alex Adronov and Dr. Peter Kruse, for their scientific advice and constructive comments.

Special thanks to Dr. Gianluigi Botton, Dr. Carmen Andrei, and David Rossouw for guiding me with electron energy loss spectroscopy experiments. They were very generous to share their expertise and knowledge.

I have been blessed to work with a smart group of scientists in Dr. Hitchcock's group, at the SM (CLS) and 5.3.2.2 (ALS) beamlines, and at the NRC including Dr. Glyn Cooper, Dr. Jian Wang, Dr. Chithra Karunakaran, Dr. Benoit Simard, Dr. Jingwen Guan, Dr. Tolek Tyliszczak, Dr. Bonnie Leung, Dr. Martin Obst, Dr. Daniel Hernandez-Cruz, Dr. Jeffrey Li, Dr. Li Li, Dr. Slava Berejnov, Karen Lam, Adam Leontowich, Sam Kalirai, Katie Harding, Jacob Stewart-Ornstein, and Saurabh Chitnis.

This thesis is dedicated to my parents and to the memory of my grandmother. I am very much grateful to my parents for giving me the gift of life. They never hesitated to invest in my education even though they had to make a lot of sacrifices; their love and

TABLE OF CONTENTS

LIST OF FIGURES

Chapter 3

Chapter 6

LIST OF TABLES

LIST OF ABBREVIATIONS AND SYMBOLS

a	Length of the Unit Vector in Graphene Lattice
$\boldsymbol{a_1, a_2}$	Unit Vector in Graphene Lattice
$a_{c\text{-}c}$	Carbon-Carbon Bond Length
A	Absorbance
ALS	Advanced Light Source
AD	Arc Discharge
β	Collection Angle
BESSY	Berliner Elektronenspeicherring-Gesellschaft für Synchrotronstrahlung
c	Speed of Light in Vacuum
$\boldsymbol{C_h}$	Chiral Vector of SWCNT
γ	Lorentz Factor
CCD	Charge-Coupled Device
CCEM	Canadian Centre Electron Microscopy
CLS	Canadian Light Source
CNT	Carbon Nanotube
CS	Central Stop
CVD	Chemical Vapour Deposition
Δr_n	Width of the Most Outer Zone (Nth) of a Zone Plate
$\Delta\phi$	Angular Spread of Synchrotron Radiation
d	The Highest Common Divisor of (n,m)
d_R	The Highest Common Divisor of (2n+m,2m+n)
d_t	Diameter of CNT
D	Distance from the Projector Cross-Over
D_A	Distance between the Cross-Over and the Entrance Aperture
DMF	Dimethylformamide
DOS	Density of States
DP	Diffraction Pattern
$\mathbf{e}$	Unit Potential Vector

E	Electric Vector
EELS	Electron Energy Loss Spectroscopy
EFTEM	Energy-Filtered Transmission Electron Microscopy
ELD	Electron Linear Dichroism
EXAFS	Extended X-ray Absorption Fine-Structure Spectroscopy
EPU	Elliptically Polarized Undulators
FEL	Free Electron Laser
FIB	Focused Ion Beam
FHS	Faculty of Health Sciences
f	Focal Length
$\langle f |$	Final Electronic State
FWHM	Full Width at Half Maximum
θ	Angle
θ_p	Pyramidalization Angle
θ_{ref}	Optimizable Parameter
HB	Hard Baking
HEP	High Energy Physics
HiPco	High Pressure Carbon Monoxide
HOMO	Highest Occupied Molecular Orbital
HOPG	Highly Ordered Pyrolytic Graphite
HRTEM	High Resolution Transmission Electron Microscopy
I	Transmitted Photon Intensity (Flux) in STXM
$| i \rangle$	Initial Electronic State
IP	Ionization Potential
I_0	Incident Photon Intensity (Flux)
$\mathbf{k_1, k_2}$	Reciprocal lattice vector in Graphene
NRC	National Research Council of Canada
q	Momentum Transfer
q$\perp$	Perpendicular Component of Momentum Transfer

$\mathbf{q}_\parallel$	Parallel Component of Momentum Transfer
λ	Wavelength of Light
l	Sample Thickness
L	Circumference of CNT
LCLS	Linac Coherent Light Source
LUMO	Lowest Unoccupied Molecular Orbital
μ	Energy Dependent Mass Absorption Coefficient
MeOH	Methanol
MWCNT	Multi-Walled Carbon Nanotube
NA	Numerical Aperture
NEXAFS	Near Edge X-Ray Absorption Fine Structure
NSLS	National Synchrotron Light Source
NSRRC	National Synchrotron Radiation Research Center
OD	Optical Density
OS	Oscillator Strength
OSA	Order Sorting Aperture
$\mathbf{p}$	Sum of the Linear Momentum Operators of the Electrons
PAY	Partial Auger Yield
PCA	Principal Component Analysis
PEEM	Photoemission Electron Microscope
PEY	Partial Electron Yield
$P_{if}(E)$	Transition Probability
PMT	Photomultiplier
ρ	Sample Density
$\rho_f(E)$	Energy Density of Final States
σ_a	Atomic Photoabsorption Cross Section
$\sigma_x(E)$	X-ray Absorption Cross Section
SASE	Self-Amplified Stimulated Emission
SEM	Scanning Electron Microscope

SGM	Spherical Grating Monochromator
SM	Spectromicroscopy
SPEM	Scanning Photoelectron Microscopy
SSRL	Stanford Synchrotron Radiation Laboratory
STM	Scanning Tunneling Microscopy
STEM	Scanning Transmission Electron Microscopy
STXM	Scanning Transmission X-Ray Microscopy
SVD	Singular Value Decomposition
SWCNT	Single-Walled Carbon Nanotube
T	Transmittance
t	Exposure Time
TEM	Transmission Electron Microscopy
TEY	Total Electron Yield
TFY	Total Fluorescence Yield
TGA	Thermogravimetric Analysis
THF	Tetrahydrofuran
TOF	Time of Flight
TXM	Transmission X-Ray Microscopy
UHV	Ultra High Vacuum
UPS	Ultraviolet Photoelectron Spectroscopy
v	Particle's Velocity
$V(E,t)$	Electromagnetic Energy- and Time-Dependent Perturbation
VLM	Visible Light Microscope
Ω	Electron Emission Solid Angle
vHS	van Hove Singularity
ω	Frequency
WCPP	Wet Chemical Purification Procedure
wt%	Weight Percent
XLD	X-ray Linear Dichroism

XMCD	X-Ray Magnetic Circular Dichroism
XMLD	X-Ray Magnetic Linear Dichroism
X-PEEM	X-ray Photoemission Electron Microscopy
XPS	X-ray Photoelectron Spectroscopy
XRD	X-ray Diffraction
ZP	Fresnel Zone Plate

Chapter 1

Introduction

This chapter gives an overview of the thesis and an introduction to carbon nanotubes (CNT). It reviews various methods of characterizing them. This chapter concludes with an outline for the whole thesis.

1.1 Overview of the thesis

CNT are allotropes of carbon that show exceptional physical, mechanical, and electronic properties. CNT are produced as single-walled (SW), or multi-walled (MW) tubes. SWCNT are graphene sheets rolled up into cylinders. The conductivity of SWCNT depends on their diameter and chirality [DDS95]. Typically, SWCNT have diameters in the range of a few nanometers while their lengths extend to a few microns. SWCNT show promise for a variety of applications such as electron transport channels in electronic devices [PTY01], and field emitters in field emission displays [FCF&99]. MWCNT consist of concentric graphitic cylinders. They exhibit exceptionally high mechanical strength and metallic conductivity. MWCNT have larger diameters than SWCNT which range from less than 10 nanometers to a few hundred nanometers. MWCNT are used as reinforcing fillers for composite materials since they are routinely produced in large volumes at reasonably low costs [CHS&03]. Polymers loaded with MWCNT show enhanced mechanical properties, improved electrical and thermal conductivities, and resistance against high energy radiation [MBA&99,NKH&05].

Despite their many interesting features, there are still several challenges associated with CNT. First, the quality of CNT depends on their synthesis method. While CNT produced by arc discharge (AD) methods have low defect content, those produced by chemical vapor deposition (CVD) methods are very defective [SY&06]. Therefore, the properties of CNT vary from one batch to another and among different individual CNT of a single batch. Second, as-produced CNT are typically highly contaminated with a number of organic and inorganic impurities. These impurities interfere with CNT functionality and reduce their performance for specific applications. Therefore, CNT powders have to undergo several purification steps to remove these contaminants. Third, highly purified CNT are virtually insoluble in common solvents which makes their processing and manipulation very difficult [BMB&02]. Thus, after purification, they are often subjected to chemical reactions to functionalize their surfaces in order to enhance their dispersion in solutions. These purification and functionalization reactions may damage CNT and introduce more defects into their structures, thus, further altering their properties. To advance CNT technology, there is a need to standardize their synthesis, purification, and functionalization. This requires a full understanding of their electronic, chemical, and structural properties. Methods for physical and chemical characterization of individual CNT, at various length scales down to atomic level, are needed to achieve this understanding and thereby to be able to predict how their properties change with various treatments.

This thesis is motivated to gain a better understanding and a more accurate characterization of the electronic, chemical, and structural properties of CNT prior to and

after physical and chemical functionalizations. Specifically, qualitative and quantitative characterizations of impurity level, degree of functionalization, and structural order in SWCNT and MWCNT were conducted using scanning transmission X-ray microscopy (STXM). STXM is a modern synchrotron technique that uses near edge X-ray absorption fine structure (NEXAFS) spectroscopy to obtain electronic and structural information at spatial resolutions of better that 30 nm [S92,AH08,HDJ&08]. STXM produces image sequences at various inner shell (core level) absorption edges, from which detailed chemical and electronic information is extracted [JWF&00]. These properties make STXM very suitable for both qualitative and quantitative spectromicroscopic studies. STXM enables spectroscopic analysis of individual CNT. Such analysis cannot be done by conventional methods as they investigate ensembles of CNT as powders; thus, the information that they provide is the average property of the batch. This thesis develops for the first time the use of STXM to quantitatively evaluate the quality of individual SWCNT (bundles) and MWCNT from various sources and understand their chemical and structural changes when they are subjected to various chemical treatments. Such quantitative information can further improve our understanding about CNT and will enable us to optimize and perhaps standardize their synthesis, purification and functionalization methods.

NEXAFS has high elemental and chemical sensitivity which was used in this work to determine the type and amount of organic moieties existing on pristine, purified, and functionalized CNT. The quantitative approach to map the chemical components in CNT samples is based on: (1) signature absorption spectrum of each component [S92];

(2) application of Beer-Lambert law; and (3) singular value decomposition of the image

sequences [DTA&06]. Furthermore, if NEXAFS is measured with linearly polarized X-

rays, it can determine spatial orientation and evaluate sample quality. By changing the

polarization angle of the incident X-rays, the intensity variation of certain features such as

the C 1s $\rightarrow$ π* transition was monitored to evaluate the quality of the samples and map

defects, including saturated sp^2 bonds, point defects, and surface irregularities. Electron

energy loss spectroscopy (EELS) and NEXAFS spectroscopy are analogues as they both

are probes of inner shell electronic excitation [E96]. Momentum (**q**) resolved EELS

reveals similar information to polarization (**E**) dependent NEXAFS spectroscopy. I have

used **q**-dependent EELS in a transmission electron microscope (TEM) in the scanning

transmission electron microscopy (STEM) mode to study defects in CNT at very high

spatial resolution (~ 1 nm). Defects in CNT are discussed in section 1.6.

1.2 Synthesis of CNT

CNT are produced by various methods such as arc discharge [EA&92,SNK&96],

laser ablation [GNR&95,GNT&95], chemical vapor deposition [YYR&93], and high

pressure carbon monoxide (HiPco) [NBB&99,CBH&01]. These methods produce

SWCNT, MWCNT, or a combination of both.

A schematic diagram of an arc discharge apparatus is shown in **Figure 1.1a**. In

this method, an electric field applied between two graphite electrodes creates a plasma of

carbon which then transforms into CNT. The electrodes are kept several millimeters apart

throughout the reaction by continuously feeding the anode. The chamber is connected to a

vacuum line with a diffusion pump and to a helium supply. Continuous flow of helium at

a constant pressure is preferred over static conditions. The electric discharge between the

electrodes is sustained by DC voltage, normally 20 V; the current between the electrodes

depends on the diameter of the electrodes but it is usually between 50 ~100 A. CNT

produced by the arc discharge method are mainly MWCNT. Metal catalysts are added to

the cathode to favor the formation of SWCNT although they also facilitate the formation

of a variety of graphitic impurities such as carbon onions. It has been demonstrated that

the yield and quality of AD-CNT depend on the pressure of helium inside the chamber

[EA&92], electric current between the electrodes [EHF&93,TFP&94], and water cooling

of the electrodes [ZOW&97].

Laser ablation method employs pulses of laser to evaporate a graphite target in a

controlled environment oven (**Figure 1.1b**); the vapor is then condensed on a cold

substrate to form MWCNT. Similar to the arc discharge method, adding metal catalysts to

the graphite rod favors the formation of SWCNT. The diameter of SWCNT depends on

the size of metal catalysts used in the process [GNR&95].
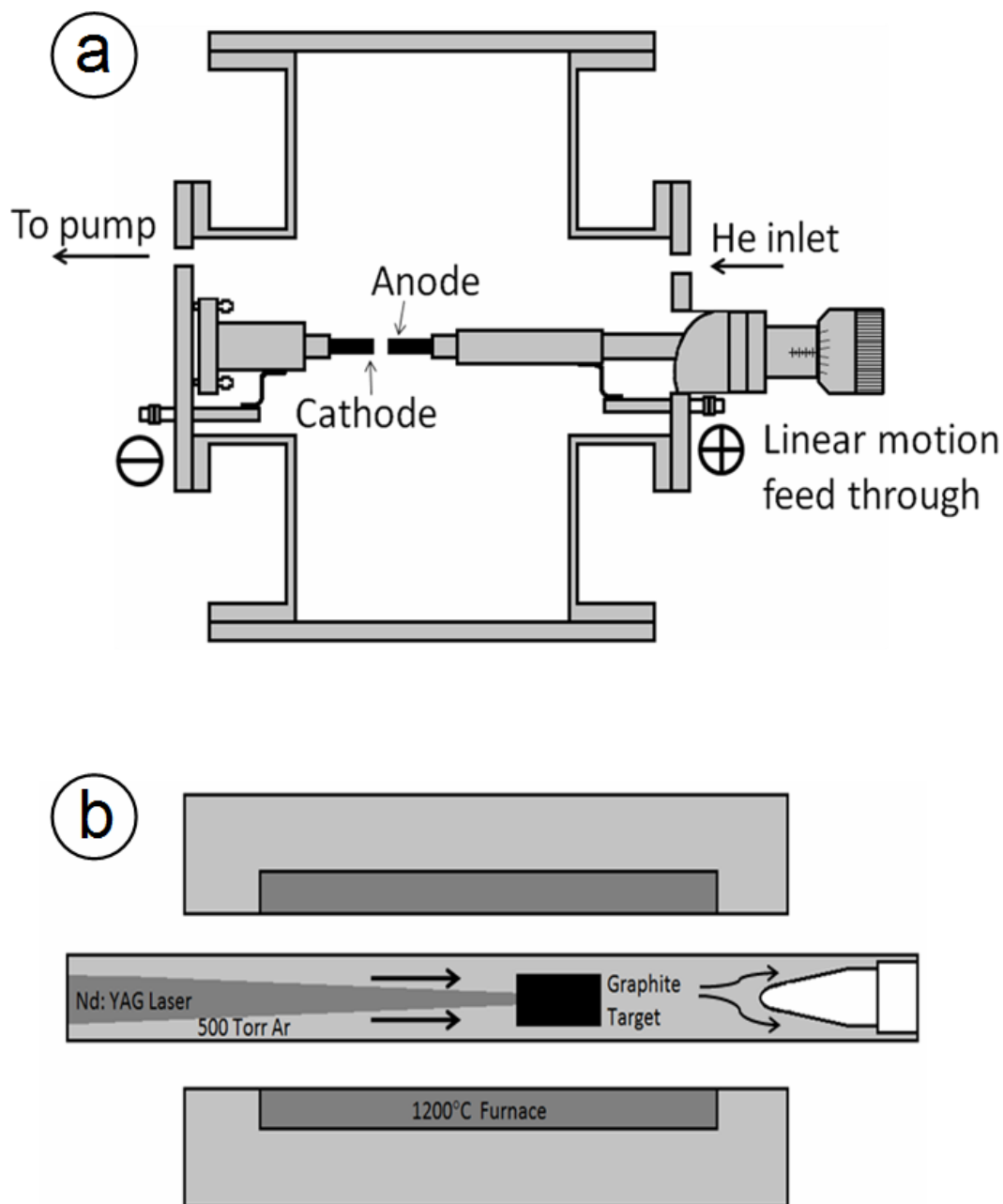
Figure 1.1 Schematic diagrams of (a) arc discharge (Adapted from [GNR&95]) and (b) laser ablation (Adapted from [SNK&96]) apparatus. Arc discharge and laser ablation methods produce MWCNT; addition of metal catalysts to the cathode favours the formation of SWCNT.

In the CVD method, a process gas such as ammonia, nitrogen or hydrogen and a carbon containing gas such as acetylene, ethylene, or ethanol are flowed into a vessel (**Figure 1.2**). CNT grow on a substrate heated to 700°C which has been prepared with a layer of metal catalyst particles such as nickel, iron, or cobalt or a combination of them. On the surface of the metal catalysts, the carbon containing gas is broken down and the carbon is transported to the edge of the particles where it forms CNT; the catalytic particles remain as metal impurities in CNT. The CVD method is being aggressively pursued since its production cost is relatively low, and also gives the possibility to grow CNT on integrated circuits [LTY&04], or to align them on substrates [TCA&01].
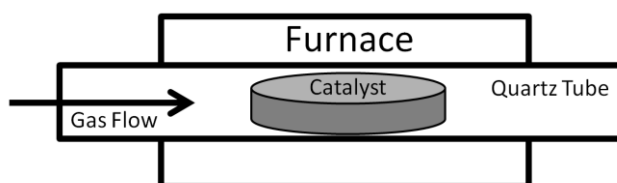
Figure 1.2 Schematic diagram of chemical vapour deposition method.

HiPco (high pressure carbon monoxide) synthesizes SWCNT from the gas phase reaction of iron pentacarbonyl with high pressure carbon monoxide in a heated reactor. Iron pentacarbonyl is used to produce iron nanoparticles that provide sites to transform carbon monoxide into carbon and carbon dioxide during the growth of SWCNT. In HiPco process, the concentration of the catalyst, temperature, and pressure are the parameters that control the quality of SWCNT [NBB&99,CBH&01].

1.3 Purification of CNT

CNT batches contain a large amount of organic and inorganic impurities such as amorphous carbon, graphitic particles, and metal catalysts. These impurities agglomerate and form big blobs that encapsulate CNT; this makes their removal a crucial step. **Figure 1.3** shows SWCNT subjected to purification processes to reduce contamination level.

1.3.1 Purification of MWCNT

Most purification methods are based on the difference between the reactivity of MWCNT and the impurities. Ebbesen et al. [EAH&94] argued that nanoparticles with their defect-rich structures oxidize more readily than the relatively perfect MWCNT. However, when they subjected MWCNT to a range of oxidizing treatments, they found that purification is obtained only at the expense of losing a major portion of the sample. This observation suggests that the reactivities of MWCNT and nanoparticles are very similar such that there is a fine line between the selective removal of the impurities and complete oxidation of the sample. An alternative approach takes advantage of the open structure of carbon nanoparticle onions and graphitic impurities which can be more readily intercalated than MWCNT. By intercalating with copper chloride and then reducing it to copper, Ikazaki et al. [IOU&94] were able to preferentially oxidize nanoparticles, using copper as an oxidation catalyst. Centrifugation, filtration, and chromatography of MWCNT-surfactant suspensions are also common methods to remove impurities [BSS97,DBM&98]. However, one is faced with the problem of removing the surfactant, which can be very challenging.
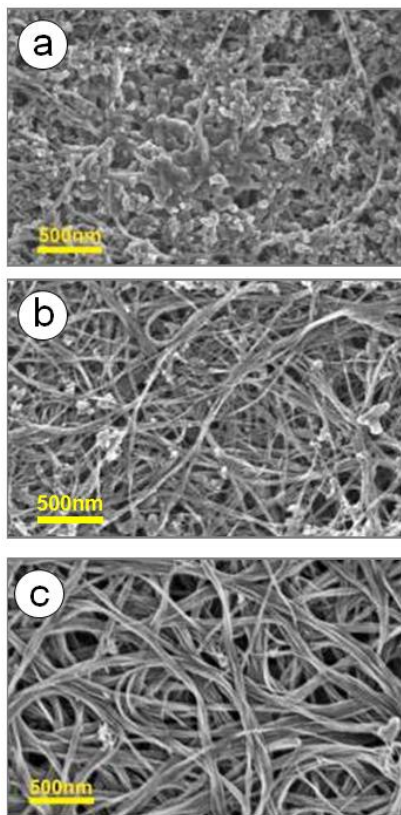
Figure 1.3 Scanning electron microscopy (SEM) images of (a) pristine single-walled carbon nanotubes (SWCNT), (b) SWCNT after wet chemical purification procedure (WCPP), and (c) further purified by hard baking after WCPP purification. SEM images were acquired using a 1.5 kV beam [NWH10].

1.3.2 Purification of SWCNT

Purification of SWCNT is more challenging than MWCNT since SWCNT powders contain more impurities. The inorganic impurities are often coated with carbon which makes their removal even harder. Furthermore, the purification methods developed for MWCNT are often too destructive for SWCNT. A step-by-step procedure developed by Tohji et al. [TGT&96,TTS97] has proven able to highly purify SWCNT. In their procedure, the raw soot is refluxed in distilled water for 12 hours, followed by filtering and drying to remove some of the graphitic particles and amorphous carbon. In a Soxhlet apparatus, fullerenes are washed away by toluene. The remaining amorphous carbon and the graphite covering metal particles are oxidized by heating the soot at 470°C for 20 minutes. Finally, the remaining soot is reacted with concentrated hydrochloric acid to remove the metal particles. Bandow et al. [BRW97] suggested multi-step filtration of surfactant-SWCNT suspensions. This method, however, is very slow and inefficient. Shelimov et al. [SER&98] improved this method by sonicating the suspension during filtration; they could purify 150 mg of the soot in less than 6 hrs by 90%. However, excessive sonication damages the structure of SWCNT [MK08]. Recently, Hersam et al. developed a method based on density gradient ultracentrifugation (DGC) of SWCNT solutions to separate them according to their chirality. This process could separate semiconducting and metallic SWCNT by up to 99 wt% [GH11,H08].

1.4 Chemical functionalization of CNT

CNT have inert surfaces and tend to agglomerate and precipitate in common organic and inorganic solvents. This makes the processing of CNT difficult. Therefore, CNT are often functionalized through covalent and non-covalent functionalizations to enhance their dispersion in solvents. Adding functional groups to CNT also facilitates charge and load transfer between CNT and polymers in polymer-CNT composite systems [WLW&08]. Covalent functionalization forms chemical bonds between CNT and organic and inorganic species whereas non-covalent functionalization forms physical bonds between them. In both processes, CNT undergo chemical reactions that modify their structures and may impair their properties.

1.4.1 Covalent functionalization

In graphite, the angle (θ) between the π-orbital and the σ-orbitals is 90° whereas in CNT, due to the curvature of the tubular structure, this angle increases. The pyramidalization angle (θ_p) measures this deviation as [DDS95]:

$$\theta_p = \theta - 90°$$
$\qquad\qquad$ Equation 1.1

In thin CNT, θ_p is close to that of sp^3-hybridized carbon atoms (θ_p=19.5°); thus, favoring the reactions that lead to the saturation of π-bonds [H93]. Furthermore, unlike graphite, misalignment of the π-orbitals weakens the π-bonds in CNT, making them easier to break. **Figure 1.4** compares the pyramidalization angle and misalignment of the π-bonds in graphite and CNT. These bond distortions are larger in thinner CNT, making them more vulnerable to chemical oxidation [CL04].
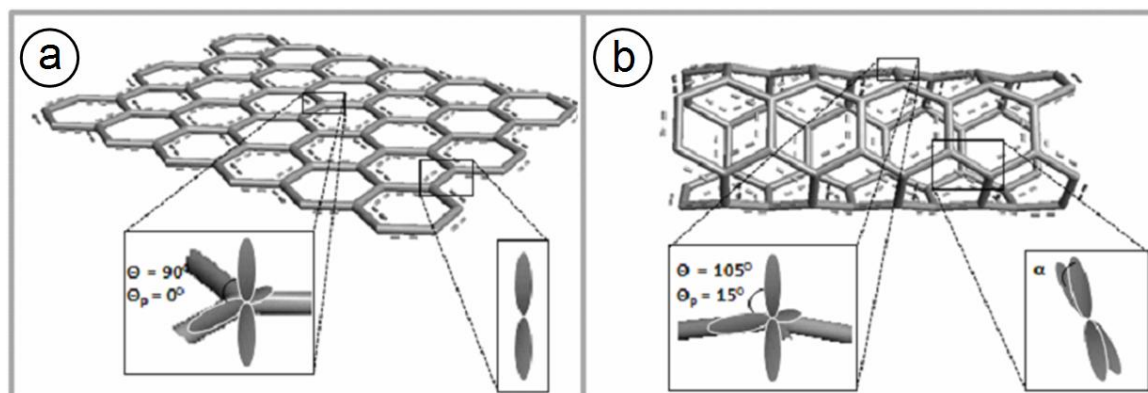
Figure 1.4 In graphene (a), the pyramidalization angle of the sp^2 hybridized carbon atoms is zero and the π-orbitals are perfectly aligned. In CNT (b), due to the curvature, the pyramidalization angle increases and the π-orbitals misalign.

CNT are often functionalized by oxidizing reagents such as sulfuric acid, nitric acid, or a combination of them. Reaction with aqueous oxidizers introduces carbonyl, hydroxyl, and carboxyl groups on CNT surfaces [MSB&01,HET95,EHB&96,LRD&98]. Other oxidizing reagents such as potassium permanganate [ZXV02], hydrogen peroxide [PL06], and ozone [SNB&06] have proven effective to functionalize CNT. The reaction begins at the end caps as they are more reactive than the sidewalls. The degree of oxidation depends on the reagent, reaction temperature, and reaction time. Oxidized CNT show enhanced dispersion in water and amide-type organic solvents [APL&00]. Shorter CNT are dispersed better than longer CNT. Oxidized CNT are often used as templates for further chemical functionalizations. The carboxyl groups on CNT have been successfully converted to aniline, octadecylamine, 4-tetradecylamide, and steary alcohol by using thionyl chloride (**Figure 1.5**) [CHH&98,HCH&99,HCB&02].

Sidewall functionalization of CNT is the subject of ongoing research. Carbene reaction using phenyl(bromodichloromethyl) mercury in toluene [CHH&98,CHF&98,HVH&01], nitrene addition [CHH&98,HVH&01], hydrogenation via Birch reaction [CHH&98,PSJ&0], fluorination [MHR&98,MCZ&99], alkylation [BLM99], arylation [BYK&01,BT01], and 1,3-dipolar cycloaddition [GKP&02] are some of the methods employed to functionalize CNT.
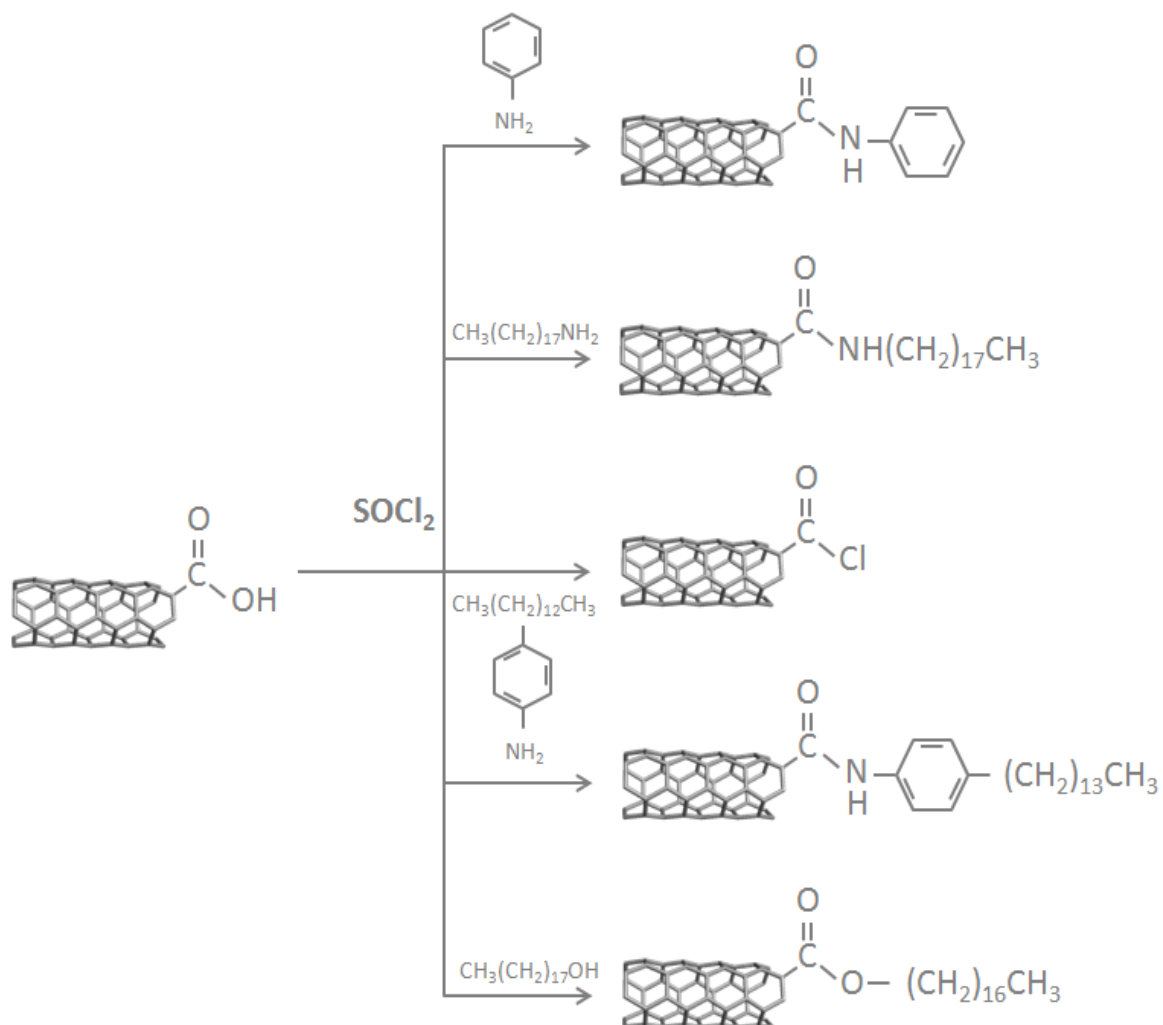
Figure 1.5 Covalent functionalization of SWCNT via conversion of carboxyl groups
[CHH&98,HCH&99,HCB&02].

1.4.2 Non-covalent functionalization

Non-covalent functionalization involves attachment of organic molecules to CNT surfaces through π-stacking and van der Waals interaction. Small molecules such as pyrene, porphyrin, and their derivatives interact with SWCNT though π-stacking. In fact, N-succinmidyl-1-pyrenebutanoate adsorbed onto SWCNT in N,N-dimethylformamide (DMF) or methanol is so resistant against desorption in aqueous solutions that further functionalization of SWCNT is possible [CZW01]. Guldi et al. [ERJ&06,GRJ&04,GRZ&05] reported that SWCNT functionalized with pyrene and porphyrin derivatives form electron donor/acceptor systems which generate charge separated species under photoexcitation. Biomacromolecules such as saccharides, polysaccharides, proteins, and enzymes have been attached to SWCNT [BS&06,CZW01,SSH&02]. Start et al. [SSH&02] reported that while SWCNT are insoluble in aqueous solutions of starch, they are soluble in aqueous solutions of starch-iodine. They argued that iodine rearranges the starch into a helical geometry and makes its hydrophobic cavity accessible to SWCNT. This process is reversible by enzymatic hydrolysis, using amyloglucosidase. Polymers are excellent wrapping materials for non-covalent functionalization of SWCNT. Poly (*m*-phenylenevinylene)-co-(2,5-dioctoxy-*p*-phenylene) [SSS&01], poly (2,5-pyridinlenevinylene)-co-(2,5-dioctoxy-*p*-phenylene)vinylene [SSN&02], poly (5-alkoxy-*m*-phenylenevinylene)-co-(2,5-dioctoxy-*p*-phenylene)-vinylene [SLG&03] are some of the polymers successfully used to improve the solubility of SWCNT in various solvents.

1.5 Structure of CNT

In graphite, the carbon atoms are sp^2 hybridized, forming three strong in-plane σ-bonds with 120° bond angle and a π-bond perpendicular to the σ-plane. The π-bond is responsible for the relatively high electronic conductivity within the planes and weak van der Waals interactions between them. In high quality graphite, stacking is ABAB and it is referred to as Bernal structure, named after John D. Bernal who first proposed this in 1924. Graphite belongs to space groups D_{6h}^4, and its unit cell has four carbons [R68].

The carbon atoms in CNT are normally sp^2 hybridized. However, as discussed in section 1.4.1, the degree of hybridization is a function of the diameter of CNT. In small diameter CNT, due to strain produced by the curvature, carbon atoms lose some of their sp^2 character and become somewhat sp^3. In large diameter CNT, carbon atoms are similar to those in graphite and show similar properties [ET95].

1.5.1 Structure of SWCNT

SWCNT are defined by their (n,m) indices and classified as: 1) zigzag SWCNT for m=0; 2) armchair SWCNT for n=m; and 3) chiral SWCNT for n≠m [DDS95]. The structures of a zigzag (8,0) and an armchair (8,8) CNT are shown in **Figure 1.6**. The synthesis of single chirality SWCNT has not yet been achieved whereas the diameter of SWCNT can be controlled by optimizing the synthesis conditions. Thus, a synthesized batch contains a variety of chiral SWCNT with mixed metallic and semiconducting properties. Separation techniques to isolate them have recently been developed [GBW10,MBS&09,KHL&03]. The simplest way to specify the structure of SWCNT is though the chiral vector, Ch [DDS95]:

$$C_h = na_1 + ma_2 \equiv (n, m) \qquad\qquad \text{Equation 1.2}$$

and

$$|C_h| = 0.246\sqrt{(n^2 + nm + m^2)} \qquad\qquad \text{Equation 1.3}$$

where a_1 and a_2 are the unit vectors of the hexagonal lattice with the same length of $a_0 = 2.46$ Å. The chiral vector connects equivalent crystallographic sites in the 2D graphene sheet (O and A in **Figure 1.7**). When lines AB' and OB (shown in **Figure 1.7**) are superimposed, a seamless SWCNT is formed.

The chiral angle is defined as the angle between the C-C bonds and the chiral vector and it is determined by:

$$\theta = \sin^{-1} \frac{\sqrt{3}m}{2\sqrt{(n^2 + nm + m^2)}} \qquad\qquad \text{Equation 1.4}$$

The diameter of SWCNT is given by:

$$d_t = \frac{a_0\sqrt{(n^2 + nm + m^2)}}{\pi} = \frac{a_0}{\pi}\sqrt{N} \qquad\qquad \text{Equation 1.5}$$

where $N = n^2 + nm + m^2$. If one considers SWCNT as a one dimensional molecule, one can define a unit cell along the tube axis. In general, the translation period (a) for SWCNT is determined from the chiral indices:

$$a = -\frac{2m + n}{d\Re} a_1 + \frac{2n + m}{d\Re} a_1 \qquad\qquad \text{Equation 1.6}$$

and

$$|a| = \frac{\sqrt{3(n^2 + nm + m^2)}}{d\Re}$$ Equation 1.7

where $\Re = 3$ if $\dfrac{n-m}{3n} = \text{int}$ and $\Re = 1$ if $\dfrac{n-m}{3n} \neq \text{int}$; d is the greatest common devisor of

(*n,m*). The direction of the axis of SWCNT is OB in **Figure 1.7**. It turns out that the unit

cell for armchair SWCNT has a width of a_1 (unit vector in the original 2D graphite sheet)

whereas the width of the unit cell for zigzang SWCNT is $\sqrt{3}a_1$. For low symmetry chiral

SWCNT, the width of the unit cell depends on the chirality of the tube. The number of

hexagons (*q*) and the number of carbon atoms (*n_c*) per unit cell of SWCNT are

determined by:

$$q = \frac{2(n^2 + nm + m^2)}{d\Re}$$ Equation 1.8

$$n_c = \frac{4(n^2 + nm + m^2)}{d\Re}$$ Equation 1.9
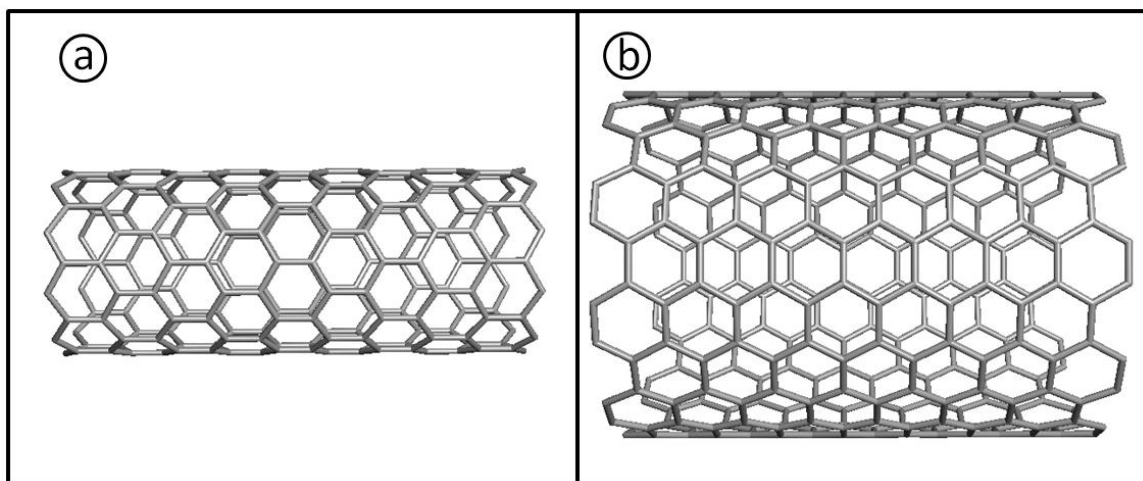
Figure 1.6 Structure of a) zigzag (8,0) and b) armchair (8,8) SWCNT .
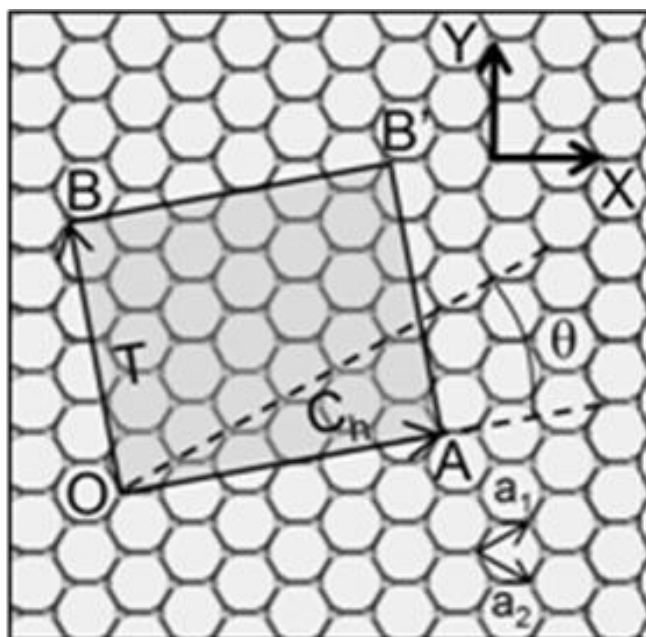
Figure 1.7 The formation of SWCNT from a 2D graphite sheet (Adapted from [DDS95]).

1.5.2 Structure of MWCNT

MWCNT contain at least two layers which makes them complex systems to study. Zhang et al. [ZZV&93] and Reznik et al. [RON&95] studied MWCNT systems, assuming that the individual tubes are concentric rather than scroll like. They argued that if the interlayer distance is 0.334 nm, the successive tubes should differ in circumference by approximately 2.1 nm. This, however, seems unlikely for the zigzag tubes as 2.1nm is not a precise multiple of 0.246 nm which is the width of the hexagon. This could be resolved if one assumes that the interlayer distance is 0.352 nm. Zhang et al. [ZZV&93] showed that, in zigzag MWCNT, the ABAB stacking observed in perfect graphite is only possible for small and isolated areas. For armchair MWCNT, the ABAB stacking is maintained and the interlayer distance is 0.340 nm. The energy gain due to adding new layers to MWCNT has been shown to be similar to adding an additional layer to graphite [CM93].

Table 1.1 Structural parameters of CNT (Adapted from[DDS95])

Symbol	Name	Formula	Value
$a_{c\text{-}c}$	bond length		1.421 Å
a	length of the unit vector	$\sqrt{3}a_{C-C}$	2.45 Å
a_1, a_2	unit vectors	$\left(\dfrac{\sqrt{3}}{2}, \dfrac{1}{2}\right)a_0, \left(\dfrac{\sqrt{3}}{2}, -\dfrac{1}{2}\right)a_0$	in (x,y) coordinate
k_1, k_2	reciprocal lattice vector	$\left(\dfrac{1}{\sqrt{3}}, 1\right)\dfrac{2\pi}{a_0}, \left(\dfrac{1}{\sqrt{3}}, -1\right)\dfrac{2\pi}{a_0}$	in (x,y) coordinate
C_h	chiral vector	$C_h = na_1 + ma_2 \equiv (n, m)$	n,m: integers
L	Circumference	$L = |C_h| = a_0\sqrt{n^2 + mn + m^2}$	$0 \le |m| \le n$
d_t	diameter	$d_t = \dfrac{L}{\pi} = \dfrac{a_0\sqrt{n^2 + mn + m^2}}{\pi}$	
θ	chiral angle	$\sin\theta = \dfrac{\sqrt{3}m}{2\sqrt{n^2 + nm + m^2}}$	$0 \le |\theta| \le 30°$
d	the highest common devisor of (n,m)		
d_R	the highest common devisor of (2n+m ,2m+n)	$\mathfrak{R} = 1 \quad \text{if } \dfrac{n-m}{3n} \ne \text{int}$ $\mathfrak{R} = 3 \quad \text{if } \dfrac{n-m}{3n} = \text{int}$	
q	number of hexagons per 1D unit cell	$N = \dfrac{2(n^2 + nm + m^2)}{d\mathfrak{R}}$	2N≡n_c/unit cell

1.6 Defects in CNT

SWCNT were initially considered as perfect cylindrical graphene sheets solely made of hexagons. However, theoretical and experimental studies have revealed various types of defects in SWCNT. Defects or defective sites modify the electronic structure and chemical reactivity of SWCNT and therefore they are aggressively studied by various groups. Ebbesen et al. [ET95] classified defects in SWCNT as: 1) topological defects; 2) rehybridization defects; and 3) incomplete bonding defects. Since MWCNT contain many concentric SWCNT, similar defects are observed in them.

1.6.1 Topological defects

Topological defects are produced by introducing rings other than hexagons in CNT. This is a direct consequence of Euler's theorem, assuming that all the carbon atoms in each ring are in the same plane. From Euler's theorem, the following relationship between the number and type of the rings necessary to close the network of a graphene sheet is derived:

$$3n_3 + 2n_4 + n_5 - n_7 - 2n_8 - 3n_9 = 12$$

This relationship states that, in the absence of other rings, one needs 12 pentagons to close the structure. Addition of one heptagon structure will increase this number to 13. So far, only the existence of pentagons and heptagons has been proven experimentally in CNT. Ebbesen et al. [ET95] argued that individual pentagon and heptagon can be thought of as point defects. Such point defects exist at low concentration in CNT except close to the tips where they polygonize the structure.

Stone-Wales defects (**Figure 1.8**) are topological defects formed by the rotation of two

carbon atoms relative to the midpoint of the chemical bond to transform four hexagons

into two pentagons and two heptagons [AII93]. Stone-Wales defects produce a small

local deformation in CNT, but as they become more concentrated, the deformation

becomes larger. These defects annihilate at elevated temperatures.
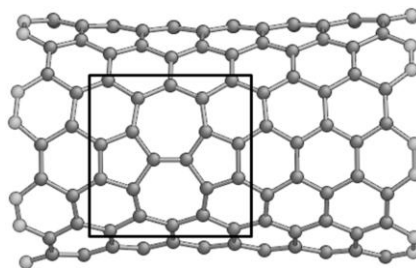
Figure 1.8 The stone-Wales defects in CNT due to formation of pentagon and heptagons.

1.6.2 Rehybridization defects

The carbon atoms in graphite are sp^2 hybridized. As the 2D graphite sheet is bent

to form SWCNT, it loses some of its sp^2 character and gains $sp^{2+\alpha}$ character where α

depends on the degree of curvature. The complete folding of the sheet results in the

formation of a sp^3 defect line in SWCNT. Such defects which are produced by the

transformation of the sp^2 bonds to sp^3 bonds are also referred to as sp^2-defects; this

involves a pair of carbon atoms since a double bond is perturbed. Ebbesen et al. showed

that, in graphene sheets, line defects having sp^3 character are formed preferentially along

their symmetry axis. In hexagonal network of graphene, there are different pairs of carbon

atoms along which sp^3 type line defects can form. Examples of such defect lines are

shown in **Figure 1.9** [HEF&94].

In mechanically deformed CNT, the walls appear to ripple which indicates the presence of ridges with sp^3 character. Since the symmetry axis of graphene and the long axis of CNT are not always aligned, any defect line will be discontinuous on atomic levels. In MWCNT, since each shell has its own helicity, the discontinuity will not be super-imposable.

The sp^2-defects can be also formed by the oxidation of sp^2 bonds in SWCNT due to chemical reactions. This reduces the number of available sp^2-like final states and modifies the electronic structure of SWCNT. Depending on the extent of oxidation, the modification of perfect SWCNT can be localized, forming small defect patches, or occur uniformly along the tubes.

1.6.3 Incomplete bonding defects

Point defects, vacancies, and dislocations are incomplete bonding defects which are regularly observed in graphite. However, Ebbesen et al. [ET95] argue that such defects are rare in the SWCNT produced or annealed at high temperatures as they are thermodynamically unstable, but they could exist in SWCNT produced by catalytic methods.

Figure 1.9 Examples of conformations of defect lines that can occur in graphene sheets [HEF&94].

1.7 Characterization of CNT

In order to understand the chemical, physical, and electronic properties of CNT, various characterization methods are employed.

1.7.1 Resonance Raman spectroscopy

Raman spectroscopy is a fast method widely used to characterize CNT. This technique relies on inelastic scattering (Raman scattering) of a beam of laser by a sample. The laser light interacts with molecular vibrations, or other excitations in the sample, resulting in energy shift of the laser photons. Raman spectroscopy is conventionally performed by green, red or near-infrared laser which produce weak signals. When the wavelength of the exciting laser is set within the electronic transitions between the valence and conduction bands of CNT, the intensity of some Raman-active vibrations increases by a factor of 10^2-10^4 due to the coupling between the electrons and phonons [P99]. This is referred to as resonance enhanced Raman spectroscopy.

All allotropes of carbon are active in Raman spectroscopy i.e. their peak positions and intensities vary in the Raman spectra. The characteristic Raman features of SWCNT (shown in **Figure 1.10**) include [DDS&05]: 1) radial breathing mode (RBM) (< 200 cm^{-1}) whose frequency depends on the diameter of SWCNT; 2) defective graphite band (D-band) (1340 cm^{-1}) corresponding to incomplete bonding defects in SWCNT; 3) graphite band (G-band) (between 1500 cm^{-1} and 1600 cm^{-1}) corresponding to stretching modes in SWCNT; 4) G'-mode corresponding to the first overtone of the D-line (2380 cm^{-1}) ; and 5) combinations of D and G modes (2840-2940 cm^{-1}). The spectrum in **Figure 1.10** was recorded for a SWCNT sample with the average diameter of 1.07 nm using a laser beam

with the wavelength of 1064.5 nm. The Raman line shapes differ for metallic and semiconducting SWCNT which allows determining the electronic properties of SWCNT [DDS&05].
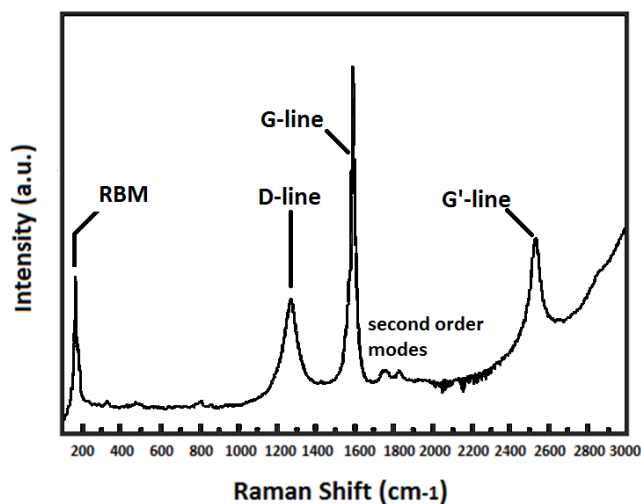
Figure 1.10 The spectral features in a Raman spectrum of SWCNT with an average diameter of 1.07 nm (λ_{laser}= 1064.5 nm) [BE05].

1.7.2 Photoluminescence spectroscopy

In photoluminescence spectroscopy, a laser beam electronically excites electrons in the sample and when they de-excite spontaneously, they photoluminesce. In SWCNT, photoluminescence occurs due to the recombination of electron-hole pairs at the band gap. Typically, SWCNT exist as mixed bundles of metallic and semiconducting tubes. Therefore, the luminescence of semiconducting SWCNT is often relaxed in the conducting ones and quenched. Optical transitions in semiconducting SWCNT are attributed to transitions between the corresponding van Hove singularities (vHS) in the conduction and valence bands. The explanation of vHS is discussed in **Appendix A**. The

transitions are called E_{11}, E_{22},... where E_{11} is the real band gap and the remaining sharp

transitions are pseudo-gaps and are due to vHS maxima (**Figure 1.11a**) [WBT04]. The

photoluminescence emission is due to the E_{11} transition. The energy of the vHS is related

to the diameter and chirality of SWCNT; thus, the emission spectrum is the superposition

of distinct E_{xx} transitions appearing at different wavelengths [OBH03].

Figure 1.11b shows a surface plot of photoluminescence intensity as a function of

excitation and emission wavelengths. The peaks having excitation wavelengths near 700

nm are due to optical absorption in E_{22} transitions followed by emission in E_{11} transitions,

(**Figure 1.11a**). Therefore, the position of the peaks provides the E_{11} and E_{22} values for

semiconducting CNT [WBT04].

1.7.3 Infrared spectroscopy

Infrared (IR) spectroscopy of materials probes the vibrational transitions. IR

spectroscopy is mainly used to characterize the organic moieties produced on CNT due to

chemical functionalization. For instance, Saito et al. [SMT&02] employed IR

spectroscopy to characterize MWCNT modified by amino compounds. Wang et al.

[WZL&04] and Pereira et al. [PFO&04] used IR spectroscopy to investigate the catalytic

properties of MWCNT.
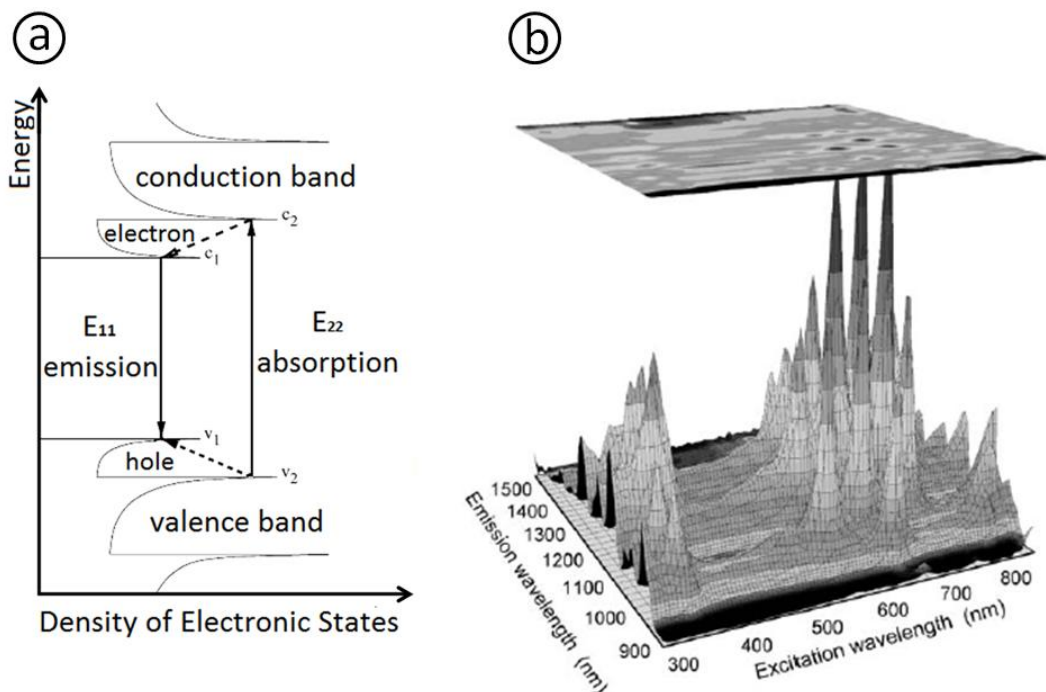
Figure 1.11 Transitions between vHS in SWCNT due to optical de-excitations in photoluminescence spectroscopy (a) surface plot of photoluminescence (fluorescence) intensity as a function of excitation and emission wavelengths for a sample of SWNT in aqueous surfactant suspension. Each peak arises from a distinct (n,m) structural species (b).

1.7.4 Scanning tunneling microscopy (STM)

STM is used to characterize the electronic properties of metallic surfaces. In STM, a conducting tip is brought near to a surface and a voltage difference applied between the two allows electrons to tunnel through the vacuum between them. The resulting tunneling current is a function of tip position, applied voltage, and the local density of states (DOS) of the sample [B93]. Information is recorded by monitoring the current as the tip's

position scans across the surface, and is usually displayed in image forms.

To perform STM characterization, CNT are required to be deposited on conducting substrates such as gold or highly ordered pyrolytic graphite (HOPG) graphite. STM determination of SWCNT structure has been done by various groups and has confirmed the dependence of their electronic properties on their chirality and diameter [HSO92,MDW92,SFD&92]. Atomically resolved STM images have helped to measure the chiral angle of different types of SWCNT.

1.7.5 X-ray photoelectron spectroscopy (XPS)

XPS spectra are obtained by irradiating a material with a beam of X-rays while simultaneously measuring the kinetic energy and the intensity of the electrons escaping from its top layers. The typical sampling depth of XPS is 0.5-5 nm, depending on kinetic energy and take-off angle of photoelectrons [B98]. XPS is employed to investigate the chemistry of CNT. Droppa et al. [DHC02] used XPS to study the incorporation of nitrogen in CNT. The C 1s peak in the spectrum showed a shift and asymmetric broadening to higher binding energies. This shift is due to the polar character of the carbon-nitrogen bond and is evidence of nitrogen incorporation in the tubes. Lee et al. [LCL&03] showed that the XPS spectrum of undoped SWCNT is dominated by C-C peaks (284.3 eV and 285 eV), and C-O peaks (288.5 eV). Chen et al. [CWS99] compared the XPS spectra of MWCNT and graphite and noticed differences in peak positions, full width at half maximum, and fine structures in the C 1s peaks.

1.7.6 Near edge X-ray absorption fine structure spectroscopy (NEXAFS)

NEXAFS is a synchrotron technique that probes the transition energies of core electrons excited to partly or fully unoccupied bands (ground to excited state transitions). This provides element specific and sometimes bond sensitive information and reveals the chemical properties of the samples [S92]. Kramberger et al. [KRS&07] used high resolution NEXAFS to study the electronic properties of SWCNT; they observed a C 1s →π* fine structure which they attributed to vHS of the SWCNT DOS. However, since the sample was a powder and a mixture of various types of SWCNT, they could not assign the transitions. Using the density functional theory calculations with the help of equivalent core hole approximation, Gao et al. [GWA&09] showed that such fine structures at the π*-resonance are related to the diameter and chirality of SWCNT. While these results are intriguing, more evidence is required to confirm them. The fine structure observed at the π*-resonance peak is so subtle that it could be due to various reasons, including sample contaminations and beamline artifacts. So far, despite my many efforts, I have not been able to convincingly reproduce these results.

X-ray linear dichroism (XLD) is defined as the changes in absorption of linearly polarized X-rays as one varies the angle between the electric vector (**E**) of the light and the orientation axis of the sample (e.g. the long axis of CNT). XLD at the C 1s →π* transition in CNT is a significant effect. XLD can be used to evaluate the quality of CNT since, in high quality CNT, XLD is large and as the quality lowers the XLD decreases too [BHB04]. However, if multiple CNT are being studied, CNT are required to be perfectly aligned because if they are randomly oriented, the XLD is reduced due to the random

orientations and thus it does not reflect the quality of CNT (**Figure 1.12**) [HBS&06].

Previously reported XLD measurements of CNT samples do not account for their random

orientation; therefore, the results could be somewhat misleading [SKR&03].

The quality of CNT can also be evaluated by taking the sp^2/sp^3 ratio. This is done

by measuring the area under the C 1s $\rightarrow\pi^*$ and C 1s$\rightarrow\sigma^*$ transition peaks. However, for

this to be valid, the X-rays should have circular polarization (left or right) to cancel XLD

in CNT. See **Appendix B** for the evaluation of circular polarization in beamline 10ID1

(Spectromicroscopy beamline) at the Canadian Light Source (CLS).

NEXAFS is widely used to investigate the chemical properties of SWCNT prior to

and after chemical functionalization. Kuznetsova et al. [KPY&01] used NEXAFS to

investigate the concentration of oxygen surface groups on SWCNT due to heat treatment.

Banerjee et al. [BHB04] employed NEXAFS to verify the formation of oxygen groups

such as carbonyl, hydroxyl, and carboxyl groups on SWCNT surfaces due to ozonation.

In this thesis, I used spatially resolved NEXAFS in transmission mode to evaluate

the quality of SWCNT bundles and individual MWCNT. The detailed description of the

measurements is discussed in the following chapters. This study relies on probing the

XLD at the C 1s $\rightarrow\pi^*$ transition in CNT i.e. the XLD is strong in high quality CNT, and

rather small in highly defective CNT. I also used NEXAFS to map chemical components

that exist on raw and functionalized CNT. This was conducted by deconvoluting the

NEXAFS spectrum of CNT which is a linear combination of the NEXAFS spectrum of

each chemical component.
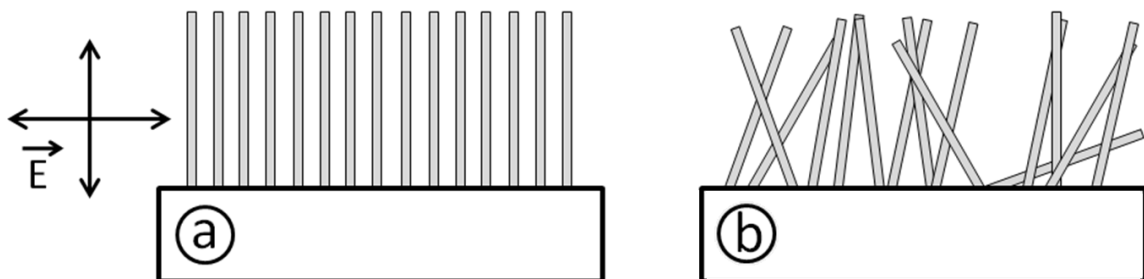
Figure 1.12 XLD is a measure of the quality of CNT if they are perfectly aligned perpendicular to the substrate (a). If CNT are randomly oriented, XLD reflects both quality and orientation of CNT (b).

1.7.7 Transmission electron microscopy (TEM)

TEM is often employed to characterize structural properties of CNT. Kiang et al. [KEA&98] measured the interlayer distance in MWCNT by TEM to be in the range of 0.34 to 0.39 nm, depending on their diameter. This distance is larger than that measured for graphite which is attributed to the curvature and weaker interaction between the layers in MWCNT than in graphite. This result was supported by quantum calculations of Tanaka et al. [TAA&97]. High resolution TEM (HRTEM) is a powerful method to study structural order in CNT [GBD&04]. An example of HRTEM image of an AD-MWCNT recorded by FEI Titan 80-300 Cryo TEM is presented in **Figure 1.13**.
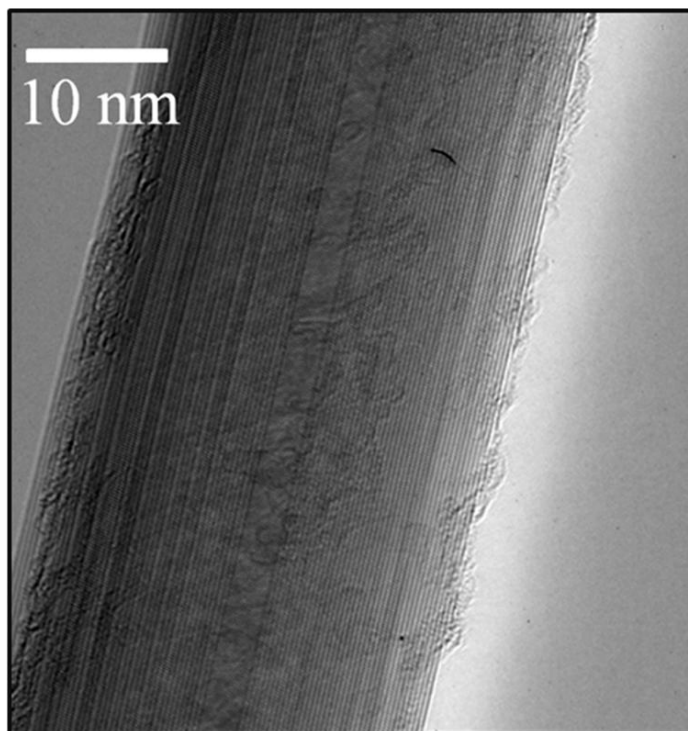
Figure 1.13 High resolution TEM image of an AD-MWCNT recorded by FEI Titan 80-300 Cryo TEM.

1.7.8 Electron energy loss spectroscopy (EELS)

EELS characterizes the optical and electronic properties of materials by probing their plasmon and core electron excitations at low loss and core loss regimes, respectively. [E96] Plasmons are collective oscillations of a free or quasi-free electron cloud and occur in the low energy loss range (10-50 eV) of the EELS spectra. Core loss EELS studies excitations of core electrons to unoccupied final bands, using the inelastic scattering of high energy electrons. At small scattering angles where only dipole transitions are allowed, EELS and NEXAFS are similar i.e. the C 1s electrons are excited to states with *p*-like symmetry. Therefore, similar to NEXAFS, EELS provides element specific and

bond sensitive information. EELS coupled to a TEM has been used to characterize pristine [LHB&03], thermally annealed [RS02], fluorinated [HTS&02], and aminopolymer-functionalized [LHB&03a] CNT. In general, the energy resolution in NEXAFS is better than that in TEM-EELS, although the latest generation of aberration compensated microscopes are now achieving comparable spectral resolution.

EELS can also provide information about bond orientations and structural anisotropies since the transition intensities in EELS spectra of anisotropic materials are determined by the orientation of $\mathbf{q}$ relative to the transition moment vector. Leapman et al. [LFS&83] previously proposed a procedure to perform $\mathbf{q}$-dependent measurements in anisotropic samples. This involves optimization of the collection angle of the EELS spectrometer to selectively collect scattered electrons with small inelastic scattering angles. Stephan et al. [SAC96] used this method to investigate spectral variations across an isolated MWCNT and found differences between the spectra of the edge and top of the tubes, which they attributed to $\mathbf{q}$-dependent scattering due to the curvature (the definition of edge and top of CNT is presented in chapter 4). Stephan et al. normalized the spectra to the C 1s $\rightarrow \pi^*$ transition peak; therefore, they only investigated the variations of the C 1s $\rightarrow \sigma^*$ transition peak.

In this thesis, similar observations are made and the understanding of $\mathbf{q}$-dependent EELS of CNT is significantly extended. I examined an alternative method to perform $\mathbf{q}$-dependent measurements and observed a significantly larger dichroism at both π^* and σ^*-resonance peaks than that observed by Stephan et al. The principles and experimental methods of this study are discussed in the following chapters.

1.7.9 X-ray diffraction

X-ray diffraction occurs in crystals when the repeating distance is about the same as the wavelength of the X-ray. X-ray diffraction provides information about interlayer spacing, structural strain and impurities in SWCNT. The X-ray diffraction spectrum of MWCNT contains a graphite-like (0 0 2 l) peak related to the interlayer spacing and a set of (h k 0) peaks due to the honeycomb lattice of single graphene sheet. The position and shape of the (0 0 2 l) peak is determined by the level of graphitic impurities and the diameter distribution of the individual tubes. The (h k 0) peaks are more asymmetric than those in the spectrum of graphite due to the curvature.

1.8 Outline of the thesis

Chapter 2 describes the fundamental principles of synchrotron radiation, NEXAFS spectroscopy, and scanning transmission X-ray microscopy (STXM). Chapter 2 also describes the inelastic electron scattering process, and EELS spectroscopy in a transmission electron microscope (TEM) in scanning transmission electron microscopy mode (STEM).

Chapter 3 describes STXM and EELS data acquisition modes and outlines the sample preparation methods used in this work including solution casting and vacuum drying processes. Modification of CNT by focused ion beam (FIB) method is also discussed.

Chapter 4 explores the X-ray linear dichroism (XLD) in individual MWCNT from different sources measured by STXM. This chapter is in manuscript format since it has been published in *Small*. For this work, I preformed sample preparations, STXM measurements, data analysis, and prepared the first draft of the paper.

Chapter 5 presents the applications of STXM to qualitatively and quantitatively map the chemical components in pristine, purified, and dodecyl functionalized CNT. This chapter is presented in manuscript format since it has been published in the *Journal of American Chemical Society* (*JACS*). The purification and functionalization of SWCNT samples were done at the National Research Council (NRC) of Canada by Dr. Jingwen Guan in Dr. Benoit Simard's research group. I performed all STXM measurements and data analysis required to understand chemical and physical changes in SWCNT due to the purification and functionalization processes, and prepared the first draft of the paper.

Chapter 6 discusses the applications of **q**-dependent EELS to study electron linear dichroism (ELD) and structural anisotropy in CNT. The results are compared to those obtained by polarization dependent NEXAFS. I preformed the experimental measurements with the help of David Rossouw and Professor Gianluigi Botton at the Canadian Centre for Electron Microscopy (CCEM).

Chapter 7 summarizes the results and contributions of this thesis and proposes future work.

Chapter 2

Methods

This chapter describes the principles of synchrotron radiation, near edge X-ray absorption fine structure spectroscopy (NEXAFS), and scanning transmission X-ray microscopy (STXM) with details of the ALS 5.3.2.2 and CLS 10ID1 beamlines and X-ray microscopes. It then discusses near edge electron energy loss spectroscopy (EELS) in a transmission electron microscope (TEM), followed by a description of FEI Titan 80-300 Cryo TEM which was employed in this thesis.

2.1 Synchrotron radiation

Charged particles emit electromagnetic radiation when accelerated by changing speed, or moving in curved trajectories at a constant speed. The radiated field propagates in all angular directions except in the direction of acceleration. When the electron speed (v) is significantly smaller than the speed of light (c) (non-relativistic condition), the radiation shows a dipolar pattern with the frequency comparable to the angular frequency (ω) of the electron (**Figure 2.1a**). As the electron speed approaches the speed of light, due to Doppler effect and Lorentz contraction, the radiation frequency becomes higher and on the order of $\gamma^3\omega$, where γ is the Lorentz factor [A99]:

$$\gamma = \frac{1}{\sqrt{1-\beta^2}} = \frac{1}{\sqrt{1-(\frac{v}{c})^2}} \qquad\qquad \text{Equation 2.1}$$

and

$$\beta = \frac{v}{c} \qquad\qquad\qquad \text{Equation 2.2}$$

At such a relativistic speed, the radiation pattern becomes distorted and turns into a narrow cone with angular spread of $\Delta\phi$ (**Figure 2.1b**) where $\Delta\phi \approx \gamma^{-1}$.
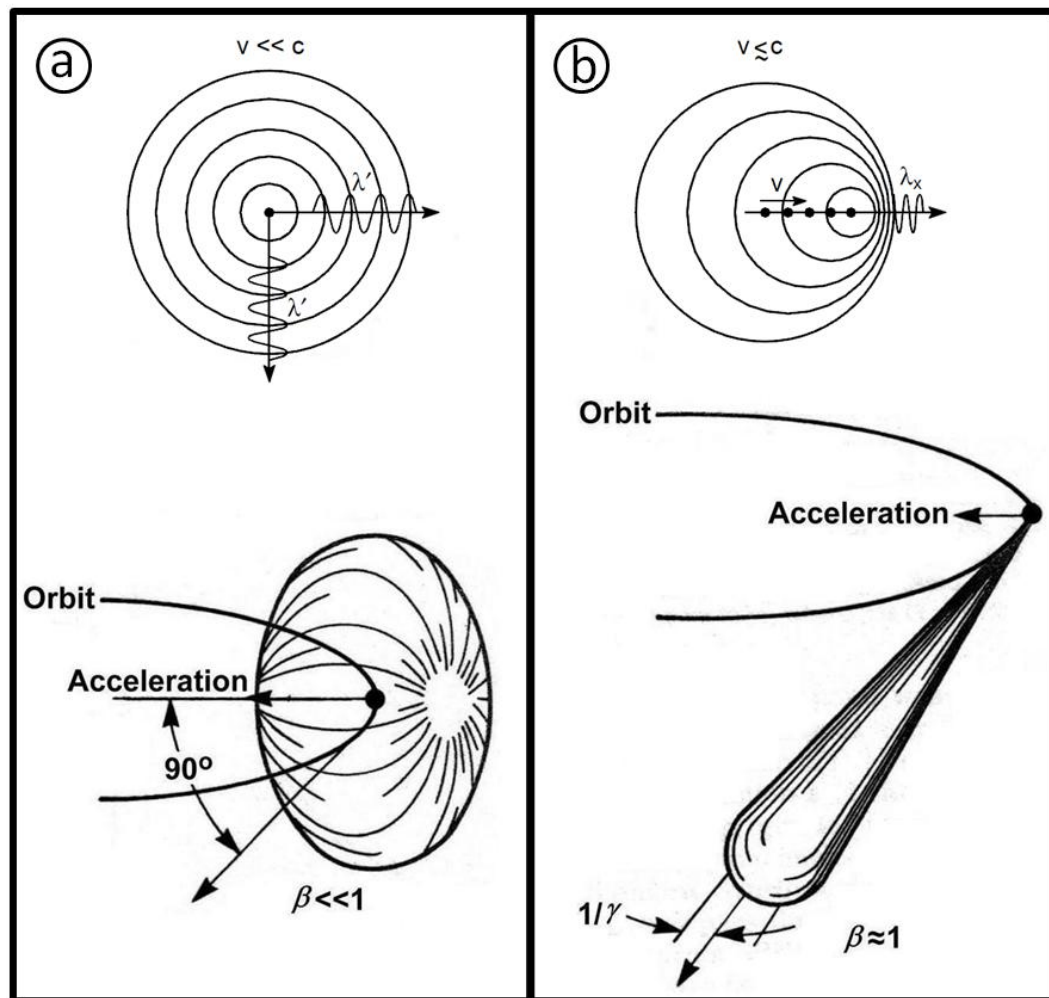
Figure 2.1 Radiation patterns of electrons in a circular motion under a) non-relativistic ($\beta \ll 1$) b) relativistic conditions ($\beta \approx 1$) (Adapted from [A99]).

Synchrotron radiation is defined as the radiation emitted by electrons travelling at relativistic speeds along a quasi-circular path whose curvature radius ranges from tens to hundreds of meters [A99]. Synchrotron radiation was first observed in General Electric synchrotron accelerator by Frank Elder, Anatole Gurewitsch, Robert Langmuir, and Herb Pollock [B98b]. A synchrotron accelerator is a particle accelerator with well synchronized electric and magnetic fields [A99]. Synchrotron facilities have evolved over time from first generation parasitic sources with low brightness whose main function was to study particle physics to dedicated second and third generation light sources with high energy and brightness radiation.

The first generation of synchrotron accelerators were parasitic as they were originally built to study subatomic particles and high energy physics (HEP). The first use of accelerators for spectroscopy studies was by Madden and Codling at the Synchrotron Ultraviolet Radiation Facility (SURF, Gaithersburg, MD) where they revealed previously unobserved features in the absorption spectra of noble gases due to inner shell and two-electron excitations [C73]. This was immediately followed by numerous studies on metal films at European and Asian facilities such as Frascati laboratory (1.15 GeV synchrotron) in Italy, Deutsches Elektronen-Synchrotron (6 GeV synchrotron) in Germany and Institute for Nuclear Studies-Synchrotron Orbital Radiation (750 MeV synchrotron) in Japan [B98b]. With rapidly elevating interest in synchrotron radiation for solid-state research, the next major progress took place with the development of electron storage rings. In many synchrocyclotrons used for particle physics studies, the beam undergoes a repeated sequence of injection, acceleration, and extraction at rates up to 50 Hz. In

contrast, in a storage ring, a continuous (or pulsed) beam of electrons is circulated at a fixed energy for a long period of time (up to several hundred hours). Storage rings improve beam stability, reduce radiation hazard, and can be operated at higher brightness than synchrocyclotrons [A99,H04].

The second generation of synchrotron accelerators were dedicated light sources with a large number of beamlines and experimental end-stations. These facilities had low brightness since the synchrotron radiation was generated by bend magnets. Many of the first generation synchrotron facilities (e.g. Stanford Synchrotron Radiation Laboratory (SSRL)) were ultimately upgraded into second generation facilities and contributed to advancement of various characterization techniques such as photoemission, extended X-ray absorption fine-structure spectroscopy (EXAFS), and high-resolution protein crystallography.

With the development of insertion devices (undulators and wigglers) in the early 1990's, the third generation of synchrotron facilities emerged. Insertion devices produce higher brightness than bend magnets. Brightness is defined as the number of photons emitted per unit time, per unit source area, per unit solid angle [A99]. An undulator consists of a set of closely spaced magnets with periodic change in polarity (**Figure 2.2**). The electrons traversing this periodic magnetic structure oscillate and radiate energy in a very different spectral pattern. The electromagnetic radiation produced by an undulator is very intense and concentrated in a narrow energy band. The polarization of the emitted radiation can be controlled by modifying the relative position of permanent magnets to induce different electron trajectories through the undulator. Wigglers are similar to

undulators with higher magnetic fields and fewer magnetic dipoles. Wigglers produce a

broadband electromagnetic radiation much like bend magnets but with higher intensity

and a shift of the spectral distribution to higher energies. **Figure 2.2** compares the shape

and spectral distribution of the radiation produced by bend magnets, wigglers and

undulators.
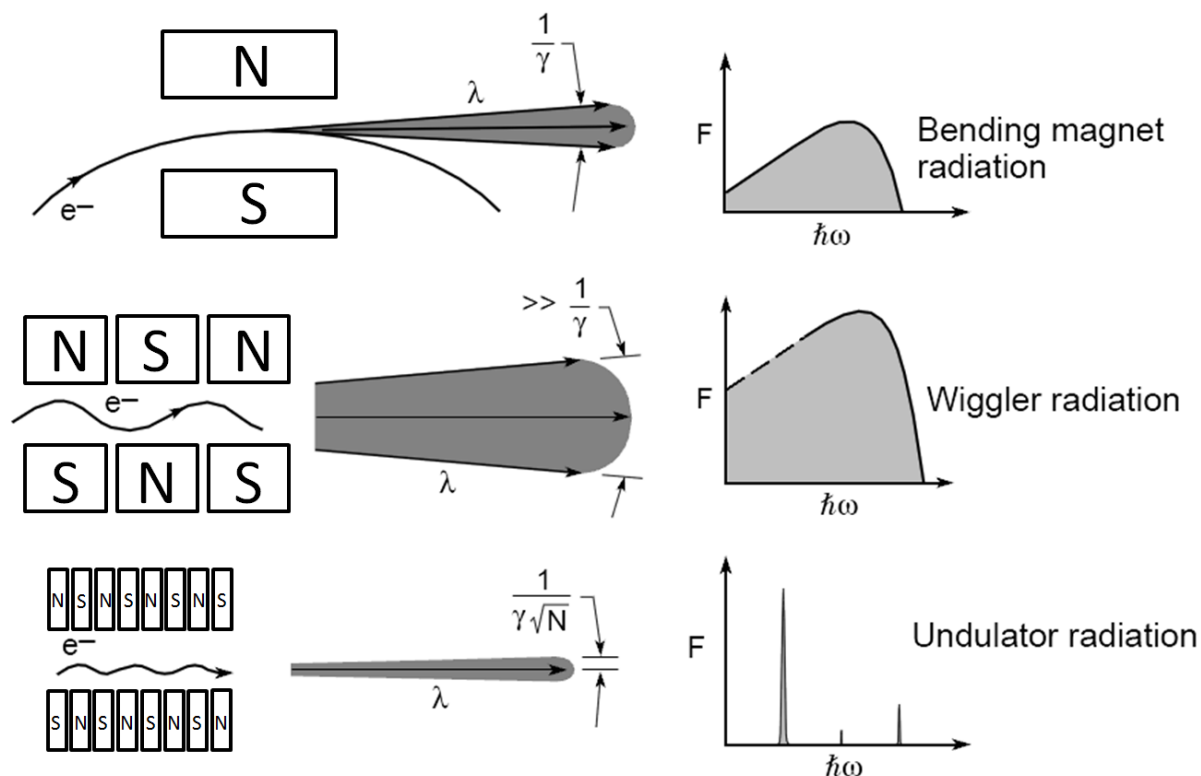
Figure 2.2 The shape of the emitted cone and bandwidth of the radiation produced by

bend magnet, wiggler, and undulator (Adapted from [A99]).

At present, the next revolution in synchrotron science is taking place. The fourth generation of synchrotron radiation sources are accelerator-based free electron lasers. Conventionally, a free electron laser (FEL) is produced by an electron beam traversing an undulator which interacts with a co-propagating photon beam of the correct wavelength. This induces bunching of the electron beam which results in coherent emission. However, the SPring-8 FEL, the Linac Coherent Light Source (LCLS), and the European X-ray free electron laser (European XFEL) will use a different approach to produce FEL based on the self-amplified stimulated emission (SASE) process. In SASE, lasing starts from the random microbunching in the electron beam instead of being coherently produced by an input seed laser source. FEL are powerful sources of electromagnetic radiation which can achieve extremely short pulses ($\sim$10 fs), high peak power, and high brightness (10^{30} versus 10^{20} in brightness units) [A99].

Synchrotron radiation is becoming a common tool for materials characterizations due to its high brightness, high spectral resolution, high temporal resolution, tunable photon energy, and tunable polarization. In this thesis, I have used soft X-rays from two third generation light sources, Advanced Light Source (ALS) in Berkeley, California and Canadian Light Source (CLS) in Saskatoon, Saskatchewan, to study properties of carbon nanotubes (CNT) in detail.

2.2 NEXAFS spectroscopy

NEXAFS spectroscopy is a synchrotron technique which was initially developed to study the electronic structure and local bond orientation of small organic molecules bonded to surfaces. In NEXAFS, a core electron is excited by X-rays to half occupied or unoccupied final states. The resulting core hole is then filled through the Auger process or by an electron from a valence shell, along with emission of an X-ray fluorescent photon. NEXAFS spectra can be recorded by measuring the transmitted photons, emitted electrons, Auger electrons, X-ray fluorescent photons, luminescent photons, or a combination of them. Absorption edges of different elements are generally separated in energy so that they can be studied independently.

X-ray absorption is characterized by an X-ray absorption cross section (σ_x), defined as the number of absorbed photons per unit time divided by the number of incident photons per unit time per unit area [S92]:

$$\sigma_x(E) = \frac{P_{if}(E)}{F_{ph}(E)}$$
Equation 2.3

Transition probability is derived by Fermi's golden rule which describes a transition from an initial state $|i\rangle$ to a final state $\langle f|$ induced by a time-dependent perturbation ($V(t) = \overline{V}e^{-i\omega t}$) [S92]:

$$P_{if}(E) = \frac{2\pi}{\hbar}\left|\langle f|V(E,t)|i\rangle\right|^2 \rho_f(E)$$
Equation 2.4

where $\rho_f(E)$ is the energy density of final states.

The X-ray absorption cross section is obtained by evaluating $V(E,t)$ and applying the

electric dipole approximation [S92]:

$$\sigma_x(E) = \frac{4\pi^2 e^2}{m^2 c\omega} \left| \langle f | e \bullet p | i \rangle \right|^2 \rho_f(E)$$
Equation 2.5

where e and m are the charge and mass of the electron, respectively; ω is the angular frequency of the electromagnetic wave, and c is the speed of light; e is the unit potential vector and p is the sum of the linear momentum operators of the electrons.

Optical oscillator strength (f) is a parameter related to the X-ray absorption cross section used to evaluate electronic transitions [S92]:

$$f = \frac{2}{m\hbar\omega} \left| \langle f | e \cdot p | i \rangle \right|^2$$
Equation 2.6

2.2.1 X-ray linear dichroism

The matrix elements depend on the angle (θ) between the electric field vector (**E**) of the X-rays and the electronic transition moment; therefore, the absorption of the X-rays by anisotropic solids or aligned molecules depends on θ [S92]:

$$I = \frac{2}{m\hbar\omega} \left| \langle f | e | \cdot | p | i \rangle \right|^2 \cos^2 \theta$$
Equation 2.7

Figure 2.3 shows the behavior of horizontal and vertical CNT when they are probed by X-rays with linear horizontal polarization. CNT are anisotropic molecules whose π* and σ* orbitals have different spatial orientations. Thus, when **E** is parallel to the long axis of the CNT (θ=90°), all C1s→π* transitions are forbidden and all C1s→σ* transitions are allowed (**Figure 2.3a**). When **E** is orthogonal to the long axis of the CNT, half of the C1s→π* transitions and half of the C1s→σ* transitions are allowed (θ=0°) (**Figure 2.3b**) [NDO&08].
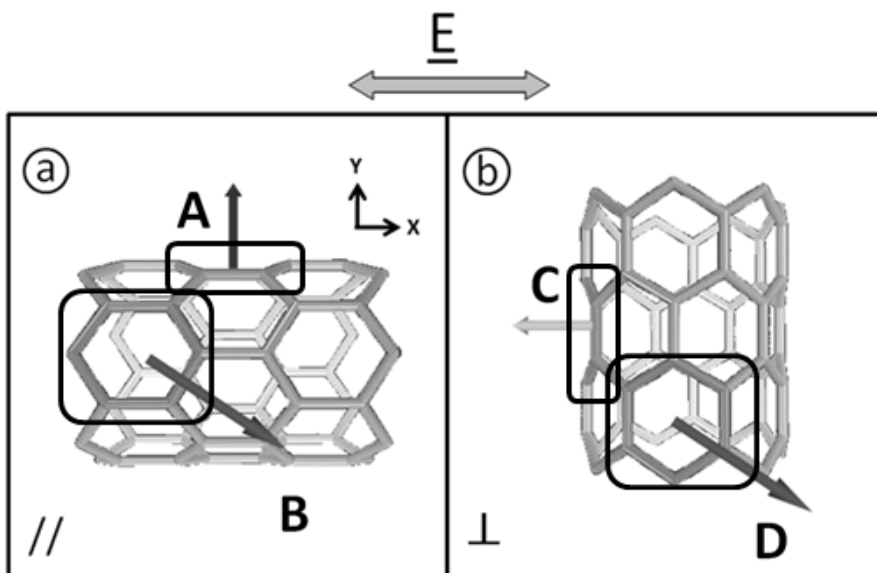
Figure 2.3 X-ray linear dichroism in CNT: a) when **E** is parallel to the long axis of the CNT, all the C1s→π* transitions are forbidden (A, B: arrows) and all the C1s→σ* are allowed (A, B: hexagons); b) when **E** is orthogonal to the long axis of the CNT, half of the C1s→π* transitions (C: arrow) and half of the C1s→σ* transitions (D: hexagon) are allowed.

2.2.2 Detection modes

When a beam of X-rays passes through a sample, it loses intensity due to X-ray absorption. In addition, X-rays are redirected spatially by scattering (X-ray photons which are not absorbed by the sample). Transmission is the most direct method of measuring X-ray absorption, and the one I used in this thesis. The transmitted signal is then converted to optical density (OD) by the Beer-Lambert law:

$$OD = -\ln(\frac{I}{I_0}) = \mu\rho l \qquad\qquad\qquad \text{Equation 2.8}$$

where I_0 and I are the incident and transmitted X-ray photon flux (photons/s) respectively, μ is the energy dependent mass absorption coefficient (cm^2/g), ρ is the density (g/cm^3) of the material, and l is the sample thickness (cm). The elemental mass absorption coefficient is obtained from the sum of the weighted atomic photoabsorption cross sections given by [H77,H79,H82]:

$$\mu_x(E) = \frac{n_m N_A}{A}\sigma_x(E) \qquad\qquad\qquad \text{Equation 2.9}$$

where n_m is the density (g/cm^3), N_A is the Avogadro's number (atom/mole), A is the atomic weight of a compound, and σ_x is the atomic photoabsorption cross section ($cm^2/atom$). The values for elemental mass absorption coefficients and X-ray absorption cross sections in the soft X-ray region have been tabulated previously [HGD93].

Transmission detection requires thin samples (~100 nm at $E_{photon} < 1000$ eV) to avoid absorption saturation. However, if the samples are too thin, the quality of the data reduces due to a decreased signal-to-noise ratio. At the C 1s edge, the optimum thickness is between 50-200 nm for unit density samples ($\rho \approx 1$). Thicker samples (1-2 microns) could be used for samples with lower densities such as bacterial cells or hydrated polymer gels, or if the measurements are performed at higher energy edges ($E_{photon} > 1000$ eV). In this case, one is limited by the natural thickness of CNT samples. Fortunately, single-walled carbon nanotube (SWCNT) bundles or individual multi-walled carbon nanotubes (MWCNT) have diameters between 50-200 nm which is ideal for STXM characterization at carbon, nitrogen, and oxygen edges. However, for engineering applications, thinner

MWCNT and individual SWCNT are needed to be able to harness their useful electrical, physical, and mechanical properties. The technique developed in this thesis can eventually be used for NEXAFS studies of thin CNT as ZP technology advances.

2.2.3 NEXAFS spectra of graphite, SWCNT and MWCNT

The C1s NEXAFS spectrum of graphite, SWCNT bundles and MWCNT are plotted in **Figure 2.4**. The assignment of the spectroscopic features in CNT is based on similar features in graphite as well as comparison to compounds containing oxygen groups. The most intense peaks are at 285.1 eV and 292.2 eV are due to transitions to anti-bonding π^* and σ^* bands. These peaks are sharp indicating that the final states have relatively long lifetimes. The relationship between the lifetime of a transition and its linewidth (ΔE) is determined by the Heisenberg uncertainty principle [S92]:

$$\Delta E \Delta t \approx \hbar \qquad\qquad \text{Equation 2.10}$$

The intensity of the C $1s \rightarrow \pi^*$ peak is determined by the number of available final states with sp^2 symmetry and the orientation of **E** relative to the transition moment vectors. The peak at 291.8 eV is due to C $1s \rightarrow \sigma^*$ exciton transition. The peaks observed between 286-290 eV are the C $1s \rightarrow 1\pi^*_{C=O}$ transitions in carbonyl, hydroxyl, and carboxyl groups existing as impurities in the SWCNT bundles. Similar features are often seen in MWCNT.
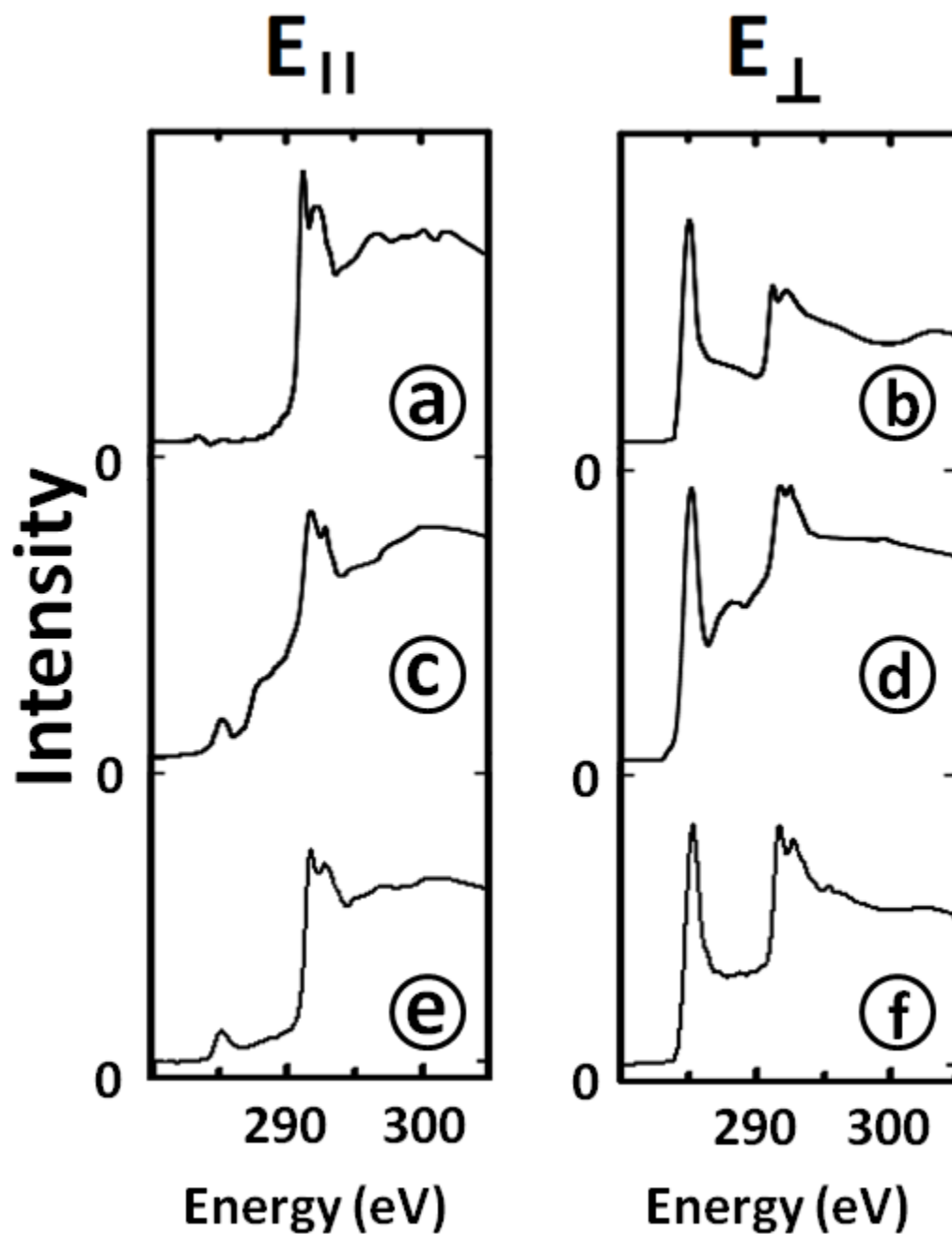
Figure 2.4 C 1s spectra of graphite (a,b), SWCNT (c,d), and MWCNT (e,f) recorded at

parallel and perpendicular orientations of **E**. Note that, for the graphite sample,

perpendicular orientation refers to the angle of 45° between **E** and the basal plane since

the sample was mounted on a tomography holder and could not be rotated further.

2.3 Introduction to X-ray microscopy

X-ray microscopy is becoming a preferred technique to study nanomaterials and thin films in the soft and hard X-ray regimes, thanks to the increasing number of third generation synchrotron X-ray sources and the development of high performance and user-friendly X-ray microscopes. X-ray microscopes exist for both full field imaging and scanning microscopy.

2.3.1 Full field X-ray microscopy

In a transmission X-ray microscope (TXM), an X-ray beam is concentrated to a ~10 μm spot on the sample by using a condenser Fresnel zone plate (ZP); the transmitted beam is then magnified by an imaging ZP and recorded by a charge-coupled device (CCD) camera (**Figure 2.5a**). High resolution imaging is carried out by TXM using exposures between 0.1 - 10 seconds; imaging of larger areas is performed by stitching images of adjacent areas. TXM uses low efficiency ZPs (less than 15%) to focus the incident and magnify the transmitted X-ray beam; thus, a relatively long exposure (order of a second per image recorded at each energy) is typically required to record statistically significant signals which can cause radiation damage in the sample. Spectroscopically, TXM based on pseudo-monochromator with the condenser ZP has low energy resolving power (~100) with the line shapes far from Gaussian, making TXM a poor technique for chemical analysis. Note that there are several TXMs around the world including one in Bessy II [WYS08,ZGR&08] which produce spectroscopy results, including dichroism that are fully equivalent to STXM.

2.3.2 Scanning X-ray microscopy

Scanning X-ray microscopy includes STXM and scanning photoelectron X-ray microscopy (SPEM) (**Figure 2.5b**). SPEM is very similar to STXM except photoelectrons rather than transmitted photons are detected.
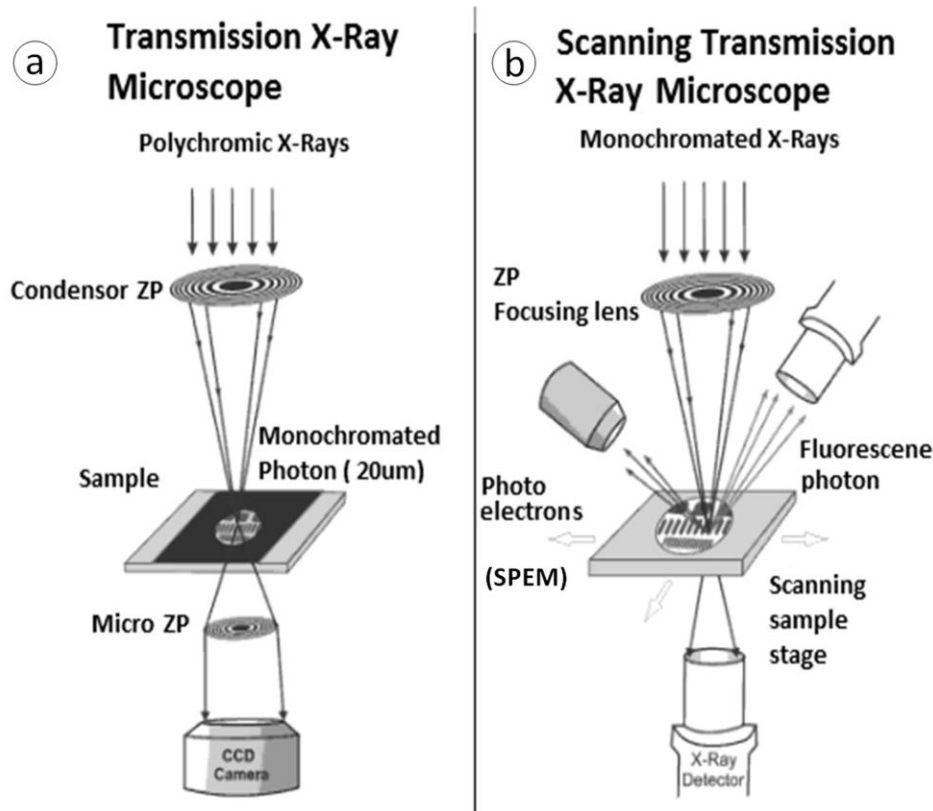
Figure 2.5 Schematic diagrams of a) TXM and b) STXM microscopes (Adapted from [SPA&98]).

In STXM, a beam of monochromated soft X-rays produced by a bend magnet or an undulator are focused by a ZP to a 20-50 nm spot. The sample is placed at the focal point (z) and it is raster scanned (x, y) while the transmitted X-rays are recorded.

A ZP is a circular diffraction grating capable of focusing light waves. ZP consists of a series of alternating concentric rings of Au or Ni (opaque to soft X-rays), and circular light transparent slots patterned on silicon nitride substrate (**Figure 2.6**). The interference condition of a transparent slot is described by:

$$r_n^2 = nm\lambda f + \frac{n^2 m^2 \lambda^2}{4}$$
Equation 2.11

where f is the focal length, r_n is the radius of the nth zone, n is the zone number, m is diffraction order, and λ is the wavelength of the incident soft X-ray. The zero diffraction order is the undiffracted light, and positive orders are converging light. When adjacent transparent and opaque slots have equal width, the even-numbered orders are suppressed and the remaining odd-numbered orders interfere constructively at the focal point [A99]. The first order light is the most intense diffracted light (~10% of the total flux) which is used in most STXM measurements [KTS&03]. An order sorting aperture (OSA) and a large central stop (CS) in the centre of the ZP with a diameter bigger than that of the OSA are used to block zero order and higher order diffracted light.

For first order diffraction ($m = 1$), the focal length is calculated by:

$$f \approx \frac{r_n^2}{\lambda}$$
Equation 2.12

The numerical aperture (NA) is defined as [A99]:

$$NA = \frac{r_n}{f} = \frac{\lambda}{2\Delta r_n}$$

Equation 2.13

For a ZP with n zones, n can be calculated from the radius of the outmost zone (r_n) whose

width is $\Delta r_n = r_n - r_{n-1}$. Then Equation 2.12 converts to:

$$f = \frac{2r_n \Delta r_n}{\lambda}$$

Equation 2.14

where $2r_n$ is the diameter of the zone plate. The focal length is reciprocally proportional

to the wavelength of the light, and thus linearly proportional to the photon energy.

The spatial resolution of a ZP can be expressed by the Rayleigh criterion

($Res. = \frac{0.610\lambda}{NA}$):

$$Res. = 1.22\Delta r_n$$

Equation 2.15

Thus, the diffraction-limited spatial resolution is determined mainly by the outer zone

width of a zone plate.

Table 2.1 List of Synchrotron Soft X-ray microscopes [HDJ&08,W08].

Type	Facility	Location	Source	E-range (eV)	Status
TXM	Alba, Mistral	Barcelona , Soain	BM	270-2600	construction
TXM	ALS , XM1	Berkeley, USA	BM	250-900	operating
TXM	ALS, XM2 (NCXT)	Berkeley, USA	BM	250-6000	operating
TXM	Astrid, XRM	Aarhus, Denmark	BM	500	operating
TXM	Bessy, U41-TXM	Berlin, Germany	Und-L	250 - 600	operating
TXM	NSRL, TXM	Hefei, China	BM	500	operating
TXM	Ritsumeikan, BL12	Kyoto, Japan	BM	500	operating
STXM	ALS, 5.3.2.2	Berkeley, USA	BM	250-750	operating
STXM	ALS, 5.3.2.1	Berkeley, USA	BM	250-2500	commissioning
STXM	ALS, 11.0.2	Berkeley, USA	EPU	100-2000	operating
STXM	Bessy	Berlin, Germany	BM	250-600	operating
STXM	Bessy, MAXYMUS	Berlin, Germany	EPU	250 – 1500	operating
STXM	CLS, 10ID1	Saskatoon, Canada	EPU	130-2500	operating
(S)TXM	Elettra, Twin-mic	Trieste, Italy	Und-L	250 - 2000	operating
STXM	NSLS, X1A (2)	Upton, USA	Und-L	250-1000	decommissioned
STXM	SLS, PolLux	Villigen, Switzerland	BM	250-750	operating
STXM	SLS, NanoXAS	Villigen, Switzerland	BM	250-750	commissioning
STXM	Soleil, X-Mou	Saint-Aubin, France	EPU	250 – 1500	construction
STXM	SSRF, SXS	Shanghai, China	EPU	200 - 2000	operating
STXM	SSRL, 13-1	Stanford, USA	EPU	250 – 1000	operating
SPEM	ALS, BL 7.0	Berkeley, USA	Und-L	90-1300	decommissioned
SPEM	ALS, Maestro	Berkeley, USA	EPU	90-1300	construction
SPEM	Elettra, BL 2.2 L	Trieste, Italy	Und-L	200-1400	operating
SPEM	Elettra, BL 3.2 L	Trieste, Italy	Und-L	27, 95	construction
SPEM	MAX-lab, BL 31	Lund, Sweden	Und-L	15-150	operating
SPEM	NSRRC, BL09A1	Hinschu, Taiwan	Und	60-1500	operating
SPEM	PAL, 8A1	Pohang, Korea	Und	20 - 2000	operating
SPEM	Soleil, Antares	Saint-Aubin, France	EPU	50 - 1500	commissioning
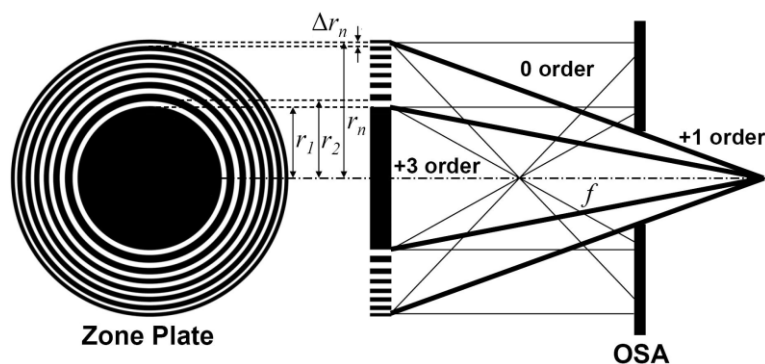
Figure 2.6 Schematic representation of a Fresnel zone plate; the OSA blocks the zero order and third order X-rays while passing the first order X-rays. (Adapted from [A99,W08])

2.4 STXM instrumentation

The initial development of STXM was carried out at the National Synchrotron Light Source (NSLS) NY, USA [KR85,RSF&88,BRA&89]. The early design of STXM microscope used a 1 μm diameter pinhole as a scanning probe to image wet biological samples [SRN&80]. The use of ZP and synchrotron radiation produced by an undulator in STXM began in late 1980's [RSF&88,BRA&89]. In 2001, a dedicated interferometery controlled STXM for polymer analysis was built on the bend magnet beam line 5.3.2.2 at the ALS [WAK&02,KTS&03]. Currently, there are a number of STXM microscopes operating around the world, as listed in **Table 2.1** [HDJ&08,W08].

In this thesis, STXM microscopes located at beamline 5.3.2.2 at the ALS and 10ID1 at the CLS were used. These microscopes have almost identical designs. The external appearance of these microscopes are shown in **Figure 2.7**. The chambers and all of the microscope components were designed to operate in air or at a vacuum of ~ 10^{-2} torr. However, the measurements are typically performed at a pressure of 100 torr He to help cool motors and stages. This is achieved by pumping the chamber to a rough vacuum (0.1 torr) and then back-filling with He gas. The helium environment provides more photon flux due to lower absorption than air [KTS&03]. In addition, the absence of oxygen significantly reduces radiation damage in the samples [CUA02]. The microscopes are mounted on massive granite blocks, which sit on vibration isolation pads to reduce vibrational coupling to the experimental floor.

Figure 2.7c is a schematic of the STXM major components. This includes the zone plate *z* stage, OSA *x, y* stages, sample *x, y* coarse stage, sample *x, y* fine piezo stage,

sample z stage, detector x, y, z stage and the interferometer system.

Photographs of the key STXM components are shown in **Figure 2.8**. Various ZPs were used in this thesis with outermost zone widths of 25 nm, 30 nm, and 40 nm. The central stop of the ZP has a diameter of 80-100 μm while the order sorting aperture (OSA) is 50 μm in diameter. The focal length, the distance between the ZP and the sample, is linearly proportional to photon energy. The STXM sample holder has six 2.8 mm diameter round holes, designed to hold TEM grids or silicon nitride windows. In the ALS STXM, only 5 of the holes can be used since moving to position #1 causes collision of the sample support structure and the detector support structure; however, in the CLS STXM samples can be mounted on all six holes. The ZP and sample must maintain relative (x,y) positioning accuracy of 10 nm (or better) between the ZP and sample which is maintained by a laser interferometer control system [KTS&03]. The interferometric system corrects for small drifts during acquisition of stacks of images.

The detector consists of a phosphor to convert soft X-rays to visible light followed by a high performance photomultiplier (PMT) which can count linearly up to 20-30 MHz (**Figure 2.9**). A very thin layer of a polycrystalline phosphor film (P43) deposited on the front tip of a lucite pipe by dusting onto the lightly greased tip is used as the X-ray detector.
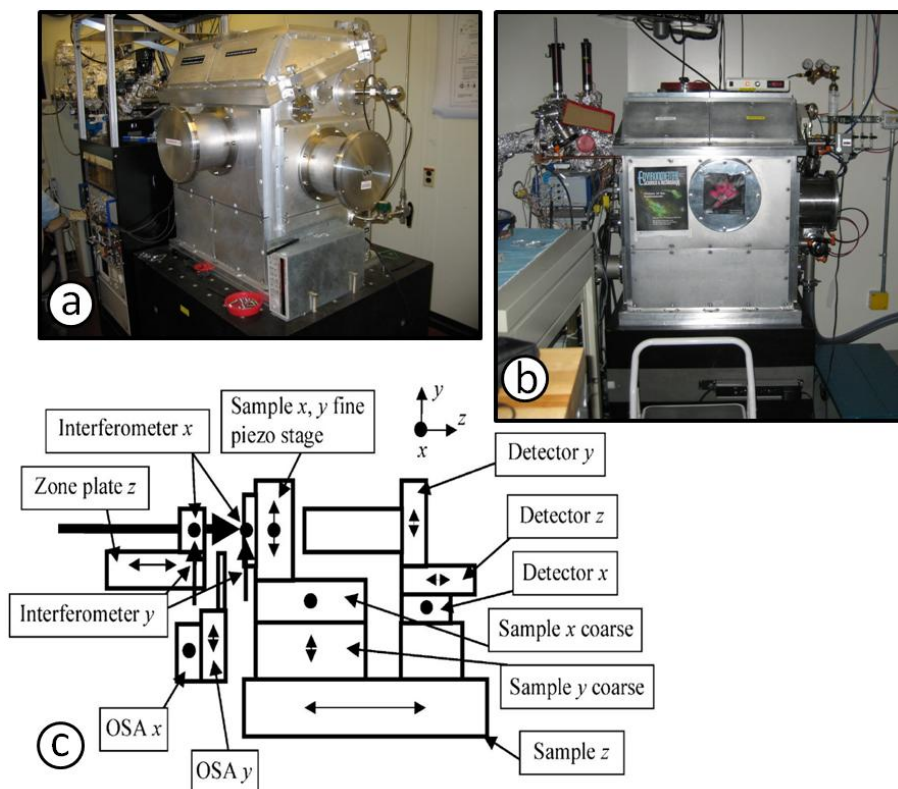
Figure 2.7 The STXM microscopes at the (a) ALS 5.3.2.2 and (b) CLS 10ID1. (c)

Various components of the STXM microscope (Adapted from [W08]).
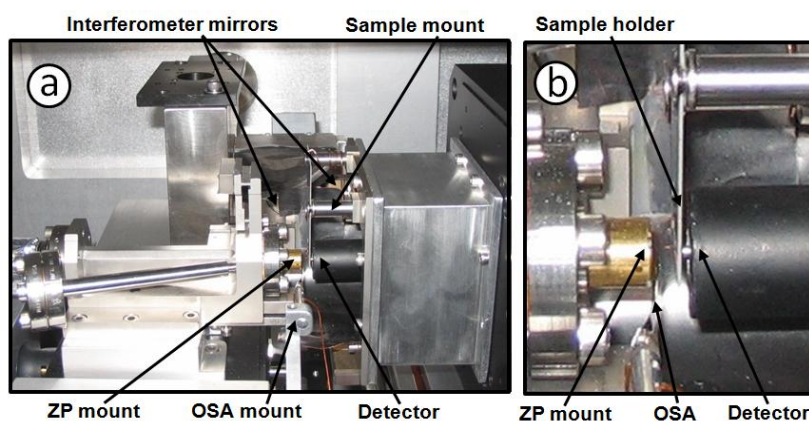
Figure 2.8 Close view at the STXM inside the chamber (Adapted from [W08]).
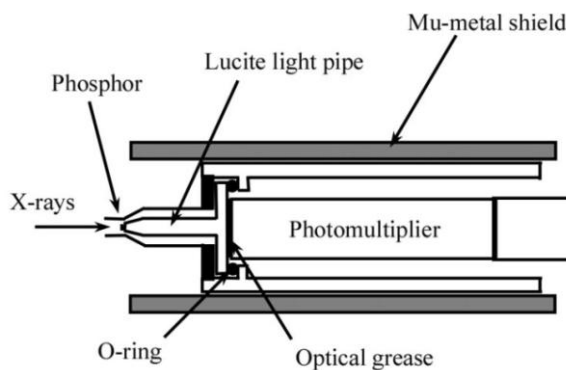
Figure 2.9 The schematic diagram of the X-ray detector in the STXM which includes a phosphor screen and a photomultiplier tube [KTS&03,W08].

2.5 Beamlines instrumentation

The STXM microscopes used in this thesis are located at beamline 5.3.2.2 at the ALS and 10ID1 at the CLS. The following sections present the details of the beamlines.

2.5.1 Beamline 5.3.2

The schematic diagram of the beamline 5.3.2.2 is illustrated in **Figure 2.10**. The optical and mechanical design of this beamline has been described in detail elsewhere [KTS&03,WPA98,WAK&02]. The synchrotron radiation generated by the bend magnet is reflected by a toroidal mirror which focuses the beam in the vertical direction at the entrance slit and in the horizontal direction at the exit slit. The combination of the entrance slit and the dispersive (horizontal) exit slit controls the energy resolution. A feedback system is used to drive two piezo motors which adjust the orientation of the toroidal mirror such that the X-ray beam is always centered on the entrance and exit slits. A spherical grating monochromator is used to horizontally disperse the soft X-rays (250 - 1100 eV) which can produce a resolving power ($E/\Delta E$) up to 5000, depending on the choice of slits.

The exit aperture consists of independently controlled dispersive and non-dispersive slits oriented horizontally and vertically, respectively. The exit aperture size controls spatial coherence by varying the sizes of the entrance and exit slits. At ALS beamline 5.3.2.2, the second order contribution is 50 - 100% of the first order light at the C 1s edge, even with the zone plate in place. (Note that ideal ZPs should not focus in the second order; besides, the first order focused light from the second harmonic should be very diffuse. Thus, the large amount of second harmonic light in STXM reflects ZP

imperfections). To remove the second-order harmonic light which interferes with spectroscopy at the C 1s edge, a differentially pumped ~1 m long gas cell containing nitrogen (0.7 torr pressure) precedes the STXM in the section containing the exit slits [KTS&03,WPA98,WAK&02]. An in-vacuum piezo shutter (~300 μs open - close action) located between the exit slits and the STXM chamber is used to block the X-rays except during each line or point of image measurements.
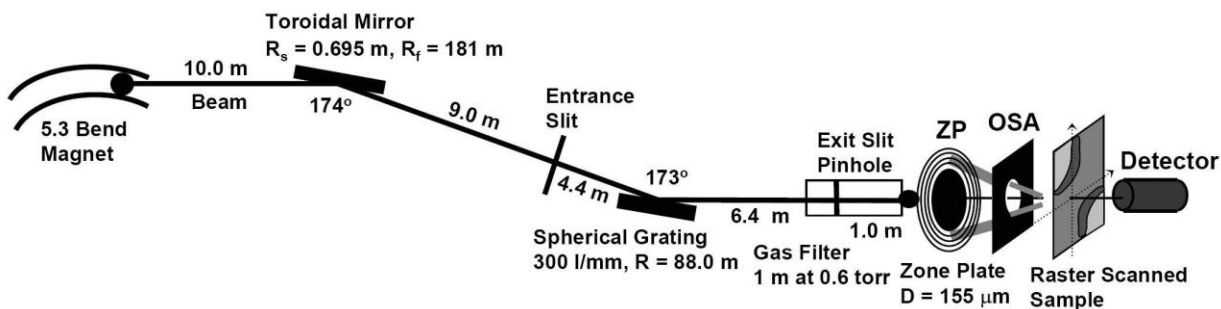
Figure 2.10 The schematic diagram of beamline 5.3.2 [http://www-als.lbl.gov/].

2.5.2 Beamline 10ID1

A schematic diagram of beamline 10ID1 (Spectromicrosco0070y (SM) beamline) at the CLS is shown in **Figure 2.11** [KKL&07]. At this beamline, X-rays are generated by an Apple II type elliptically polarized undulator (EPU); this and the monochromator are the major difference between 10ID1 and 5.3.2.2 beamlines. The EPU consists of an array of magnets with alternating magnetic orientations (**Figure 2.12**). The relative motion of the girders in the EPU controllably changes the trajectory of the electron beam which produces 100% linearly polarized X-rays whose polarization can be varied from -90° to +90°. EPU is also capable of producing left and right circularly polarized X-rays which

are essential for characterization of magnetic materials.

The beamline is equipped with an infinity corrected plane grating monochromator (PGM) with vertical dispersion plane which is designed for a nominal resolving power of 3000 and high flux. The PGM works with collimated light and allows for the free choice of grating magnification parameters which provide the best compromise between energy resolution, the grating efficiency, and high order suppression.

To remove the second-order X-rays at the beamline 10ID1, a Ti foil is used as a transmission filter at the exit slit; the Ti filter can be inserted or removed manually by the user as required.

There is a parallel branch line developed for a photoemission electron microscope (PEEM). The mirror M3 STXM directs the X-ray beam to the STXM microscope. When the X-ray beam is directed to the PEEM branch line, the STXM does not receive the X-rays and cannot be operational.
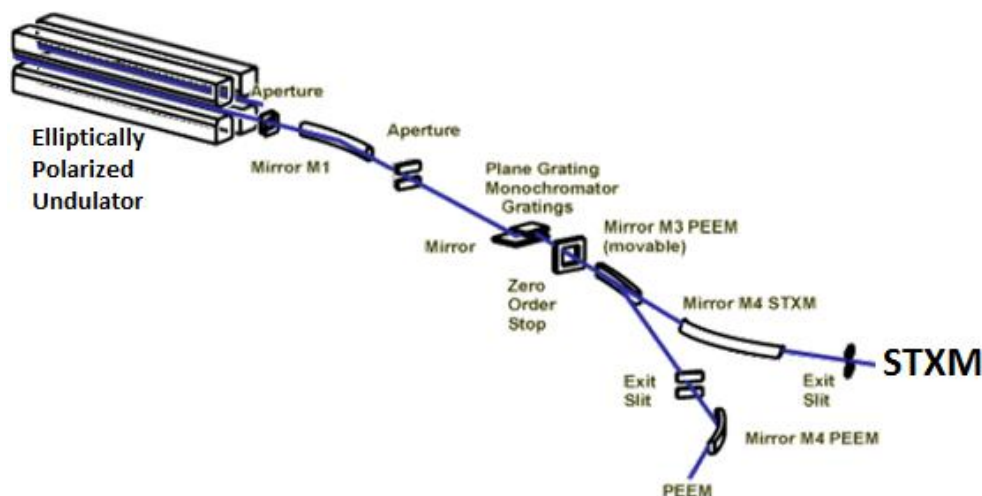
Figure 2.11 Schematic diagram of beamline 10ID1 at the CLS [KKL&07].
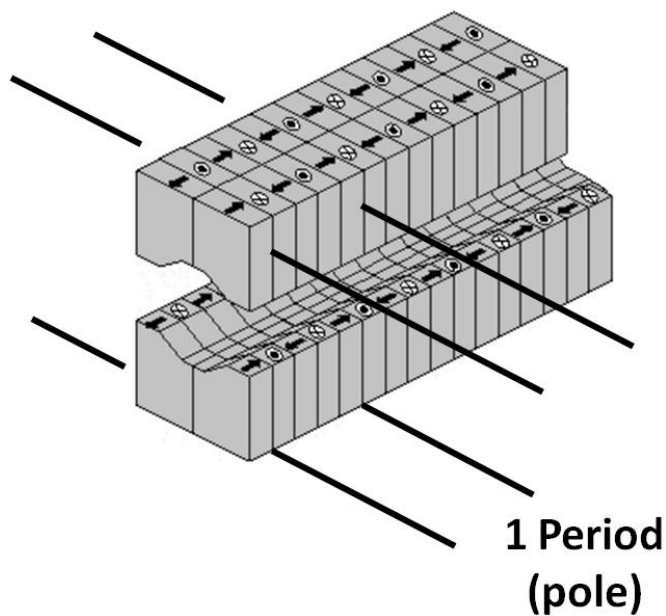
Figure 2.12 Schematic diagram of the Apple II type elliptically polarized undulator (EPU) used to generate X-rays at the beamline 10ID1 at the CLS. The EPU consists of 43 poles with 75 mm period and 15 mm (minimum) gap (Adapted from [A99,www.lightsource.ca]).

2.6 Electron scattering

Electrons travelling through a sample interact with it and scatter. The scattering process is either elastic or inelastic (**Figure 2.13**). In elastic scattering, if the incident electron approaches the nucleus closely, there is a strong interaction and the electron gets deflected through a large angle (Rutherford scattering). When the electron interacts weakly and mainly with the electron cloud of the sample, they are scattered through a much smaller angle (10-100 mrad at E_{beam}=100 keV). For electrons undergoing head-on collisions, the energy loss is rather large and can be obtained by [E96]:

$$E = \frac{2148(E_0 + 1.002)E_0}{A}$$
    Equation 2.16

where E_0 is the energy of the incident electrons in MeV, and A is the atomic weight of the target nucleus. This energy transfer (knock-on) can displace atoms from their lattice sites in light elements. However, head-on collisions are rare and the majority of elastic interactions are at small angles.

Inelastic scattering occurs due to electrostatic interactions between the incident and atomic (core and valence) electrons. Since incident and target electrons are same in mass, inelastic scattering can result in large energy transfers. The core electrons which exist in orbitials several hundreds eV below the Fermi level of the solid are excited to empty states above the Fermi level. Because the total energy is conserved in the collisions, the accelerated electrons lose an equal amount of energy. Scattering through a small angle (10-100 mrad at E_{beam}=100 keV) is much more probable than inelastic scattering through a large angle [E96]. In the decay process, the system loses its excess energy through

Auger or X-ray fluorescence emission processes.
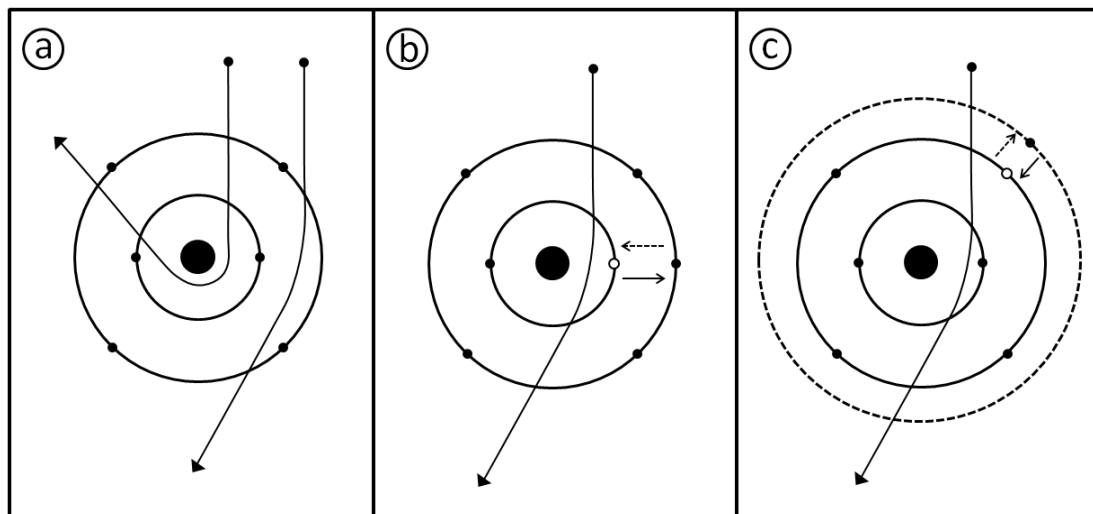
Figure 2.13 A classical view of electron scattering by an atom which includes: 1) elastic

scattering caused by electrostatic attraction of the nucleus; and 2) inelastic scattering due

to electrostatic interaction by 2) inner-; and 3) outer shell electrons (Adapted from [E96]).

Inelastic electron scattering is characterized by a differential cross section per unit solid angle (Ω) which, for small angle scattering of fast electrons, can be derived from the first Born approximation [E96,B01,LFS&83]:

$$\frac{d\sigma_n}{d\Omega} = \left(\frac{m_0}{2\pi\hbar^2}\right)^2 \frac{k_1}{k_0}\left|\int V(r)\psi_0\psi_n^* \exp(i\boldsymbol{q}\bullet\boldsymbol{r})d\tau\right|^2 \qquad \text{Equation 2.17}$$

Where $\mathbf{k_0}$ and $\mathbf{k_1}$ are wave vectors of the fast electron before and after scattering ($\frac{k_1}{k_0}$ is often taken as unity), ψ_0 and ψ_n are the wavefunctions of the initial and final states of the atomic electron, $\boldsymbol{q}$ is the momentum transferred to the target ($\boldsymbol{q} = \boldsymbol{k_0} - \boldsymbol{k_1}$) (**Figure 2.14**), m_0 is the mass of the electron, and $V(r)$ is the potential responsible for the interaction which is mainly electrostatic and can be written as [E96,B01,LFS&83]:

$$V(r) = \frac{Ze^2}{4\pi\varepsilon_0 r} - \frac{1}{4\pi\varepsilon_0}\sum_{j=1}^{Z}\frac{e^2}{\left|r-r_j\right|} \qquad \text{Equation 2.18}$$

where Z is the atomic number of the target sample, and e is the electron charge. The first term represents the Coulomb interaction by the nucleus, and the second term is the sum of repulsive effect of each atomic electron. The angular and energy dependence of Equation 2.17 is specified by a double-differential cross section and is written as [E96,B01,LFS&83]:

$$\frac{d^2\sigma_n}{d\Omega dE} = \frac{4}{a_0^2 q^4}\left|\left\langle\psi_n\left|\sum_j \exp(i\boldsymbol{q}\bullet\boldsymbol{r})\right|\psi_0\right\rangle\right|^2 \qquad \text{Equation 2.19}$$

where a_0 is the Bohr radius. The scattering vector $\mathbf{q}$ is related to the scattering angle θ; for $\theta \ll 1$ rad and $E \ll E_0$ where E_0 is the incident-beam energy, it is a good

approximation to write [B01,E96,LFS&83]:

$$q^2 = k_0^2 (\theta^2 + \theta_E^2) \qquad\qquad \text{Equation 2.20}$$

where θ_E is the characteristic angle and is defined by [B01,E96,LFS&83]:

$$\theta_E = \frac{E}{2E_0} \qquad\qquad \text{Equation 2.21}$$

The operator in Equation 2.19 can be expanded as:

$$\exp(i\boldsymbol{q} \bullet \boldsymbol{r}) = 1 + \boldsymbol{q} \cdot \boldsymbol{r} - i(\boldsymbol{q} \cdot \boldsymbol{r})^2 + \cdots \qquad\qquad \text{Equation 2.22}$$

Provided that $|\boldsymbol{q} \cdot \boldsymbol{r}| << 1$ and the initial and final states are orthogonal, the matrix element

reduces to dipole form. In terms of momentum transfer and scattering angle, dipole

approximation is valid when $\boldsymbol{q} << (2m_0 E_c)^{1/2}$ and $\theta << \left(\dfrac{E_c}{E_0}\right)^{1/2}$, respectively where E_c is

the core binding energy [B01,E96,LFS&83]:

$$I \propto \left| \left\langle f \left| \widehat{\boldsymbol{\varepsilon}}_p \bullet \boldsymbol{r} \right| i \right\rangle \right| \qquad\qquad \text{Equation 2.23}$$
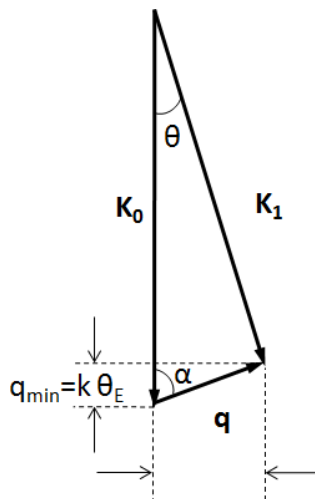
Figure 2.14 Scattering diagram showing the incident electron momentum (k_0) and

momentum transfer (q) for scattering angle (θ) (Adapted from [LFS&83]).

2.6.1 Electron energy loss spectroscopy

In EELS, a beam of monochromated electrons passes through a sample. The

transmitted beam, which has lost a characteristic energy due to interacting with the

sample, is analyzed by a spectrometer to separate the electrons according to their energy.

The intensity of the electrons is then plotted against energy loss to obtain energy loss

spectra.

Typically, an energy loss spectrum consists of zero loss (<1 eV), valence loss

(5~50 eV), and core loss (>50 eV) regimes. These three regimes can be observed in the

energy loss spectrum of $YB_2Cu_3O_7$ sample (a high temperature superconductor) in **Figure**

2.15 [E96]. Zero loss (elastic) corresponds to the transmitted electrons that have not

suffered any measurable energy loss, including those scattered elastically in the forward

direction and those exciting phonon modes. Low loss represents the electrons that have undergone inelastic scattering due to plasmon or valence electron excitations. Core loss corresponds to transmitted electrons that have induced core electron excitations in the sample and suffered inelastic scattering. In this regime, one would observe energy loss edges instead of peaks where the intensity increases rapidly at the edges and then decreases slowly; the fine structures near the edges provide information about band structure, local bonding, and oxidation states in the sample. The cross section for inner-shell scattering is small; therefore, the probability of the fast electrons to produce more than one inner-shell excitation is negligible. However, plural scattering, consisting of an inner shell loss preceded and followed by a Plasmon or valence shell loss, has a high probability, unless the sample is very thin (<30 nm). Plural scattering can be removed by deconvolution procedure [E96], but it is best to measure with samples sufficiently thin that single scattering dominates.
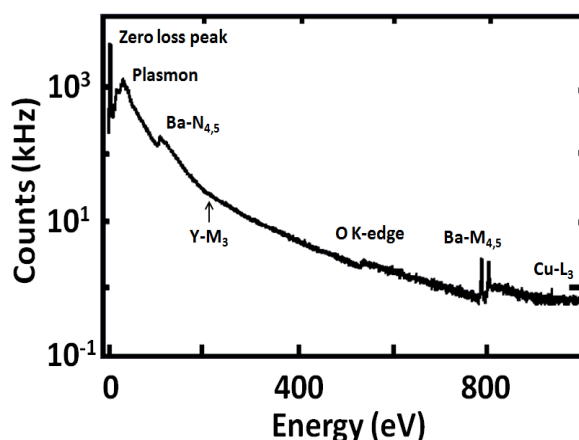
Figure 2.15 Electron energy loss spectrum of a high-temperature superconductor of composition $YB_2Cu_3O_7$ (Adapted from [E96]).

2.7 Transmission electron microscope instrumentation

TEM uses a beam of electrons to image and analyze samples at high spatial resolution.   The first TEM was constructed by Ruska and Knoll in 1931 [E96] which was capable of 400X magnification. Two years later, Ruska built a new model that exceeded the resolution attainable with an optical microscope. However, the first practical electron microscope was only constructed in 1938 at the University of Toronto by Burton and his co-workers [E96,WC09]. Although modern electron microscopes are capable of 2,000,000 X magnification, they remain based upon Ruska's prototype.

In this thesis, electron spectroscopy of the CNT samples was carried out in a FEI Titan 80-300 Cryo microscope (**Figure 2.16**). In the following section, the instrumental description of the major components of the microscope is presented.
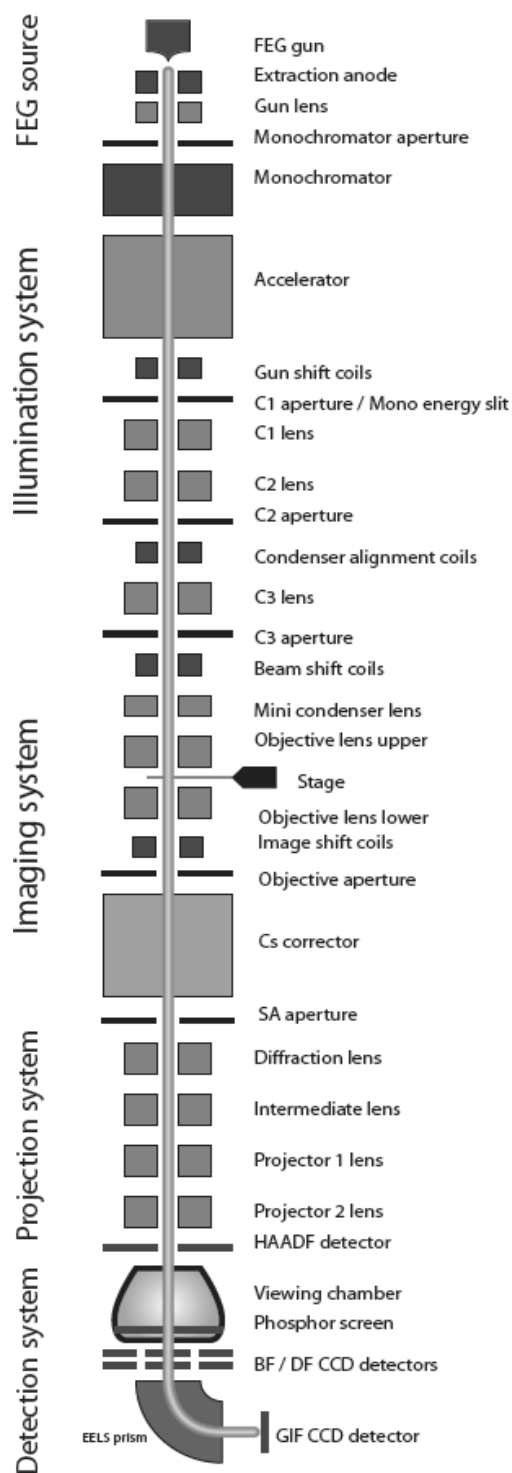
Figure 2.16 A schematic diagram of FEI Titan 80-300 Cryo microscope (Adapted from

the FEI Titan 80-300 Cryo microscope user's manual).

2.7.1 Electron source

Every electron microscope uses an electron source to produce a fine beam of electrons with a well defined energy. The electron source in FEI Titan 80-300 Cryo TEM is a field emitter operating in the Schottky mode. The emitter consists of a tungsten single crystal in <100> orientation, coated with a thin layer of zirconia (ZrO_2).

In general, a field emission source is a sharply-pointed electron emitter held at several kilovolts negative potential relative to a nearby electrode to create a sufficient potential gradient to cause field electron emission. Field emission cathodes are either cold cathode, made of single crystal tungsten sharpened to a tip radius of about 100 nm, or Schottky in which thermionic emission is enhanced by barrier lowering in the presence of a high electric field. The choice of source ultimately determines the resolution, contrast and signal-to-noise capabilities of the imaging system. The single most important characteristic of the electron source is brightness which is defined as current density per steradian solid angle. Field emission emitters offer brightness up to 1000 times greater than tungsten emitters.

2.7.2 Condenser lens

A condenser lens is a magnetic lens used to demagnify the beam in the TEM column. FEI Titan 80-300 Cryo microscope uses three condenser lenses. The C1 lens controls the spot size and the C2 lens controls the intensity (condenses the beam into a spot) of the beam; the C3 lens allows the beam convergence to be adjusted independently of the C2 aperture and allows the parallelism of the beam to be adjusted in TEM mode. In this microscope, when the C3 lens is on, the C2 and C3 lenses are adjusted together

[WC09, E96].

2.7.3 Objective lens

An objective lens is placed below the sample to magnify the sample image. The magnification of the objective lens is determined by the ratio of the distance between its objective plane and its image plane. The objective lens is affected by aberrations in the microscope; therefore, they have to be well aligned and stigmated. In fact, the errors introduced by misalignment of the objective lens are so big that even if other lenses are well optimized, the error could not be corrected [WC09, E96].

2.7.4 Aperture

An aperture is often inserted into a lens to limit its collection angle. The aperture is a hole in a disk; the metal plate around the aperture is called a diaphragm. The aperture is used to allow electrons with low scattering angles to pass through the lens while those with large scattering angles are blocked by the diaphragm (**Figure 2.17**) [WC09, E96].

2.7.5 Lens defects

In principal, electromagnetic lenses in TEM are analogous to those used in optical microscopes. However, their performance at best is compared to that of the bottom of a soft drink bottle used as magnifying glass [WC09]. Spherical and chromatic aberrations and stigmatism are the major defects in the electromagnetic lenses.
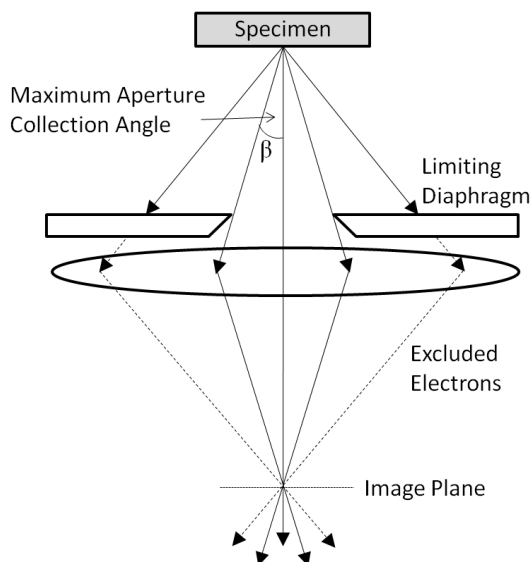
Figure 2.17 A schematic diagram showing how diaphragm restricts the angular spread of collected electrons. (Adapted from [WC09]).

2.7.5.1 Spherical aberration

Spherical aberration occurs when a lens behaves differently for off-axis versus on-axis electrons. In electromagnetic lenses, the further off-axis the electrons are, the stronger they are bent back toward the axis. Therefore, a point is imaged as a circle of high intensity surrounded by a dim halo This limits the performance of the TEM at high magnifications. The spherical aberration is compensated in a magnetic lens by creating a diverging field which spreads out the off-axis beams such that they re-converge to a point rather than a disk.

2.7.5.2 Chromatic aberration

Chromatic aberration is due to the fact that electrons produced by the source are not monochromatic. Depending on the type of electron source, energy spread in the beam can be between 0.2-2 eV. Since the objective lens bends the electrons of a lower energy more strongly, the electrons from a point become blurry and form a Gaussian image plane. The chromatic aberration is corrected by a monochromator.

2.7.5.3 Stigmatism

Stigmatism occurs when electrons feel a non-uniform magnetic field as they spiral down the optical axis in the TEM column. This effect occurs due to imperfections in the soft iron pole pieces such as microstructural inhomogeneities that cause local variations in the magnetic field strength, or geometrical deviations of the bore of the column from a perfect cylinder. To correct for stigmatism small octupoles are employed to introduce a compensating field to balance the magnetic inhomogeneities.

2.8 TEM-EELS instrumentation

The electron energy analyzer in TEM-EELS is a magnetic prism which uses a uniform magnetic field (B) to direct electrons through a circular path. The bending radius of the electrons is given by [E96,WC09]:

$$R = \left(\frac{m}{e}\right) B \upsilon \qquad\qquad\qquad \text{Equation 2.24}$$

where m is the relativistic mass, e is the charge, and υ is the velocity of the electrons. Electrons travelling off-centre through the prism experience an increase or decrease in their path length within the field which induces a greater or lesser deflection angle (**Figure 2.18a**). The prism has a focusing property. Thus, electrons of a given energy but slightly different angular trajectories originated at a single point return to a single image point. The fringing field at the edges of the pole piece focuses the electrons that deviate in the direction parallel to the magnetic field (**Figure 2.18b**). To give the spectrum a small width in the direction of the applied magnetic field, the focusing power in these two perpendicular directions is made equal by adjusting the angle of the pole piece edges. The second order aberration can be also corrected by curving the pole piece edges.
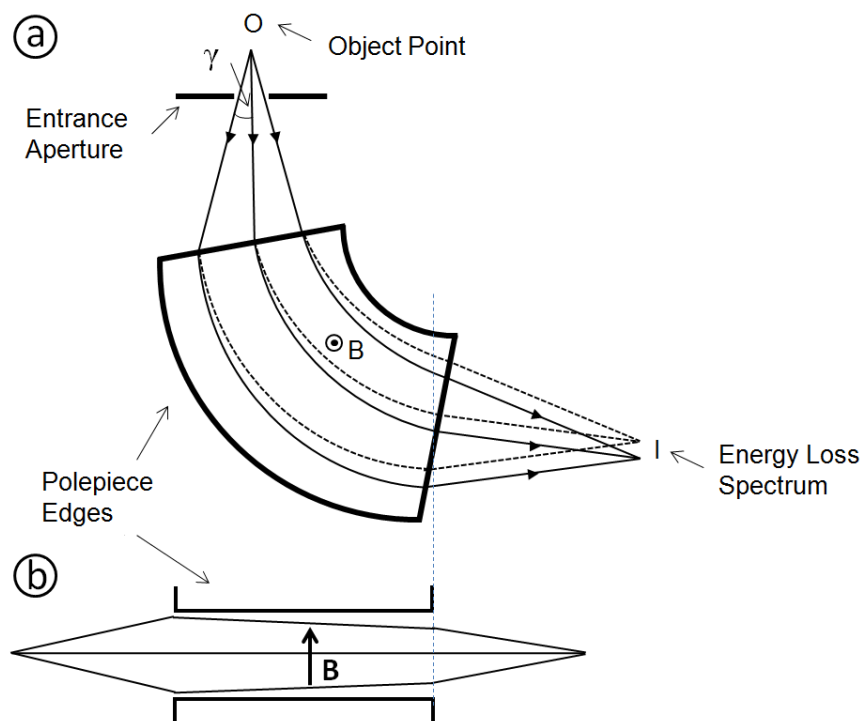
Figure 2.18 Bending and focusing of a beam of electrons in planes a) perpendicular and

b) parallel to the magnetic field. Solid lines represent zero-loss electrons and dashed lines

represent those that have lost energy during transmission through the sample (Adapted

from [E96,WC09]).

The simplest electron energy loss spectrometer consists of a magnetic prism placed under the image-viewing chamber (**Figure 2.19a**). By tilting the image screen to a vertical position, electrons are allowed into the magnetic prism where they are separated according to their kinetic energy. The entrance aperture limits the range of entrance angles and improves the energy resolution of the spectrometer.

The second approach is to incorporate the spectrometer in the TEM imaging column (**Figure 2.19b**). For image stability, it is important to preserve the TEM vertical column. Therefore, an omega filter is used which consists of four magnetic prisms that bend the beam into a Greek letter "Ω". The energy loss spectrum is obtained just below the filter and then projected by TEM lenses onto a detector. Since the magnetic prism has imaging properties, a narrow slit is often placed at the spectrum plane to remove all electrons except those within a small energy window to produce energy-filtered (EFTEM) images. When the images are aberration corrected by quadruple and sextuple lenses, the post-column magnetic prism (**Figure 2.19a**) can also produce EFTEM images.

A common energy loss system is based on the scanning transmission electron microscope (STEM) where a field emission source and strong electromagnetic lenses are used to form a small probe that can raster scan the sample (**Figure 2.19c**). Transmitted electrons scattered through a large angle are fed through an annular detector and then onto a display device to form a dark-field image. Electrons scattered through a smaller angle enter a single prism spectrometer to produce an energy loss spectrum for a given position of the probe. The collection of the energy loss spectrum recorded at each beam position yields a spectrum-image which is processed offline.
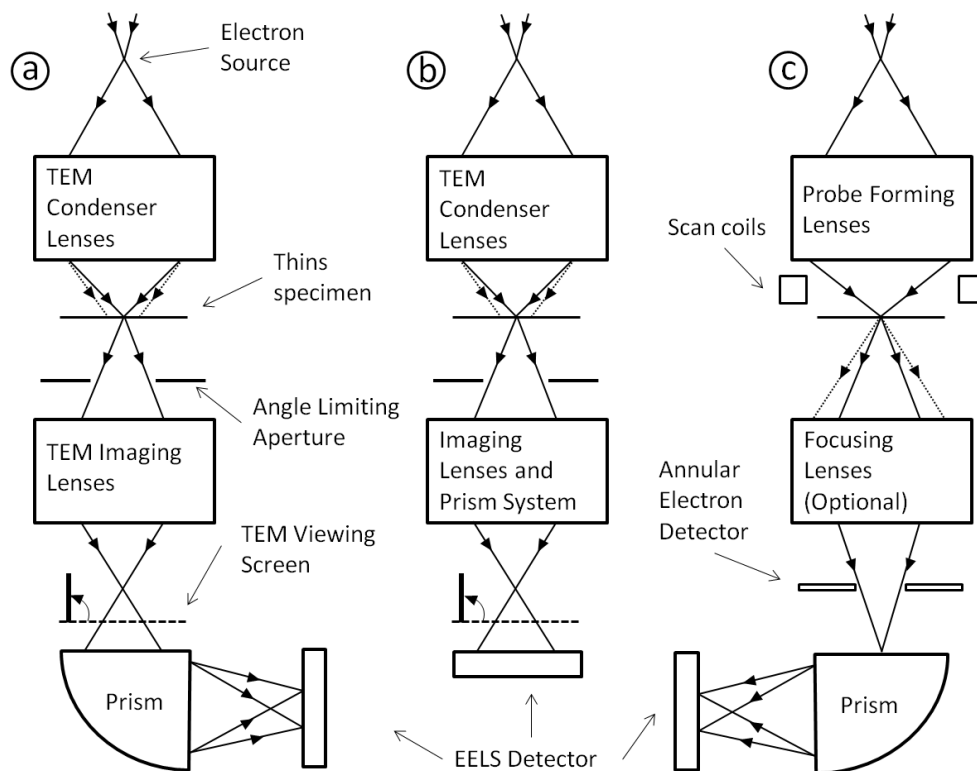
Figure 2.19 Three TEM-EELS systems: a) conventional TEM with a magnetic prism under the image viewing plane; b) TEM with incorporated magnetic in-column imaging filter; and c) scanning transmission systems (Adapted from [E96,WC09]).

2.8.1 Data acquisition

The energy loss spectra can be detected electronically by serial or parallel detection. A serial-detection system has four essential components: 1) a slit to select electrons of a particular energy loss; 2) an electron detector; 3) a method to scan the energy loss spectrum across the detection slit; and 4) a means of recording the output of the electron detector. The slit is placed at the focal plane of the spectrum and the spectrum is scanned past the slit by varying the magnetic field of the prism. The slit width

is adjustable to ensure a variety of studies including examination of fine structure (high energy resolution) and elemental analysis (low energy resolution). The single detector channel behind the slit usually consists of a scintillator to convert the electrons to visible photons which are then detected by a photomultiplier. This system works well but provides a noisy signal at high energy losses where the cross section is low. The serial detection in inefficient due to the fact that only a small range of energy loss is sampled at any instant.

Parallel-detection electron energy loss spectroscopy (PEELS) detects a wide range of energy losses simultaneously by projecting an extended energy loss spectrum onto a charge-coupled device (CCD) camera. This detection is widely used in current TEM-EELS. It is much more efficient for detecting wide energy loss spectra.

2.8.2 Spectrometer resolution

The energy resolution of the spectrometer is defined as the full width at half maximum (FWHM) at the zero loss peak. Electron guns are the major source of spread in electron energy (chromatic aberration). A zirconia coated tungsten Schottky source provides FWHM of better than 0.7 eV. A major limitation in TEM-EELS is drifts in the energy loss scale caused by drifts in the main beam potential. This can be compensated by fast read-outs of the elastic peak and software re-alignments. The energy resolution reduces at high energy losses (up to 1000 eV), but it is not greater than ~1.5× FWHM of the zero loss peak if there is no drift of the energy loss scale. Operation of the microscope at higher voltages can also degrade the energy resolution, almost tripling from 100 kV to 400 kV. Finally, since the magnetic prisms are sensitive to external magnetic fields, any

movement of objects (e.g. metal furniture) can reduce the resolution of the spectrometer [E96,WC09]. The FEI Titan 80-300 Cryo microscope at McMaster University is heavily isolated from the thermal, acoustic, electrical, and magnetic fields to prevent such disturbances.

2.8.3 Monochromator

The energy resolution is often dictated by the electron source and not the spectrometer. Therefore, to obtain sub-eV resolution, a cold cathode field emitter or a Schottky emitter is used in current spectrometers. However, it is still insufficient for high resolution spectroscopic studies that can compete with synchrotron X-ray absorption in terms of energy resolution. To further improve the energy resolution, a monochromator is placed under the electron gun (**Figure 2.20**). The monochromator is a Wien filter with perpendicular electrostatic and magnetic fields which allows electrons of a certain energy go straight down the TEM column. The monochromator provides an energy spread of 0.2 eV or smaller.
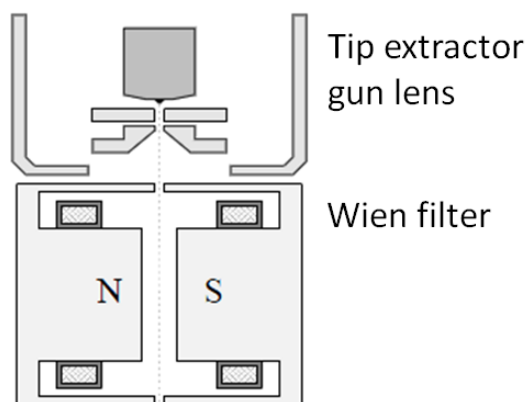
Figure 2.20 Field emission gun and Wien filter in FEI Titan 80-300 Cryo TEM (Adapted from [T99]).

2.9 EELS analysis in TEM-STEM

TEM-STEM creates a diffraction pattern (DP) on the viewing screen and also in the plane of the spectrometer-entrance aperture. This is called diffraction (or STEM) mode (**Figure 2.21a**). In this mode, the collection semi-angle of the spectrometer (β) is controlled by the size of the spectrum-entrance aperture. Thus, the larger the aperture, the higher the intensity and poorer the energy resolution (**Figure 2.21b**).

The collection angle is one of the most important variables in EELS data acquisition as it determines the range of scattering angles of electrons entering the spectrometer; a small collection angle corresponds to small scattering angles whereas a large collection angle corresponds to large scattering angles. In addition, the details of the energy loss spectra depend on the scattering angles of the electrons collected by the spectrometer. It is often misleading to compare spectra recorded by different collection angles. The collection angle is determined by:

$$\beta = \frac{Dd}{D_A L} \hspace{3cm} \text{Equation 2.25}$$

where D is the distance from the projector cross-over to the recording plane, d is the size of the spectrometer entrance aperture, D_A is the distance between the cross-over and the entrance aperture, and L is the camera length.
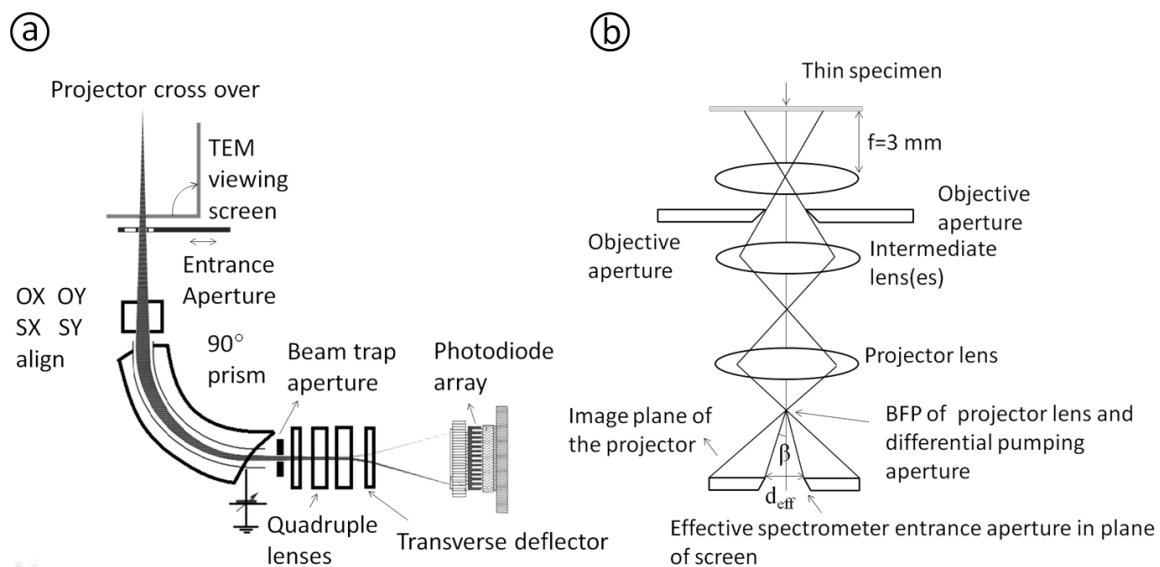
Figure 2.21 Schematic diagram of parallel collection of the energy loss spectrum (a). The value of β in TEM-STEM diffraction mode is determined by the spectrometer entrance aperture, projected into the plane of the DP (b) (Adapted from [WC09]).

2.10 Angle resolved EELS measurement

In angle resolved EELS, in addition to studying the energy spectrum of inelastically scattered electrons, one determines the momentum transfer of the energy loss electrons (See Figure 2.14). This provides information about the symmetry of electronic states which complements spatially resolved EELS.

The direction of the momentum-transfer is determined by the convergence angle of the incident beam (α) and the collection angle (β) of the spectrometer and the placement of the acceptance aperture. For a given energy loss and a given sample orientation, the momentum transfer at zero scattering angle (θ=0°) is parallel to the electron beam ($\mathbf{q}_{\parallel}$). As the scattering angle increases, a component perpendicular to the beam is introduced ($\mathbf{q}\perp$). At approximately θ_E, the characteristic angle corresponding to the energy loss (Figure 2.21), $\mathbf{q}\perp$ becomes dominant.

To perform angle-resolved EELS, one has to measure the spectra as a function of the angle between a crystal orientation and the direction of momentum transfer. This is done by either keeping the orientation fixed and changing the collection aperture, or keeping the collection angle fixed at a small angle ($< \theta_E$) and measuring the spectra as a function of tilt angle.

In this thesis, I used the scattering pattern on the TEM viewing screen to selectively collect the scattered electrons. In this approach, first, I optimized the collection angle of the spectrometer to resolve the momentum transfer by controlling various parameters such as camera length and the size of the aperture (**Table 2.2**). This provided a fan of **q** with a well defined orientation relative to CNT (**Figure 2.22**).

Table 2.2 Some of the parameters used to optimize the microscope for momentum resolved measurements.

Parameter	Value
Beam voltage	80 kV
Monochromator excitation	1.2
Condenser 3	70 um
Objective	100
Camera length	46.2 mm
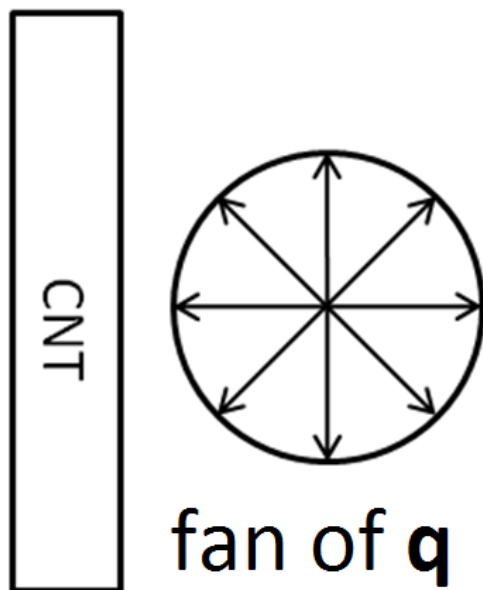
Figure 2.22 A fan of well defined **q** relative to CNT obtained by optimizing the microscope.

By moving the entrance aperture of the spectrometer on the scattering pattern, I selectively recorded the spectra which correspond to various orientations of **q** relative to the long axis of the tube. Note that since the entrance aperture cannot be physically moved, this was done by applying a magnetic field.

In order to confirm that this approach yields **q**-dependent spectra, I recorded two line scans for when **q** was perpendicular and parallel to the AD-MWCNT shown in **Figure 1.13**. The entrance aperture was placed such that only the spectra induced by **q** orthogonal to the CNT are recorded (**Figure 2.23a**). The spectra extracted from the centre and edge of the tube are plotted in **Figure 2.23c,d**. The spectrum from the centre shows a weak C 1s → π^* peak whereas that from the edge shows a strong one. This confirms that **q** is parallel to the π^* orbitals at the edge and orthogonal to the π^* orbitals at the top.

Next, the entrance aperture was placed to only record the spectra induced by **q** parallel to the CNT (**Figure 2.24a**). The spectra extracted from the centre and edge of the tube are plotted in **Figure 2.24c,d**. Both spectra show weak C 1s → π^* peaks indicating that **q** is orthogonal to the π^* orbitals at both edge and centre of the tube.
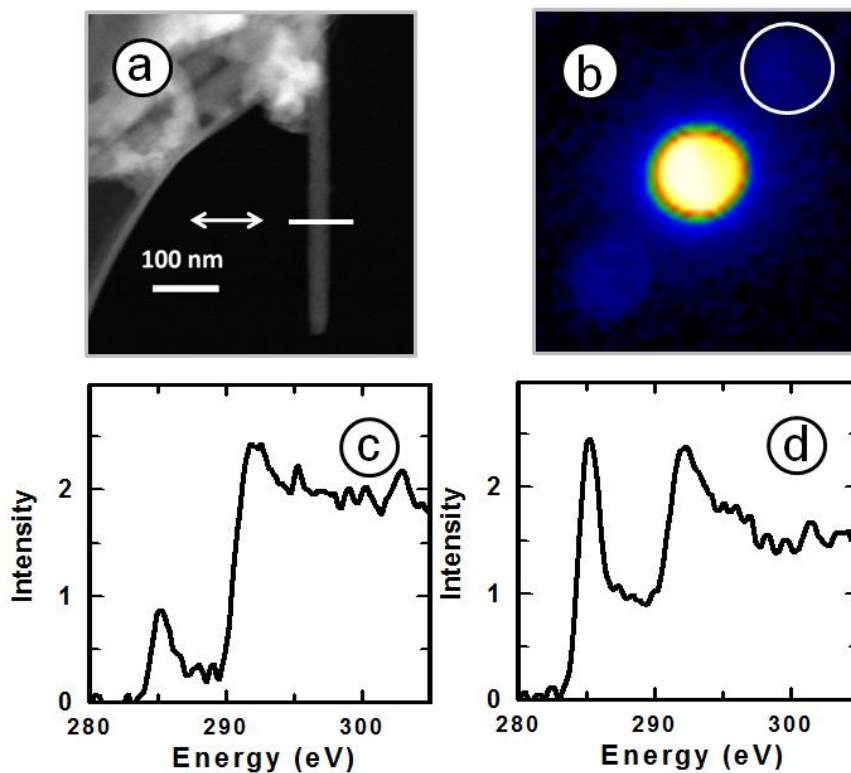
Figure 2.23 a) Placing the entrance aperture of the spectrometer to only collect spectra produced by **q** perpendicular to AD-MWCNT; b) a line scan across AD-MWCNT; c) C 1s spectrum from the centre of AD-MWCNT; d) C 1s spectrum from the edge of the AD-MWCNT.
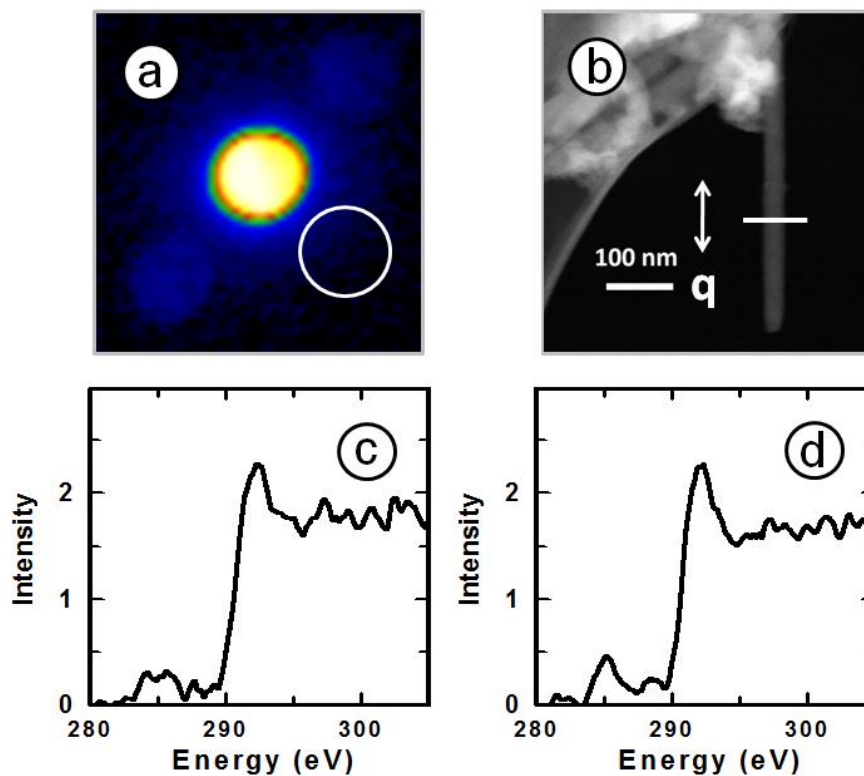
Figure 2.24 a) Placing the entrance aperture of the spectrometer to only collect spectra produced by **q** parallel to AD-MWCNT; b) line scan across AD-MWCNT; c) C 1s spectrum from the centre of AD-MWCNT; d) C 1s spectrum from the edge of the AD-MWCNT.

Chapter 3

Experimental

This chapter describes how the STXM and TEM-EELS (in STEM mode) measurements were conducted and how their data was processed. It presents recipes for preparing samples for STXM and TEM-EELS and describes the data acquisition and data analysis methods. Finally, it explains the process of focused ion beam modification of MWCNT, which was used to investigate the use of TEM-EELS to evaluate the quality of CNT structures.

3.1 Materials

The SWCNT samples were produced by a laser ablation method and obtained from Dr. Jingwen Guan in the research group of Dr. Benoit Simard at the National Research Council (NRC) of Canada. The SWCNT used in this thesis included: 1) as-produced; 2) purified; and 3) dodecyl functionalized. The samples were provided in powder form or deposited on holey carbon grids.

The MWCNT were produced by CVD and AD techniques and purchased from NanoCS Inc. and Mercorp Inc., respectively. The CVD-MWCNT was highly pure (>90 wt% purity) whereas AD-MWCNT had a lot of carbon contamination (<20 wt% purity). MWCNT were studied as received with no further treatments to avoid structural damaging.

The CNT samples were dispersed in N,N-dimethylformamide (DMF) to permit drop casting onto proper substrates; DMF was purchased from Caledon Lab. Ltd. and had

a purity of better than 99.8% .

3.2 Sample preparation

In order to prepare the samples for STXM and TEM-EELS measurements, CNT were dispersed in DMF under bath sonication. Sonication is a necessary step to overcome the large van der Waals forces between CNT. The samples were sonicated for less than two minutes to minimize modification of their chemical, physical, and electronic properties. [MK08] The solutions were drop cast onto holey carbon grids (SPI Inc.) or silicon nitride windows (Norcada Inc.); examples of these two substrates are shown in **Figure 3.1**. Holey carbon grids allowed characterization of the same CNT by both STXM and TEM. Silicon nitride windows are routinely used in X-ray spectromicroscopy of nanomaterials since their thin membrane (70-100 nm) does not absorb significantly at the low energy range except the N 1s and Si 1s edges. However, better image quality was obtained when CNT were on supported holey carbon grids even though CNT and amorphous carbon have somewhat similar spectra.

Figure 3.2 shows various stages of sample preparation for STXM and TEM-EELS measurements. After drop casting the solutions on the substrates, they were left in the lab to dry overnight and then further dried in a vacuum oven (**Figure 3.3**) for 1-7 days at 150-200 °C. The samples were kept in the vacuum at room temperature until they were shipped and measured at the ALS or CLS.
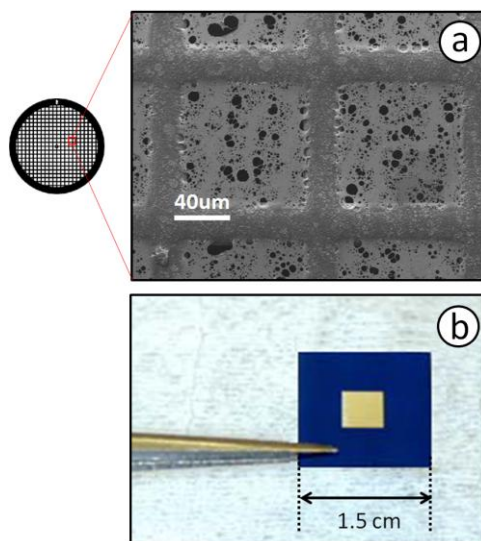
Figure 3.1 A holey carbon grid (a) and a silicon nitride window (b) used as substrates in this thesis.
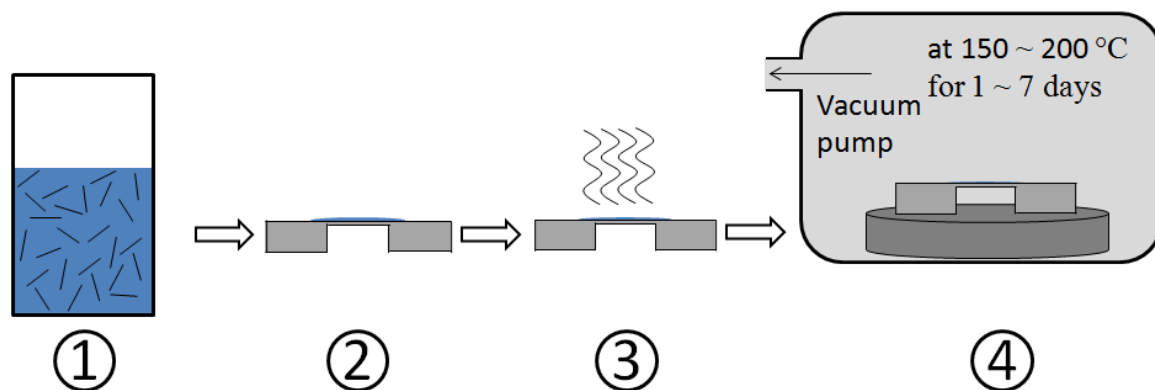
Figure 3.2 Various stages of sample preparation for STXM and TEM-EELS measurements.
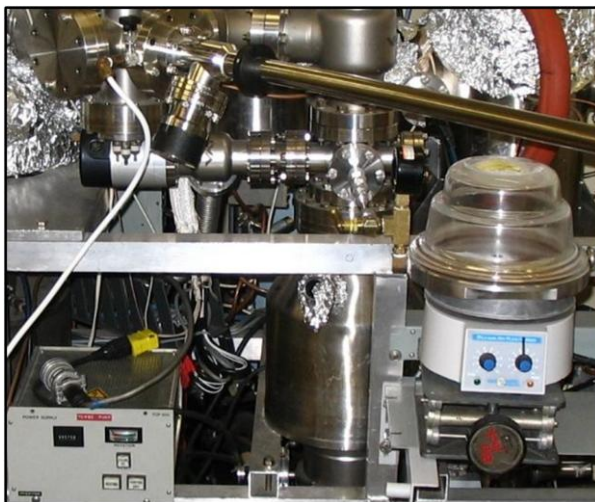
Figure 3.3 Vacuum oven setup used to dry the samples at temperatures between 150-200 °C. The glass enclosed hot surface is pumped by a liquid N_2 trapped turbo pump.

3.3 STXM data acquisition

STXM operates in single energy image, point scan, line scan spectra, and image sequence (or stack) modes. In each mode, the transmission data is recorded. It is then converted to optical density (OD) by using Beer-Lambert's law and the I_0 (incident flux spectrum) recorded either simultaneously or before/after the sample (I) scan. STXM data analysis including transmission to OD conversion is performed in *aXis2000* program. This section presents the principles and examples for each of these data acquisition modes.

3.3.1 Single energy images

In order to record a single energy image, one has to define: 1) photon energy; 2) position of the center of the image (x, y); 3) dimensions of the image $(\Delta x, \Delta y)$; 4) the point spacing (pixel size) $(\delta x, \delta y)$; and 5) dwell time at each pixel. STXM is equipped with a coarse stepper (range of 25 mm × 12 mm at CLS STXM) which is used to record

large images (>120 μm on STXM 5.3.2.2) and a piezo stage which is used to record small images (<120 μm). The transmission images are converted to OD images by normalizing to the I_0 which is usually obtained by averaging the intensity of pixels around the samples where the same support material or a hole exists.

Figure 3.4 shows the transmission (top row) and OD (bottom row) images of MWCNT recorded at the C 1s→π* (285.1 eV) and C 1s→σ* (291.8 eV) transitions. In the transmission images, dark pixels correspond to larger absorbance and bright pixels correspond to weaker absorbance at these photon energies. In the OD (absorbance) images, the contrast is reversed. The images have a size of 2.0 × 2.3 μm^2 (140 × 156 pixels) and dwell time of 2.5 ms and were recorded using the ALS STXM 5.3.2.2.

3.3.2 Point scans

Point scan is often used to obtain high quality reference spectra from homogenous samples. Point scan produces X-ray transmission signals from a single or multiple points as a function of energy. When multiple points are selected, the sample stage moves quickly from one point to another with signal acquisition at each point before the monochromator moves to the next photon energy. Two points are normally selected which include one point on the sample and the other on an empty area to record I_0. These two spectra have to be recorded quasi-simultaneously since the incident X-ray profile has a strong spectral structure and evolves over time. Moreover, the intensity of the X-ray beam decreases (at the CLS) as the storage ring current decays between the injections (~8 hours intervals). Besides, there could be sudden disturbances in the position of the electron beam in the storage ring which momentarily affects the X-ray beam.

Since the dwell time selected for point scans is usually in the order of a second, the measurements are often performed by using a defocused X-ray beam to minimize spectral distortions due to carbon photodeposition or radiation damage. In CNT, radiation damage by X-rays is negligible since CNT are conducting and the core hole is quenched by a valence electron before bond dissociation occurs.

Figure 3.5 presents an example of point scan from a graphite sample deposited on a holey carbon grid. The spectra were recorded with the CLS STXM where the electric vector (**E**) is 100% linearly polarized and in the graphite plane (polarization angle = 0°). The transmission spectrum of graphite was converted to OD using the I_0 recorded in the hole over which the graphite flake is suspended. The OD spectrum shows a weak π*-resonance intensity since **E** is orthogonal to the transition vector.

3.3.3 Line scan spectra

Line scan records a series of spectra at points along a straight line whose length and position is defined by the user. The STXM interferometric control system ensures a positioning accuracy of ~ 10 nm. Line scan spectra acquisition produces a line spectral image where the vertical axis is the length of the line in microns, and the horizontal axis is the photon energy range.

Transmission Images

Optical Density Images
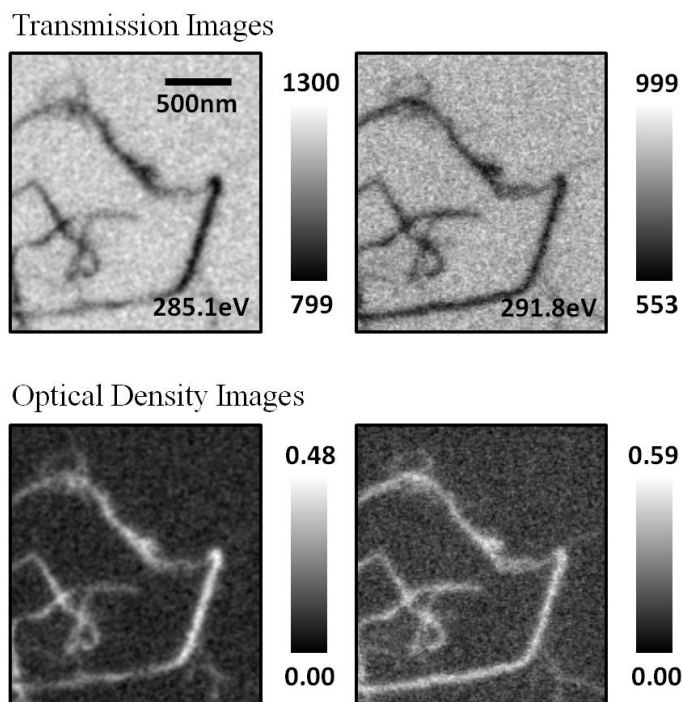
Figure 3.4 STXM images of CVD-MWCNT recorded at the π*-resonance (285.1 eV) and σ*-resonance (291.8 eV) in transmission (top row) and optical density (bottom row) modes (Image size: 2 μm × 2.3 μm, 140 × 156 pixels; dwell time: 2.5 ms). The contrast reverses from the transmission images to OD (absorbance) images; a larger OD is due to a larger absorbance and a smaller OD is due to a smaller absorbance. (ALS STXM 5.3.2.2)
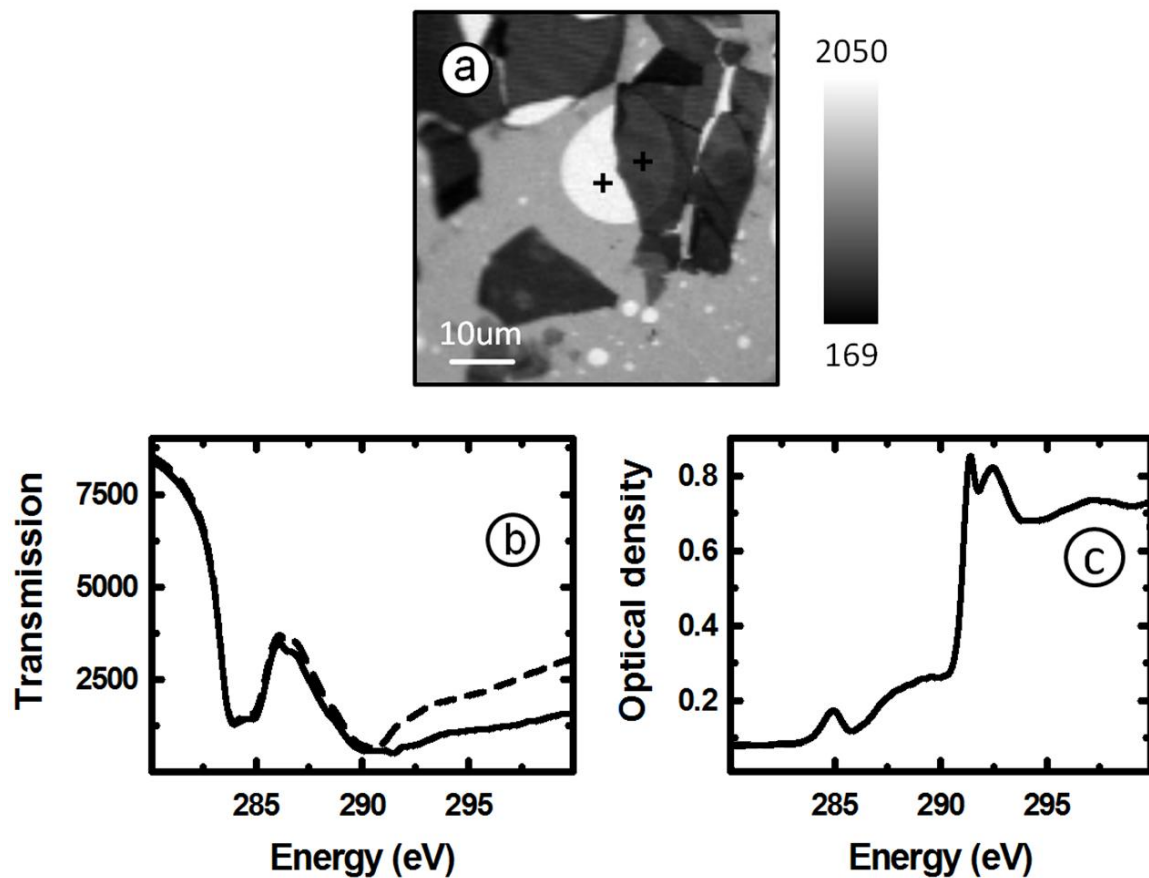
Figure 3.5 a) STXM image of graphite deposited on a holey carbon grid. b) The transmission spectra recorded on the hole (dashed line) and graphite (solid line). c) The optical density spectrum of graphite. (CLS STXM)

3.3.4 Image sequences (stacks)

Image sequence (stack) mode records a series of transmission images at user defined image and pixel sizes, energy intervals, and dwell times [JWF&00]. STXM can record image sequences for more than one region by quickly moving the sample stage. This is done by selecting "Multiple Regions" option in the scan definition panel in the STXM control software (**Figure 3.6**). The STXM control software allows the users to vary the energy sampling and dwell time within each energy range in a single measurement which significantly reduces acquisition time. Typically, one uses a fine energy sampling (0.05 - 0.1 eV) in the regions of sharp structures and a coarse sampling (0.2 - 0.6 eV) outside such regions. The interferometer in the STXM ensures the precise control of the position. However, in the image sequence mode, images often drift over time. This problem is resolved by aligning the stacks using automatic or manual alignment procedures available in *aXis2000* program.

Figure 3.7 shows selected optical density images from an image sequence recorded for bundles of SWNCT. The spectra were extracted from the two regions marked in the pre-edge image (image 1) as gray rectangles. The complete image sequence consists of a series of images, each with a size of $2.7 \times 1.6 \ \mu m^2$ (144×91 pixels), recorded at 118 energies between 280 - 320 eV. The image contrast slightly changes at the π^*-resonance (image 2) as the vertical and horizontal portions of the SWCNT absorb differently.
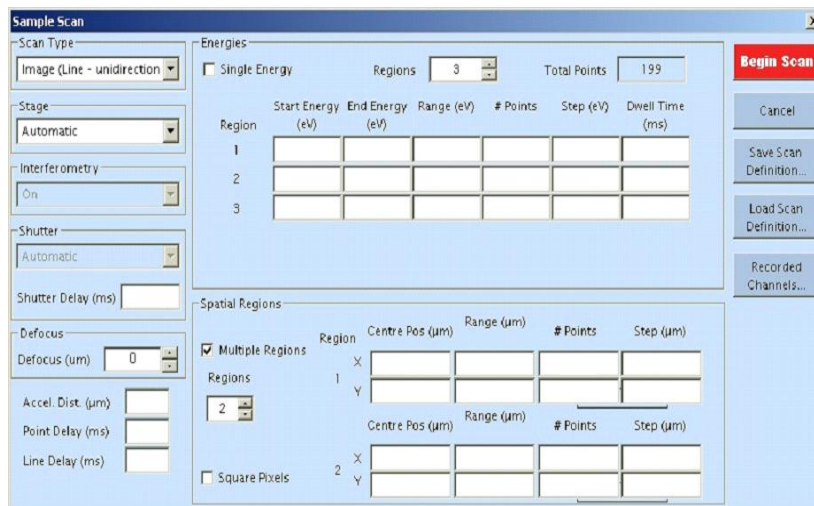
Figure 3.6 Screen shot of the scan definition panel in the STXM control software.
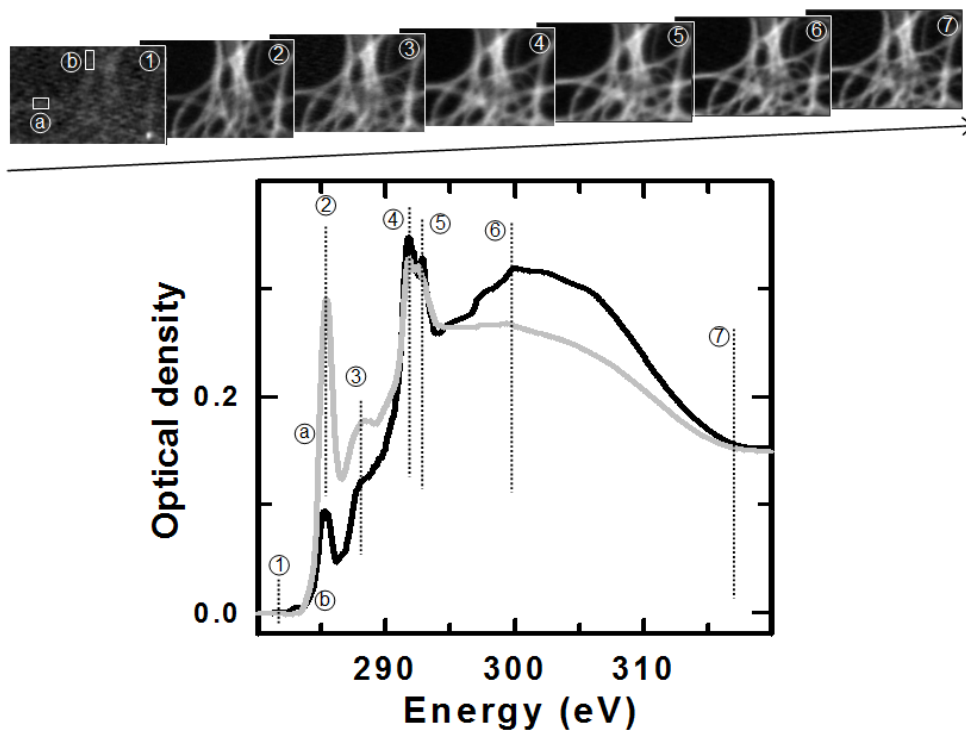
Figure 3.7 Image sequence of bundles of SWCNT. The spectra were extracted from the

highlighted rectangles (grey line: a; black line: b) in the pre-edge image (image 1). (ALS

STXM)

3.3.5 Stack map

Stack maps contain two transmission images recorded at the pre-edge (280 eV) and at the π^*-resonance (285.1 eV) energy. After being aligned and converted to OD, the pre-edge image is subtracted from the resonance one to obtain a single image that represents the height of the transition. These so-called "π^*" transition images recorded at various polarization angles of **E** are combined to form a polarization stack.

Figure 3.8 shows π^* transition images recorded at 12 polarization angles of **E** for an AD-MWCNT. The orientation of **E** is represented by the white arrows. These images were derived from stack maps, each containing two images at 280 and 285.1 eV. The intensity of the pixels on MWCNT depends on the angle between **E** and MWCNT. When **E** is orthogonal to the MWCNT, the pixels in the AD-MWCNT become brighter and when they are parallel the pixels are dimmer.
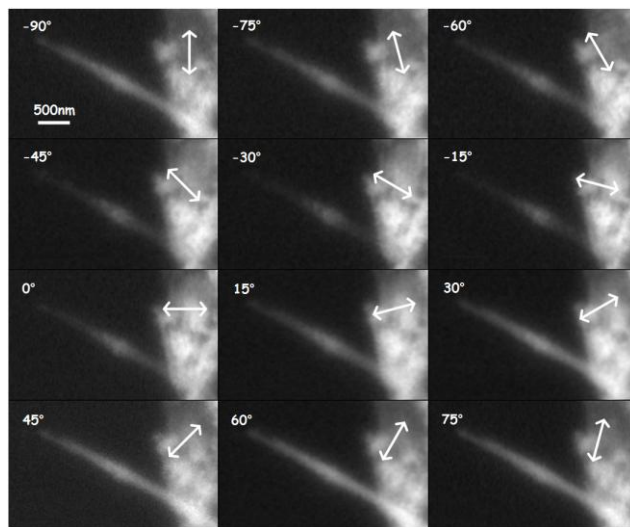
Figure 3.8 Polarization images recorded for an AD-MWCNT at various polarization angles of the E. (CLS STXM)

3.4. Challenges with STXM measurements

STXM characterization of CNT is relatively a straight forward task. However, due to their small diameter (and short length if they are subjected to chemical functionalization), their characterization may sometimes be challenging.

3.4.1 Locating the CNT

CNT diameters range from ~1.0 nm to several hundred nanometers. This makes it difficult to locate them on the substrates by low resolution STXM imaging. CNT are randomly distributed on substrates; thus, a few high resolution STXM images are usually recorded from various areas on the substrate to find appropriate CNT for further characterizations. This is a time consuming process. In order to avoid this step, I previewed the samples by a scanning electron microscope (SEM) before I shipped them to the ALS or CLS for STXM measurements. The SEM images were measured with the JEOL 7000F field emission SEM at the Canadian Centre for Electron Microscopy (CCEM) and the Vega II Tescan in the Faculty of Health Sciences (FHS) electron microscope facility, both at McMaster University (**Figure 3.9**).

Figure 3.10 shows a micrograph of an AD-MWCNT sample recorded by the JEOL 7000F SEM using 5.0 kV beam at working distance of 5.0 mm. The samples were imaged at low magnifications to avoid carbon contamination. CNT and their locations were identified so that they could be easily found by STXM.

Figure 3.9 7000F JEOL (a) and Tescan Vega II (b) SEM used to preview the CNT

samples prior to STXM measurements.
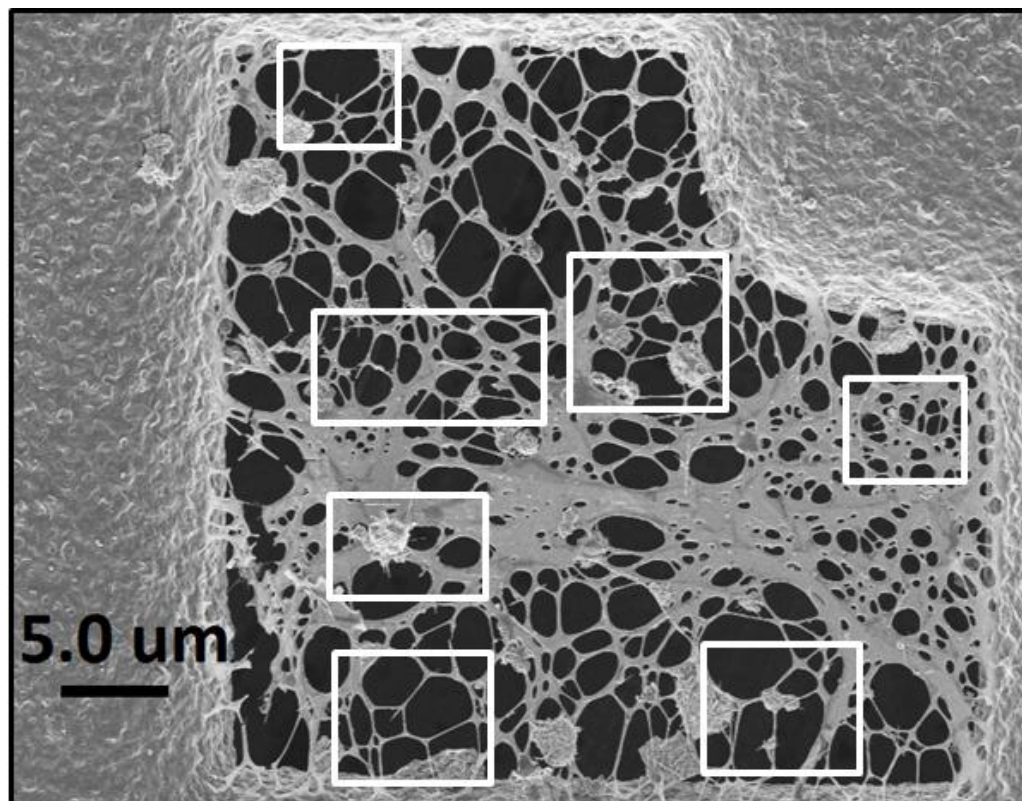
Figure 3.10 A typical SEM preview image recorded by JEOL 7000F SEM on an AD-

MWCNT sample.

3.4.2 Carbon photodeposition

To obtain high quality image sequences and stack maps of CNT samples, I often use a dewll time of 2-5 ms and pixel size of 10-15nm. This exposes the samples to high doses of X-rays and contaminates them with amorphous carbon.

Figure 3.11 shows two images recorded at the π*-resonance (285.1eV) before (a) and after (b) an image sequence (polarization = 0°). The sample is AD-MWCNT deposited on a holey carbon grid. The image sequence contained 60 images with a size of 0.65×1.25 um^2 (90×163 pixels) and dwell time of 2.5 ms. While the features are sharp in **Figure 3.11a**, they become fuzzy with diffuse edges in **Figure 3.11b**. The **Figure 3.11c** is the difference image and indicates up to 56% increase in the OD due to carbon contamination. This is potentially misleading when interpreting the spectra. In polarization stacks, this OD increase could be mistakenly interpreted as an enhanced polarization signal and interfere with the analysis.
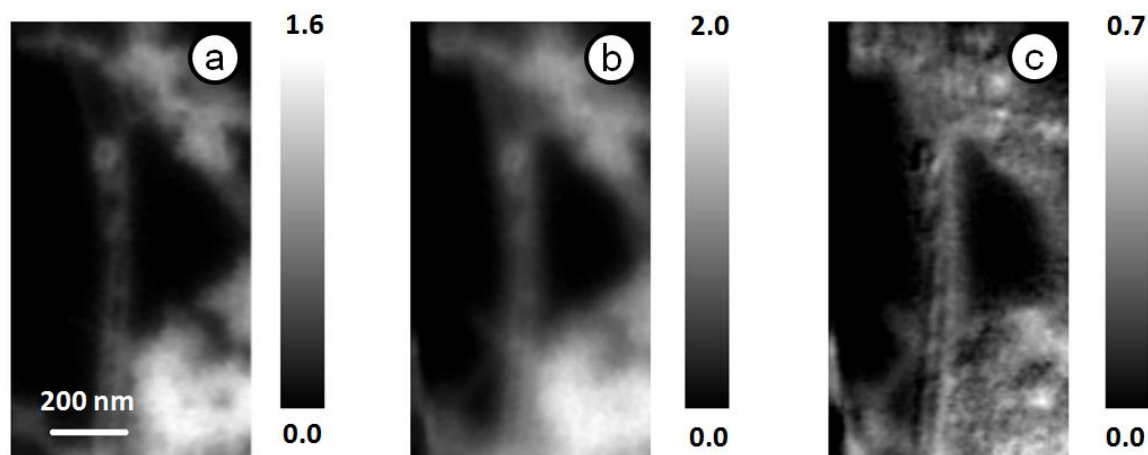
Figure 3.11 STXM images recorded at the π*-resonance before (a) and after (b) recording an image sequence; (c) the photodeposition map obtained by taking the difference of the before and after images. (CLS STXM)

Carbon photodeposition is caused by: 1) residual solvents in the sample; and 2) organic vapors from fingerprints and the oil used to lubricate the mechanical stages of the STXM. These organic substances break down into free radicals under the X-ray beam and then polymerize, leaving an X-ray opaque coating on the sample. The samples are usually annealed in a vacuum oven prior to STXM measurements for several days at 150°-200°C. Therefore, they are relatively clean for STXM measurements. In order to reduce the second source of carbon photodeposition, I examined several approaches, including isolating the samples between silicon nitride windows as well as using a cold finger. I deposited AD-MWCNT on a TEM grid and then sandwiched the grid between two silicon nitride windows as shown in **Figure 3.12a**. Then, I sealed the windows with epoxy glue. The sample was left in the lab for a week to let the glue set and then dried further in the vacuum oven at 150°C for 24hrs. In principle, this setup should have prevented organic molecules from reaching the sample; thus, preventing carbon photodeposition. However, when I compared the STXM images recorded at the π*-resonance (polarization = 0°) before (**Figure 3.12b**) and after (**Figure 3.12c**) an image sequence, I noticed up to 20% increase in the optical density. The image sequence contained 90 images with a size of 0.9×0.7 um^2 (67×54 pixels) and dwell time of 5.0 ms (280 - 320 eV). I tried this approach several times and I obtained the same or worse results. Another disadvantage of this approach is the loss of flux which reduces the signal-to-noise ratio and contrast.
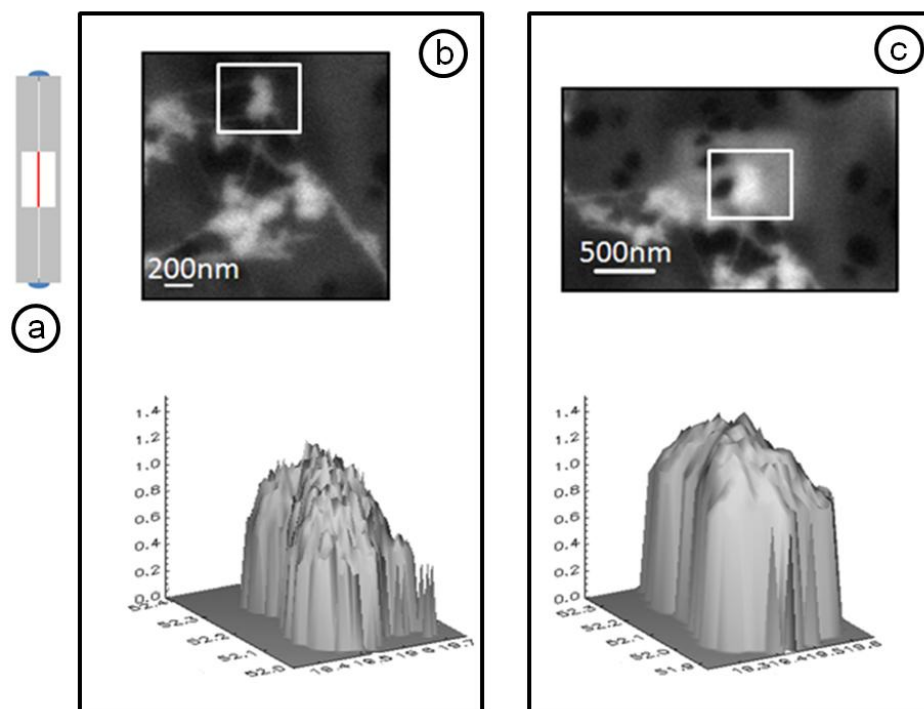
Figure 3.12 TEM grid sandwiched between two silicon nitride windows and sealed with epoxy glue (a). π^*-resonance images recorded before and after a stack containing 90 images with a size of 0.9×0.7 um^2 (67 × 54 pixels) and dwell time of 5.0 ms. (ALS STXM)

Cold fingers are routinely used in SEM and TEM to condense and remove organic vapors. Recently, a cold finger has been designed and fabricated for the CLS STXM (**Figure 3.13**). However, my experiments showed that it was inefficient in reducing carbon contamination. Furthermore, since the cold finger is placed next to the sample plate inside the STXM, it caused thermal drifts which dramatically reduced the quality of the image sequences.

Figure 3.13 Cold finger designed and fabricated for the CLS STXM.

To get around carbon photodeposition problem, I only selected the CNT that were
on supported films. When CNT are freestanding, the carbon photodeposition occurs only
on them, increasing their thickness. This becomes a severe problem when recording
polarization stacks or image sequences. However, when they are on supported films, this
growth occurs fairly uniformly everywhere. Since the I_0 is selected in the area next to
CNT, the effect of carbon photodeposition is removed when the transmission images are
converted to OD images.

3.5. STXM data analysis

Most of the STXM measurements in this thesis were performed by using image sequences and stack maps. Point scan and line scan modes proved ineffective when measuring nano-materials due to large drifts.

3.5.1 Chemical mapping

A typical sample usually contains more than one chemical component. Therefore, its NEXAFS spectrum is the sum of the spectrum of each component. *aXis2000* is equipped with a *singular value decomposition* (SVD) algorithm that quantitatively maps these components.

Figure 3.14 shows an example of SVD analysis of a stack recorded on SWCNT bundles with X-rays of linear horizontal polarization (ALS STXM). The components correspond to vertical (a), horizontal (b), and oxidized (c) SWCNT. Horizontal MWCNT show a weak π^*-resonance whereas vertical SWCNT show a strong π^*-resonance and therefore, despite their fairly similar spectra, they are detected as two separate components. The map of the oxidized region of the SWCNT corresponds to carbonyl, hydroxyl, and carboxyl groups. The gray scales of each image indicate thickness of each component in nanometers. **Figure 3.14d,e** are scaled and un-scaled color-coded composites of the horizontal (red), vertical (green) and oxidized (blue) maps, respectively. To scale the images, the intensity of 3.14a, 314b and 3.14c are each mapped to the full 8-bit scale of its color. Color-coded composite images help to gain a better understanding of relative distribution of the components.
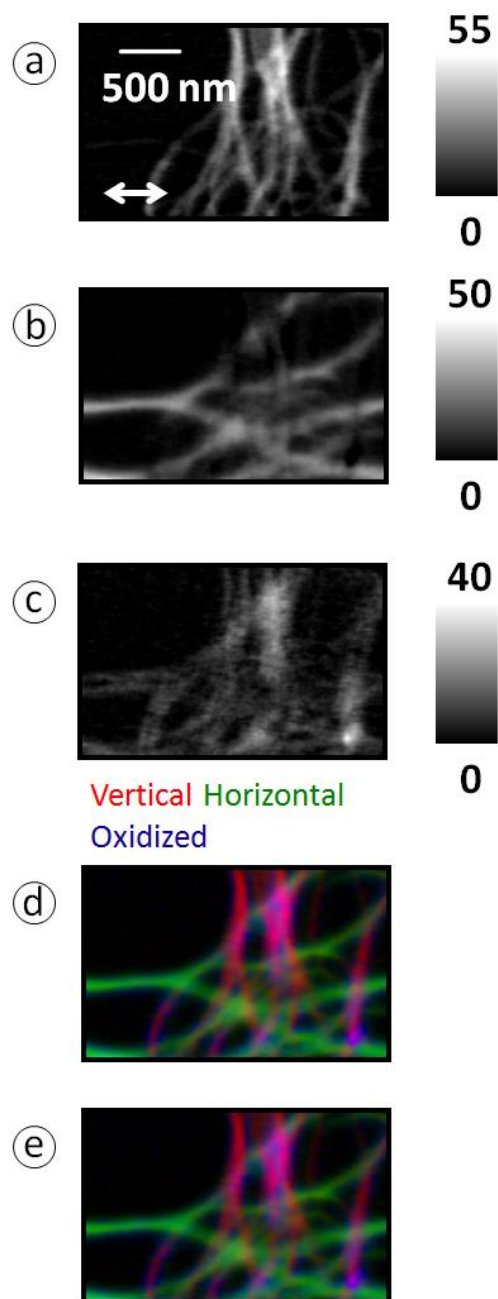
Figure 3.14 Vertical (a), horizontal (b), and oxidize (c) SWCNT maps obtained by SVD

analysis of the image sequence. The color coded scaled (d) and unscaled (e) composites

show the relative distribution of these components. (ALS STXM)

In order to map the chemical components by SVD, their reference spectra are needed. The reference spectra of horizontal and vertical CNT are very different when linearly polarized X-rays are used for excitation since they absorb differently at the π^*- and σ^*-resonances.

For SWCNT, the reference spectra of horizontal and vertical SWCNT were obtained from a purified SWCNT. The sample was received on a holey carbon grid from the NRC and kept under vacuum until it was measured at the ALS STXM. I recorded a stack at the C 1s edge with 118 images at 1.0 ms dwell time where the images had the size of 3×2 um^2 (150×100 pixels). I extracted the spectra from the horizontal and vertical portions of the SWCNT bundles as shown in **Figure 3.15a**. The intensity scales of these spectra were normalized to 1.0 nm by matching the pre-edge and post-edge regions to the sum of tabulated atomic mass absorption coefficients for elemental carbon multiplied by the density of the CNT it its standard form. Since **E** at the beamline 5.3.2.2 at the ALS is only 85% linearly polarized, I corrected the spectra for the non-linearly polarized portion of the X-rays [WA08]. This was done by subtracting 15% of the averaged spectrum from the spectra of the horizontal and vertical SWCNT. The resulting reference spectra of the horizontal and vertical SWCNT are plotted in **Figure 3.15b, c**.
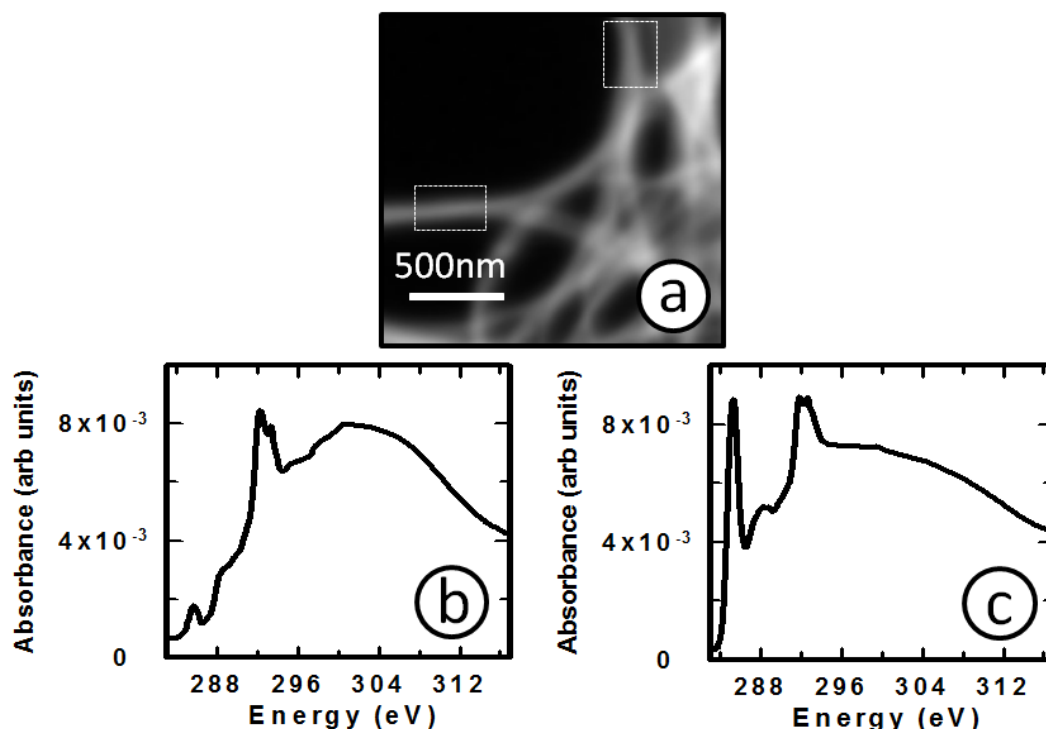
Figure 3.15 a) STXM image of SWCNT bundles (a) recorded at the π^*-resonance (285.1 eV). The spectra of the horizontal (b) and vertical (c) SWCNT were extracted from the highlighted rectangles on the SWCNT. The spectra were corrected for non-linearly polarized portion of the X-rays and then normalized for 1.0 nm. (ALS STXM)

I followed the same procedure to obtain the reference spectra of horizontal and vertical MWCNT from an AD-MWCNT sample deposited onto holey carbon grids. I performed the STXM measurements at ALS beamline 5.3.2.2 by manually rotating the sample by 90° to record stacks for horizontal and vertical orientations of the same MWCNT relative to **E**. This process is shown in **Figure 3.16a,b**. The spectra were normalized to 1.0 nm and then corrected for the non-linearly polarized portion of the X-ray.
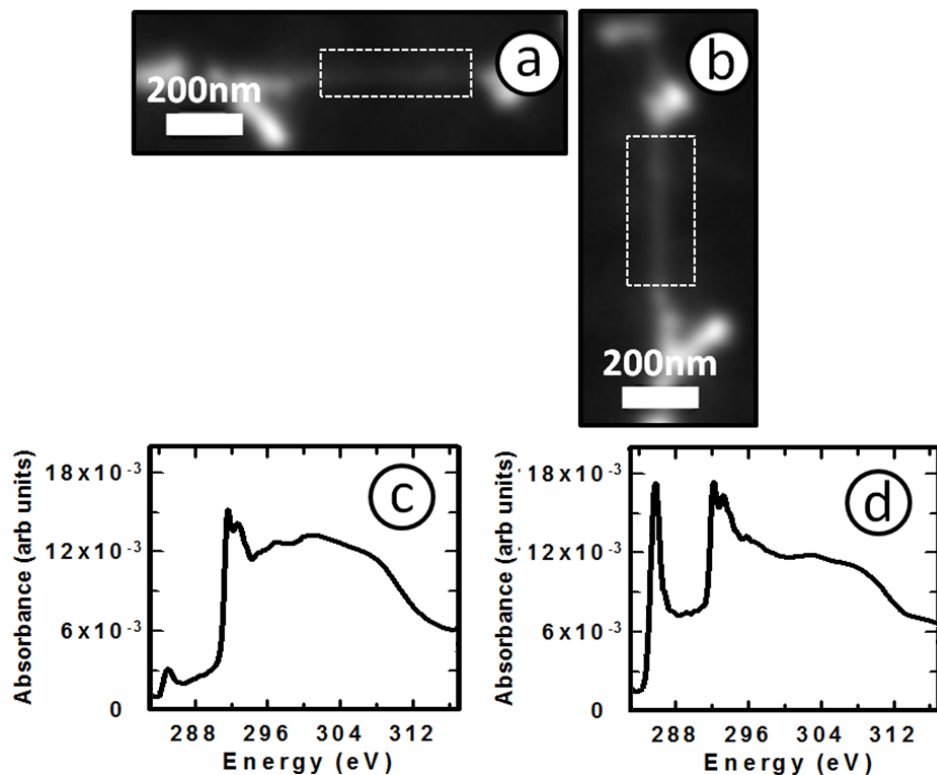
Figure 3.16 a) STXM images of MWCNT at horizontal (a) and vertical (b) orientations of MWCNT relative to **E** recorded at the π^*-resonance (285.1 eV). The reference spectra of the horizontal (b) and vertical (c) MWCNT were extracted from the highlighted rectangles; the spectra were corrected for the non-linearly polarized portion of the X-rays and then normalized for 1.0 nm. (ALS STXM)

The reference spectra of carbon impurities, oxidized CNT, and short chain alkyl molecules used in this thesis are plotted in **Figure 3.17**. The reference spectra of carbon impurities and oxidized CNT plotted in **Figure 3.17** were those reported earlier and extracted from MWCNT samples [FHB&06,FBP&07]. The reference spectrum of dodecyl was that of an amorphous C-60 short-chain polyethylene wax [HAI&03].
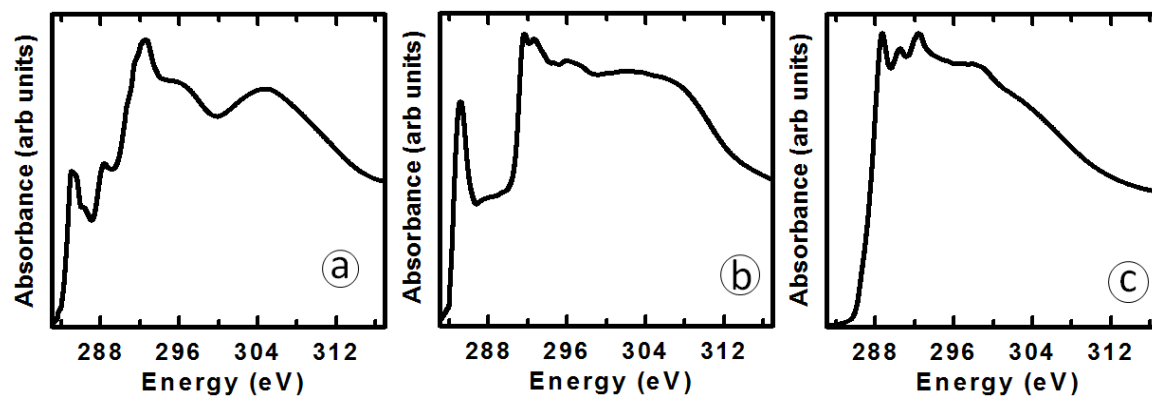
Figure 3.17 The reference spectra of the oxidized MWCNT (b) carbon impurities (c) short chain alkyl molecules.

3.5.2 Studies of X-ray linear dichroism of individual CNT

Polarization stacks obtained from stack maps were used to study X-ray linear dichroism (XLD) in SWCNT and MWCNT. **Figure 3.18** plots the experimental π^* intensities extracted from the indicated box in the inset. The polarization stack was constructed by combining the polarization images in Figure 3.10. The axis of MWCNT was located at 30° relative to horizontal. Based on the expected polarization response, the C 1s→π^* transition should have the lowest intensity when **E** is parallel to the MWCNT (-30°) and the highest intensity when **E** is normal to the MWCNT (+60°). The experimental values were consistent with this expectation.
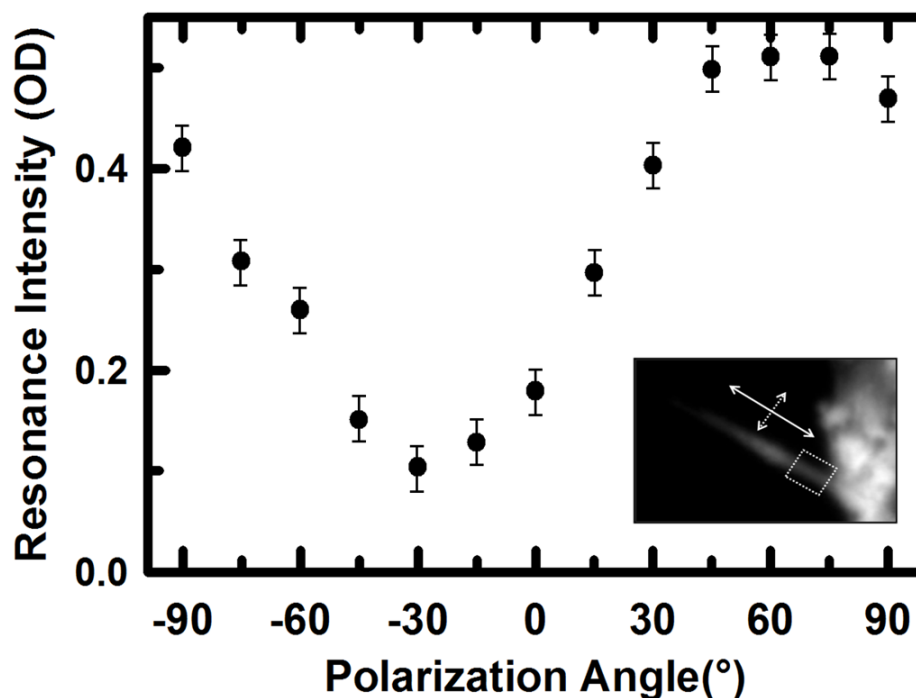
Figure 3.18 π^* intensities extracted from the highlighted rectangle in the inset. (CLS STXM)

To verify that the experimental data ($I(\theta)$) are associated with linear dichroism, they were fitted to the polarization function:

$$I(\theta) = C + A \cdot \cos^2\left(\theta - \theta_{ref}\right)$$ Equation 3.1

where θ_{ref} is an optimizable parameter which, if the model is correct, should correspond to the angle between the long axis of CNT and the horizontal (θ=0° corresponds to horizontal E). In the polarization function, C is the portion of the signal that does not show dichroism and A is the magnitude of the XLD. **Figure 3.19** shows a typical fitting process carried out in *aXis2000* which determines C, A, and θ_{ref} through an iteration process.
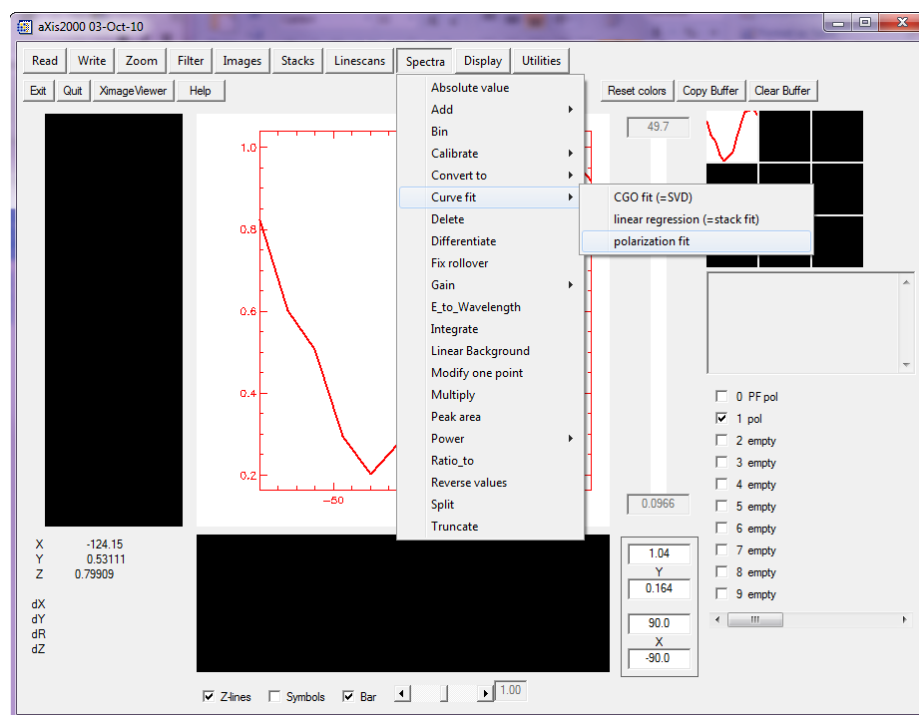
Figure 3.19 Fitting process of the experimental intensities in *aXis2000*.

3.5.3 Evaluation of quality of CNT

The major motivation of this thesis is to explore the use of the XLD signal at the π^*-resonance to evaluate the quality of CNT. In CNT, the C $1s\to\pi^*$ transition is most intense when **E** and CNT are orthogonal $\left(I_{\parallel}\right)$ and weakest when they are parallel $\left(I_{\perp}\right)$. In defective CNT, $I_{\parallel}$ is reduced and $I_{\perp}$ is increased. Therefore, it is possible that the polarization ratio $\left(\dfrac{I_{\perp}}{I_{\parallel}}\right)$ of isolated CNT is a measure of their quality. This thesis has explored and documented this relationship. In high quality CNT, the polarization ratio is large and as the quality lowers this ratio decreases. For instance, **Figure 3.20** plots the π^*-resonance intensities from selected portions of the CVD-MWCNT (a) (triangles in the plot) and AD-MWCNT (b) (circles in the plot). The experimental values were fitted by the polarization function; in each case the CVD-MCNT (dashed line) showed a smaller dichroism than the AD-MWCNT (solid line). The polarization ratio was calculated to be 3.0 and 6.7 respectively, suggesting a lower structural quality for the CVD-MWCNT. This was in agreement with previously published reports that attribute a better quality to the CNT produced at higher temperatures [KHO&03].
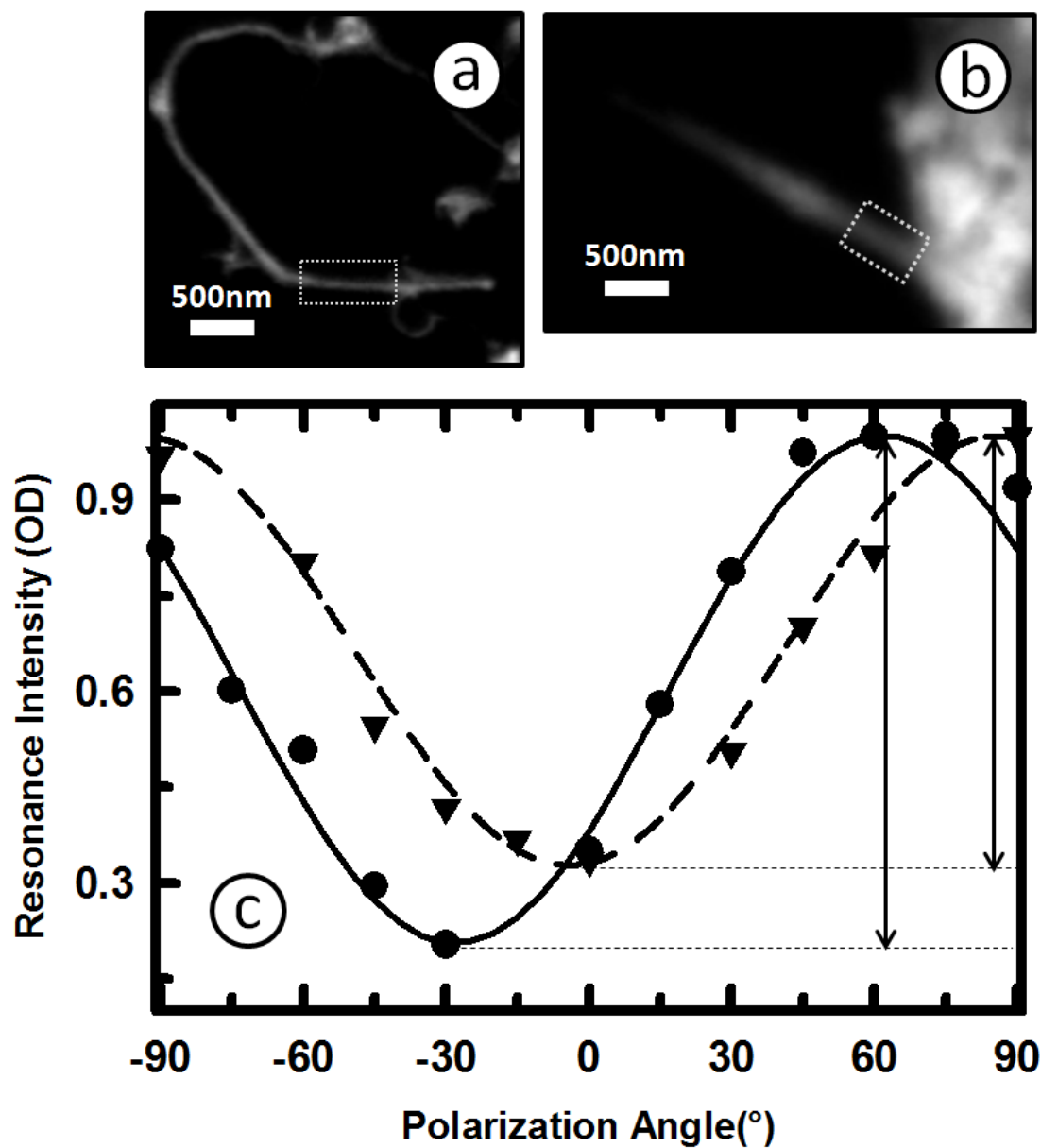
Figure 3.20 Experimental π^* intensities from CVD (a) and AD (b) MWCNT fitted to polarization function. The experimental values are normalized to remove the effects of thickness. (CLS STXM)

3.6 TEM-EELS characterization of CNT

TEM-EELS characterization of the AD-MWCNT was performed in STEM mode using the FEI Titan 80-300 Cubed (Titan 1) at the CCEM at McMaster University. Similar to STXM, TEM-EELS characterizes isolated MWCNT and acquires their spectra in point scan, line scan, and image sequence modes. However, TEM-EELS records the near edge electron energy loss spectra of the samples. Examples of point scan and line scan are presented in **Figure 3.21** and **Figure 3.22**.
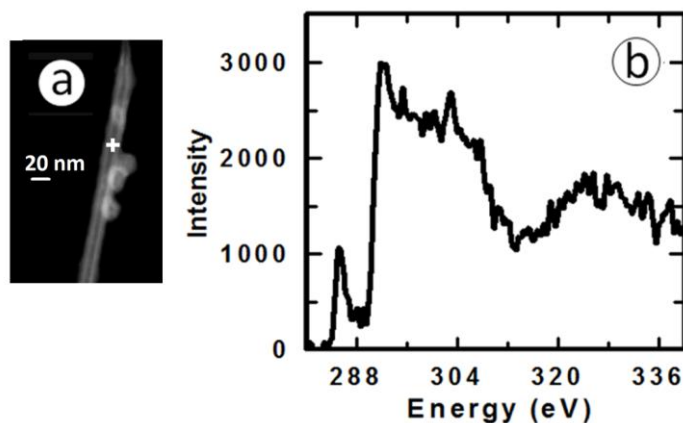
Figure 3.21 STEM image of an AD-MWCNT (a). Point scan EELS spectrum recorded from the gray cross in the centre of the AD-MWCNT (b).
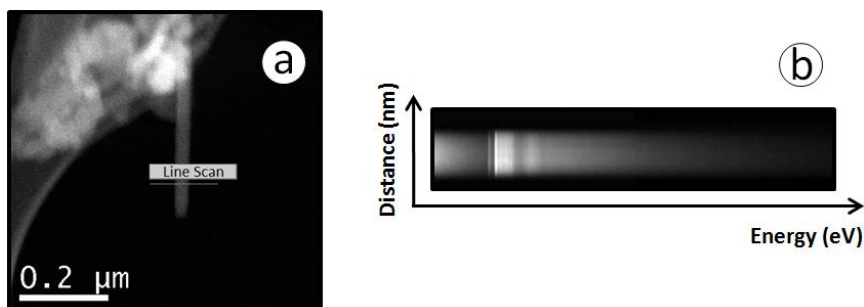
Figure 3.22 STEM image of an AD-MWCNT (a). The line scan spectral image recorded along the gray line (b).

The recorded EELS spectra contain a large background due to low energy signal and plural volume loss inelastic scattering. *Digital Micrograph* automatically removed this background by using a power law algorithm in a manner shown in **Figure 3.23**. This automatic background subtraction was executed on point and line spectra as well as image sequences.
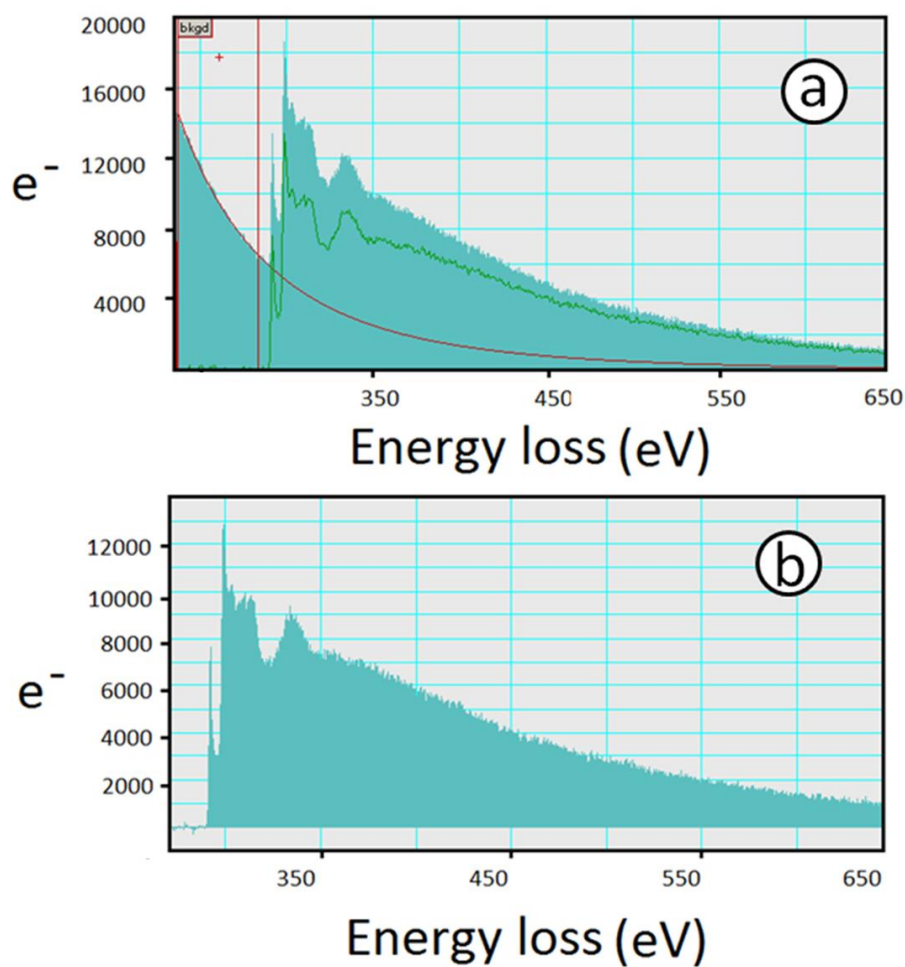
Figure 3.23 The process of removing the background from the EELS spectra in *Digital Micrograph* program.

3.6.1 TEM-EELS setup

TEM-EELS measurements were performed in STEM mode using 80 kV beam energy to avoid structural (knock-on) damage to MWCNT. The measurements were done with the help of David Rossouw, currently a graduate student in Professor Gianluigi Botton's research group. Titan 1 can operate in the range of 80 to 300 kV for imaging and spectroscopy. However, changing the beam voltage destabilizes the beam and causes large drifts while recording spectra. Thus, Titan 1 was set to 80 kV at least two days before the measurements were carried out to give the microscope enough time to stabilize.

Since the aim of this study was to produce momentum resolved C 1s spectra from CNT, the microscope was optimized to control the orientations of the momentum transfer. This optimization resulted in convergence angles (α) of 6.5 and 8.4 mrad, collection angles (β) of 4.5 and 6.6 mrad and FWHM at zero loss of better than 0.2 eV.

The TEM grid was mounted on a tomography holder to tilt the sample as shown in

Figure 3.24. This was to study the spectral changes of MWCNT as a function of tilt angle

(θ angle).
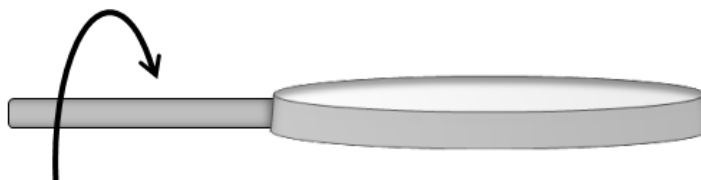
Figure 3.24 Schematic of tilting the sample by using the tomography holder.

3.6.2 EELS data analysis

The point spectra, line spectra, and image sequences recorded from MWCNT

were saved as *text* files in *Digital Micrograph* and then opened in *Matlab 7.9* and

aXis2000 program for comparison. Both *Matlab 7.9* and *aXis2000 program* had import

algorithms and therefore no extra computer coding was necessary. Since the spectra

correspond to various thicknesses, they were normalized to the continuum intensity at 340

eV to remove thickness effects.

3.6.3 Principal component analysis (PCA) of image sequences

In order to remove random and systematic noises from image sequences, PCA

was employed. PCA projects data points onto hyperplanes and subspaces that best

describe the variations in datasets. Variations in datasets are due to some underlying

physical effects. PCA defines and ranks the direction of these variations as principal

components (PCs). Once the major variations are detected as dominant components, the

remaining components are interpreted as random noises. Regardless of how large a

dataset is, only a few PCs are usually necessary to explain 99% of variations in it.

Figure 3.25 shows a geometrical interpretation of PCA where a three-dimensional data set is projected onto a hyperplane. The hyperplane is described by PC_1 and PC_2 which explain the direction of variations.
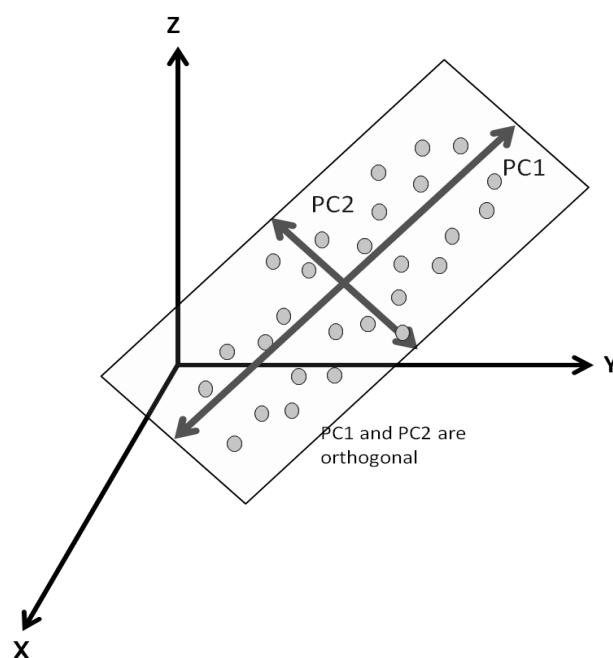
Figure 3.25 Geometrical interpretation of PCA.

PCA involves decomposing a dataset (X) into a structure part (TP^T) and a noise part (E):

$$X = TP^T + E$$

where T is called the score matrix and P is called the loading matrix. The score matrix contains the original data points in the transformed coordinate. Loadings are the weights

of the variables in X on the score T. The loadings show which variables are responsible for the observed structures in the score matrix.

In order to perform PCA on image sequences, they were unfolded into two dimensional matrices such that each column in these matrices contained the spectral information of one pixel as schematically shown in **Figure 3.26**. The resulting two dimensional matrices were subjected to PCA.
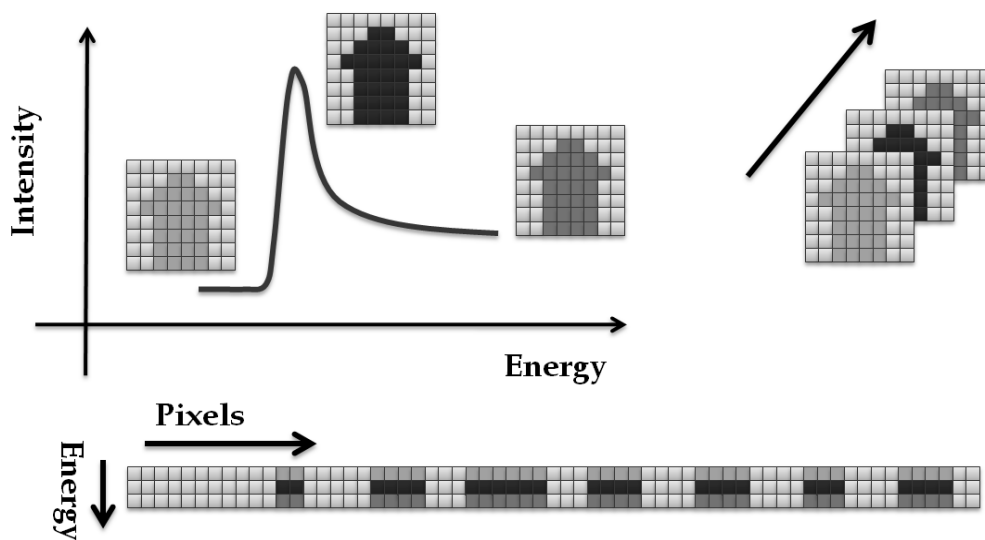
Figure 3.26 The process of unfolding image sequences into two dimensional matrices.

Since only a few PCs are required to capture the main variations in the dataset, the remaining PCs can be simply discarded. This can help to remove random and some of the systematic noises from the image sequences that lower their quality. The components corresponding to systematic noises were examined to ensure that they do not contain chemical information. **Figure 3.27** shows some of images in a STXM image sequences recorded on dodecyl functionalized SWCNT before (left panel) and after (right panel) removing random noises by PCA (PC_8 and above were removed). The Matlab code written for removing noise from stacks is presented in **Appendix C**.
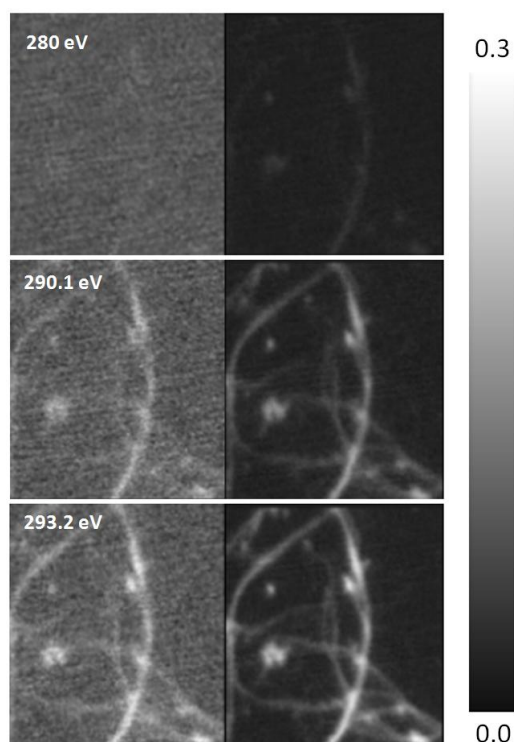
Figure 3.27 Selected images from a STXM image sequence before (left panel) and after (right panel) noise filtering by PCA.

3.7 Focused ion beam (FIB) modification of CNT

Focused ion beam modification of CNT was performed by Zeiss NVision 40 dual FIB/SEM with the help of Miss Julia Huang. The microscope provides 475 x - 500 kx magnification and up to 4.0 nm spatial resolution at 30 kV in FIB mode (**Figure 3.28**).

Gallium ion beam in the microscope allows high precision milling of the sample at various beam sizes and beam currents. **Figure 3.29** shows a CVD-MWCNT subject to FBI modification with a 30 kV beam and 10 pA beam current for 1, 2, and 3 seconds. The effects of FIB on CNT were studied by TEM-EELS.

Figure 3.28 Zeiss NVision 40 dual FIB/SEM used for FIB modification of the CNT.
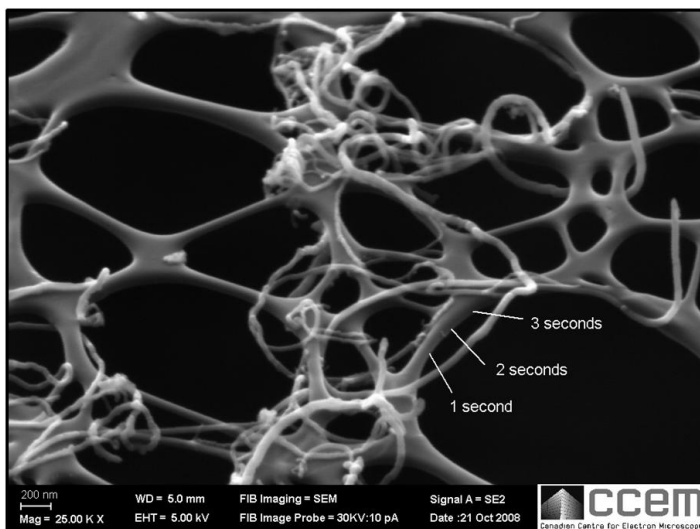
Figure 3.29 A CVD-MWCNT subjected to FIB modification.

Chapter 4

Polarization dependence of the C 1s X-ray absorption spectra of individual multi-walled carbon nanotubes

This chapter discusses polarization dependence of the C 1s spectra of individual MWCNT measured by STXM. Specifically, it studies intensity variations at the C 1s→π when the orientation of **E** of the incident X-rays relative to the long axis of MWCNT changes.*

*Reprinted with permission from Small 4 (**2008**) 2279-2285, Ebrahim Najafi, Daniel Herna´ndez Cruz, Martin Obst, Adam P. Hitchcock, Bastien Douhard, Jean-Jacques Pireaux, and Alexandre Felten, "Polarization Dependence of the C 1s X-ray Absorption Spectra of Individual Multi-Walled Carbon Nanotubes", Copyright 2008, Wiley-VCH Verlag GmbH & Co. KGaA, Weinheim.*

The author of this thesis prepared the MWCNT samples, performed the STXM measurements, and analyzed all the STXM data and wrote the publication under the guidance of Prof. A. P. Hitchcock.

Polarization Dependence of the C 1s X-ray Absorption Spectra of Individual Multi-Walled Carbon Nanotubes

Ebrahim Najafi, Daniel Hernández Cruz, Martin Obst, Adam P. Hitchcock,* Bastien Douhard, Jean-Jacques Pireaux, and Alexandre Felten

The polarization dependence (linear dichroism) of the C 1s X-ray absorption spectrum of individual multi-walled carbon nanotubes (MWCNTs) is measured using scanning transmission X-ray microscopy. A very strong dichroic effect is found in the C 1s → π* transition, with almost complete disappearance of this transition when the electric-field (E)-vector is aligned parallel to high-quality (low-defect) MWCNTs and maximum intensity when the E-vector is orthogonal to the tube axis. In contrast, there is very little dichroism in the C 1s → σ* transitions. The origin of this polarization effect is explained. The magnitude of the polarization dependence is found to differ in MWCNTs synthesized by different methods (arc discharge versus chemical vapor deposition). This is ascribed to differences in densities of sp²-type defects. The potential for use of this signal to characterize defects in single-carbon-nanotube devices is discussed.

Keywords:
- carbon nanotubes
- linear dichroism
- scanning transmission X-ray microscopy
- sp² defects
- X-ray absorption spectroscopy

1. Introduction

Carbon nanotubes (CNTs) are often regarded as the building blocks of nanotechnology. Due to their exceptional properties CNTs are candidates for many engineering applications, such as electronic devices, field emitters, and gas sensors.[1–3] The potential of perfect CNTs is widely accepted. However, in most cases the actual materials are far from perfect, and so to realize such applications it is important to be able to monitor their electronic and mechanical character. The electronic, chemical, and mechanical properties of CNTs are correlated with their structure. From one sample to another, the composition of the powder and structure of the nanotubes can vary significantly. This is one of the most important challenges for advancing CNT-based nanotechnologies.[4] Electronic applications require nanotubes without chemical impurities or structural defects, since these cause electron

scattering, which reduces electron mobility.[5,6] In other applications, certain types of defects are desirable since they can be used to control resistance,[6] to act as chemically specific sensors,[7] or as reactive sites for functionalization.[8] Thus, depending on the application, defective nanotubes may be either desirable or undesirable.

Conventional spectroscopy techniques such as near-edge X-ray-absorption fine-structure spectroscopy (NEXAFS)[9] and photoelectron spectroscopy (PES) are often used to study the electronic structure of CNTs. These techniques sample a large area and, therefore, the information obtained is an average property of the batch. Spectromicroscopy techniques, on the other hand, measure with high spatial resolution, thus allowing study of individual nanostructures. Kuzuo et al.[10] used electron-energy-loss spectroscopy (EELS) in transmission electron microscopy (TEM) to confirm the covalent character of the bonding across bundles of single-walled CNTs (SWCNTs) and multi-walled CNTs (MWCNTs). They reported two intense peaks for both SWCNTs and MWCNTs in the carbon edge region corresponding to the C 1s → π* and C 1s → σ* transitions, with those of the SWCNTs broader than those of the MWCNTs. Kuzuo et al. attributed this to the strong curvature of SWCNTs.[10] Stephan et al.[11] examined isolated SWCNTs and MWCNTs by TEM-EELS and showed that the spectral broadening was due to the presence of amorphous carbon impurities rather than tube curvature.

[*] Prof. A. P. Hitchcock, E. Najafi, Dr. D. H. Cruz, Dr. M. Obst
Brockhouse Institute for Materials Research
McMaster University
Hamilton, ON L8S 4M1 (Canada)
E-mail: aph@mcmaster.ca

B. Douhard, Prof. J.-J. Pireaux, Dr. A. Felten
LISE, University of Namur
61 rue de Bruxelles, Namur 5000 (Belgium)

125

A. P. Hitchcock et al.

Further, they investigated spectral variations across an isolated MWCNT and found differences between the spectra of the edges and center of the tubes, which they attributed to q-dependent scattering,[12] an effect analogous to linear dichroism in X-ray photoabsorption.[9] Recently, Saitoh et al.[13] employed an energy-filtered TEM-EELS system to study angular distributions of inelastically scattered electrons following core electron ionization of a MWCNT. They related the observed anisotropic angular distributions to the symmetry of the π* and σ* final states.

Previously, C 1s NEXAFS spectroscopy of CNT powders, films, and "forests"[14–16] has been used to characterize the degree of order and quality of CNT samples, typically correlating the intensity of the C 1s → π* transition with the fraction of sp² carbon sites. A detailed explanation of the expected systematic variation of the intensities of the C 1s → π* and C 1s → σ* peaks in an individual CNT as a function of the X-ray incident angle (i.e., the dichroic effect) has been given[15,16] but the predicted effect was not demonstrated experimentally since previous nonspatially resolved studies integrated over many CNTs that had different spatial orientations. To the best of our knowledge, this is the first experimental measurement of this effect in individual MWCNTs. Our results fully validate the published theoretical treatment of the linear dichroism of the C 1s spectra of CNTs.[15,16]

Scanning transmission X-ray microscopy (STXM) is a synchrotron-based microprobe technique that combines NEX-AFS spectroscopy and microscopy with a spatial resolution currently routinely better than 30 nm.[17–20] We previously demonstrated the power of STXM to study isolated MWCNTs and to differentiate between the CNTs and various types of carbon impurities.[21,22] Although TEM-EELS provides much higher spatial resolution, it causes more radiation damage per unit analytical information than X-ray microscopy,[23] it has a significantly lower energy resolution than that of synchrotron-based spectromicroscopy, and measurement of linear dichroism via the momentum-transfer directional dependence is much less convenient than linear dichroism measurements with synchrotron X-ray sources.

This work reports the use of STXM to study the polarization dependence (linear dichroism) of the C 1s spectrum of individual CNTs. MWCNTs produced by arc discharge (AD) and chemical vapor deposition (CVD) are examined. The quantitative polarization dependence of the C 1s → π* transition is measured and shown to fit the function $C+A\cos^2(\theta)$, where A and C are constants and θ is the angle between the electric-field (E)-vector and the long axis of the CNT. This study provides the first measurement of NEXAFS dichroism of CNTs and shows that STXM has the potential to quantitatively probe defects in individual tubes.

2. Results and Discussion

2.1. Polarization-Dependent Spectroscopy

Figure 1 displays TEM (a, c, and d) and STXM (b and e) images of two different AD MWCNTs, one oriented approximately horizontally and the other approximately vertically. A higher resolution TEM image (Figure 1c) shows that the
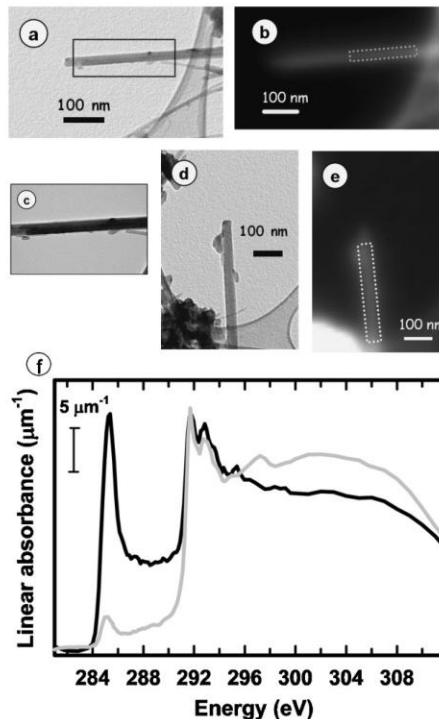
Figure 1. a, c, and d) TEM and b, and e) STXM images of two AD-MWCNTs. c) An expansion of (a), showing that it consists of two parallel MWCNTs enclosed in a third nanotube. f) C 1s spectra of these two nanotubes recorded with linear horizontally polarized light ([82 ± 5]%) using the STXM at beamline 5.3.2 at the Advanced Light Source (ALS). The gray curve corresponds to the spectrum of the tube oriented approximately horizontally (b), while the black curve corresponds to the tube oriented approximately vertically (e). In each case the spectrum is that of the region indicated by the dotted gray rectangles (ALS).

horizontal tube is actually composed of three tubes; one large one of 44 nm diameter, and two smaller ones of 16 and 21 nm. Figure 1f plots the C 1s spectra of parts of each tube. The dotted lines on Figure 1b and e identify the sub-regions from which these spectra were extracted. In order to remove the effect of the differences in thickness and number of layers of the two different tubes, the intensity scale of each spectrum was set by matching the intensity above 320 eV to that for 1 nm of elemental carbon at a density of 2.2 g cm⁻³ (that of graphite). Since the size and shape of each MWCNT are well characterized by TEM, it is possible to use the intensity of the measured spectrum along with the optical response of carbon, as reported in a standard database for X-ray constants,[24] to estimate the density for each MWCNT. The density for the vertical tube is estimated to be 0.60 g cm⁻³ from the ratio of the observed OD to that predicted for carbon of the known size, assuming unit density. In the same way, the density for the

small

assembly of three horizontal tubes is estimated to be $0.80\,g\,cm^{-3}$. This approach assumes that i) the MWCNT is approximated as a solid structure (i.e., ignoring the likely presence of a large hole at the center); ii) STXM has a spatial resolution such that the spectral signal only comes from the MWCNT and not the adjacent region of empty space. In fact, both of these approximations are invalid, so the density is clearly underestimated.

While some details are different, the polarization-dependent C 1s spectra displayed in Figure 1f are similar to those of highly oriented pyrolitic graphite (HOPG).[15,25] There is a sharp $1s \rightarrow \pi^*$ transition at 285.1 eV, a sharp $1s \rightarrow \sigma^*$ excitonic transition at 291.5 eV, and a broad $1s \rightarrow \sigma^*$ band peaking at 292.8 eV. This is followed by broad transitions of mixed symmetry peaking at 297 and 304 eV. These same features are observed in literature NEXAFS spectra of CNTs.[15,16] The main π^* (285.1 eV) and broad σ^* (292.8 eV) bands are seen in TEM-EELS spectra but the sharp excitonic transition at 291.5 eV is not present in TEM-EELS spectra, probably because of energy-resolution limitations. Although there is a broad intensity plateau between 287 and 290 eV, corresponding to an extended π^* band, the spectra of the arc discharged MWCNTs do not exhibit sharp features in this range, where C $1s \rightarrow \pi^*_{C=O}$ transitions of oxygenated moieties occur,[22,23,26] indicating that the AD-MWCNT tubes were not significantly oxidized.

While the transition energies for both orientations are identical, the transition intensities differ dramatically. In particular, the C $1s \rightarrow \pi^*$ transition is very weak in the horizontal orientation, whereas it is the strongest transition in the vertical orientation. The σ^* exciton (291.5 eV) has the same intensity for the two orientations, while the C $1s \rightarrow \sigma^*$ band (292.8 eV) is slightly weaker for the horizontal than for the vertical MWCNT. This is consistent with the observations of Banerjee et al.[15] who also observed little variation in intensity of the σ^* resonances with changes in experimental geometry (in their case, changes in the angle of photon incidence). Other studies have shown that there is significant symmetry mixing of higher energy σ^* and $\sigma^*+\pi^*$ orbitals of HOPG,[25] which is further enhanced in nanotubes due to curvature-induced rehybridization effects. This mixing probably explains why the exciton peak at 291.5 eV is less prominent in MWCNTs than in HOPG. For orientation analysis of nanotubes, it is more informative to focus on the C $1s \rightarrow \pi^*$ peak, and the remainder of this paper deals only with the dichroic aspects of this feature.

2.2. A Simple Model for the Polarization Dependence

The following is a simple model for the linear dichroism of the C 1s spectrum of an isolated CNT. A similar analysis has been presented in greater detail elsewhere.[15]

The intensity of an inner shell excitation transition is determined by the matrix element $|\langle f|\underline{E} \cdot \underline{r}|i\rangle|^2$, where f and i are the final and initial states of the transition, $\underline{E}$ is the E-vector of the light, and $\underline{r}$ is a position vector. This equation can be reduced to $A\cos^2\theta$, where θ is the angle between $\underline{E}$ and a reference direction (which in this work is taken to be the long axis of the CNT) and $\underline{A}$ is a constant.[9] As with other highly anisotropic materials where the electronic states adopt specific

spatial orientations, an angular dependence of the electronic-excitation intensity is expected. The local structure of a CNT can be regarded as approximately the same as that of graphene.[27] In graphene, when the E-vector is normal to the surface, only C $1s \rightarrow \pi^*$ transitions are allowed, whereas when the E-vector is parallel to the surface, only C $1s \rightarrow \sigma^*$ transitions are allowed. The situation is considerably modified in CNTs since rolling the graphene sheet breaks down this simple picture.

Figure 2a and b shows cartoons of a section of nanotube in both horizontal and vertical orientations. We consider the allowed or forbidden character of $1s \rightarrow \pi^*$ transitions with a fixed, horizontal E-vector and four situations: i) top/bottom and ii) sides of a horizontal nanotube, and iii) top/bottom and iv) sides of a vertical nanotube. Table 1 summarizes the expected allowed or forbidden character for these four situations which are depicted in Figure 2a and b. When the E-vector is aligned along the tube ($E_{//}$), $1s \rightarrow \pi^*$ transitions are forbidden at both carbon sites (A_1, B_1) whereas all of the $1s \rightarrow \sigma^*$ transitions are allowed. When the E-vector is orthogonal to the tube ($E_\perp$), $1s \rightarrow \pi^*$ transitions are only allowed at carbon atoms on the sides of the tube (B_1), while
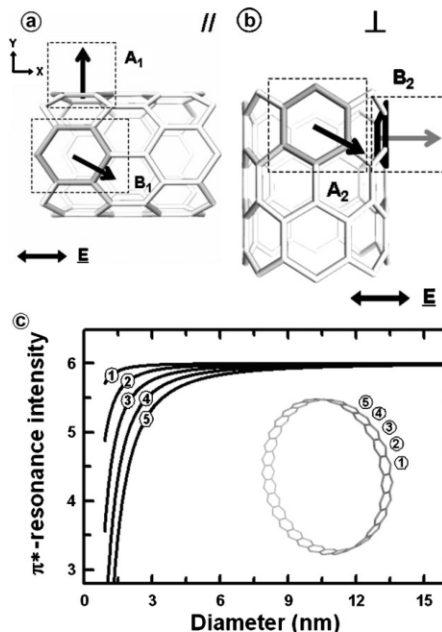
Figure 2. Cartoon explaining origin of the polarization effect. E-vector is fixed horizontally. a) The long axis of the nanotube is parallel to $\underline{E}$. b) The long axis of the nanotube is perpendicular to $\underline{E}$. A_1, B_1, A_2, and B_2 are transition moment vectors for C $1s \rightarrow \pi^*$ transitions in the selected rings (indicated by dashed rectangles; B_1 and A_2 transitions are out of the plane of the figure. c) Variation of the π^* transition intensity as a function of the nanotube diameter, calculated for the rings number-coded in the inset image. The E-vector is perpendicular to the tube axis.

Table 1. Qualitative explanation of polarization dependence of the C 1s spectral features of large CNTs treated as rectangular tubes of graphene sheets.

Orientation[a]	Transition	Site[b]	Status
Parallel (see Figure 2a)	C 1s → π*	A_1	Forbidden
		B_1	Forbidden
	C 1s → σ*	A_1	**Allowed**
		B_1	**Allowed**
Perpendicular (see Figure 2b)	C 1s → π*	A_2	Forbidden
		B_2	**Allowed**
	C 1s → σ*	A_2	**Allowed**
		B_2	Forbidden

[a] Orientation of the long axis of the CNT relative to the E-vector.
[b] See Figure 2 for identification of these sites.

$1s \rightarrow \sigma*$ transitions are allowed only at carbon atoms at the top/bottom of the tube (A_1). Within this simple model, the intensity of the π* transition is either on ($E_\perp$) or off ($E_{//}$) while the intensity of the σ* features only changes partially. Thus, one expects the largest linear dichroism in the C $1s \rightarrow \pi*$ transitions, as is observed. This perspective is valid when the diameter of the tube is sufficiently large so that each side of the tube behaves like a graphene sheet. As the diameter of the nanotube decreases, each ring contributes partially to the in-plane and out-of-plane transitions. For a zigzag SWCNT and $\underline{E}$ normal to the tube, π* intensities in six-membered carbon rings are given by $I_{\pi*}(i) = 6\cos^2(2\pi\phi_i)/N$ where ϕ_i corresponds to the location of the ring and N is the total number of rings around the circumference. Figure 2c plots the predicted variation of the π*-resonance intensity as a function of the tube diameter, determined using this formula. At small diameters, the angle between the adjacent rings is large, leading to significant changes in the projected E-vector on adjacent rings. This is analogous to π–σ mixing in small-radius nanotubes.[10] As the diameter increases, this angle decreases such that, for tube diameters above ≈8 nm, the tube can be treated as a hollow rectangular box with graphene walls.

2.3. Polarization Dependence for AD-MWCNTs

It is well established that MWCNTs produced by AD methods are highly crystalline. In contrast, MWCNTs produced by CVD methods have much more defective structures. We have measured the polarization-dependent C 1s spectra of AD and CVD MWCNTs to show that these differences in defect concentrations result in differences in the linear dichroism measured from individual MWCNTs.

At the Canadian Light Source (CLS) spectromicroscopy beamline (10ID1) the beam is 100% linearly polarized and the polarization angle can be varied from −90 to +90°[28] by changing the relative posi-

tions of the girders in the elliptically polarized undulator (EPU). This makes it much easier to measure the intensity of the π* transition as a function of the angle between the axis of the MWCNT and the E-vector, and thus the detailed polarization results are taken from studies at the CLS STXM. Measurements of the full angular dependence were also made at the Advanced Light Source (ALS) using sample rotation. Those results (not shown) are in good agreement with the CLS results, when the incomplete linear polarization ($[82 \pm 5]\%$)[29] of the ALS bend magnet beamline is taken into account. The intensity of the C $1s \rightarrow \pi*$ transition was measured as a function of polarization angle (varied by changing the EPU phase) by recording images at 283.0 eV (pre-edge) and 285.1 eV (π* peak), converting to optical density, and subtracting them from each other. The resulting difference is called a π* image.

Figure 3 shows π* images of an AD-MWCNT at various polarization angles in the −90° and +90° range. The tube axis was located at 30° relative to horizontal. Based on the expected polarization response, the C $1s \rightarrow \pi*$ transition should have the lowest intensity when the E-vector is parallel to the tube (−30°) and the highest intensity when the E-vector is normal to the tube (+60°). The π* images shown in Figure 3 are consistent with these expectations. We also observed a polarization dependence for some portion of the carbon impurities located at the right-hand side of the image, indicating that such impurities are some type of crystalline form of graphite such as carbon onions. In contrast, other parts of the impurities such as the "blob" in the middle of the tube were not polarization sensitive, suggesting that such impurities are amorphous carbon.
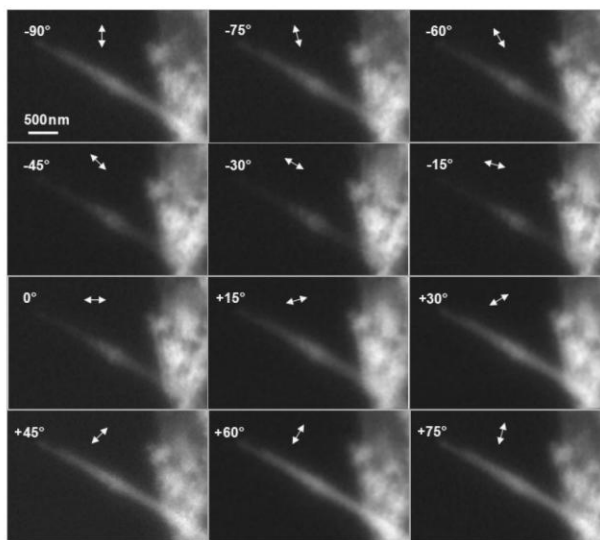
Figure 3. π* images (difference in optical density images at 285.1 and 283.0 eV) of an AD-MWCNT recorded with the indicated angles of the E-vector (0° is horizontal) (CLS).

C 1s NEXAFS dichroism of CNTs
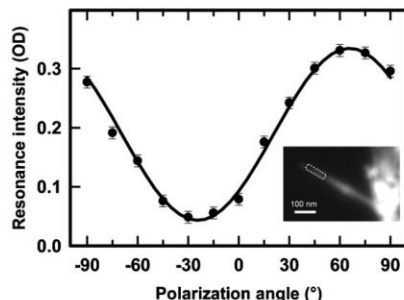
Figure 4. Polarization dependence of the C 1s → π* transition from the indicated region (gray outlined rectangle) of an AD-MWCNT (CLS).

The π* images obtained at various polarization angles were aligned and combined to form an angle-dependent image sequence. The angle-dependent intensity was then extracted from the region of the AD-MWCNT exhibiting the largest effect. Figure 4 plots this intensity as a function of the angle of the E-vector (horizontal = 0°, anticlockwise is positive). The inset shows the average of all the π* images, and identifies the subregion from which the signal was extracted. The minimum intensity was obtained at −30° and the maximum intensity was obtained at +60°. The experimental values were fit to $C + A\cos^2(\theta - \theta_{ref})$, where θ_{ref} is an optimizable parameter corresponding to the angle between the long axis of the MWCNT and the horizontal. There is good agreement between the fit (solid line) and the experimental data (Figure 4). Table 2 presents the results of the fit. The derived angle for the maximum signal was 65°, consistent with the spatial orientation of the MWCNT. Overall, the good agreement of the measured and predicted polarization dependence confirms that this signal is due to linear dichroism.

2.4. Polarization Dependence of CVD-MWCNTs

The polarization dependence of the C 1s → π* intensity of a CVD-MWCNT sample was also measured in order to investigate the effect of structural defects on the polarization signal. Figure 5 shows π* images of a CVD-MWCNT sample, recorded at various polarization angles over a range of −60 to +90°. Some regions are oriented horizontally while others are inclined with a large vertical component, thus allowing a sampling of a range of dichroic responses.

Figure 6 plots the C 1s → π* intensities extracted from two sub-regions as a function of polarization angle. The inset in Figure 6 indicates the locations of these two

Table 2. Parameters derived from analysis of the polarization dependence of C 1s → π* transition intensities in individual AD- and CVD-MWCNTs.

Sample—region	Observed angle[a]	θ_{ref}	C	A
AD—dashed lines	30	65 ± 4	0.05 ± 0.01	0.27 ± 0.01
CVD—solid lines	0	86 ± 4	0.12 ± 0.01	0.22 ± 0.01
CVD—dashed lines	56	38 ± 4	0.11 ± 0.01	0.24 ± 0.01

[a] Reference line for angle determination is horizontal ($\theta = 0°$, clockwise is positive).

sub-regions, one approximately horizontal and the other inclined at 56° relative to horizontal. The results confirm the visual observation (Figure 5) that the maximum (minimum) intensity occurs when the E-vector angle is at 90° (0°) for the horizontal region, represented by solid lines, and at 38° (−52°) for the selected inclined region, represented by dotted lines. The experimental values were fit as was done for the AD-MWCNT data. Table 2 presents the results of the fit. There is good agreement between the experimental values (points) and the fits (solid lines) (Figure 6). The derived reference angles were 86 ± 4° and 38 ± 4°, consistent with the observed orientations of the selected regions in the CVD-MWCNT.

For a defect-free nanotube, the π*-resonance intensity is zero when E is parallel to the tube and maximum when it is perpendicular to the tube. Thus the $I_{\parallel}/I_{\perp}$ ratio can be used as a
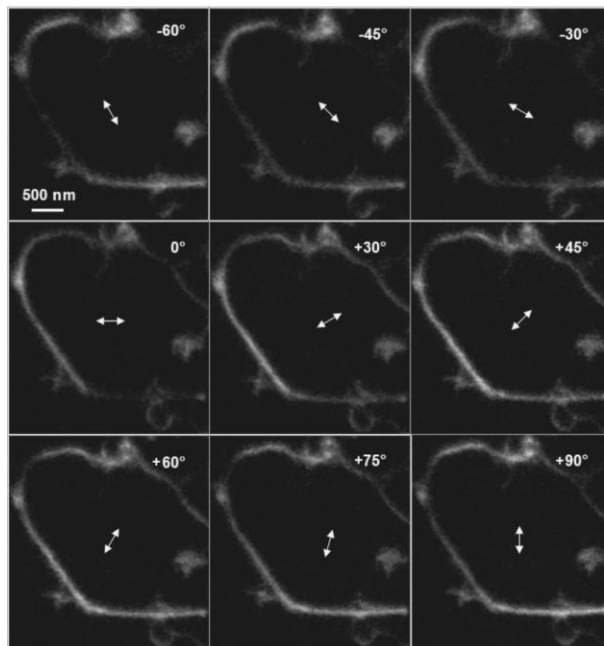
Figure 5. π* images of a CVD-MWCNT recorded with the indicated angles of the E-vector (0° is horizontal) (CLS).
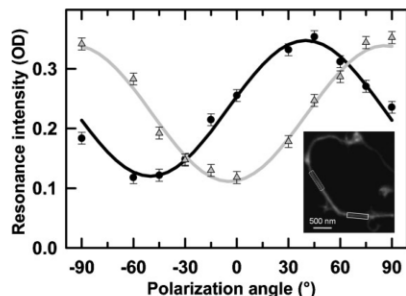
Figure 6. Polarization dependence of the intensity of the C $1s \rightarrow \pi*$ transition from the indicated regions of a CVD-MWCNT (solid and dotted lines correspond to the gray and black curves, respectively) (CLS).

quantitative measure of the extent of non-sp^2 character (called sp^2 defects). Evaluating CNT quality with this ratio directly accounts for variations in thickness or density among a set of nanotubes. For the regions with their dichroism plotted in Figure 4 and 6, $I_\parallel/I_\perp = 0.15 \pm 0.03$ for the AD-MWCNT and $I_\parallel/I_\perp = 0.33 \pm 0.03$ for the CVD-MWCNT, indicating that the CVD nanotube is significantly more defective than the AD nanotube, as expected. Maps of the $I_\parallel/I_\perp$ ratio along individual CNTs provide a means of probing the spatial distributions of sp^2 defects. As the spatial resolution of STXM improves, or if similar dichroic signals can be measured with TEM-EELS, it will be possible to obtain detailed characterization of sp^2-defect density along individual nanotubes.

3. Conclusions

STXM applied to individual MWCNTs has shown for the first time that the C $1s \rightarrow \pi*$ transition exhibits a strong linear dichroism with maximum intensity when the E-vector is perpendicular to the MWCNT axis. Using an STXM with an EPU capable of inclining the E-vector over a full 180° greatly facilitates characterization of dichroism. Comparison of AD- and CVD-MWCNTs showed that the $\pi*$ dichroic magnitude correlates with the quality of the CNT, indicating that the dichroic effect can be used to map sp^2 defects along individual nanotubes and thus help optimize single CNT-based devices. We note that Sfeir et al.[30] recently demonstrated that the polarization dependence of Rayleigh and Raman scattering of visible laser light from individual CNTs can be used to characterize their quality. Relative to that approach, STXM constitutes a further advance, since it is able to probe small regions (≈ 25 nm) along individual CNTs.

4. Experimental Section

MWCNT powders were purchased from Mercorp (AD grown)[31] and NanoCS (produced by metal catalyzed CVD)[32] and used

without modification. Nanotubes produced using these two methods were chosen because of their known structural differences. The AD method, which produces CNTs through vaporization of two opposing carbon rods in a chamber filled with an inert gas at high temperature, results in very crystalline nanotubes containing very few defects, but there are many side products such as graphitic onion particles, which are difficult to separate from the high quality AD-MWCNTs. The CVD method, which produces the tubes via vapor deposition of hydrocarbons on metal catalysts at relatively lower temperatures, results in higher purity, but the MWCNTs have much inferior mechanical and electronic properties due to the presence of many defects. Despite the lower quality, the CVD method is being aggressively pursued since it gives the possibility to grow CNTs on integrated circuits[33] or to align them on substrates.[34]

The AD-MWCNTs were dispersed in ethanol while the CVD-MWCNTs were sonically dispersed in dimethyl formamide. The solutions were drop cast onto a holey carbon TEM grid (AD) or onto a Si$_3$N$_4$ window (CVD). To remove residual solvent, the samples were heated overnight at 50 °C in the laboratory ambient. The AD-MWCNTs were previewed by TEM to pre-identify CNTs and to provide higher spatial resolution images for morphological characterization.[21,22]

Linear dichroism is an important aspect of NEXAFS of anisotropic samples. NEXAFS is electronic spectroscopy in which the excited state corresponds to events where an electron is excited from a core level to a level that is unoccupied in the ground state. Due to the short lifetime of the core excited state and the localized core hole the excitation occurs at a specific atom in a given structure. The excitation follows electric dipole selection rules, which means that excitation from a 1s core level is strongest to unoccupied levels in which there is a p-orbital lying along the E-vector. Here we focus on the $1s \rightarrow \pi*$ transition which is only excited when the E-vector is oriented perpendicular to the surface of the CNT. A STXM[17−20] is used to measure NEXAFS of individual MWCNTs. In STXM a monochromated beam of X-rays is focused to ≈ 25 nm by a Fresnel zone plate, imaging at specific photon energies is performed by raster scanning the sample through the focal spot while measuring transmitted X-rays, spectral images are measured by recording images over a range of photon energies, and the linear dichroism is recorded by measuring multiple spectral images with the sample reoriented relative to a fixed linear polarization (ALS STXM532) or by using an EPU to rotate the E-vector in the plane of the fixed sample (CLS-STXM 10ID1).

The samples were measured using two different microscopes: the STXM on beamline 5.3.2 at the ALS[35,36] and the STXM on beamline 10ID1[37] at the CLS. At the ALS bend magnet beamline at the time of these measurements the X-rays were measured to be (82 ± 5)% linearly polarized.[29] At the CLS the X-rays are produced in an Apple-II type EPU, which produces essentially 100% linearly polarized light for which the spatial orientation of the E-vector can be adjusted over the range of -90 to $+90°$ by changing the relative positions of the quadrants (phase) of the EPU.[28,38]

The MWCNT samples were measured using image sequences,[39] which were converted from transmission to optical density using the Io spectrum recorded simultaneously in the empty area around the MWCNT. After aligning the image sequence, spectra of the whole or a sub-region of an individual MWCNT were extracted.

130

C 1s NEXAFS dichroism of CNTs

The polarization dependence of the C 1s → π* transition (285.1 eV) was then derived. For the ALS measurements, spectra were recorded from two separate MWCNTs oriented roughly perpendicular or parallel to the E-vector. For the CLS measurements, the polarization dependence of the same MWCNT was examined by using the EPU to rotate the orientation of the E-vector relative to the long axis of the MWCNT, and recording images at 283.0 eV (pre-C 1s onset) and 285.1 eV (π* peak). These images were then converted to optical density and subtracted from each other to obtain a single image corresponding uniquely to the π* signal.

[1] H. W. Ch. Postma, T. Teepen, Z. Yao, M. Grifoni, C. Dekker, *Science* **2001**, *293*, 76.

[2] S. Fan, M. G. Chapline, N. R. Franklin, T. W. Tombler, A. M. Cassell, H. Dai, *Science* **1999**, *283*, 512.

[3] J. Kong, N. R. Franklin, C. Zhou, M. J. Chapline, S. Peng, K. Cho, H. Dai, *Science* **2000**, *287*, 622.

[4] N. Grobert, *Phys. Today* **2006**, *9*, 64.

[5] S. Frank, P. Poncharal, Z. L. Wang, W. A. de Heer, *Science* **1998**, *280*, 1744.

[6] C. Gómez-Navarro, P. J. De Pablo, J. Gómez-Herrero, B. Biel, F. J. Garcia-Vidal, A. Rubio, F. Flores, *Nat. Mater.* **2005**, *4*, 534.

[7] L. Valentini, F. Mercuri, I. Armentano, C. Cantalini, S. Picozzi, L. Lozzi, S. Santucci, A. Sgamellotti, J. M. Kenny, *Chem. Phys. Lett.* **2004**, *387*, 356.

[8] M. S. Raghuveer, A. Kumar, M. J. Frederick, G. P. Louie, P. G. Ganesan, G. Ramanath, *Adv. Mater.* **2006**, *18*, 547.

[9] J. Stöhr, *NEXAFS Spectroscopy*, Springer-Verlag, Berlin **1992**.

[10] R. Kuzuo, M. Terauchi, M. Tanaka, Y. Saito, *Jpn. J. Appl. Phys.* **1994**, *33*, 1316.

[11] O. Stephan, M. Kociak, L. Henrard, K. Suenaga, A. Gloter, M. Tencé, E. Sandré, C. Colliex, *J. Electron. Spectrosc. Relat. Phenom.* **2001**, *209*, 114.

[12] A. P. Hitchcock, T. Tyliszczak, *Surf. Rev. Lett.* **1995**, *2*, 43.

[13] K. Saitoh, K. Nagasaka, N. Tanaka, *J. Electron. Microsc.* **2006**, *55*, 281.

[14] Z. Li, L. Zhang, D. E. Resasco, B. S. Mun, F. G. Requejo, *Appl. Phys. Lett.* **2007**, *90*, 103115.

[15] S. Banerjee, T. Hemraj-Benny, S. Sambasivan, D. A. Fischer, J. A. Misewich, S. S. Wong, *J. Phys. Chem. B* **2005**, *109*, 8489.

[16] T. Hemraj-Benny, S. Banerjee, S. Sambasivan, M. Balasubramanian, D. A. Fischer, G. Eres, A. A. Puetzky, D. B. Geohegan, D. H. Lowndes, W. Han, J. A. Misewich, S. S. Wong, *Small* **2006**, *2*, 26.

[17] J. Kirz, C. Jacobsen, M. Q. Howells, *Rev. Biophys.* **1995**, *28*, 33.

[18] H. Ade, S. G. Urquhart, in *Chemical Applications of Synchrotron Rad*, Vol. *12A*, World Scientific, River Edge, NJ **2002**, p. 285.

[19] H. Ade, A. P. Hitchcock, *Polymer* **2008**, *49*, 643.

[20] A. P. Hitchcock, J. J. Dynes, G. A. Johansson, J. Wang, G. Botton, *Micron* **2008**, *39*, 741.

[21] A. Felten, H. Hody, C. Bittencourt, J. J. Pireaux, D. Hernandez-Cruz, A. P. Hitchcock, *Appl. Phys. Lett.* **2006**, *89*, 093123.

[22] A. Felten, C. Bittencourt, J. J. Pireaux, M. Reichelt, J. Mayer, D. Hernández-Cruz, A. P. Hitchcock, *Nano Lett.* **2007**, *7*, 2435.

[23] E. G. Rightor, A. P. Hitchcock, H. Ade, R. D. Leapman, S. G. Urquhart, A. P. Smith, G. Mitchell, D. Fischer, H. J. Shin, T. Warwick, *J. Phys. Chem. B* **1997**, *101*, 1950.

[24] a) B. L. Henke, E. M. Gullikson, J. C. Davis, *At. Data Nucl. Data Tables* **1993**, *54*, 181; b) X-ray Interactions with Matter. http://www-cxro.lbl.gov/opticalconstants/ (accessed January 2008).

[25] A. V. Sokolov, E. Z. Kurmaev, J. MacNaughton, A. Moewes, N. A. Skorikov, L. A. Finkelstein, *JETP Lett.* **2003**, *77*, 108.

[26] S. Banerjee, T. Hemraj-Benny, M. Balasubramanian, S. Sambasivan, D. A. Fischer, J. A. Misewich, S. S. Wong, *Chem. Phys. Chem.* **2004**, *5*, 1416.

[27] A. K. Geim, K. S. Novoselov, *Nat. Mater.* **2007**, *6*, 183.

[28] K. V. Kaznatcheev, Ch. Karunakaran, F. He, M. Sigrist, T. Summers, M. Obst, A. P. Hitchcock, *Nucl. Instrum. Methods Phys. Res., Sect. A* **2007**, *582*, 103.

[29] B. Watts, H. Ade, *J. Electron. Spectrosc. Relat. Phenom.* **2008**, *162*, 49.

[30] M. Y. Sfeir, F. Wang, L. Huang, C. C. Chuang, J. Hone, S. P. O'Brien, T. F. Heinz, L. E. Brus, *Science* **2004**, *306*, 1540.

[31] M. E. R. Corporation Homepage. http://www.mercorp.com/ (accessed January 2008).

[32] Nanocs Homepage. http://www.nanocs.com/ (accessed January 2008).

[33] R. G. Lacerda, A. S. Teh, M. H. Yang, K. B. K. Teo, N. L. Rupesinghe, S. H. Dalal, K. K. K. Koziol, D. Roy, G. A. Amaratunga, W. I. J. Milne, M. Chhowalla, D. G. Hasko, *Appl. Phys. Lett.* **2004**, *84*, 269.

[34] K. B. K. Teo, M. Chhowalla, G. A. J. Amaratunga, W. I. Milne, D. G. Hasko, G. Pirio, P. Legagneux, F. Wyczisk, D. Pribat, *Appl. Phys. Lett.* **2001**, *79*, 1534.

[35] A. L. D. Kilcoyne, T. Tyliszczak, W. F. Steele, S. Fakra, P. Hitchcock, K. Franck, E. K. Anderson, B. Harteneck, E. G. Rightor, G. Mitchell, A. P. Hitchcock, L. Yang, T. Warwick, H. Ade, *J. Synchrotron Radiat.* **2003**, *10*, 125.

[36] T. Warwick, H. Ade, A. L. D. Kilcoyne, M. Kritscher, T. Tyliszczak, S. Fakra, A. P. Hitchcock, P. Hitchcock, H. A. Padmore, *J. Synchrotron Radiat.* **2002**, *9*, 254.

[37] K. V. Kaznatcheev, Ch. Karunakaran, U. D. Lanke, S. G. Urquhart, M. Obst, A. P. Hitchcock, *Nucl. Instrum. Methods Phys. Res., Sect. A* **2007**, *582*, 96.

[38] A. T. Young, E. Arenholz, S. Marks, R. Schlueter, C. Steier, H. A. Padmore, A. P. Hitchcock, D. G. Castner, *J. Synchrotron Radiat.* **2002**, *9*, 270.

[39] C. Jacobsen, S. Wirick, G. Flynn, C. Zimba, *J. Microsc.* **2000**, *197*, 173.

131

Chapter 5

Characterization of Single-Walled Carbon Nanotubes by Scanning Transmission X-ray Spectromicroscopy: Purification, Order and Dodecyl Functionalization

This chapter presents the results of STXM characterization of pristine, purified and alkyl functionalized SWCNT samples. STXM determined the functional groups produced in SWCNT bundles by these treatments. This chapter compares the X-ray linear dichroism at the C 1s→π* transition in SWCNT and MWCNT.

Reprinted with permission from Journal of American Chemical Society 132 (2010) 9020-9029, Ebrahim Najafi, Jian Wang, Adam P. Hitchcock, Jingwen Guan, Stephane Dénommée, and Benoit Simard, "Characterization of Single-Walled Carbon Nanotubes by Scanning Transmission X-ray Spectromicroscopy: Purification, Order and Dodecyl Functionalization", Copyright 2010, American Chemical Society.

The author of this thesis obtained the purified and alkyl functionalized SWCNT samples from Dr. Jingwen Guan in Dr. Benoit Simard's research group at the National Research Council (NRC) of Canada, performed the STXM measurements, analyzed all the STXM data and wrote the publication in collaboration with Dr. Jingwen Guan and under the guidance of Prof. A. P. Hitchcock.

J|A|C|S

A R T I C L E S

Characterization of Single-Walled Carbon Nanotubes by Scanning Transmission X-ray Spectromicroscopy: Purification, Order and Dodecyl Functionalization

Ebrahim Najafi,[†] Jian Wang,[†] Adam P. Hitchcock,[*,†] Jingwen Guan,[‡]
Stephane Dénommée,[‡] and Benoit Simard[‡]

Brockhouse Institute for Materials Research, McMaster University, Hamilton, Ontario L8S 4 M1, Canada, and Steacie Institute for Molecular Sciences, National Research Council of Canada, Ottawa, Ontario K1A 0R6, Canada

Received February 10, 2010; E-mail: aph@mcmaster.ca

Abstract: The C 1s X-ray absorption spectra of several isolated bundles of single-walled carbon nanotubes (SWCNT) have been measured using scanning transmission X-ray microscopy. First the C 1s and O 1s spectra of a purified but unfunctionalized SWCNT were measured. The C 1s → π^* transition at 285 eV exhibited almost as strong a dichroic effect (spectral dependence on orientation) as that found in multiwalled carbon nanotubes (Najafi; et al. *Small* **2008**, *7*, 2279−2285). Second, purified SWCNT were functionalized with dodecyl and then investigated by STXM. Spectral evidence for the dodecyl functionalization is presented and discussed in comparison to the X-ray absorption spectra of aliphatic hydrocarbons. Both orientation and functionalization mapping of an individual SWCNT bundle is demonstrated.

1. Introduction

Carbon nanotubes (CNT) are often regarded as building blocks for nanotechnology, thanks to their exceptional electronic, physical, and mechanical properties. CNT are versatile materials that show promise for a wide range of applications, including electron channels in electronic devices,[1] field emitters in field emission displays,[2] or reinforcing fillers in composite materials.[3] However, many of these applications are restricted by the limited solubility of carbon nanotubes in most organic and inorganic solvents.

CNT have inert surfaces and tend to agglomerate in solutions, making further processing hard or even impossible.[4] To improve their solubility and achieve their full potential CNT are often functionalized through chemical reactions. Chemical functionalization modifies the physical and chemical properties of the tubes. For instance, functionalized tubes can have enhanced interfacial interactions with polymer matrices, modified electrical and thermal conductivity, and modified mechanical strength of composite systems.[5−7] Defects are produced on CNT during

functionalization. These defects act as scattering centers for electrons and phonons, thereby impairing the electrical and thermal conductivity of individual tubes.[8,9] For some applications such as chemical sensors, defects are advantageous since they can increase the sensitivity of the CNT to certain species by modifying band structures.[10,11]

In order to fabricate high-performance devices, controlled treatment of tubes is crucial to obtain a certain level of dispersion and processability while preserving structural integrity. Optimization of a given functionalization requires post-treatment analysis of the CNT by spectroscopy and microscopy. Spectroscopic methods such as Raman, X-ray photoemission (XPS), and X-ray absorption fine structure spectroscopy (NEXAFS) probe a large sample area, and therefore, the information that they provide is the average property of the batch. However, spectromicroscopy techniques can probe individual tubes or bundles at high spatial resolution. Previously, Suenaga et al.[12] used electron energy loss spectroscopy (EELS) in a transmission electron microscope (TEM) to map Gd atoms inside a single chain of metallofullerene molecules generated within a SWCNT. TEM-EELS can distinguish between atoms with small differences in atomic number. However, TEM-EELS has limited energy resolution; therefore, it typically has difficulties identifying organic molecules that may exist on or inside the tubes.

† Brockhouse Institute for Materials Research, McMaster University.
‡ Steacie Institute for Molecular Sciences, National Research Council of Canada.
(1) Postma, H. W. Ch.; Teepen, T.; Yao, Z.; Grifoni, M.; Dekker, C. *Science* **2001**, *293*, 76–79.
(2) Fan, S.; Chapline, M. G.; Franklin, N. R.; Tombler, T. W.; Cassell, A. M.; Dai, H. *Science* **1999**, *283*, 512–514.
(3) Xu, X. B.; Li, Zh.-M.; Shi, L.; Bian, X. Ch.; Xiang, Zh. D. *Small* **2007**, *3* (3), 408–411.
(4) Bahr, J. L.; Mickelson, E. T.; Bronikowski, M. J.; Smalley, R. E.; Tour, J. M. *Chem. Commun.* **2001**, *2*, 193–194.
(5) Najafi, E.; Kim, J.; Han, S. H.; Shin, K., *Colloids Surf., A* **2006**, *284−285*, 373–378.
(6) Ganguli, S.; Roy, A. K.; Anderson, D. P. *Carbon* **2008**, *46* (5), 806–817.
(7) Byrne, M. T.; McNamee, W. P.; Gun'ko, Y. K. *Nanotechnology* **2008**, *19*, 1–8.

(8) Charlier, J. C. *Acc. Chem. Res.* **2002**, *35*, 1063–1069.
(9) Hone, J.; Whitney, M.; Piskoti, C.; Zettl, A. *Phys. Rev. B* **1999**, *59* (4), R2514–R2516.
(10) Collins, Ph. G.; Bradley, K.; Ishigami, M.; Zettl, A. *Science* **2000**, *287*, 1801–1804.
(11) Valentini, L.; Mercuri, F.; Armentano, I.; Cantalini, C.; Picozzi, S.; Lozzi, L.; Santucci, S.; Sgamellotti, A.; Kenny, J. M. *Chem. Phys. Lett.* **2004**, *387*, 356–361.
(12) Suenaga, K.; Tence, M.; Mory, C.; Colliex, C.; Kato, H.; Okazaki, T.; Shinohara, H.; Hirahara, K.; Bandow, S.; Iijima, S. *Science* **2000**, *290*, 2280–2282.

Furthermore, the electron beam that probes the sample causes severe structural damage even in short spectroscopic exposures, especially at high beam energies where the best spatial resolution is typically achieved.

Recently, scanning transmission X-ray microscopy (STXM) has been applied to study individual multiwalled carbon nanotubes (MWCNT) in order to characterize and differentiate commercial products in the market,[13,14] and to map defect distributions quantitatively using the linear dichroism of the C $1s \rightarrow \pi^*$ transition (285 eV).[15−17] STXM is a synchrotron-based technique that combines NEXAFS spectroscopy[18] and microscopy with a spatial resolution currently routinely better than 30 nm.[19,20] NEXAFS spectroscopy was used by Banerjee et al.[21] to identify functional groups on CNT following exposure to UV-generated ozone. They could identify various oxygenated moieties by their C 1s and O 1s spectral signatures.

Here, we have investigated a number of aspects of SWCNT, including their purification, order, and dodecyl functionalization, using NEXAFS spectroscopy of individual bundles, measured in a STXM. Image sequences were measured at the carbon and oxygen edges. Fits of these sequences to appropriate reference spectra provide maps that visualize various components of the bundles. In addition, the linear dichroism of the SWCNT bundles was explored and compared to that of our previous studies of the linear dichroism of MWCNT.[13−17] A surprisingly large linear dichroism was observed.

2. Experimental Section

SWCNT were synthesized using the double-laser-oven approach as described in our previous publication.[22] Briefly, an inert environment of flowing Argon (250 SCCM) was maintained through a 45-mm inner diameter quartz tube fitted with a Brewster window. A gas inlet was positioned at one end, while a sample collector and a pumping port were placed at the other end. The pressure and temperature inside the quartz tube were maintained at 500 Torr and 1450 °C, respectively, throughout the process. Two types of lasers were used. The first was a nanosecond-pulsed Nd: YAG laser (Spectra-Physics Pro 290-30) operating at 1064 nm and 30 Hz with a fluence of approximately 2 J cm^{-2}/pulse. This laser vaporized the target which was graphite doped with 0.6% in atoms each of cobalt and nickel. The second laser was a Nd:YAG laser (Spectra-Physics Tornado S240-TN50-106Q), operating either continuously (CW) or at 20 kHz, at a wavelength of 1064 nm and measured powers of 50 or 48 W. This laser was used to alter the rate of cooling of the condensing plume generated by the vaporizing laser. The raw product from this process contained SWCNT, metal particles from the catalyst used, and other carbon impurities including amorphous and onion-like graphitic carbon

particles as well as quartz glass debris from the quartz tube.[23] Onion-like particles are graphitic impurities that are always produced during SWCNT growth.

The pristine (as-produced, without any purification) SWCNT were subsequently purified by a procedure referred to as WCPP (wet chemical purification procedure) developed at Steacie Institute for Molecular Sciences, National Research Council of Canada (NRC-SIMS).[24] Briefly, this procedure employs sonication-centrifugation cycles in the following order of solvents: toluene to remove fullerenes, N,N-dimethylformamide (DMF) to remove amorphous carbon, methanol (MeOH) to remove residual DMF, and finally 2 N HCl aqueous solution with MeOH to remove residual metal catalyst. After the WCPP purification the sample was thoroughly washed with water and methanol and oven-dried. This purification procedure produces a material which is pure enough for general applications (>90 wt % SWCNT).[24] More recently, we have also followed the WCPP with a hard baking (HB) procedure to further remove the remaining onion-like graphitic carbon impurities. Briefly, WCPP-purified SWCNT was placed on a centrally mounted fritted coarse disk in a quartz tube assembled vertically into a tube furnace (22 mm diameter or larger, depending on the quantity of the sample). Argon gas was passed through a hot water bubbler then through the WCPP-SWCNT, with the tube heated to 850 C. After cooling to room temperature under argon flow, the sample was resubjected to part of WCPP. This process (named Hard Baking) can be repeated on the basis of the analysis of the sample and purity required. The combined WCPP-HB procedure achieves a higher-purity product than WCPP alone. The advantages of the WCPP and the combined WCPP-HB purification procedures include simplicity, scalability, very high purity, and high yields; furthermore, the procedure does not cause obvious side-wall damage or functionalization.

For this work, WCPP-SWCNT were functionalized with dodecyl by reductive alkylation using Li and 1-iodo-dodecane according to the procedure reported by Liang et al.[25] More precisely, into a 500-mL round-bottom Schlenk flask maintained at dry ice−acetone temperature (−78 °C) was added 25 mg of fine SWCNT powder to 350 mL of liquid ammonia. Subsequently, 70 mg of small pieces of Li foil was added into the flask under magnetic stirring. The mixture turned ink-blue instantly, and the SWCNT$^-$−Li$^+$ intercalation complex was observed as a golden deposit on the wall of the flask. After stirring for one hour, 1.8 mL of 1-iodo-dodecane was injected. The mixture was stirred for an additional 6 h at −78 °C after which the mixture was warmed to room temperature. During this process the ammonia slowly evaporated, leaving a solid gray residue. The residue was slowly diluted with 20 mL of methanol followed by 20 mL of water under nitrogen. The mixture was sonicated for 20 min and filtered through a polycarbonate membrane (>20 μm pore size). The filtrand was washed sequentially with water, 2 N HCl, water, ethylacetate, methanol, and hexane. The wet solid was quite soluble in THF, and the resulting solution was stable for a few weeks after which gradual agglomeration occurred. It is difficult to redisperse the agglomerated SWCNT precipitate back into the same mother liquor.

Raman spectra were recorded on a custom-built spectrometer consisting of an Ar$^+$ Spectra-Physics Laser (model 277-GA04), a WiTec confocal microscope fiber-coupled to an Acton 2500i spectrograph fitted with a Roper Scientific CCD array detector. Measurements were carried out using 514.5 nm excitation attenuated to a power density well below 2 kW cm^{-2} at the sample to avoid laser heating effects. In addition, a neutral density filter was applied as needed to further reduce the laser power. Raman samples were

(13) Felten, A.; Hody, H.; Bittencourt, C.; Pireaux, J.-J.; Hernandez-Cruz, D.; Hitchcock, A. P. Appl. Phys. Lett. 2006, 89 (093123), 1–3.
(14) Felten, A.; Bittencourt, C.; Pireaux, J. J.; Reichelt, M.; Mayer, J.; Hernández-Cruz, D.; Hitchcock, A. P. Nano Lett. 2007, 7, 2435–2440.
(15) Najafi, E.; Hern, 940 > andez; Cruz, D.; Obst, M.; Hitchcock, A. P.; Douhard, B.; Pireaux, J.-J.; Felten, A Small 2008, 4, 2279–2285.
(16) Hitchcock, A. P.; Najafi, E.; Hern, 940 > andez; Cruz, D.; Obst, M.; Felten, A.; Douhard, B.; Pireaux, J.-J. Microsc. Microanal. 2008, 4 (S-2), 190–191.
(17) Felten, A.; Gillon, X.; Gulas, M.; Pireaux, J.-J.; Ke, X.; Van Tendeloo, G.; Bittencourt, C.; Kilcoyne, A. L. D. ; Najafi, E.; Hitchcock, A. P.; ACS Nano (in review)
(18) Stöhr, J. NEXAFS Spectroscopy; Springer-Verlag: Berlin, 1992.
(19) Ade, H.; Hitchcock, A. P. Polymer 2008, 49, 643–675.
(20) Hitchcock, A. P.; Dynes, J. J.; Johansson, G. A.; Wang, J.; Botton, G. Micron 2008, 39, 741–748.
(21) Banerjee, S.; Hemraj-Benny, T.; Balasubramanian, M.; Fischer, D. A.; Misewich, J. A.; Wong, S. S. Chem. Commun. B 2004, 772–773.
(22) Kingston, C. T.; Jakubek, Z. J.; Dénommée, S.; Simard, B. Carbon 2004, 42, 1657–1664.

(23) Bendjemil, B.; Borowiak-Palen, E.; Graff, A.; Pichler, T.; Guerioune, M.; Fink, J.; Knupfer, M. Appl. Phys. A 2004, 78, 311–314.
(24) Jakubinek, M. B.; Johnson, M.; White, M. A.; Guan, J. W.; Simard, B. J. Nanosci. Nanotechnol. 2010. In press. More details of WCPP will be published elsewhere.
(25) Liang, A.; Sadana, K.; Peera, A.; Chattopadhyay, J.; Gu, Z.; Hauge, R. H.; Billups, W. E. Nano Lett. 2004, 4, 1257–1260.

prepared by sonicating a few milligrams of SWCNT in a few milliliters of methanol in a sonication bath for 15 min.

Thermogravimetric (TG) analysis of nanotube samples was performed on a Netzsch TG 209 F1 Iris with simultaneous coupling of an Aëolos QMS403C mass spectrometer and a Bruker Tensor 27 Fourier Transform Infrared (FTIR) spectrometer via a TGA A588 TGA-IR module. The system was run with BOC UHP argon (5.3) gas; residual oxygen was trapped with a Supelco Big-Supelpure O oxygen/water trap. The transfer lines between the TG instrument, mass spectrometer, the FTIR spectrometer and the IR cell were all heated to a temperature of 200 °C. Operation details for the TG analysis can be found in the Supporting Information.

IR and mass spectral data were collected concurrently with the TGA data. IR data were collected from 4500 to 500 cm^{-1} at a resolution of 4 cm^{-1}. The integration ranges used for analysis of specific chemical signatures in the IR data were: 2402−2242 cm^{-1} for CO_2, 3026−3002 cm^{-1} for the Q-branch of methane, 3001−2850 cm^{-1} for the P-branch of methane, 3042−2788 cm^{-1} for total CH, and 2849.83−2787.89 cm^{-1} for low-frequency CH (CH outside the P-branch of methane). Mass spectra were recorded from 1 to 80 mass units.

TEM images were obtained using a Philips CM20 microscope equipped with a field emission gun operating at 200 kV. To prepare the samples for TEM imaging a few mg of dry SWCNT sample was bath-sonicated in methanol or tetrahydrofuran (THF) to form a well-dispersed suspension. The suspension was then pipetted onto the sample holder and allowed to dry completely prior to the measurements. Scanning electron microscopy (SEM) images were obtained using a Hitachi S-4800 FE microscope, operating at 1.2 KV at a distance of 3 mm. SEM samples were prepared by pipetting a few drops of a suspension of SWCNT in methanol onto an aluminum SEM sample stub.

To prepare samples for STXM measurements, the SWCNT were dispersed in *N,N*-dimethylformamide (DMF) by bath-sonication for 10 min. The solution was subsequently drop-cast on a lacy carbon grid which was then annealed at 200 °C for 48 h in a vacuum oven to remove residual DMF solvent. The unfunctionalized WCPP-HB SWCNT and dodecyl-functionalized WCPP-SWCNT were measured on bend magnet beamline 5.3.2 at the Advanced Light Source (ALS)[26,27] and undulator beamline 10ID1 (spectromicroscopy beamline) at the Canadian Light Source (CLS).[28] In STXM a monochromated beam of X-rays is focused to 30 nm by a Fresnel zone plate. Imaging at specific photon energies is performed by raster scanning the sample through the focal spot while measuring transmitted X-rays. Spectral image sequences (stacks) are measured by recording images over a range of photon energies. At ALS STXM 5.3.2, the π^* linear dichroism—the intensity of the C 1s → π^* transition as a function of the angle between the axis of the SWCNT and the electric vector (*E*-vector)—is recorded by measuring multiple images at 285.2 eV as a function of sample orientation relative to the fixed linear polarization. The light at 285 eV in the ALS STXM 5.3.2 has been measured to be 82(5)% horizontally linearly polarized.[29] At the CLS STXM, the orientation of the *E*-vector can be varied from −90° to +90° by changing the relative position of the girders in the elliptically polarized undulator (EPU) which produces nearly 100% linearly polarized X-rays.[30] As it is much easier to measure the dichroism there, detailed polarization measurements were done using the CLS STXM. The intensity of the C 1sπ^* transition was measured as a function of polarization angle (varied by changing the EPU phase) by recording images at 280.0 eV (pre-edge) and 285.2 eV (π^*-peak). The pre-edge and π^*-peak images were then converted to optical density, and the 280.0 eV image was subtracted from the 285.2 eV image. The resulting image is referred to as a π^* image.

The samples were also measured using C 1s and O 1s image sequences[31] which were converted from transmission to optical density using the incident flux (I_O) spectrum recorded simultaneously in the area off of, but around the SWCNT bundles where the same support material exists. After aligning the image sequence, spectra of the whole or a subregion were extracted for comparison. In addition, stacks were fit to reference spectra of the components using the singular value decomposition technique.[32] All STXM data analysis was performed using aXis2000 (http://unicorn.mcmaster.ca/aXis2000.html).

3. Results and Discussion

Figure 1 shows SEM images of (a) pristine single-walled carbon nanotubes (SWCNT), (b) WCPP-SWCNT, the SWCNT after subjecting them to a WCPP, and (c) WCPP-HB-SWCNT (further purified by hard baking (HB) after WCPP purification). The images clearly indicate that the impurities were significantly reduced from the pristine to the WCPP-HB purified SWCNT samples. We estimate that the SWCNT content in the WCPP-SWCNT sample is >90 wt %.[24] The further hard baking (HB) treatment yielded a high-purity SWCNT with an Itkis index[33] of over 0.23 and a purity >98 wt %. As clearly seen in Figure 1c, the tubes formed larger bundles when purified.

Figure 2 shows Raman spectra of WCPP-SWCNT and dodecyl-functionalized SWCNT. The Raman scattering spectra were obtained using a 514 nm Argon ion laser. The intensity of all the spectra in Figure 2 were normalized to yield the same intensity for the G-band located at ~1585 cm^{-1}. This G-band is close to that observed for well-ordered graphite (i.e., E_{2g} band at 1582 cm^{-1}), and therefore it is traditionally called the G-band. The G-band in well-ordered nanotubes actually contains several components that originate from the perfect cylindrical symmetry of the nanotube. The Raman-active radial breathing modes (RBM) are observed at low frequency in the left-hand side of the spectra at ~190 cm^{-1} in Figure 2. The position of the RBM band is inversely proportional to the tube diameters. In these samples the RBM band is pretty sharp, indicating that the diameter distribution is quite small and centered at ~1.2 nm. More important and useful is the band with its maximum near ~1330 cm^{-1} that is common in disordered sp^2 carbon material and has been called the D-band. It is activated by disorder in the sp^2 carbon network. The D-band intensity, G-bandwidth, and D/G intensity ratio, have been considered as sensitive probes of SWCNT wall integrity or functionalization. When G-bands are normalized to the same intensity, it is simple to compare and follow the variation of the D-band intensities from the starting SWCNT to the functionalized SWCNT.

Upon functionalization, the sp^2 carbons were converted to sp^3 carbon due to the covalent connection of network sp^2 carbon

(26) Kilcoyne, A. L. D.; Tyliszczak, T.; Steele, W. F.; Fakra, S.; Hitchcock, P.; Franck, K.; Anderson, E. K.; Harteneck, B.; Rightor, E. G.; Mitchell, G.; Hitchcock, A. P.; Yang, L.; Warwick, T.; Ade, H. *J. Synchrotron Rad.* **2003**, *10*, 125–136.
(27) Warwick, T.; Ade, H.; Kilcoyne, A. L. D.; Kritscher, M.; Tyliszczak, T.; Fakra, S.; Hitchcock, A. P.; Hitchcock, P.; Padmore, H. A. *J. Synchrotron Rad.* **2002**, *9*, 254–257.
(28) Kaznatcheev, K. V.; Karunakaran, Ch.; Lanke, U. D.; Urquhart, S. G.; Obst, M.; Hitchcock, A. P. *Nucl. Instrum. Methods* **2007**, *582*, 96–99.
(29) Watts, B.; Ade, H. *J. Electron Spectrosc. Relat. Phenom.* **2008**, *162*, 49–55.

(30) Kaznatcheev, K. V.; Karunakaran, Ch.; He, F.; Sigrist, M.; Summers, T.; Obst, M.; Hitchcock, A. P. *Nucl. Instrum. Methods Phys. Res., Sect. A* **2007**, *582*, 103–106.
(31) Jacobsen, C.; Wirick, S; Flynn, G.; Zimba, C. *J. Microscopy* **2000**, *197*, 173–184.
(32) Dynes, J. J.; Tyliszczak, T.; Araki, T.; Lawrence, J. R.; Swerhone, G. D. W.; Leppard, G. G. *Environ. Sci. Technol.* **2006**, *40*, 1556–1565.
(33) Itkis, M. E.; Perea, D. E.; Jung, R.; Niyogi, S.; Haddon, R. *J. Am. Chem. Soc.* **2005**, *127*, 3439–3448.
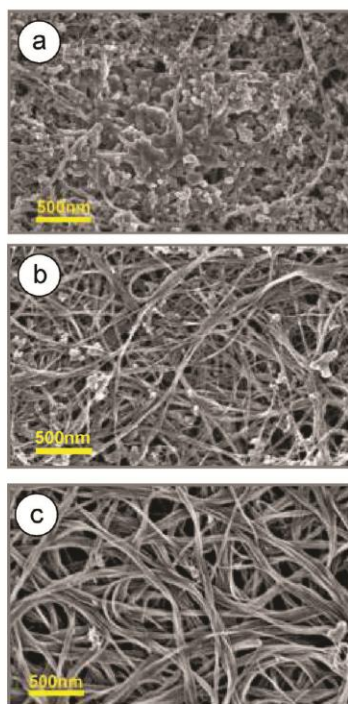
Figure 1. Scanning electron microscopy (SEM) images of (a) pristine single-walled carbon nanotubes (SWCNT) (pristine = unpurified), (b) WCPP-SWCNT, the SWCNT after subjecting them to a wet chemical purification procedure (WCPP), and (c) WCPP-HB-SWCNT (further purified by hard baking (HB) after WCPP purification). SEM images were acquired using a 1.5 kV beam.

Figure 2. (a) Raman spectra of the WCPP-SWCNT (red), and dodecyl-functionalized SWCNT (black). (b) Thermal gravimetric analysis (TGA) (red solid line) and differential TGA (red dashed line) of a dodecyl-functionalized SWCNT sample with the corresponding evolution of dodecane fragment (blue solid line) and CO_2 gases (pink solid line).

to the functional group. Therefore, the sp^3 character of the SWCNT increased, resulting in an increase in the D-band in the Raman spectrum, as shown in Figure 2a (black line). Although the quantitative relationship between the functionalization degree and the increase of D-band intensity is unclear and somewhat controversial, it is definitely true that the D-band intensity increases when functionalization has occurred.

The differential thermal gravimetric analysis (DTGA) curve in Figure 2b is quite symmetric and shows a minimum between 300 and 320 °C. The curve profile correlates very closely with the appearance of dodecane whose presence is confirmed by fragments (M^+/e) at 57, 43, and 29 and by the FTIR spectra (see Supporting Information, Figure S-1). This indicates that the functionalization chemistry was fairly specific and introduced only dodecyl as functional groups. On the basis of a measured mass loss of 27 wt %, the degree of functionalization is estimated to be 2.5 C%, that is, on average, 1 dodecyl group per 40 SWCNT carbon atoms.

Figure 3 displays TEM (a) and STXM (b) images of a WCPP-HB-SWCNT sample which was similar to that used for dodecyl functionalization but has higher purity due to further treatment with HB processes after WCPP purification (>98 wt % SWCNT with Itkis' index >0.23); the images are from the same sample but not the same area. Figure 3c plots the C 1s spectra and

Figure 3d plots the O 1s spectra of two specific regions of this sample, which are indicated by the red bar (horizontal, $E_{\parallel}$ to tube axis) and the blue bar (vertical, $E_{\perp}$ to tube axis) in Figure 3b. The spectra were corrected for the nonlinearly polarized portion of the X-ray beam at the ALS STXM 5.3.2[29] by removing 18% of the averaged spectrum from both horizontal and vertical spectra. Note that the E-vector of the light at the ALS STXM 5.3.2 bend magnet is horizontal. The C 1s spectra of SWCNT bundles with their long axis oriented parallel versus those perpendicular to the E-vector are remarkably different, indicating there is a strong dichroic effect at the C 1s → π^* transition in single-walled carbon nanotubes. Previously a similar effect was found for arc discharged MWCNT.[15,16] This large polarization effect is characteristic of low levels of sp^2 defects. An sp^2 defect is a carbon in the CNT structure where the local atomic geometry no longer has sp^2 character. The presence of a significant dichroic signal in the C 1s spectrum of the WCPP-HB-SWCNT indicates these are high-quality tubes with low sp^2 defect content. The magnitude of the polarization effect decreases as the structural quality of the tube lowers.[15–17] Furthermore, a closer look at the C 1s spectra extracted from the red bar shows weak peaks at 287.7, 288.2, and 289.2 eV (Figure 3e) which correspond to oxygen-rich surface moieties such as carbonyl and carboxylic groups.

To obtain detailed information about the extent of oxidation of the tubes, an O 1s image sequence was recorded, and O 1s spectra were extracted from the regions indicated by horizontal and vertical lines in Figure 3b. The spectra were smoothed by averaging three neighboring points and plotted in Figure 3d.

136
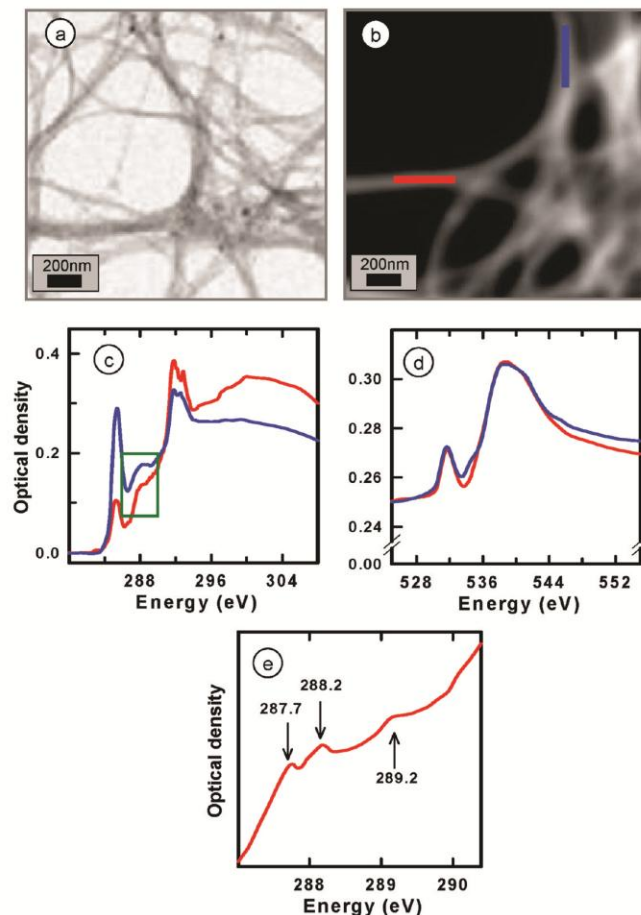
Figure 3. (a) TEM and (b) STXM images of a WCPP-HB-SWCNT sample, (c) C 1s and (d) O 1s spectra of the specific regions indicated by the red (horizontal) and blue (vertical) bars (image and spectra recorded with a bending magnet STXM in which the *E*-vector is horizontal); (e) expansion of the C 1s spectrum from the red bar (horizontal) in the region of $\pi*_{C=O}$ transitions. Spectra have been 3-point smoothed. (ALS STXM 5.3.2)

The spectra of both regions are quite similar, indicating that the tubes are relatively uniformly oxidized. Moreover, the weak O 1s signal is consistent with the C 1s spectroscopy, where the peaks in the 286−288 eV region, which indicate the presence of C=O bonds,[22] are very weak, indicating that the oxidation was not severe. The major peaks in the O 1s spectra at 531.7, 538.4, and 540.8 eV are attributed to transitions in carbonyl and carboxylic groups. This is again in agreement with the functional groups predicted from the minor peaks in the C 1s spectra. STXM measurements of pristine SWCNT (no WCPP or WCPP-HB treatment) show that they have similar although somewhat elevated levels of oxygen relative to the purified sample (see Supporting Information Figure S-2). This suggests that WCPP purification is able to remove certain amounts of oxygen containing impurities, although it may also introduce some oxygen on the SWCNT (The WCPP and WCPP-HB

procedures are not intended to remove oxygen that originally existed on the tubes). The level of oxygen in WCPP-HB-SWCNT that is detectable by XPS is 3−5%. Annealing WCPP-HB-SWCNT to 950 °C achieves some further reduction of the oxygen level in the sample (see Supporting Information, Table S-1). In addition, we have observed that the purified WCPP-SWCNT slowly oxidizes during air storage. This issue is being carefully investigated.

Figure 4a plots the carbon map obtained by subtracting the averaged images of the pre-edge (278−282 eV) from those of the postedge (296−320 eV) in the stack recorded to obtain the spectra in Figure 3. Figure 4a shows that there are bundles of different thicknesses. Figure 4b is the oxygen distribution map, derived by taking the difference between the averaged images from 527−560 eV and those from 524−530 eV. Figure 4c plots the ratio of the O 1s to the C 1s map. Regions with no signal
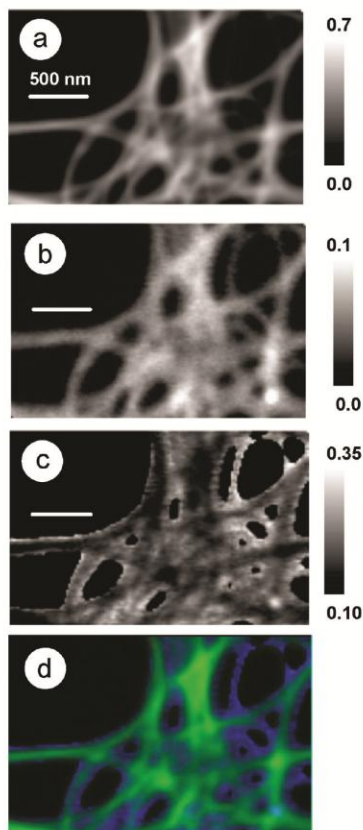
Figure 4. Elemental maps of a WCPP-HB-SWCNT sample giving the distribution of (a) carbon (average of 10 STXM images from 296−320 eV minus those from 278−282 eV) and (b) oxygen (the difference between the sum of images from (540−560 eV) and those images from (524−530 eV) in order to remove the large background from carbon absorption), (c) is a ratio map (O/C) that visualizes the relative oxygen to carbon content at different locations on the tubes; (d) is a color composite (rescaled) of the carbon (green, a) and oxygen/carbon ratio (blue, c) signals. (ALS STXM 5.3.2)

Figure 5. Component maps, derived from a C 1s image sequence of the WCPP-HB-SWCNT sample, of (a) WCPP-HB-SWCNT where the long axis of the SWCNT is oriented perpendicular to the E-vector, (b) WCPP-HB-SWCNT where the long axis of the SWCNT is oriented parallel to the E-vector and (c) oxidized regions. The reference spectra of the horizontally and vertically aligned tubes were extracted from the WCPP-HB-SWCNT sample (Figure 3), whereas those for oxygenated tubes were reported earlier for AD-MWCNT.[13,14] (see Supporting Information Figure S-3 for plots of the reference spectra). (d) Rescaled color-coded composite image (SWCNT long axis perpendicular to E-vector is coded in red, SWCNT long axis parallel to E-vector is coded in green, and oxidized areas are coded in blue). The arrow indicates the orientation of the E-vector (ALS STXM 5.3.2).

have been masked (set to 0) to remove artifacts. Brighter pixels in Figure 4 correspond to more oxygen relative to carbon (thus, more oxidation) whereas darker pixels correspond to less oxygen relative to carbon (thus, less oxidation). There are more bright pixels at the edges than at the centers of the tubes, clearly indicating that more oxidation has occurred at the edges. Figure 4d is a color-coded composite of the carbon (green) and ratio (blue) maps from 4a and 4c, with the scaling such that the intensity of 4a and 4c are each mapped to the full 8-bit scale of its color. The color-coded composite confirms the existence of more oxygen relative to carbon at the edges of the tube. Furthermore, there are much higher levels of oxidation in thin SWCNT bundles such as that at the upper right of Figure 4d, suggesting that oxidation is more severe in thin SWCNT bundles.

Figure 5 presents component maps for a WCPP-HB-SWCNT sample derived by fitting the C 1s image sequence to reference spectra for (a) WCPP-SWCNT where the long axis of the WCPP-SWCNT is oriented perpendicular to the E-vector, (b) WCPP-SWCNT where the long axis of the WCPP-SWCNT is oriented parallel to the E-vector, and (c) oxidized MWCNT. The C 1s reference spectra used for this analysis are reported in Figure S-3 (Supporting Information). The gray scales of each image in Figure 5 indicate thickness, in nanometers, of each component. Figure 5d is a color-coded composite of these component maps. This analysis clearly shows a strong dichroic
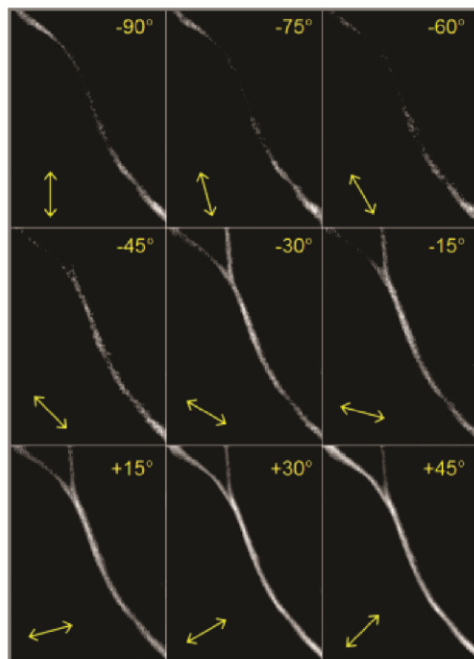
Figure 6. π^* images (difference in optical density images at 285.2 and 280.0 eV) of WCPP-HB-SWCNT recorded with an orientation of the E-vector indicated by the double-headed arrow (0 = horizontal) (CLS STXM).

Figure 7. Polarization dependence of the C $1s \rightarrow \pi^*$ transition from the indicated region of a single bundle of WCPP-HB-SWCNT (gray, taken from the gray outlined rectangle on the inset image), compared to that from an arc discharge, AD-MWCNT (black).[15] (CLS STXM)

signal from bundled SWCNT. This analysis supports the simpler analysis done by ratioing the C 1s and O 1s images (after background removal), in that there is clear indication of preferential oxidation of the thinner SWCNT. It is possible that the magnitude of the oxidation signal derived from the C 1s stack is overestimated since less oriented regions of SWCNT are often fit as the oxidized component, as well as the actual oxidized regions (see Supporting Information Figure S-3).

In order to confirm the strong polarization effect observed in the C 1s spectra of the WCPP-HB-SWCNT at the C $1s \rightarrow \pi^*$ transition, π^* images for an isolated WCPP-HB-SWCNT were recorded at different polarization angles at the CLS STXM (Figure 6). The tube axis was located at 60° relative to horizontal. On the basis of the known relationship of carbon nanotube orientation and transition intensity,[15] the C $1s \rightarrow \pi^*$ transition should have the lowest intensity when the E-vector is parallel to the tube (−60°) and the highest intensity when the E-vector is normal to the tube (+30°). The π^* images are consistent with these expectations.

The π^* images obtained at various polarization angles were aligned and combined to form an angle-dependent image sequence. The angle-dependent intensity was then extracted from the region of the SWCNT exhibiting the largest effect indicated by the box in the inset in Figure 7. Figure 7 plots this intensity (gray) as a function of the angle of the E-vector (horizontal = 0, anticlockwise is positive) together with the results for an arc discharge (AD) MWCNT (black) reported previously.[15] The experimental values were normalized to $I_\perp$ (E-vector normal to

the tubes) to remove the thickness effect and subsequently fit to $a \pm b \times \cos^2(\theta - \theta_f)$, where θ_f is an optimizable parameter corresponding to the angle between the long axis of the MWCNT and horizontal. There is good agreement between the fits (solid line) and the experimental values. In fullerene, the local $\pi - \sigma$ bonding and $\pi^* - \sigma^*$ antibonding symmetry mixing is large, which results in very low dichroism.[36] Due to the large curvature in SWCNT, a similar phenomenon might have been expected in SWCNT. However, Figure 7 shows that the linear dichroism of the π^*-signal of these SWCNT is as strong as that found in AD-MWCNT. This suggests that $\pi^* - \sigma^*$ mixing in SWCNT is very different and much less than that in fullerenes. STXM has a limited spatial resolution compared to TEM-EELS; therefore, the spectra measured in STXM are the average of the top and the edges of tubes at different orientations. Previously, Stéphan et al.[36] used TEM-EELS to measure the C 1s spectra at different points across an individual SWCNT. They observed that the C $1s \rightarrow \pi^*$ transition is about 30% stronger at the edge than at the center of the tube (relative to the C 1s continuum signal above 300 eV). In EELS the change in peak intensities with changes in the orientation of the sample relative to the direction of the momentum transfer vector (q) is the equivalent to linear dichroism in X-ray absorption, with q being directly analogous to the E-vector. Using q-dependent TEM-EELS to study polarization effects is challenging since it is hard to define and adjust the orientation and dispersion of q. Since the signal measured in STXM is much less spatially localized than that in TEM-EELS, the large dichroism observed in this work indicates that the intrinsic π^* dichroism of well-ordered SWCNT with a low-defect content is very large.

Panels a and b of Figure 8 show TEM and STXM images of the dodecyl-functionalized SWCNT sample; the images were recorded from the same sample grid but not from identical areas. C 1s spectra were extracted from the indicated horizontal (red) and vertical (blue) regions, matched at the pre-edge and continuum to normalize for thickness, and corrected for the fraction of nonlinear polarized X-rays, as explained earlier. The C 1s spectra of the dodecyl-functionalized SWCNT show a much smaller dichroic effect than the WCPP-HB-SWCNT sample, and also much less σ^* exciton signal (291.8 eV). There is also a significant difference in the σ^* exciton region between

(34) Henke, B. L.; Gullikson, E. M.; Davis, J. C. *At. Data Nucl. Data Tables* **1993**, *54*, 181–342.
(35) Azami, S. M.; Pooladi, R.; Sheikhi, M. H. *J. Mol. Struct. (THEOCHEM)* **2009**, *901* (1−3), 153–156.
(36) Stéphan, O.; Kociak, M.; Henrard, L.; Suenaga, K.; Gloter, A.; Tencé, M.; Sandré, E.; Colliex, C. *J. Electron Spectrosc. Relat. Phenom.* **2001**, *114−116*, 209–217.
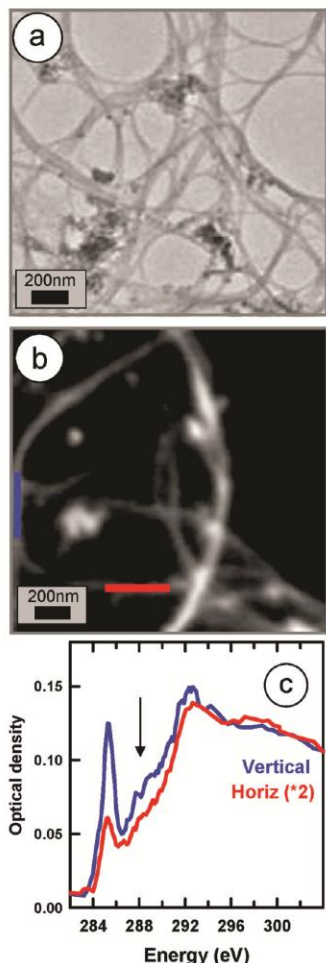
Figure 8. (a) TEM and (b) STXM images of a dodecyl-functionalized WCPP-SWCNT. (c) The C 1s spectra of the regions indicated by the red and blue bars. Spectra have been 3-point smoothed. (ALS STXM 5.3.2)

the vertical and horizontal SWCNT for which the spectra are displayed in Figure 8c. This perhaps indicates an enhanced σ^* dichroism, or inhomogeneous functionalization chemistry. The π^* dichroic signal is somewhat reduced relative to that observed in the WCPP-HB-SWCNT (Figure 3). This is attributed to the increased defect content caused by the covalent functionalization of the SWCNT. The increase in disorder indicated by the reduced dichroism is also clearly reflected in the increased intensity of the disorder D-band in the Raman spectrum shown in Figure 2b. Oxygen is known to open the sp^2 hybridized carbon–carbon bonds and reduce the number of available states with p-like symmetry, thus reducing the magnitude of the

dichroic effect.[37] The increased defect concentration due to chemical functionalization is often accompanied by new functional groups on the surface of SWCNT. A close examination of the spectra in Figure 8c shows a new peak at 287.7 eV (see arrow) which corresponds to the C 1s→ (C−H) transition in the dodecyl chains.

The left panels of Figure 9 display the C 1s spectra of five components used to fit the C 1s image sequence measured from the dodecyl-functionalized SWCNT. The right panels in Figure 9 are the associated semiquantitative maps for each component. Note that the gray scales of the component maps give an estimate of the thickness (in nm) of that chemical component at any point in the imaged area. Quantitative thicknesses are given by the fitting coefficients since the intensity scales of the reference spectra are set to the response of 1 nm of carbon, using tabulated mass absorption coefficients.[35] The reference spectra of the horizontally and vertically aligned SWCNT were obtained from the WCPP-HB-SWCNT sample (Figure 3c) by matching the spectra at the pre-edge and postedge regions to the sum of tabulated atomic mass absorption coefficients for the elemental composition of the pure component.[34] The reference spectra of carbon impurities and oxidized tubes were those reported earlier and extracted from MWCNT samples.[13,14] The reference spectrum of dodecyl was that of an amorphous C-60 short-chain polyethylene wax. Spectra a and b of Figure 9 are components for horizontally (π^*-weak) and vertically (π^*-strong) aligned SWCNT. One can see that horizontally oriented tubes are only present in Figure 9a, whereas the vertical tubes and onion components appear in both component maps. Although dodecyl-functionalized SWCNT have weaker dichroism than the WCPP-HB-SWCNT (see Figure 3), the C 1s → π^* transition of functionalized SWCNT is still orientation dependent. Figure 9c maps the oxidized regions on the bundles which are probably produced during sample storage or caused by the chemical modification. It is interesting to note that the oxidation mainly occurs on the outer walls of the bundles where they were unprotected and exposed to air. We have observed that purified SWCNT slowly oxidize on storage in air. Figure 9d shows the carbon onions and other carbon particle impurities that are either stuck to the sides of the bundles or exist as "blobs". Finally, Figure 9e maps the dodecyl chains that were produced on the bundles by the chemical functionalization. It is apparent that the chains cover the tubes completely, indicating a successful chemical functionalization. Surprisingly, this analysis suggests that there are more dodecyl chains on the vertically aligned tubes than the horizontally aligned ones, which is very unlikely. Other alternative explanations might be (1) local ordering of the dodecyl chains that results in a dichroic effect; (2) nonuniform functionalization on the side wall of the tubes; or (3) errors due to an improper fit. The first possibility was investigated using a detailed dichroism study at the CLS STXM; a dichroic effect from the heavily dodecyl-functionalized regions was not observed (results not presented in this paper). Nonuniform functionalization is not expected. The last possibility is the most likely—fitting errors might arise because the dodecyl C 1s spectrum (Figure 9e) is much closer to that of horizontally (Figure 9a) than vertically (9b) aligned SWCNT. Figure 9e also shows that the amount of dodecyl is relatively greater on graphitic particles than on SWCNT. The larger

(37) Hemraj-Benny, T.; Banerjee, S.; Sambasivan, Sh.; Balasubramanian, M.; Fischer, D. A.; Eres, G.; Puretzky, A. A.; Geohegan, D. B.; Lowndes, D. H.; Han, W.; Misewich, J. A.; Wong, S. S. *Small* **2006**, *2* (1), 26–35.
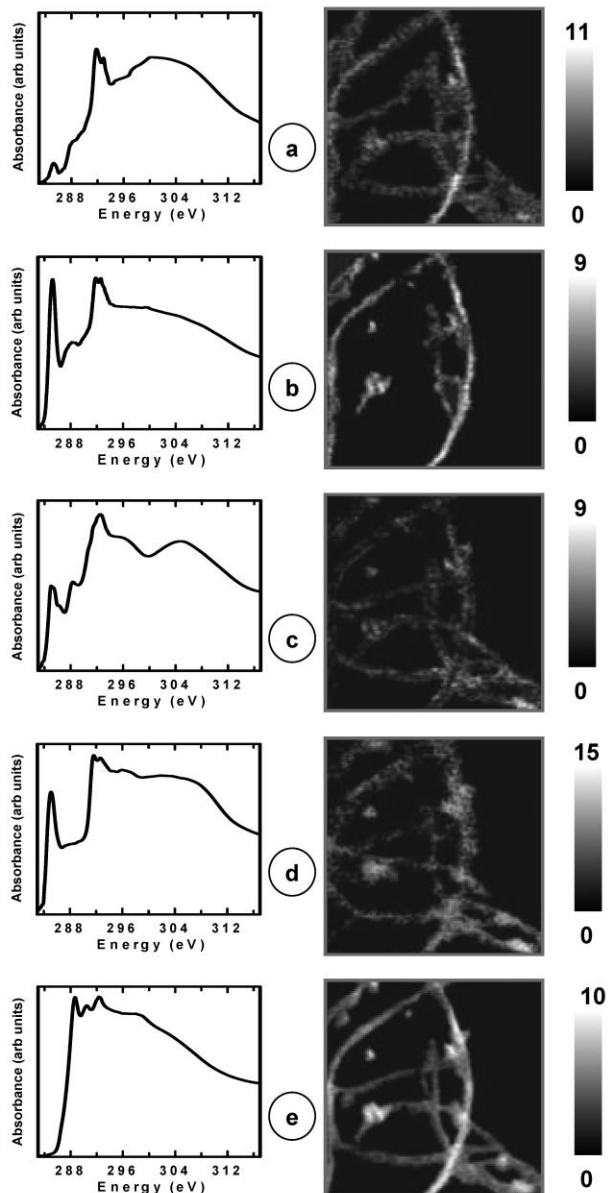
Figure 9. STXM of the dodecyl-functionalized WCPP- SWCNT: (left panels) C 1s reference spectra used to fit the C 1s image sequence in order to derive the associated component maps (right panels). Component maps of (a) horizontal SWCNT (π^*-weak); (b) vertical SWCNT (π^*-strong); (c) oxidized SWCNT; (d) carbon onions and other carbon contaminations (CNP); (e) dodecyl. The reference spectra of the horizontally and vertically oriented tubes were extracted from WCPP-HB-SWCNT sample (Figure 3), whereas those for oxygenated tubes and graphitic impurities were from previous studies of impure CNT samples.[13,14] The reference spectrum of dodecyl was that of an amorphous C-60 short-chain polyethylene wax.[38] The gray scales of the component maps give the thickness in nm. (ALS STXM 5.3.2)

residual strain in the particles could make them more reactive than tubes. Further work is needed to refine the reference spectrum of the dodecyl substituent and improve the differentiation of dodecyl and horizontally aligned CNT spectral signals in the fitting in order to provide a fully quantitative analysis of the loading.

4. Summary

STXM, in combination with SEM, FTIR, Raman, and thermal analysis, has been used to study SWCNT in the pristine and purified states. A strong dichroic signal has been detected in high-purity bundled WCPP-HB-SWCNT, with an intensity very similar to that observed in MWCNT. The same techniques were also used to characterize dodecyl-functionalized SWCNT. The C 1s signal of the dodecyl functionalization was detected and mapped. These results have demonstrated the STXM is a powerful tool to characterize functionalized SWCNT, which in combination with other methods such as SEM, TEM, FTIR, TGA, and Raman spectroscopy, can help improve purification and chemical functionalization methods. Our ultimate goal is to develop high-strength fibers based on braided alkyl-functionalized SWCNT. In addition to helping to optimize chemical functionalization of nanomaterials, STXM spectromicroscopy

will also play a role in understanding and optimizing interactions between nanotubes and different matrices in nanotube−polymer composites.

Supporting Information Available: FTIR, Raman spectra, STXM of pristine SWCNT, XPS results of oxygen content, and reference spectra. This material is available free of charge via the Internet at http://pubs.acs.org.

JA101001T

(38) Hitchcock, A. P.; Araki, T.; Ikeura-Sekiguchi, H.; Iwata, N.; Tani, K. *J. Phys. IV (France)* **2003**, *104*, 509–512.

Chapter 6

Electron energy loss spectromicroscopy of multi walled carbon nanotubes

This chapter presents studies of C 1s electron energy loss spectroscopy of multi-walled carbon nanotubes (MWCNT). Specifically, it discusses different approaches used to perform angle-dependent electron energy loss spectroscopy (EELS) in a transmission electron microscope (TEM) in MWCNT in a way that controls the direction of the momentum transfer vector relative to the tube axis. It is demonstrated that signals analogous to those of the X-ray absorption linear dichroism can be measured by TEM-EELS. Finally, it shows examples of using TEM-EELS to map defects in pristine and focused ion beam modified MWCNT.TEM-EELS measurements in this chapter were made in the scanning transmission electron microscopy (STEM) mode of the microscope.

6.1 Introduction

In previous chapters, the use of scanning transmission X-ray microscopy (STXM) to measure X-ray linear dichroism from individual carbon nanotubes (CNT) was demonstrated and its use to evaluate structural quality and map defects was explored. However STXM has a limited spatial resolution (~25 nm with the instrument used; ~10 nm with current state-of-the-art microscopes with the best zone plate and mechanics). For many technological applications, single walled carbon nanotubes (SWCNT) or narrow diameter MWCNT are preferred and thus the spatial resolution of STXM is a limitation. The momentum transfer vector (**q**) in inelastic electron scattering is analogous to the

electric vector (**E**) of light. Thus, in principle, EELS can provide an 'electron linear

dichroism' (ELD) signal [E96, H02, HS03] similar to X-ray linear dichroism (XLD). By

adjusting the orientation of an anisotropic sample such as carbon nanotubes relative to a

well defined **q** in a TEM then the resulting spatially resolved ELD signals will provide

defect sensitive information at a much higher spatial resolution than can currently be

achieved with STXM.

Using the state-of-the-art Titan 1 system at the Canadian Centre for Electron

Microscopy (CCEM) at McMaster, and with the guidance and collaboration of Professor

Gianluigi Botton and his student, David Rossouw, I have explored a number of

geometries to measure q-dependent EELS from sections of individual MWCNT,

including a mode which provides signals that appear identical to those from STXM.

The conventional approach to control the orientation of **q** in TEM-EELS involves

optimizing the collection angle of the spectrometer (β) by varying the size of the

spectrometer entrance aperture [BBS95]. A large aperture (large β) collects a wide range

of scattered electrons which carry an average **q** with a dominant component perpendicular

to the beam (**q**$\perp$) (**Figure 6.1a**). A small aperture reduces the range of the angular

acceptance of the scattered electrons which enhances the component parallel to the beam

(**q**$_{\parallel}$) (**Figure 6.1b**). The grey surfaces in **Figure 6.1** represent all possible values for

scattering angles which result in a variety of **q** orientations. Leapman et al. [LFS83]

employed this approach to study the electronic properties of graphite and boron nitride

films. Specifically, they used a small collection aperture to enhance **q**$_{\parallel}$ and then tilted the

films to study intensity variations of certain resonances as a function of tilt angle.

Browning et al. [BYB91] proposed an alternative approach based on the comparison of

the energy loss spectra recorded at both small and large collection angles.
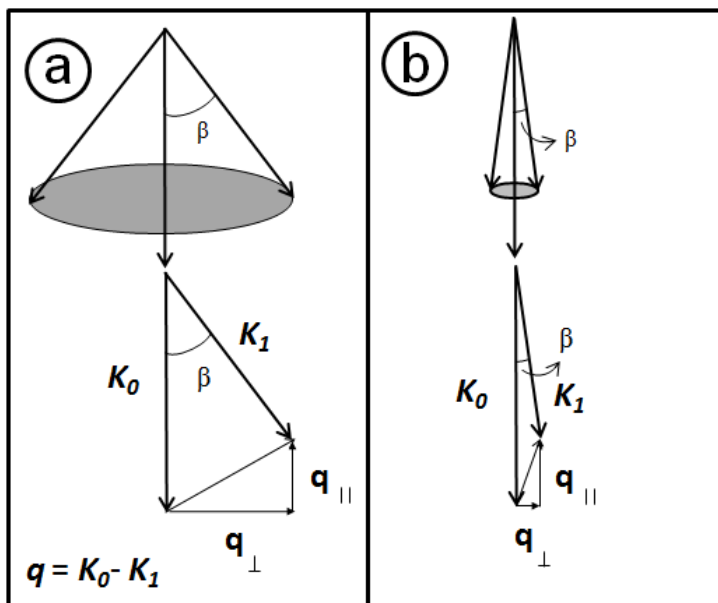
Figure 6.1 Scattering geometries at a) small and b) large scattering angles corresponding

to small and large spectrometer entrance aperture, respectively (Adopted from [BYB91]).

The intensity of the C 1s$\rightarrow \pi^*$ transition in the C 1s spectra of CNT depends on

the angle between the transition vector (**r**) and **q**. At large collection angles, **q**$\perp$ fans out in

a plane containing the CNT. Assuming that **q**$_{||}$ is negligible, the C 1s$\rightarrow \pi^*$ transition

becomes allowed at the edge where **q**$\perp$ and **r** are parallel and forbidden at the centre

where they are orthogonal. When the CNT is tilted to become parallel to the beam, all the

C 1s$\rightarrow \pi^*$ transitions become allowed (**Figure 6.2a**). At small collection angles,

assuming that **q**$\perp$ is negligible, the C 1s$\rightarrow \pi^*$ transition is forbidden at the edge and

allowed at the centre. When the CNT is oriented parallel to the beam, all the C 1s$\rightarrow \pi^*$

transitions become forbidden (**Figure 6.2b**). In this thesis, for a CNT in a plane perpendicular to the beam, edge refers to a region on the CNT whose normal is orthogonal to the beam and centre refers to a region whose normal is parallel to the beam (**Figure 6.3**). I assume that these locations do not change when CNT are tilted out of the plane.

To the best of my knowledge, **q**-dependent EELS spectroscopy and imaging using the method described in this chapter, which provides information close to that provided by the STXM dichroism measurements, has not been reported previously for carbon nanotubes, although it has been applied to the Ti 2p spectrum of the rutile form of TiO_2 [HHS&07]. Signals related to the strong anisotropy of the electronic structure of CNT have been observed previously by TEM-EELS [SKH&01,SY05a,SY05b,HSY08,SNT06]. The first q-dependent TEM-EELS study of CNTs was a comparison of C 1s EELS spectra of the edge and centre of a MWCNT which showed a small change in the relative intensities of the C 1s $\rightarrow \pi^*$ to C 1s $\rightarrow \sigma^*$ transition when the spectra were normalized at the continuum [SKH&01]. This was interpreted as changes in the orientation of graphitic-like planes relative to a fixed distribution of **q** directions. The observation of this type of edge/centre effect has been repeated and its interpretation extended by Sun et al. [SY05a,SY05b,HSY08] who have also defined experimental conditions to measure dichroic-free (so-called 'magic angle') TEM-EELS of high aspect ratio structures. However the edge/centre comparison is not the same as the anisotropic core excitation signal measured in the STXM-NEXAFS studies since the latter refers to a comparison of spectra measured with the electric vector (**E**) either perpendicular or parallel to the long

axis of MWCNTs, whereas in the edge/centre TEM-EELS studies **q** is always

perpendicular to their long axis.
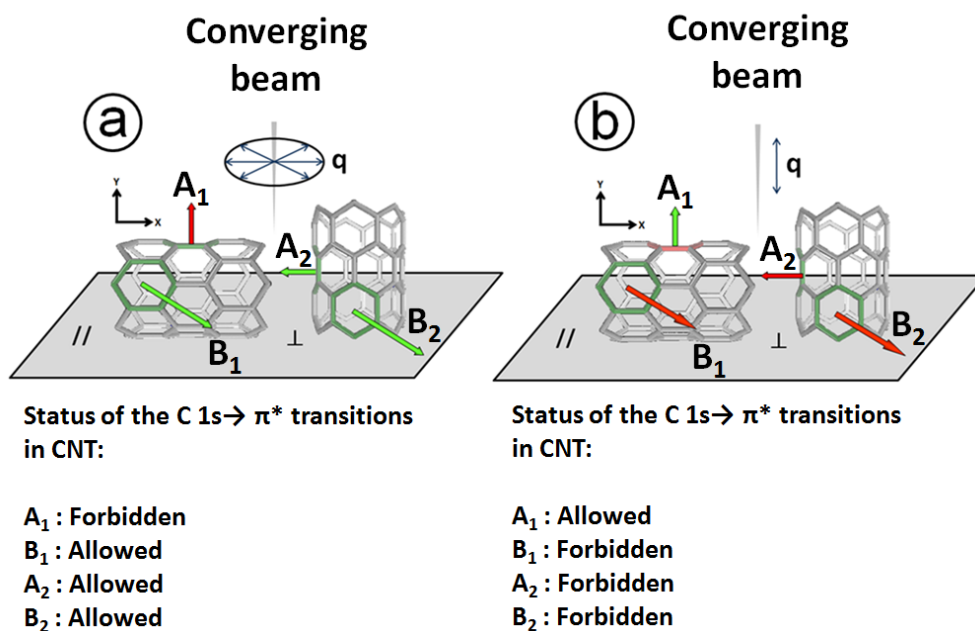
Figure 6.2 Status of the C 1s→ π^* transitions in CNT oriented perpendicular and parallel

to the beam at large (a) and small (b) collection angles.
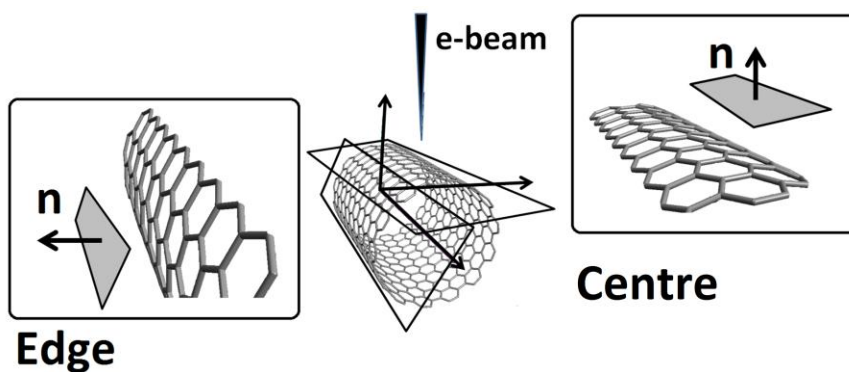
Figure 6.3 Edge and centre of CNT refer to regions whose normal are perpendicular and

parallel to the beam, respectively. These locations were assumed not to change when

CNT were tilted.

6.2 RESULTS

In order to perform q-dependent EELS measurements in AD-MWCNT, various methods were examined which are discussed in chapter 3. The results of these measurements are presented in this section.

6.2.1 TEM imaging of AD-MWCNT

Arc discharge multi-wall carbon nanotubes (AD-MWCNT) are predominantly straight with highly ordered graphitic walls. **Figure 6.4** is a low resolution TEM image of the AD-MWCNT selected for angle-dependent TEM-EELS studies. Various forms of impurity by-products are found in the sample, such as those within the dotted circle. High resolution TEM (HRTEM) images reveal those impurities are mostly graphitic structures.

A HRTEM image of the high quality region of the AD-MWCNT was recorded for rectangle *a* in Figure 6.3, and is shown in **Figure 6.5**. While the inner layers in this region of the AD-MWCNT are highly ordered, the outer layers are somewhat distorted. This is due to surface oxidation which transforms sp^2 bonds into sp^3 bonds and peels off the layers [DKP&08]. The central hollow of the AD-MWCNT has a diameter of ~2.6 nm and remains uniform along the tube.

In general, pristine CNT are capped with hemispheres of buckyballs. These caps are vulnerable to chemical oxidation so they are easily removed by oxidizing reagents. MWCNT consist of many concentric tubes each of which has its own cap. But, the structure of the caps is determined by the location of the tubes in the MWCNT. The HRTEM image of the tip of the AD-MWCNT (rectangle *b* in Figure 6.4) shown in **Figure 6.6** indicates that the caps are buckyball-like for the inner tubes, but they stretch

out for the outer tubes and become planar. This results in a graphitic box at the tip with almost perpendicular edges. The undamaged tip of the AD-MWCNT suggests that the tube is not severely oxidized.
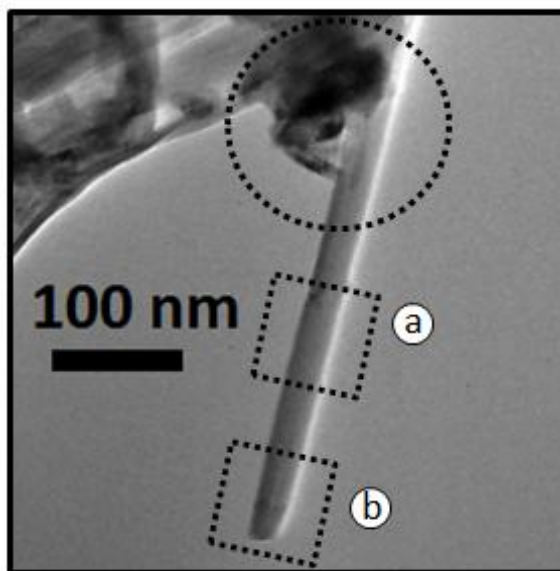
Figure 6.4 Low resolution TEM image of the AD-MWCNT selected for TEM-EELS studies (diameter ~35 nm; length ~1.5 um).
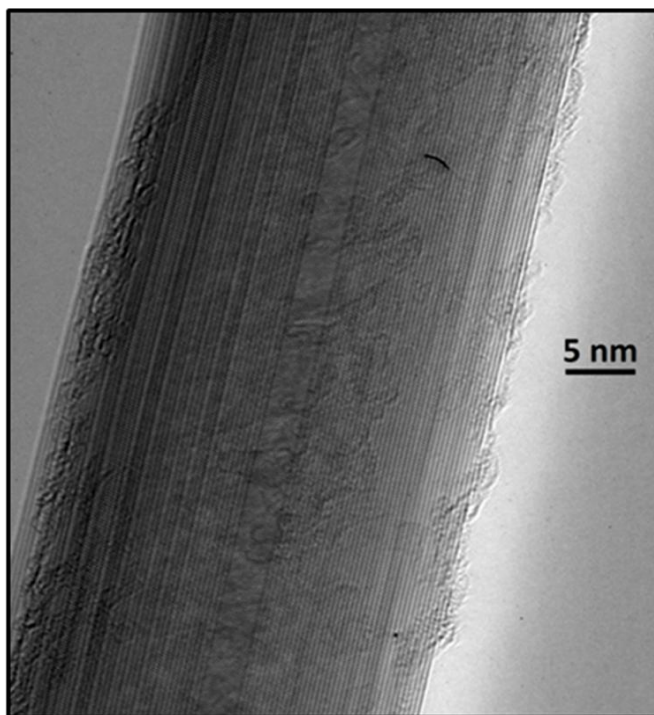
Figure 6.5 HRTEM image of the AD-MWCNT recorded for rectangle *a* in Figure 6.4.
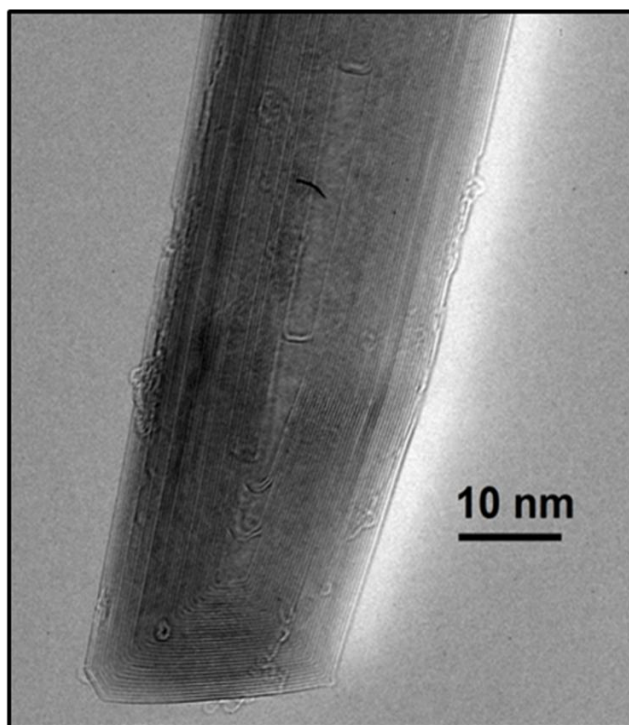
Figure 6.6 HRTEM image of the AD-MWCNT recorded for rectangle *b* in Figure 6.4.

6.2.2 Momentum-resolved EELS measurements in AD-MWCNT

The C 1s spectra of the AD-MWCNT shown in the STEM image in **Figure 6.7a** are plotted in **Figure 6.7b**. The spectra show a stronger C 1s→π* transition (285.1 eV) at the edge of the AD-MWCNT than the centre. This suggests that either **q** is not perfectly horizontal or it is not a well resolved unidirectional vector, or a combination of both. This also explains the small dichroism observed in the C 1s→π* transition.

The C 1s spectra of horizontal (**Figure 6.8a**) and vertical (**Figure 6.8b**) AD-MWCNT which are in a plane perpendicular to the beam are plotted in **Figure 6.8c,d**. The spectra of the edges (**Figure 6.8c)** show only slight differences which suggests that while the orientation of the vertical component (vertical to the electron beam) of **q** (**q**⊥) varies within the plane containing the tubes, its magnitude remains almost the same. Similar observation is made for the spectra of the centre (**Figure 6.8d)** due to the fact that they are induced by the parallel component (parallel to the electron beam) of **q** (**q**$_{\parallel}$) which has a single magnitude/orientation.
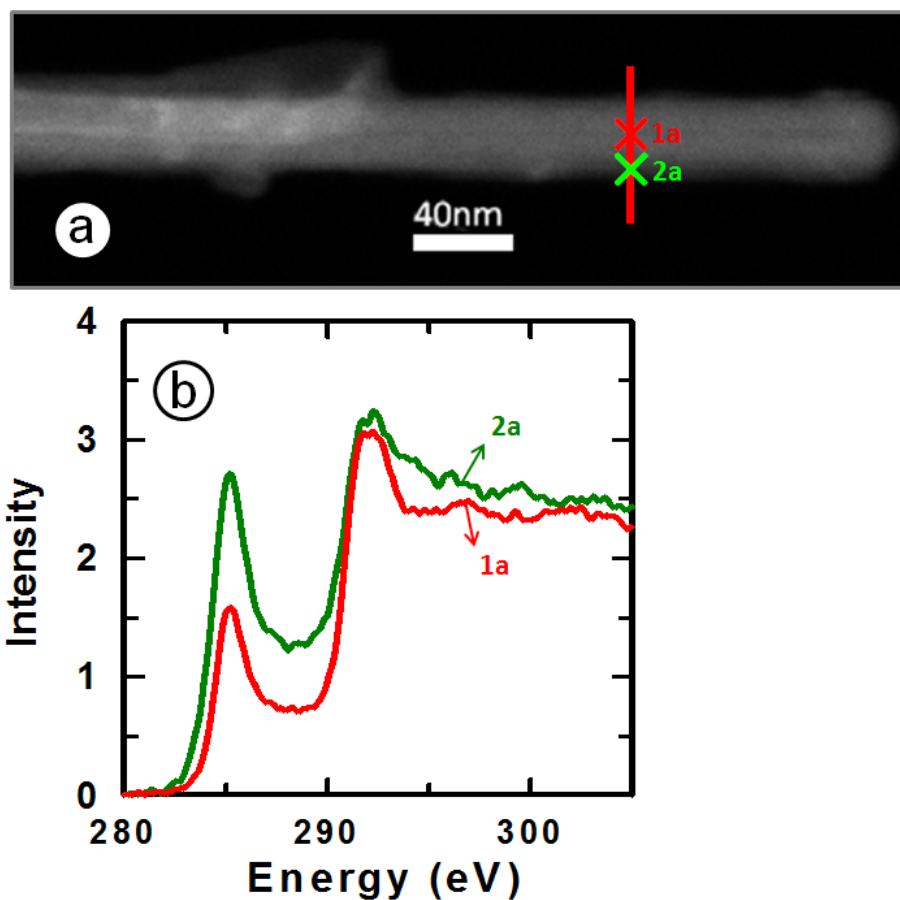
Figure 6.7 a) STEM image of an AD-MWCNT. b) C 1s spectra extracted from the centre

(1a) and the edge (2a) of the AD-MWCNT (E= 80 kV, α=6.5 mrad, β=4.5 mrad).
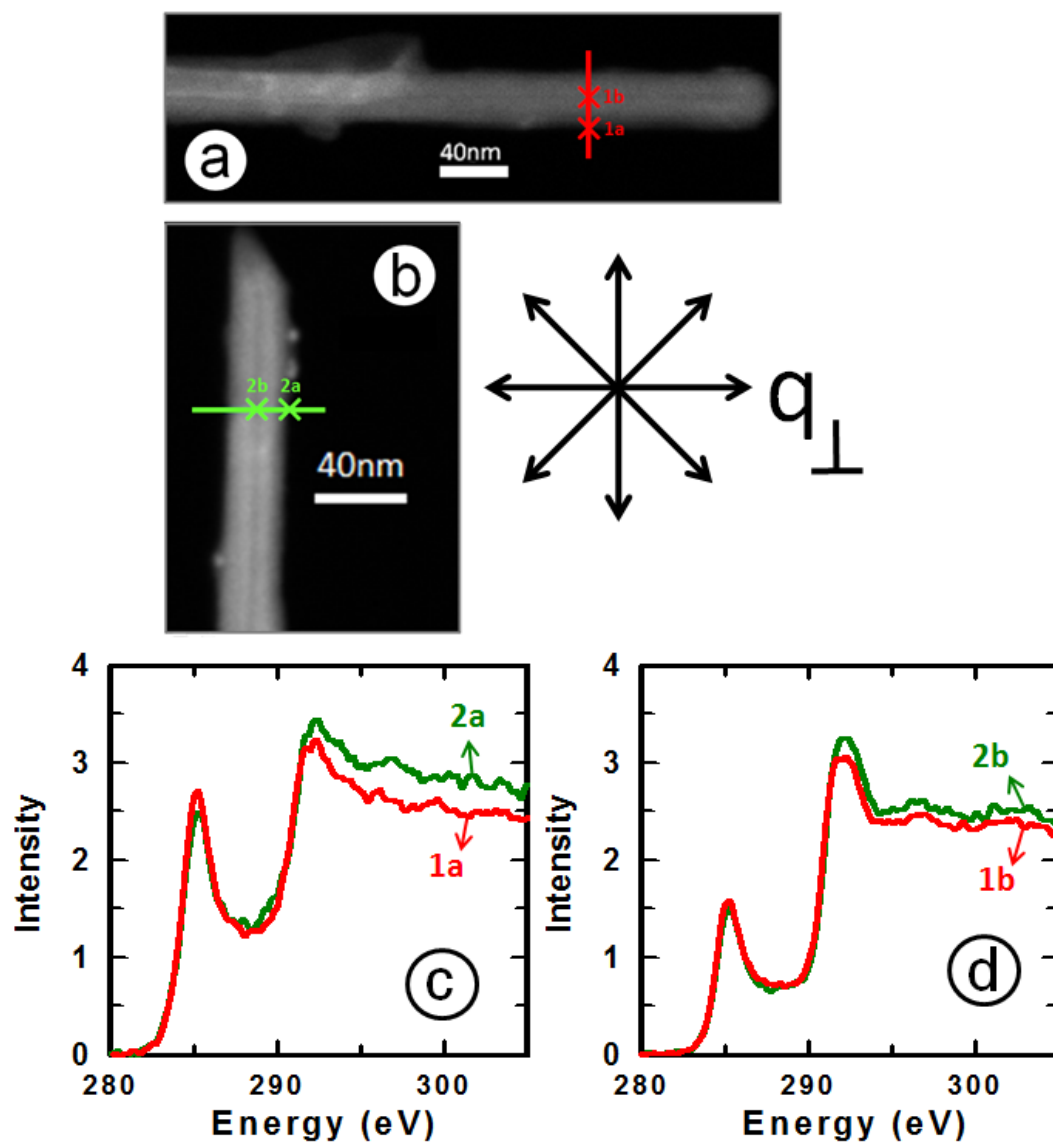
Figure 6.8 STEM images of a) horizontal and b) vertical AD-MWCNT in a plane perpendicular to the beam. The C 1s spectra extracted from c) the edges and d) centers of the AD-MWCNT (E= 80 kV, α=6.5 mrad, β=4.5 mrad).

TEM-EELS were measured using small convergence (α) and collection ($\square$) angles which were expected to produce a well resolved **q** (experimental detail is explained in chapter 3). The α and $\square$ values used for the measurements are presented in **Table 6.1** (please see page 171). In order to obtain angle dependent EELS spectra, an AD-MWCNT which was in a plane perpendicular to the beam and oriented at 77° relative to horizontal was selected. The orientation of the AD-MWCNT and the axis of tilt are shown in **Figure 6.9a**. As the MWCNT was tilted, an increase in the intensity of the C 1s→π* transition at the centre of the tube was expected. However, the C 1s spectra obtained at 0° and 70° tilt angles did not show any significant variation at the π*-resonance (**Figure 6.9b**). This unexpected result suggests that there are still a variety of **q** orientations which dramatically influence the outcome of the measurements. Note that the spectra plotted in Figure 6.9b are normalized at the continuum (360 eV) for thickcness.

In order to resolve this issue, I used a different approach based on the work of Botton et al. [BBS95] and Radtke et al. [RBV06] which involves the displacement of the EELS entrance aperture relative to the scattering pattern obtained at small angles about the beam. At the spectrometer entrance plane, **q**⊥ fans out radially in all directions with a magnitude determined by β (**Figure 6.10**). This results in a complex set of transitions in AD-MWCNT.
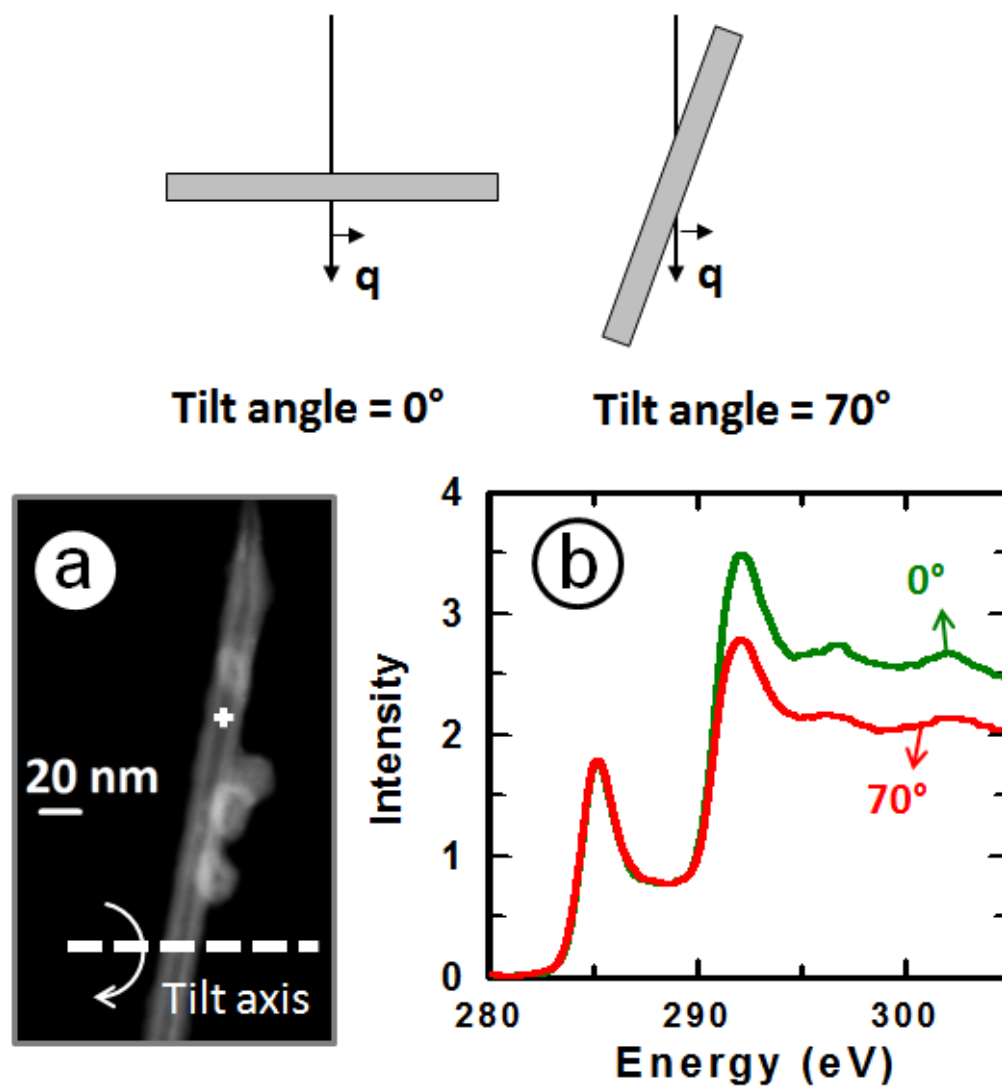
Figure 6.9 a) STEM image of an AD-MWCNT in a plane perpendicular to the beam and oriented at ~77° relative to horizontal; b) C 1s spectra extracted from the center of the AD-MWCNT at 0° and 70° tilt angles (E= 80 kV, α=6.5 mrad, β=4.5 mrad).
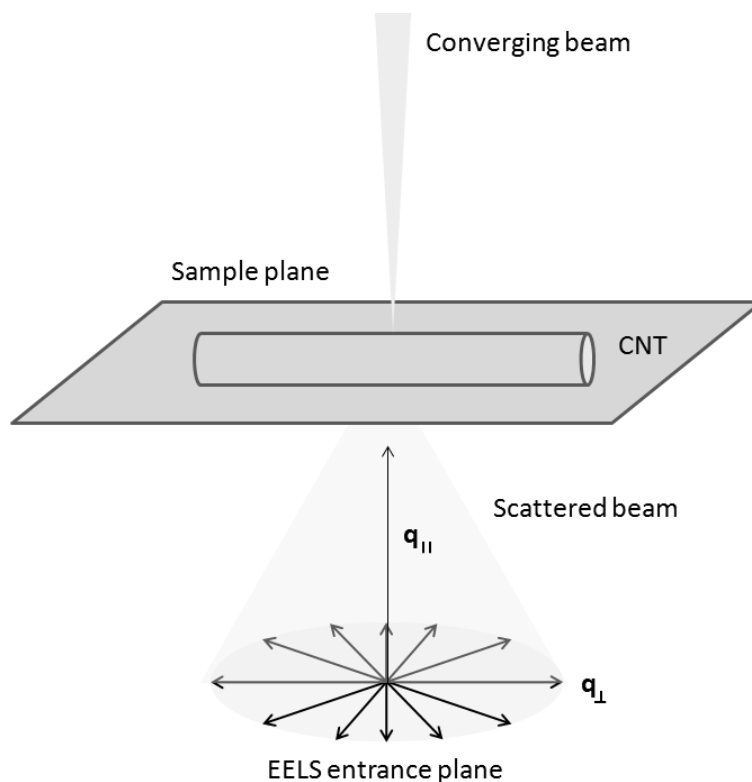
Figure 6.10 The orientation of **q**⊥ at the EELS entrance plane.

q⊥ with specific orientations relative to AD-MWCNT were selected by positioning the scattering signal relative to the spectrometer (fixed) entrance aperture. This pattern for scattering (from the AD-MWCNT depicted in **Figure 6.11a)** is shown in **Figure 6.11b**. The low angular resolution and a somewhat smeared pattern are due to the use of a convergent STEM beam (α=8.4 mrad). Figure 6.11b shows the direction of the walls in the AD-MWNCT as well as its long axis.

When the entrance aperture of EELS spectrometer is placed in position *i* (**Figure 6.12a**) relative to the scattering pattern, all $q\perp$ orientations are collected (**Figure 6.12b**). When placed at position *ii*, $q\perp$ with perpendicular orientations relative to the AD-MWCNT enter the spectrometer whereas when placed at position *iii*, those with parallel orientations relative to the AD-MWCNT enter the spectrometer.
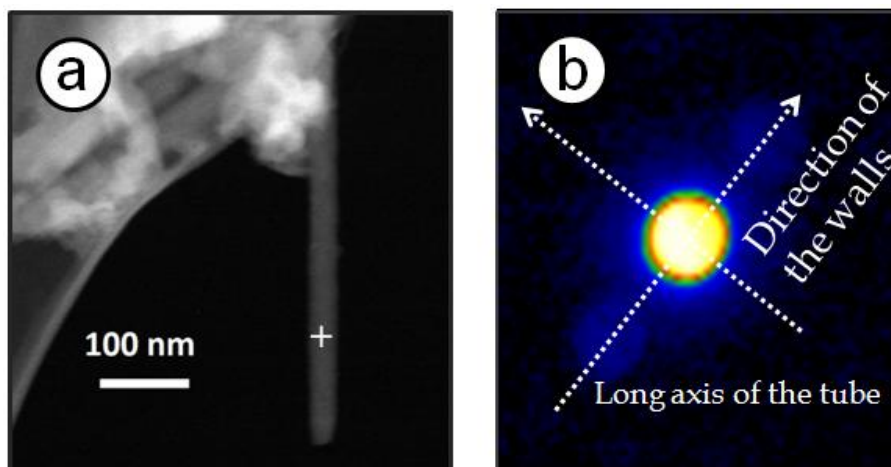
Figure 6.11 a) STEM image of an AD-MWCNT. b) Diffraction pattern from the white cross; the arrows show the directions of the walls and long axis of the tube (E=80 kV, α=8.4 mrad, β=6.6 mrad).
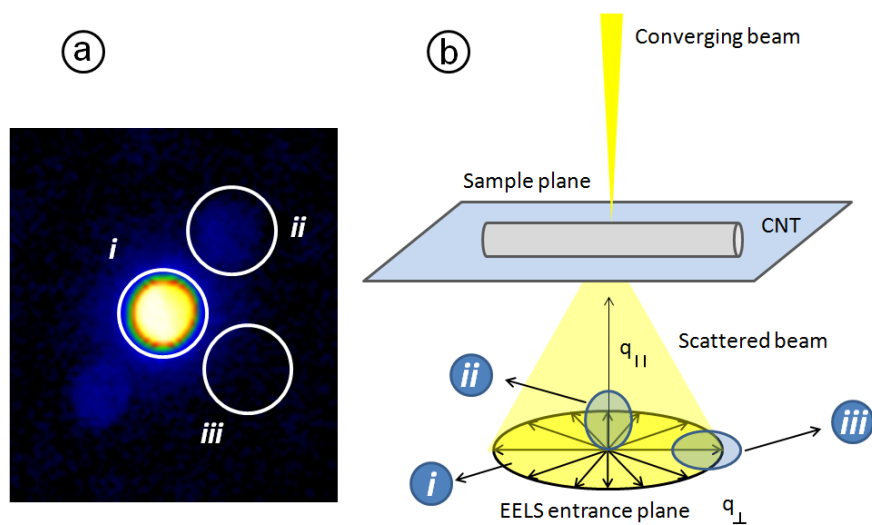
Figure 6.12 The position of EELS entrance aperture on the diffraction pattern (a) determines the orientations of $q_\perp$ that entre EELS spectrometer (b): *i*) collects all orientations of $q_\perp$; *ii*) collects $q_\perp$ with perpendicular orientations relative to the AD-MWCNT; *iii*) collects $q_\perp$ with parallel orientations relative to the AD-MWCNT.

To determine if this approach improves the directional specificity of **q**, the EELS spectra of an AD-MWCNT (**Figure 6.13a**) was measured. The tube is oriented at 77° relative to horizontal in a plane perpendicular to the beam. Note that the screen image of the AD-MWCNT was virtually rotated to a vertical orientation to reduce acquisition time by making the line scan a horizontal line (or a rectangle with minimal off-CNT area if recording an image stack). The entrance aperture was placed to collect only $q_\perp$ parallel to the AD-MWCNT (**Figure 6.13b**). The C 1s spectra extracted from the edge and centre of the AD-MWCNT are plotted in **Figure 6.13c,d**, respectively. The spectra show rather

weak C1s→π* transitions at both the edge and centre of the AD-MWCNT which is expected since at this orientation $\mathbf{q}\perp$ and $\mathbf{r}$ (at the centre and the edge) are orthogonal, making the C1s→π* transition forbidden.

The spectra were recorded again after the entrance aperture was placed to collected $\mathbf{q}\perp$ perpendicular to the AD-MWCNT (**Figure 6.14a,b**). While the intensity of the C1s→π* transition increased significantly at the edge, it remained almost invariant at the centre (**Figure 6.14c,d**). This was also expected since in this orientation, $\mathbf{q}\perp$ and $\mathbf{r}$ are parallel at the edge inducing strong transition and orthogonal at the centre forbidding the transition.
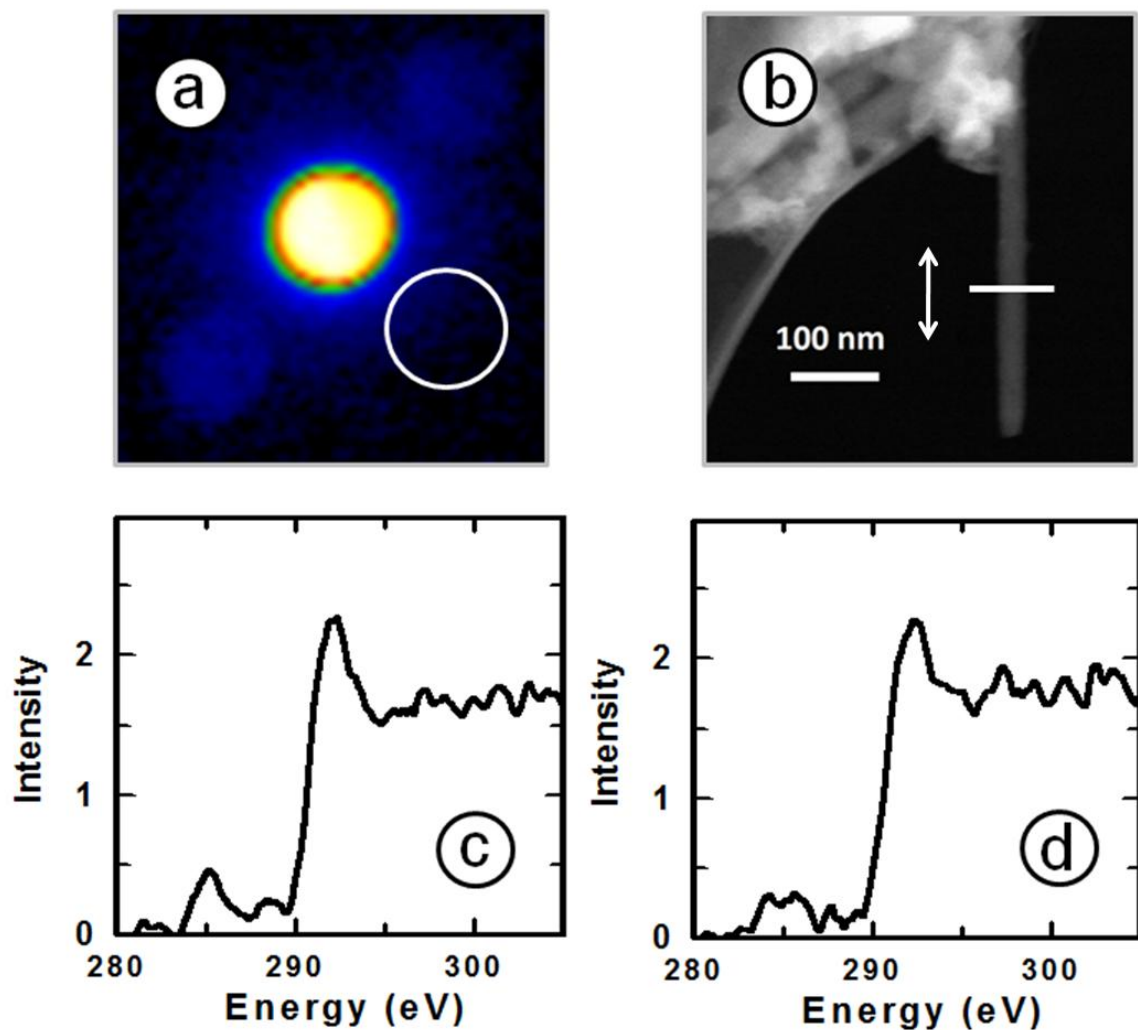
Figure 6.13 a) STEM image of the AD-MWCNT oriented at 77° relative to horizontal in a plane perpendicular to the beam. b) EELS entrance aperture placed to collect $\mathbf{q}\perp$ parallel to the AD-MWCNT. The C 1s spectra were extracted from (c) the edge and (d) centre of the AD-MWCNT from a line scan recorded across the tube (E=80 kV, α=8.4 mrad, β=6.6 mrad).
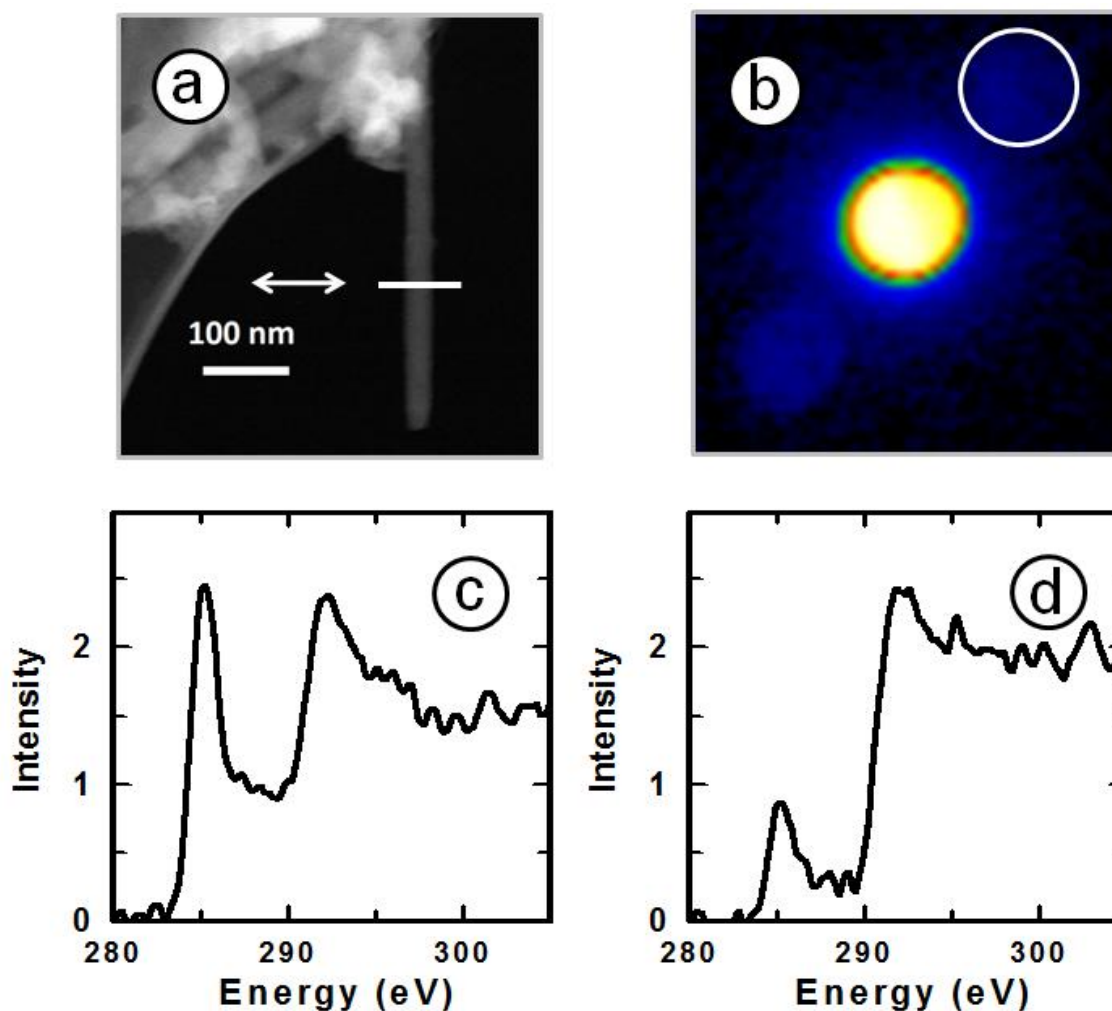
Figure 6.14 a) STEM image of the MWCNT oriented at 77° relative to horizontal in a plane perpendicular to the beam. b) EELS entrance aperture placed to collect **q**⊥ perpendicular to the AD-MWCNT. The C 1s spectra were extracted from (c) the edge and (d) centre of the AD-MWCNT from a line scan recorded across the tube (E=80 kV, α=8.4 mrad, β=6.6 mrad).

6.2.3 Angle dependent EELS measurements in AD-MWCNT

Since the approach outlined above could successfully resolve **q**, it was employed to obtain angle-dependent spectra from the centre of the same AD-MWCNT. The HRTEM image of the investigated area on the MWCNT is shown in Figure 6.4 (rectangle b). The sample orientation relative to **q** was adjusted by positioning the sample mounted on a tomographic holder, at different out-of-plane, tilt angles and then recording spectral line scans across the MWCNT. At zero tilt where **q**⊥ is orthogonal to **r**, the C1s→π* transition is forbidden (**Figure 6.15a**) and the π* signal is very small. When the AD-MWCNT was tilted, the angle between **q**⊥ and **r** decreased which allowed the C1s→π* transition to occur. At a tilt angle of 30°, the projection of **q**⊥ on **r** is rather small which results in a modest π* intensity (**Figure 6.15b**). At a tilt angle of 60°, this projection becomes larger which significantly increases the π* intensity (**Figure 6.15c**).

The experimental values of the π*-resonance intensity from the centre of the AD-MWCNT (Figure 6.15) are plotted in **Figure 6.16** as a function of tilt angle. These values were subsequently fit to the linear dichroic polarization equation, $a \pm b \times \cos^2 (\theta - \theta_f)$, where θ_f is an optimizable parameter corresponding to the angle between the long axis of the AD-MWCNT and horizontal. The fitting parameters are presented in **Table 6.2** (see page 171). There is good agreement between the polarization fit (solid line) and the experimental values which confirms that this measurement protocol is measuring electron linear dichroism in AD-MWCNT. The polarization ratio ($\frac{I_\perp}{I_\parallel}$, where $I_\perp$ and $I_\parallel$ are determined from the fit to the tilt dependent intensities) is **13.5**.
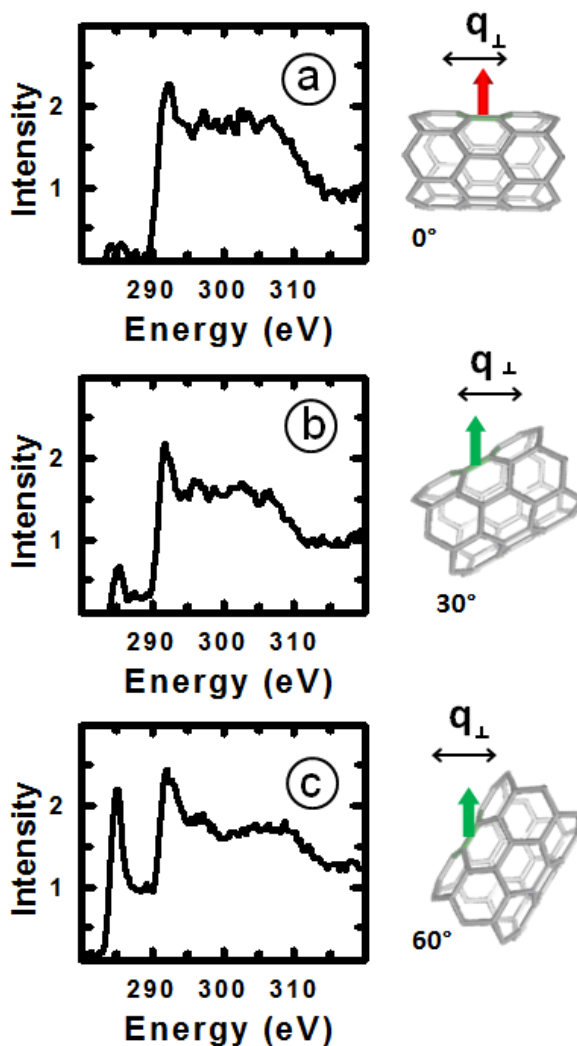
Figure 6.15 C 1s spectra extracted from the centre of the AD-MWCNT recorded at different tilt angles. The EELS entrance aperture was placed to collect spectra resulted by $q\perp$ with parallel orientation relative to the AD-MWCNT (similar to Figure 6.13) (E=80 kV, α=8.4 mrad, β=6.6 mrad).
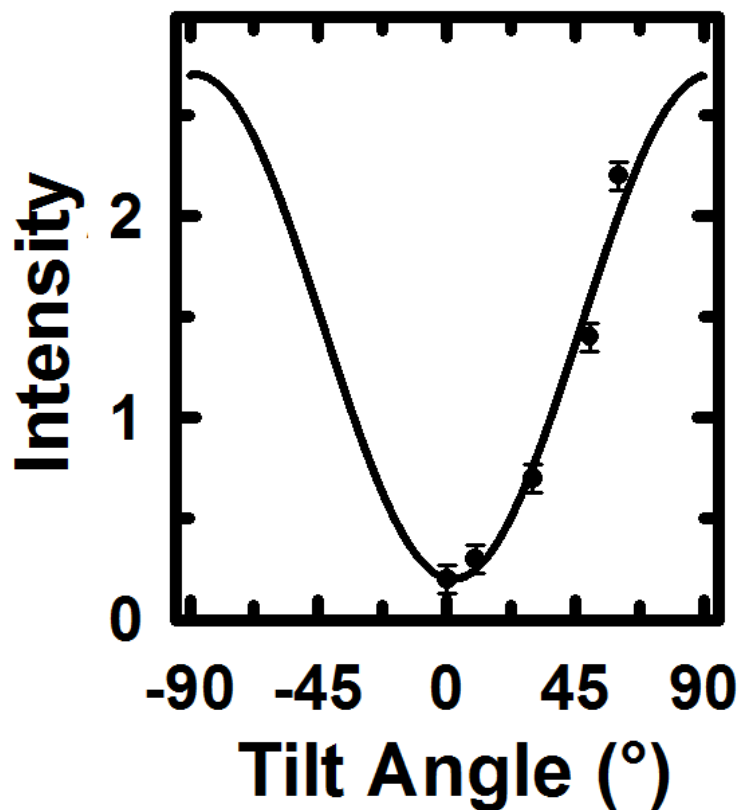
Figure 6.16 π^*-resonance intensities (circles) at the centre of the AD-MWCNT plotted versus tilt angle and fitted to the polarization function (solid line).

Unlike TEM-EELS, STXM-NEXAFS does not distinguish between the edge and centre of a MWCNT due to its limited spatial resolution. Therefore, dichroic signal obtained by STXM-NEXAFS is the average response of the AD-MWCNT. To investigate this difference, an AD-MWCNT from the same TEM-grid was characterized by STXM. The same AD-MWCNT was not chosen due to possible carbon build up and beam damage during TEM-EELS measurements. Since each AD-MWCNT differs from another, the comparison is not as meaningful as if the same AD-MWCNT was measured. **Figure 6.17** shows the π^*-images recorded for two perpendicular AD-MWCNT at different

polarization angles. The images clearly show that when the electric vector (E-vector) of the incident X-rays is orthogonal to the AD-MWCNT, the tubes become brighter and when they are parallel the tubes become darker. The tubes are contaminated by graphitic impurities some of which show polarization effect reflecting their graphitic nature. The tubes are oriented at 5° and 95° relative to horizontal. The maximum intensity for these tubes is observed when the E-vector is oriented at -90° and 0° respectively, which was expected.

500 nm
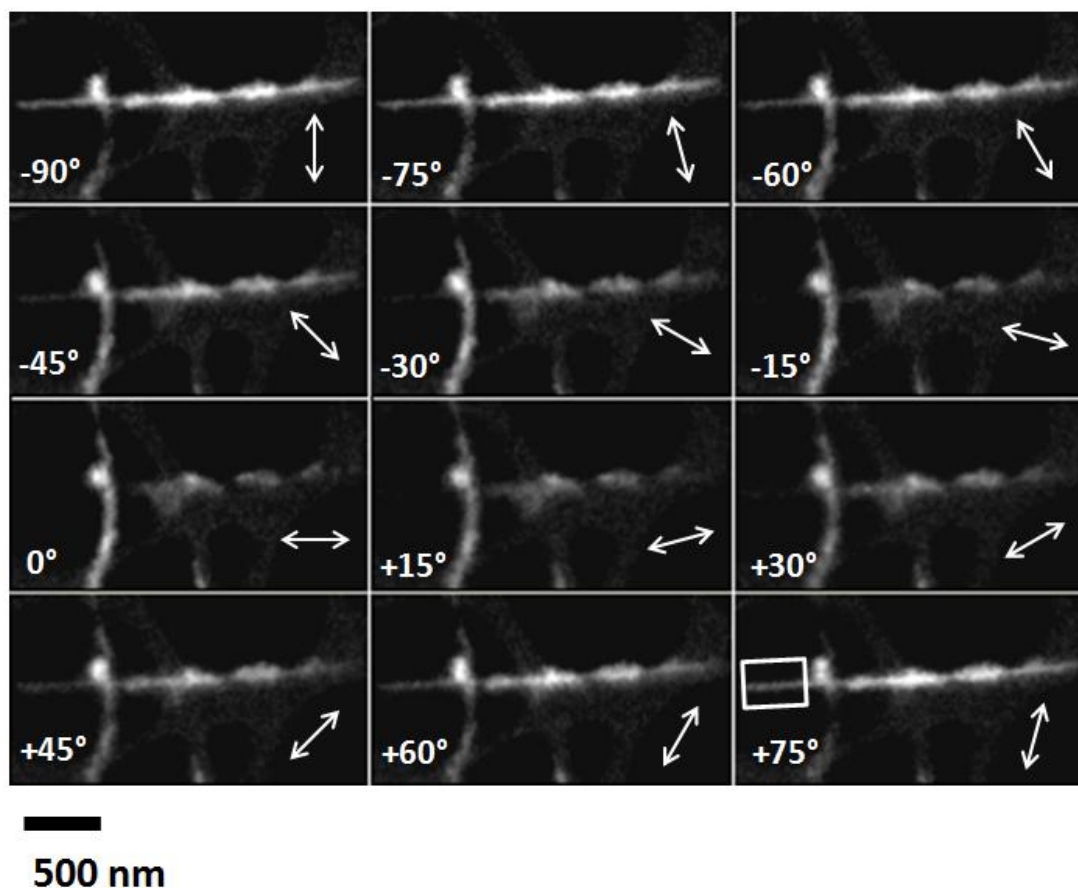
Figure 6.17 π*-images recorded for AD-MWCNT at different polarization angles (CLS STXM).

The experimental values of the π^*-resonance intensity were extracted from the white rectangle in the STXM image in **Figure 6.18a** and plotted as a function of polarization angle in **Figure 6.18b**. Minimum and maximum intensities are observed at 0° and 90° respectively; this is in accordance with the orientation of the MWCNT. The experimental values are fitted with the polarization function which is indicative of the polarization effect in the tube (**Table 6.2**). The polarization ratio was calculated to be **5.6** which is significantly smaller than that of the TEM-EELS measurements in Figure 6.16. This large difference is due to the fact that STXM-NEXAS signal is the average response of many layers in the AD-MWCNT. This exists at a lower extent in TEM-EELS data. Note that since the STXM and EELS measurements were made on two different tubes, these values are influenced by their defect content.
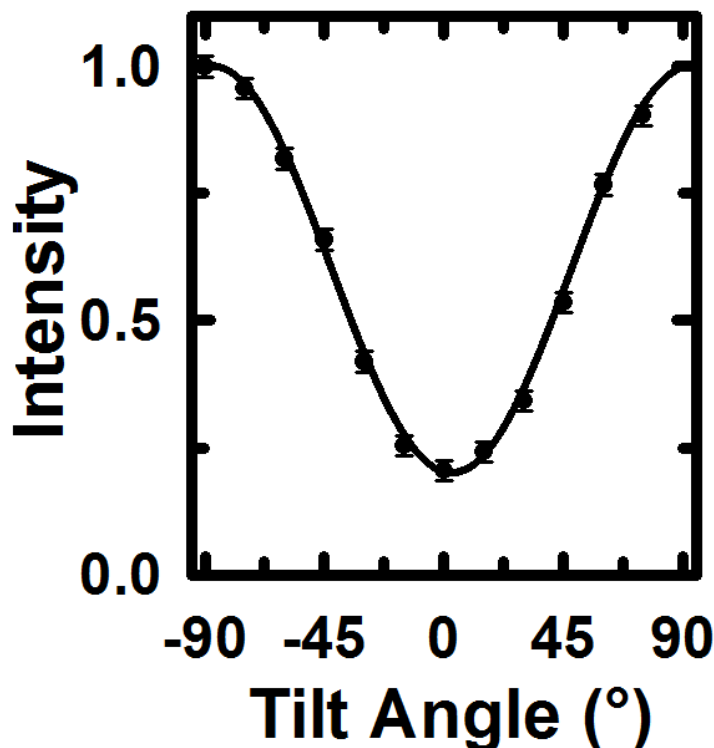
Figure 6.18 π^* intensities extracted from the white rectangle in the STXM image in Figure 6.17 and plotted versus polarization angle.

6.2.4 Quality evaluation in AD-MWCNT

Figure 6.19a,b are TEM images of a somewhat defective AD-MWCNT which was selected for polarization studies for comparison to the higher quality AD-MWCNT for which the TEM-EELS results were presented in Figures 6.14-6.16. Further TEM imaging (not reported here) made at different tilt angles showed that the tube is fairly straight and in a plane perpendicular to the beam except at ~150 nm away from the tip, where it bends and points upward; it is also oriented at 67° relative to horizontal. The HRTEM image in **Figure 6.19a** shows a lot of surface irregularities in the AD-MWCNT which are indicative of a damaged structure. The white box in **Figure 6.19b** shows the

area for which spectrum images were recorded at various tilt angles.
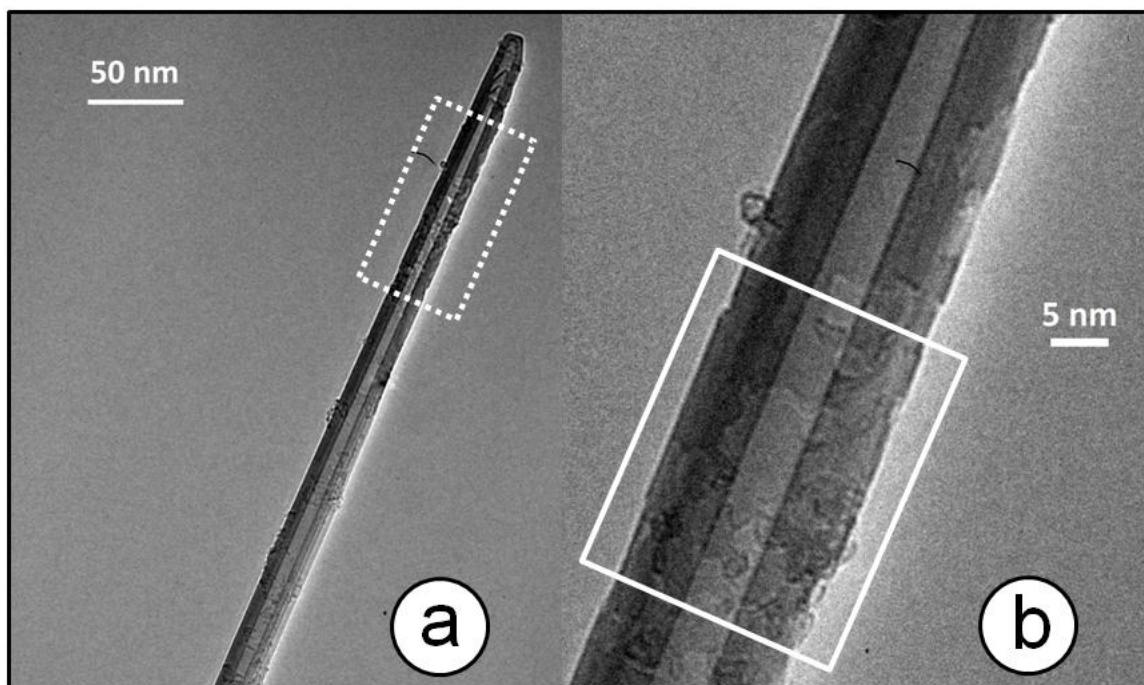
Figure 6.19 TEM images of the defective AD-MWCNT selected for angle dependent TEM-EELS studies for comparison.

The C 1s spectra of the centre of the defective AD-MWCNT were extracted from image sequences and plotted in **Figure 6.20**. The intensity variations at the π^*-resonance in the spectra follows a similar trend as that observed for the perfect AD-MWCNT. The relatively strong transition at zero tilt could be due to the fact that the region is not perfectly horizontal as well as due to the surface irregularities in the tube. As the tilt angle increases, the intensity of the π^*-resonance systematically increases and reaches maximum at 50°.
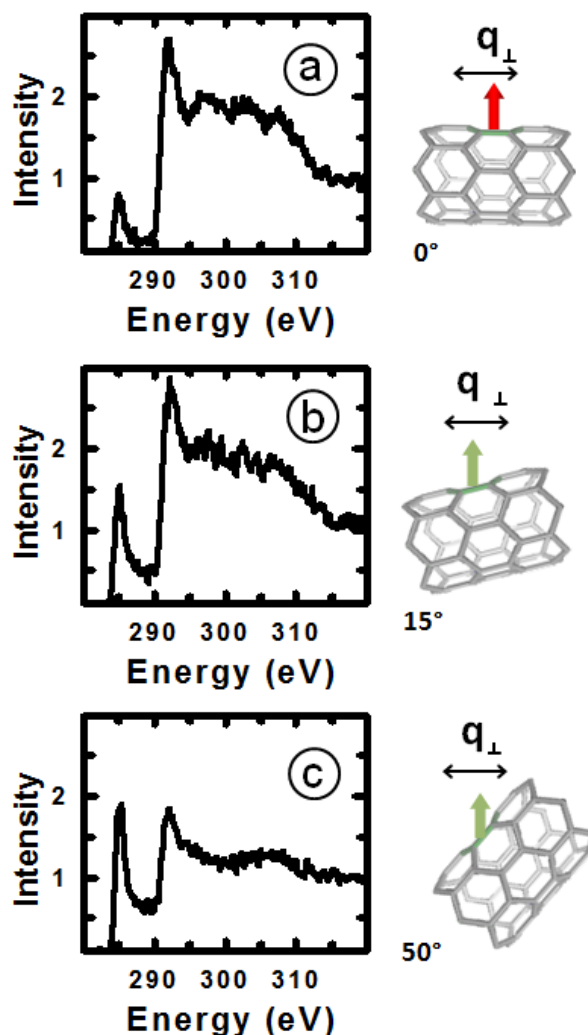
Figure 6.20 C 1s spectra extracted from the centre of the defective AD-MWCNT recorded at different tilt angles. The EELS entrance aperture was placed to collect spectra resulted by $\mathbf{q}\perp$ with parallel orientation relative to the AD-MWCNT (similar to Figure 6.13) (E=80 kV, α=8.4 mrad, β=6.6 mrad).

Figure 6.21 plots π^*-intensity values (black circles) extracted from the centre of the defective AD-MWCNT as a function of tilt angle. The polarization function with optimized parameters is a good fit to the experimental π^*-intensity values indicating that, despite the presence of defects, the tube is still mostly graphitic (**Table 6.2**). The minimum intensity is observed at -30±5°which corresponds to the angle between the AD-MWCNT and a plane perpendicular to the beam. The polarization ratio was calculated to be **2.2** which is significantly smaller than that expected for a perfect AD-MWCNT which, in principle, is infinity and also much less than that found for the more perfect tube (**13.5**, see Figure 6.16). Since the experimental conditions were similar for both measurements and the signals were normalized for thickness, this difference reflects the relative structural quality of the tubes.
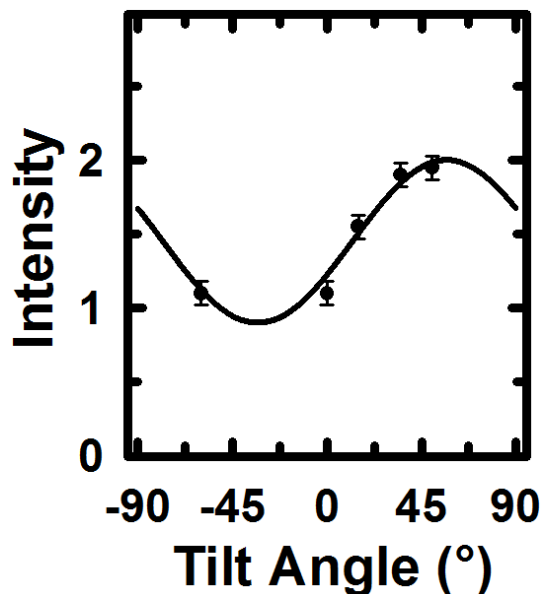
Figure 6.21 π^*-resonance intensities (circles) from the centre of the defective AD-MWCNT plotted versus tilt angle and fitted to the polarization function (solid line).

Table 6.1- Beam energy and convergence (α) and collection (β) angles used to record line
scans and image sequences.

|	**Energy**	**α**	**β**
Figure 6.8	80 kV	6.5 mrad	4.5 mrad
Figure 6.9	80 kV	6.5 mrad	4.5 mrad
Figure 6.15	80 kV	8.4 mrad	6.6 mrad
Figure 6.20	80 kV	8.4 mrad	6.6 mrad
Figure 6.21	80 kV	8.4 mrad	6.6 mrad

Table 6.2- Fitting parameters of EELS and STXM data.

	Observed angle [a]	**a**	**b**	**θ_f**
Figure 6.16	0°	0.2±0.03	2.5±0.03	-88°± 5°
Figure 6.18	20°	0.8±0.01	1.2±0.01	57°± 5°
Figure 6.21	0°	0.2±0.03	0.8±0.03	-87°± 5°

[a] Reference line for angle determination is horizontal (clockwise is positive).

By combining the π^*-resonance images recorded at different tilt angles and then fitting each pixel in the resulting polarization stack to the polarization function, one can obtain a map of the polarization amplitude. This map represents the magnitude of the polarization effect at each pixel of the image of an AD-MWCNT, i.e. the bright pixels correspond to a strong polarization effect and dark pixels correspond to a weak polarization effect. Since the polarization effect is directly related to the local concentration of defects, this map can be considered as a map of sp^3 defects map. **Figure 6.22a** shows the region for which amplitude map shown in **Figure 6.22b** was obtained. Note that in order to have sufficient statistical quality the data was (2x2) binned from (14 × 8) pixels (2 nm) pixel size to (7 × 4) pixels (6 nm) pixel size. The map of the polarization amplitude should reflect the spatial distribution of defects, and in fact it does correspond relatively well to the distribution of structural imperfections seen in the TEM image. For instance, the region with more surface irregularities in the TEM image (lower right) is mapped as dark pixels in the amplitude image. The defects in this AD-MWCNT which are responsible for lowering the ELD seems to be mostly sp^3 defects resulted from the attachment of surface contaminations to the tube. The quality of the amplitude image can be improved by recording π^*-resonance at more tilt angles and at more spatial pixels. The tilt series of spectral image stacks in this demonstration measurement took ~3 hours to record. It would be practical to increase the sampling up to 5-10 fold in terms of instrument access and stability.
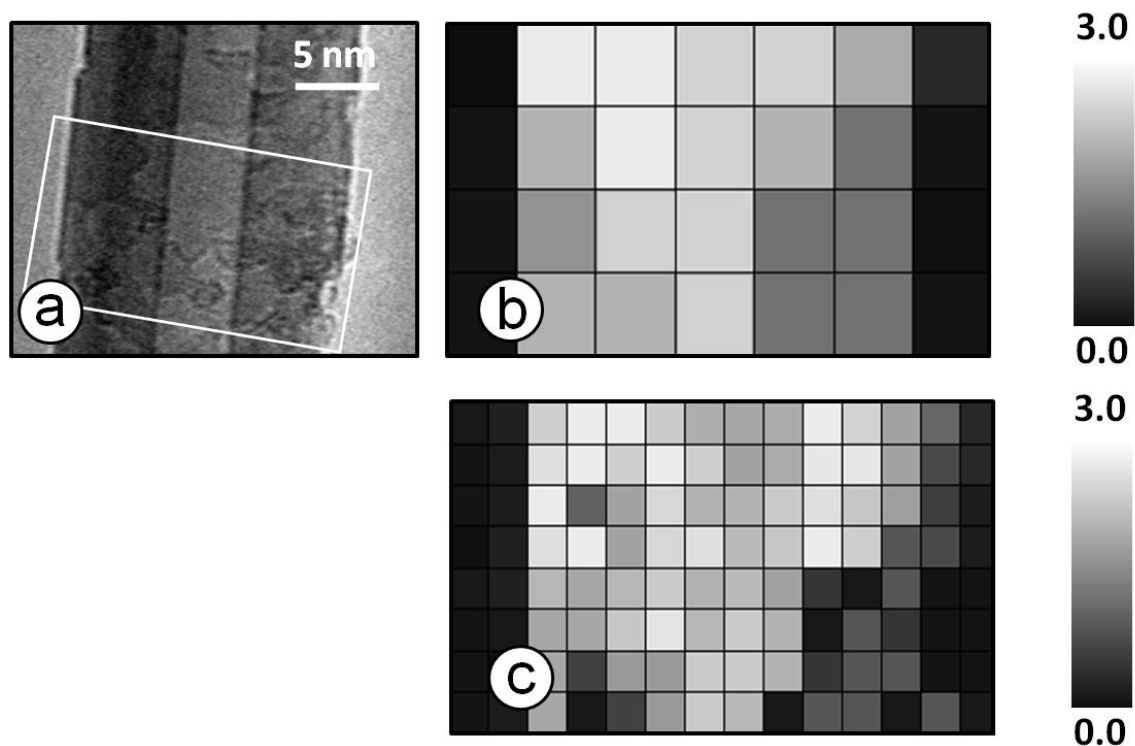
Figure 6.22 TEM image of the region studied by TEM-EELS (a); binned (b) and unbinned (c) amplitude images obtained by fitting each pixel in the polarization stack to the polarization function (E=80 kV, α=8.4 mrad, β=6.6 mrad).

6.2.5 Focused ion beam modification of AD-MWCNT

Controlled introduction of defects into CNT with the help of high energy particles is often pursued to alter the electronic, chemical, and physical properties of CNT for various applications. This process can change the reactivity and morphology of CNT, weld them together to make junctions, or attach them to metal plates. Particle irradiation damages materials mainly through ionization and knock-on processes. While ionization is quenched in CNT, knock-on collisions transfer energy and momentum to carbon atoms, causing atomic displacements or atom removal. A knocked atom can also displace adjacent atoms if its kinetic energy is above the threshold for further displacements. In MWCNT, as in graphite, particle irradiation may lead to $sp^2 \rightarrow sp^3$ transformation which cross links the walls and forms stable sp^3 clusters. Prolonged exposures rupture, bend, and shrink MWCNT and eventually remove their central hollow. Previously, Felten et al. [FGG&10] showed that the extent of damage in MWCNT irradiated by a focused ion beam can be quantified by monitoring the changes in the dichroism at the C 1s$\rightarrow \pi^*$ transition along the tube. They showed that in areas far from the irradiated region dichroism is fairly large but close to this region dichroism dramatically reduces. This chapter documents a McMaster based exploration of the effect of ion bombardment. It uses studies of CNT which were intentionally damaged by ion beam bombardment to demonstrate the defect sensitive character of this EELS signal.

Figure 6.23a is the scanning electron microscopy (SEM) image of the AD-MWCNT (dotted rectangle) selected for FIB modification. The tube received a dose of $4.0 \times 10^5 \frac{Ga^+}{cm^2}$ along the white line shown in **Figure 6.23b**. The low resolution TEM

image displayed in **Figure 6.23c** shows that the AD-MWCNT was bent as a result of FIB modification.

HRTEM image of the irradiated region (**Figure 6.24a**) shows that the graphitic structure of the AD-MWCNT is completely damaged and the tube has been transformed into amorphous carbon. This is accompanied by the destruction of the central hollow of the tube. TEM studies of several FIB-modified AD-MWCNT revealed that although irradiation was localized, in some cases, damage was spread up to several hundred nanometers along the tube. However, carbon onions which were physically attached to these tubes, even those in the vicinity of irradiated regions, were intact (**Figure 6.24b**). This suggests that such a large range transformation is a secondary process induced by the knocked carbon atoms and not by the spatial tail of the Ga^+ beam (halo effect).
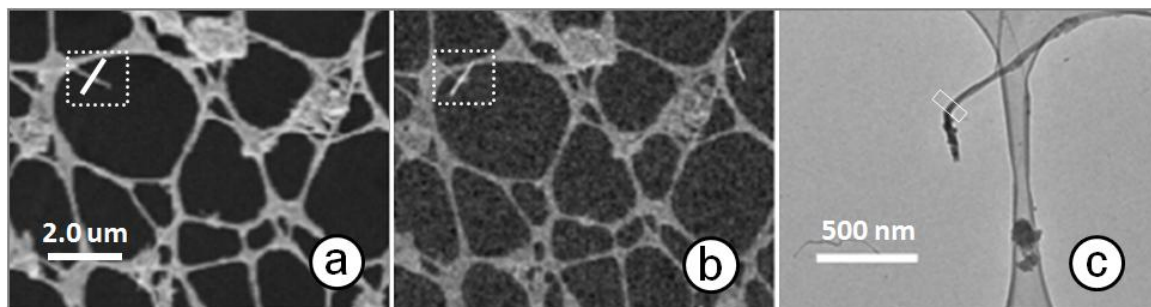
Figure 6.23 a) SEM image of the AD-MWCNT chosen for FIB modification. b) The AD-MWCNT was bent by the beam. c) Low resolution TEM image of the AD-MWCNT shows its actual orientation while TEM-EELS study was conducted.
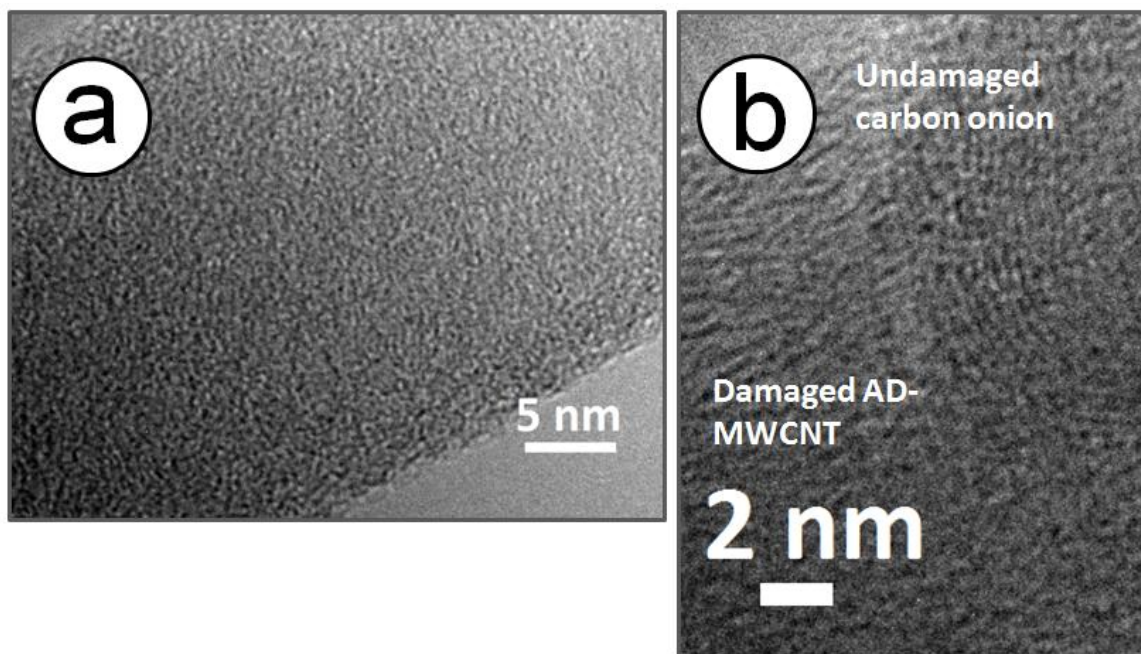
Figure 6.24 HRTEM image of the irradiated region (white box in Figure 6.19c). b) HRTEM image comparing structural changes due to FIB modification in the AD-MWCNT and a carbon onion physically attached to the tube.

To study structural changes in the AD-MWCNT due to ion beam irradiation, an energy loss stack was recorded at the C 1s edge (250-400 eV). **Figure 6.25a** plots the energy loss spectrum of the region directly irradiated by the FIB (in the vicinity of the dotted arrow in the STEM image). The wide π^*- and smeared σ^*-resonance peaks in the spectrum indicates that the AD-MWCNT has completely transformed into graphitized amorphous carbon. Spectra from two regions away from the irradiated zone are plotted in **Figure 6.25b,c.** These spectra are more graphitic-like, suggesting that these regions have resisted damage spread and preserved their graphitic character.

The C 1s energy loss stack was fit to the reference spectra of AD-MWCNT and amorphous carbon by using the *singular value decomposition* (SVD) technique. The reference spectra (**Figure 6.26a,b**) were obtained by normalizing the spectra in Figure 6.21a,b in the far continuum (360 eV). This produced amorphous carbon and AD-MWCNT maps shown in **Figure 6.26c,d**. The former shows the spatial extent of transformation of the AD-MWCNT into amorphous carbon as a result of ion beam irradiation. It is surprising that the fine ion beam which was localized at a specific spot on the tube could effectively spread damage up to 100 nm in the straight arm of the AD-MWCNT. However, the damage did not spread as far in the bent arm which may suggest that damage migration was slowed down by the bend. **Figure 6.26e** is a color composite image constructed from the maps of the amorphous carbon (red) and AD-MWCNT (green) in Figure 6.23c,d which shows the relative distribution of each component and the distribution of sp^2 defects in the AD-MWCNT.
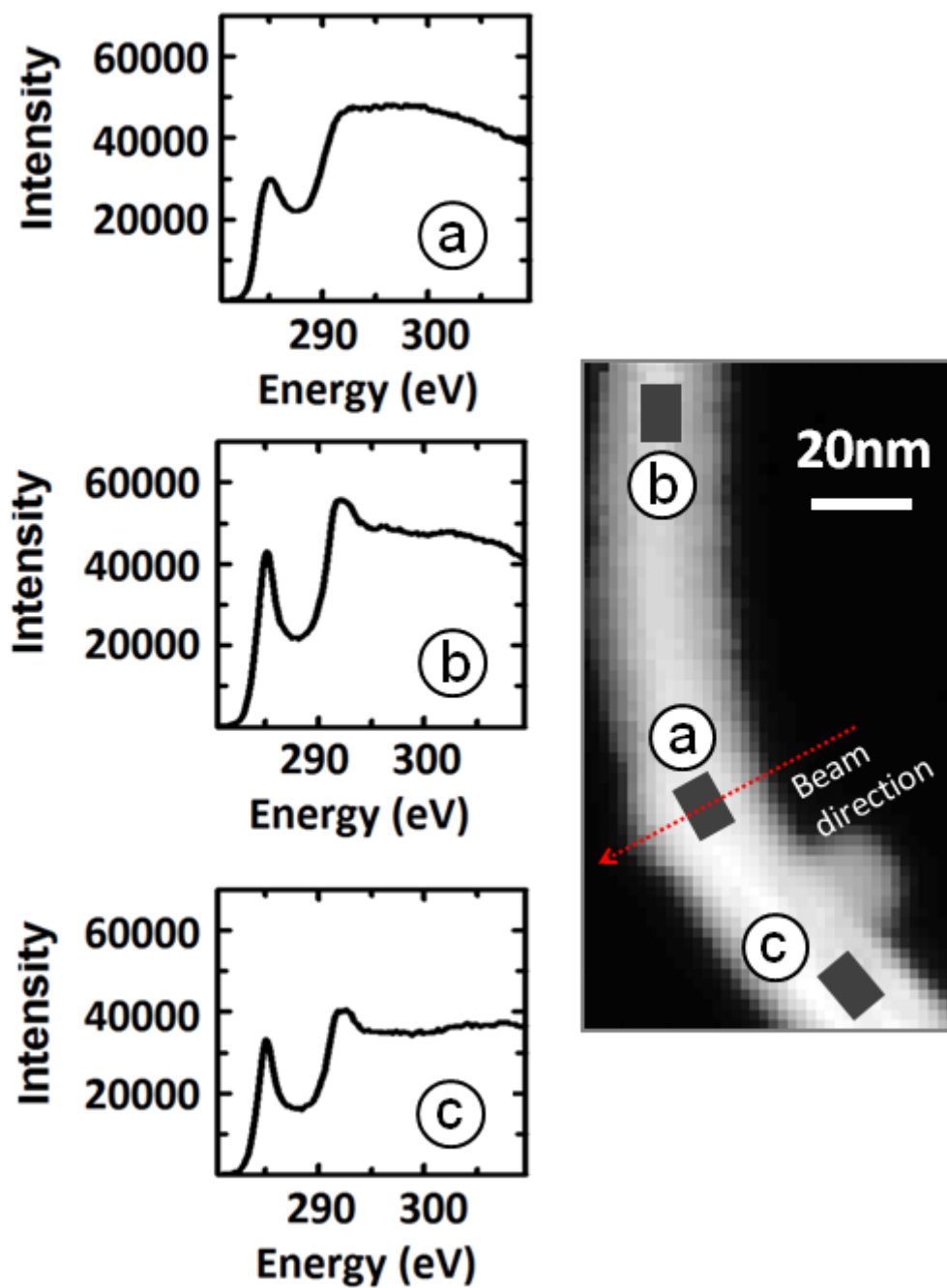
Figure 6.25 C 1s energy loss spectra extracted from irradiated (a) and non-irradiated (b,c)

regions on the AD-MWCNT (E=80 kV, α=6.5 mrad, β=4.5 mrad).
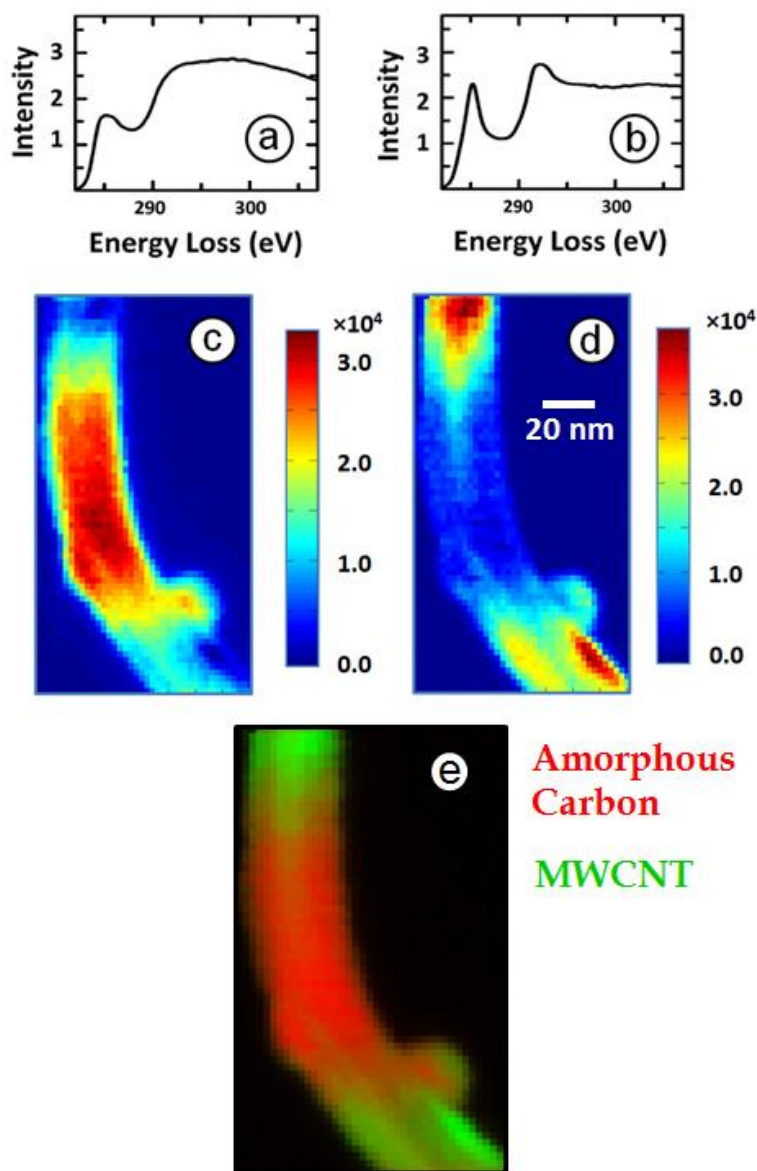
Figure 6.26 Amorphous carbon (a) and AD-MWCNT (b) reference spectra obtained by normalizing internal spectra at the continuum (360 eV). Amorphous carbon (c) and AD-MWCNT (d) maps obtained by fitting the C 1s stack to the reference spectra. The RGB image (each color independently rescaled) constructed from scaled amorphous carbon (red) and AD-MWCNT (green) maps (e).

6.**3. Discussion**

The conventional approach to study dichroism, which involves optimizing the convergence and collection angles to resolve **q** in TEM-EELS, did not provide the same dichroic effect as that observed by STXM of MWCNTs. In fact, the spectra of the edge and centre of MWCNTs at various tilt angles matched at the C 1s→π* transition where a large dichroism should have occurred (**Figure 6.9**). This suggests that even at such small convergence and collection angles (α=6.5 mrad, β=4.5 mrad), the spatial orientation of **q** is not well enough defined to extract dichroic signal from MWCNT. However, this method could differentiate between the edge and centre of MWCNT with similar magnitude as that previously reported by Stéphan et al. [SKH&01] and Sun et al. [SY05a,SY05b,HSY08] (**Figure 6.7**).

A large dichroism was detected when the method based on the displacement of the scattering pattern over EELS entrance aperture was employed. In fact, the comparison of this technique to that used earlier [SY05a,SY05b,HSY08] showed a significant increase in the dichroic effect. This comparison was made based on the changes of the intensity of the C 1s→π* transition at the edge and centre of MWCNT; some of this difference is due to the fact that MWCNT with different structural quality were used for these measurements. Furthermore, the spectra recorded from the centre of MWCNT at different tilt angles showed a similar dichroism as that routinely obtained by STXM. This method effectively uses only a certain orientations of $q\perp$ relative to MWCNT while removing $q_{||}$. This well-resolved directionality of **q** is clearly demonstrated in Figure 6.13, Figure 6.14. The response of the π*-resonance shows that $q\perp$ has been weakened and the collection of

$q_{||}$ has been limited to certain orientations. This can be further improved by using a smaller entrance aperture and placing it further away from the bright diffraction spot at the centre (See Figure 6.11). However, this reduces the number of the electrons that enter the spectrometer and thus lowers the signal-to-noise ratio. So, in order to improve the quality of the spectra, one has to use a longer exposure which may damage the sample. The variations of the intensity of the π^*-resonance in a high quality MWCNT could be used as a measure to evaluate to what degree q has been resolved as the size and location of the aperture changes. This evaluation will allow the TEM-EELS community to perform dichroic evaluations of anisotropic samples such as carbon nanotubes that, at present, can only be done on a very small number of synchrotron spectromicroscopy beamlines, and with much lower spatial resolution than TEM-EELS provides. In principal, this method is not limited to MWCNT systems and can be used to characterize the dichroism and thus the structural anisotropy in a variety of anisotropic systems such as TiO_2 and BN nano-wires and nano-fibers.

In addition, TEM-EELS could successfully map the extent of bonding transformation that occurred in AD-MWCNT as a result of focused ion beam irradiation. To my knowledge, this ability to differentiate and identify chemical bonding at such a high spatial resolution is limited to TEM-EELS and cannot be achieved by other techniques.

The unique ability of TEM-EELS to determine structural order and chemical bonding in CNT at nanometer scales enabled me to obtain more insight about the electronic and structural properties of CNT. TEM-EELS confirmed my previous

observation by STXM that defects can reduce linear dichroism in CNT and that ion bombardment, no matter how subtle, can create and spread defects in them. These demonstration experiments show that TEM-EELS can examine defects and their spatial distributions along CNT at very high spatial resolution. In cases, such as the CCEM FEI Titan microscopes with monochromated incident electron beams the energy resolution is almost as good as at the synchrotron, so it will also be possible to identify chemical functional groups or dopants in CNT and visualize their precise locations along them.

Chapter 7

Summary and future work

This chapter summarizes the work of this thesis, and highlights the major contributions that this thesis has made to advance carbon nanotube science. In addition, it provides suggestions for future studies.

7.1 Summary

Scanning transmission X-ray microscopy (STXM) was used to study the near edge X-ray absorption fine structure (NEXAFS) spectra of single walled (SW) and multi-walled (MW) carbon nanotubes (CNT). The results showed a large dichroic effect at the C 1s→π* transition at 285.1 eV. The maximum intensity was observed when the electric vector (**E**) of the incident X-rays was perpendicular to the long axis of CNT; the minimum intensity was observed when they were parallel. This is the first observation of the X-ray linear dichroism (XLD) at the C 1s→π* transition in isolated SWCNT bundles and individual MWCNT. The XLD was found to be similar in relatively perfect SWCNT (**Figure 7.1**) bundles and MWCNT. This was unexpected as the larger curvature in SWCNT which increases the symmetry mixing should have reduced the XLD.
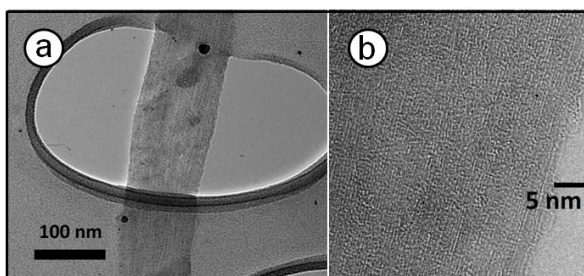
Figure 7.1 TEM images of SWCNT samples used for XLD measurements.

The XLD was found to be weaker in defective CNT than relatively perfect CNT. This was expected as defects reduce the number of available final states with sp^2 symmetry. Furthermore, in the vicinity of defects, CNT rearranges the graphitic layers to minimize the energy; such local irregularities reduce the XLD as they assume random orientations relative to **E**. This thesis introduced a parameter known as polarization ratio ($I_\parallel / I_\perp$) as a quantitative measure to evaluate the quality of individual CNT. In high quality CNT, this polarization ratio is close to zero and as CNT becomes defective this value increases. In addition, this thesis provided a recipe to map defects along CNT by fitting the polarization stacks with the polarization function. This process produces constant, amplitude and angle images. The constant image shows the portion of CNT that does not exhibit dichroic effect. The amplitude image maps the magnitude of the dichroic effect in CNT; bright pixels in the amplitude image correspond to stronger XLD (low defect content) and dark pixels correspond to weaker XLD (high defect content). The angle image shows the orientation of each pixel on CNT relative to **E**.

STXM was also employed to map chemical components in pristine, purified, and alkyl functionalized SWCNT bundles. The C 1s and O 1s spectroscopy revealed chemical changes occurring in SWCNT due to wet purification, hard baking, and alkyl functionalization. In addition, singular value decomposition (SVD) of image sequences provided chemical maps which quantitatively showed the spatial distribution of functional groups in SWCNT. The structural changes in SWCNT due to these treatments were evaluated by probing their dichroic response.

STXM has a limited spatial resolution (better than 30 nm). Thus, to investigate

MWCNT at resolutions close to atomic scale, electron energy loss spectroscopy (EELS) in a transmission electron microscope (TEM) was employed. The measurements were performed in scanning transmission electron microscopy (STEM) mode of the TEM. TEM-EELS produced similar dichroic effect as STXM when the relative orientation of the momentum transfer ($\mathbf{q}$) and long axis of MWCNT was changed (tilting the sample). Various methods were employed to resolve $\mathbf{q}$ to a high degree. However, only a method based on the displacement of the scattering pattern over the EELS entrance aperture could produce a highly resolved $\mathbf{q}$. Similar to STXM measurements, the intensity variations at the C 1s→π* transition was used to map defects in MWCNT.

TEM-EELS was also used to map the extent of sp^2→sp^3 transformation in individual MWCNT due to focus ion beam irradiation (FIB). The results indicated that curvatures and bandings in MWCNT may play a positive role in delaying the spread of structural damage in MWCNT.

7.2 Original contributions of this thesis

Based on the specific experimental observations, results and conclusions, the major original contributions of this thesis are:

- Quantitative measurements of the XLD in SWCNT bundles and individual MWCNT.

- Proposing a recipe to use the XLD to quantitatively evaluate the structural quality of CNT from various sources and to determine the structural changes occurring in CNT due to chemical and physical treatments.

- Proposing a method to use STXM together with advanced statistical methods to map

chemical components in CNT.

- Proposing a method based on the displacement of the scattering pattern over the EELS entrance aperture to produce highly resolved **q.**

- Obtaining similar dichroic signal by TEM-EELS as STXM.

- Using TEM-EELS to map defects close to atomic scale in pristine and FIB damaged MWCNT.

7.3 Future work

7.3.1 Assignment of NEXAFS transitions by quantum calculations

CNT have rich NEXAFS spectra which provide detail of information about their electronic, chemical, and physical states. However, to be able to use these spectra to fully characterize CNT, one must accurately identify the transitions and understand their implications. In principle, quantum calculations can expand our knowledge about CNT; they can help us understand why the polarization at the C $1s \rightarrow \sigma^*$ transition is very subtle or how defects can alter the dichroic response of CNT. I began the use of GSCF3 (Gaussian self-consistent field version 3) and ADF (Amsterdam density functional) programs to calculate the NEXAFS spectra of various SWCNT models. However, the results were far from what I have observed from STXM experiments. To help the calculated spectra converge to those obtained by experiments, a possible approach that I propose is to use programs that include the electronic band structure of CNT into calculations. This would provide a more accurate picture about CNT while reducing processing time.

Atomic defects break the local symmetry in CNT and alter their NEXAFS spectra. STXM and TEM-EELS measurements cannot characterize such small defects due to their limited spatial resolution. To investigate how the NEXAFS spectra of defects deviate from those of CNT, quantum calculations are required. My attempts to use GSCF3 to study defects have failed. I believe using programs that considers the band structure of CNT in the calculations will enable such studies.

7.3.2 NEXAFS spectroscopy of semiconducting and metallic SWCNT

Synthesized batches of SWCNT are mixtures of semiconducting and conducting tubes. Thus, to be able to use SWCNT for electronic applications such as electron transfer channels in electronic devices, one has to devise a method that can determine their electronic conductivity. Previously, Kramberger et al. [KRS&07] attributed the fine structure that they observed in the C 1s $\rightarrow \pi^*$ peak to transitions to vHS of the DOS of SWCNT; vHS reflect the electronic conductivity of SWCNT. Since Kramberger et al. used a powder sample which contained a variety of chiralities, they could not interpret this fine structure in detail. It would be a breakthrough in SWCNT technology to be able to use this fine structure to determine the electronic conductivity of SWCNT. There are several commercial and academic sources that provide SWCNT samples with single chirality for which one can obtain NEXAFS spectra at high energy resolution which is achievable at both ALS 5.3.2.2 and CLS 10ID-1 beamlines. When recorded spectra for semiconducting and metallic SWCNT are compared, one can assign the transitions in the fine structure and use them to predict the conductivity of unknown SWCNT. Using such information, SXTM will be able to map conducting and semiconducting portions of

SWCNT bundles. With advances in ZP technology, maybe someday STXM can determine the electronic character of isolated SWCNT too.

7.3.3 High resolution TEM-EELS measurements

My TEM-EELS measurements could successfully produce ELD signals that mimic those of the X-ray absorption linear dichroism. I used these signals to map defects along CNT. However, due to time limitations, image sequences were recorded using coarse pixels and at only five tilt angles. In order to improve the quality of the defect map, I propose using much finer pixels (preferably at sub-nanometer scales), more tilt angles and longer exposures. After the microscope is fully optimized, such measurements would not take more than a few hours.

7.3.4 Studies of structural order in other nano-materials

The technique developed to measure the structural order in CNT can be used to study other anisotropic systems such as nano-wires and nano-ribbons too. In collaboration with Dr. Carla Bittencourt et al. from University of Antwerp, we have used the STXM at the beamline 10ID1 at the CLS to measure the XLD in TiOx nano-ribbons at the O 1s edge (**Figure 7.1**). The aim of this study is to evaluate the anisotropic structure of the system. As a future work, I recommend to obtain high resolution STXM images at resonance energies that show dichroic effect to map out the orientation of the crystals. This, however, requires a theoretical study to identify the transition. This study would help optimizing the synthesis of the nano-ribbons.
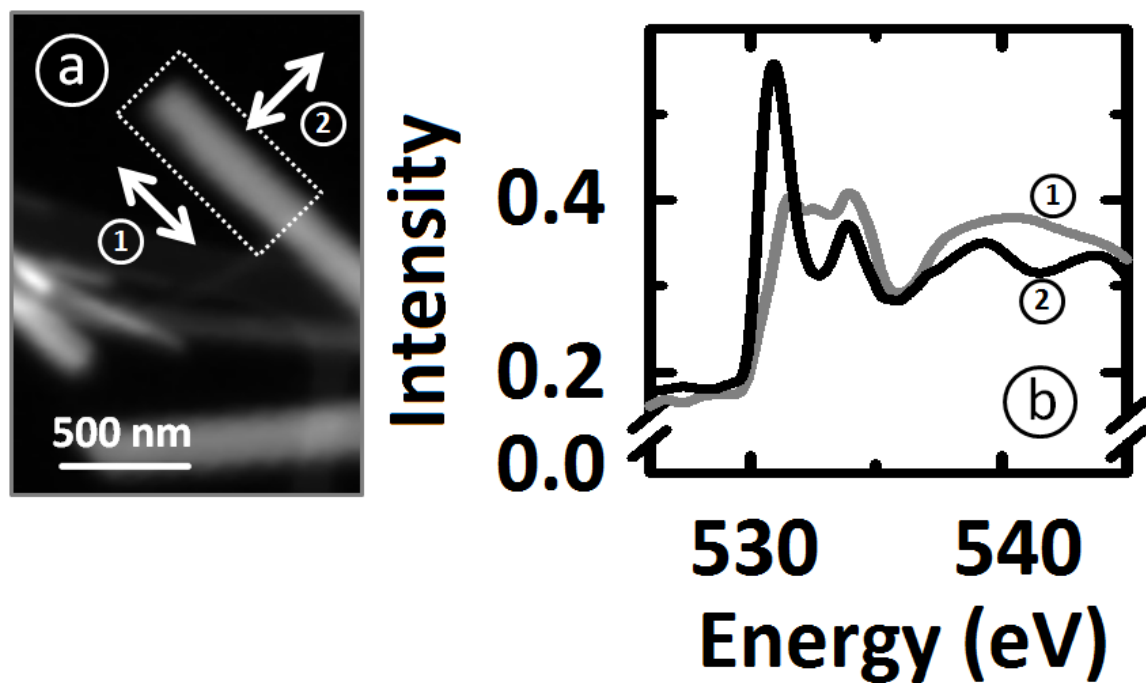
Figure 7.2 (a) STXM image of TiOx nano-ribbons. (b) The NEXAFS spectra recorded at the O 1s edge and extracted from the highlighted rectangle; the polarization of the incident X-rays was set to -45° (1) and +45° (2) to make **E** parallel and perpendicular to the nano-ribbons, respectively.

References

The reference code is formulated from the first letter of the last name of the first three authors, followed by the year of publication. If a reference has more than three authors, the initials are followed by an ampersand. If two references have the same author-year code, a sequence letter is added after the year for each publication.

[A99] D. Attwood, Soft X-rays and Extreme Ultraviolet Radiation: Principles and Applications, Cambridge University Press, Cambridge, **1999**.

[AH08] H. Ade, A. P. Hitchcock, *Polymer 49* (**2008**) 643.

[AII93] P.M. Ajayan, T. Ichihashi, S. Iijima, *Chem. Phys. Lett.* 202 (**1993**) 384.

[APL&00] K. D. Ausman, R. Piner, O. Lourie, R. S. Ruoff, M. Korobov, *J. Phys. Chem. B* 104 (**2000**) 8911.

[B01] R. Brydson, *Electron energy loss spectroscopy* Royal Microscopical Society, **2001**.

[B93] Dawn A. Bonnell, Scanning tunneling microscopy and spectroscopy : theory, techniques, and applications, John Wiley & Sons Inc. **1993**.

[B98a] D. Briggs, *Surface Analysis of Polymers by XPS and static SIMS*, Cambridge University Press, New York, **1998**.

[B98b] J. P. Blewett, *J. Synch. Rad.* 5 (**1998**) 135.

[BBS95] A. Botton, C. D. Boothroyd, W. M. Stobbs, *Ultramicroscopy* 59 (**1995**) 93.

[BE05] T. Belin, F. Epron, *Mater. Sci. Eng. B* 119 (**2005**) 105.

[BHB04] S. Banerjee, T. Hemraj-Benny, M. Balasubramanian, D. A. Fischer, J. A. Misewich, S. S. Wong, *ChemPhysChem* 5 (**2004**) 1416.

[BLM99] P. J. Boul, J. Liu, E. T. Mickelson, C. B. Huffman, L. Ericson, I. W. Chiang, K. A. Smith, D. T. Colbert, R. H. Hauge, J. L. Margrave, R. E. Smalley, *Chem. Phys. Lett.* 310 (**1999**) 367.

[BMB&02] J. L. Bahr, E. T. Mickelson, M. J. Bronikowski, R. E. Smalley, J. M. Tour, *Chem. Commun. 2* (**2001**) 193.

[BRA&89] C. Buckley, H. Rarback, R. Alforque, D. Shu, H. Ade, S. Hellman, N. Iskander, J. Kirz, S. Lindaas, I. Mcnulty, M. Oversluizen, E. Tang, D. Attwood, R. DiGennaro, M. Howells, C. Jacobsen, Y. Vladimirsky, S. Rothman, D. Kern, D. Sayre *Rev. Sci. Inst.* 60 7 (**1998**) 2444.

[BRW97] S. Bandow, A. M. Rao, K. A. Williams, A. Thess, R. E. Smalley, P. C. Eklund, *J. Phys. Chem. B* 101 (**1997**) 8839.

[BS&06] P. W. Barone, M. S. Strano, Angew. *Chem. Int. Ed.* 45 (**2006**) 8138.

[BSS97] J. M. Bonard, T. Stora, J. P. Salvetat, F. Maier, T. Stockli, C. Duschl, L. Forro, W. A. de Heer, A. Chatelain, *Adv. Mater.* 9 (**1997**) 827.

[BT01] J. L. Bahr, J. L. Tour, *Chem. Mater.* 13 (**2001**) 3823.

[BYB91] N. D. Browning, J. Yuan, L. M. Brown, *Ultramicroscopy* 38 (**1991**) 291.

[BYK&01] J. L. Bahr, J. Yang, D. V. Kosynkin, M. J. Bronikowski, R. E. Smalley, J. M. Tour, *J. Am. Chem. Soc*. 123 (**2001**) 6536.

[C73] K. Codling, *Rep. Prog. Phy.* 36 (**1973**) 541.

[CBH&01] I. W. Chiang, B. E. Brinson, A. Y. Huang, P. A. Willis, M. J. Bronikowski, J. L. Margrave, R. E. Smalley, R. E. Hauge, *J. Phys. Chem.* B 105 (**2001**) 8297.

[CHF&98] J. Chen, R. C. Haddon, S. Fang, A. M. Rao, P. C. Eklund, W. H. Lee, E. C.

Dickey, E. A. Grulke, J. C. Pendergrass, A. Chavan, B. E. Haley, R. E. Smalley, *J. Mater. Res.* 13 (**1998**) 2423.

[CHH&98] J. Chen, M. A. Hamon, H. Hu, Y. Chen, A. M. Rao, P. C. Eklund, R. C. Haddon, *Science* 282 (**1998**) 95.

[CHS&03] E. Couteau, K. Hernadi, J. W. Seo, L. Thiên-Nga, C. Mikó, R. Gaál, L. Forró, *Chem. Phys. Lett.* 378 (**2003**) 9.

[CL04] C. W. Chen, M. H. Lee, *Nanotech.* 15 (**2008**) 480.

[CM93] J. C. Charlier, J. P. Michenaud, *Phys. Rev. Lett.* 70 (**1993**) 1858.

[CUA02] T. Coffey, S.G. Urquhart, H. Ade, *J. of Elect. Spectroscopy and Rel. Phen* 122 (**2002**) 65.

[CWS99] P. Chen, X. Wu, X. Sun, J. Lin, W. Ji, K. Tan, *Phys. Rev. Lett.*, 82 (**1999**) 2584.

[CZW01] R. J. Chen, Y. Zhang, D. Wang, H. Dai, *J. Am. Chem. Soc.* 123 (**2001**) 3838.

[DBM&98] G. S. Duesberg, M. Burghard, J. Muster, G. Philipp, S. Roth, *Chem. Commun.* 435 (**1998**) 19.

[DDE96] M. S. Dresselhaus, G. Dressehhaus, P. C. Eklund, Science of Fullerene and Carbon Nanotubes, Academic Press, San Diego, **1996**.

[DDS95] M. S. Dresselhaus, G. Dressehhaus, R. Saito, *Carbon* 33 (**1995**) 883.

[DDS&05] M.S. Dresselhaus, G. Dresselhaus, R. Saito, A. Jorio, *Phys. Rep.* 409 (**2005**) 47.

[DHC02] R. Droppa, P. Hammer, A. Carvalho, M. Dos Santos, F. Alvarez, *J. Non-Cryst. Solids* 299-302 (**2002**) 874.

[DKP&08] V. Datsyuk, M. Kalyva, K. Papagelis, J. Parthenios, D. Tasis, A. Siokou, I. Kallitsis, C. Galiotis, *Carbon* 46 (**2008**) 833.

[DTA&06] J. J. Dynes, T. Tyliszczak, T. Araki, J. R. Lawrence, G. D. W. Swerhone, G. G. Leppard, *Environ. Sci. Technol. 40* (**2006**) 1556.

[E96] R. F. Egerton, Electron Energy Loss Spectroscopy in the Electron Microscope Springer, Berlin, **1996**.

[EA&92] T. W. Ebbesen, P. M. Ajayan, *Nature* 358 (**1992**) 220.

[EAH&94] T.W. Ebbesen, P. M. Ajayan, H. Hiura, K. Tanigaki, *Nature* 367 (**1994**) 519.

[EHB&96] T. W. Ebbesen, H. Hiura, M. E. Bisher, M. M. J. Treacy, J. L. Shreeve-Keyer, R. C. Haushalter, *Adv. Mater.* 8 **(1996)** 155.

[EHF&93] T. W. Ebbesen, H. Hiura, J. Fujita, Y. Ochiai, S. Matsui, K. Tanigaki, *Chem. Phys. Lett.* 209 (**1993**) 83.

[ERJ&06] C. Ehli, G. M. A. Jux, D. Balbinot, D. M. Guldi, F. Paolucci, M. Marcaccio, D. Paolucci, M. Melle-Franco, F. Zerbetto, S. Campidelli, M. Prato, *J. Am. Chem. Soc.* 128 (**2006**) 11222.

[ET95] T. W. Ebbesen, T. Takada, *Carbon* 33 (**1995**) 973.

[FBP&07] A.Felten, C. Bittencourt, J.-J. Pireaux, M. Reichelt, J. Mayer, D. Herna´ndez-Cruz, A. P. Hitchcock, *Nano Lett.*7 (**2007**) 2435.

[FCF&99] S. Fan, M. Chapline, N. R. Franklin, T. W. Tombler, A. M. Cassell, H. Dai, *Science 283 (***1999)** 512.

[FHB&06] A. Felten, H. Hody, C. Bittencourt, J.-J. Pireaux, D. Hernandez-Cruz, A.P Hitchcock, *Appl. Phys. Lett.*80 (**2006**) 093123, 1.

[GH11] A. A. Green, M. C. Hersam, *Adv. Mater.* 23 19 (**2011**) 2185.

[GI&00] A. Gloter, J. Ingrin, D. Bouchet, C. Colliex, *Phys. Rev. B* 61 (**2000**) 2587.

[GKP&02] V. Georgakilas, K. Kordatos, M. Prato, D. M. Guldi, M. Holzinger, A. Hirsch, *J. Am. Chem. Soc.* 124 (**2002**) 760.

[GNR&95] T. Guo, P. Nikolaev, A. G. Rinzler, D. Tomanek, D. T. Colbert, R. E. Smalley, *J. Phys. Chem.* 99 (**1995**) 10694.

[GNT&95] T. Guo, P. Nikolaev, A. Thess, D. T. Colbert, R. E. Smalley, *Chem. Phys. Lett.* 243 (**1995**) 49.

[GRJ&04] D. M. Guldi, G. M. Rahman, N. Jux, N. Tagmatarchis, M. Prato, *Angew. Chem. Int. Ed.* 43 (**2004**) 5526.

[GRZ&05] D. M. Guldi, G. M. Rahman, F. Zerbetto, M. Prato, *Acc. Chem. Res.* 38 (**2005**) 871.

[GWA&09] B. Gao, Z. Wu, H. Agren, Y. Luo, *J. Chem. Phys.* 131(**2009**) 034704.

[H02] A. P. Hitchcock, *Jpn. J. Appl. Phys.* 32 (suppl. 2) (**1992**) 176.

[H04] A . Hofmann, *The Physics of Synchrotron Radiation*, Camberidge University Press New York, **2004**.

[H08] M. C. Hersam, *Nature Nanotech.* 3 (**2008**) 387.

[H77] J. H. Hubbell, W. J. Veigele, E. A. Briggs, R. T. Brown, D. T. Cromer, R. J. Howerton, *J. Phys. Chem. Ref. Data* 4 (**1975**) 471.

[H79] J. H. Hubbell, *J. Phys. Chem. Ref. Data* 8 (**1979**) 69.

[H82] J. H. Hubbell, *Int. J. Appl. Rad. Isotopes* 33 (**1982**)1269.

[H93] R. C. Haddon, *Science* 261 (**1993**) 1545.

[HAI&03] A. P. Hitchcock, T. Araki, H. Ikeura-Sekiguchi, N. Iwata, K. Tani, *J. Phys. IV 104* (**2003**), 509.

[HBS&06] T. Hemraj-Benny, S. Banerjee, S. Sambasivan, M. Balasubramanian, D. A. Fischer, G. Eres, A. A. Puretzky, D. B. Geohegan, D. H. Lowndes, W. Han, J. A. Misewich, S. S. Wong, *Small* 2 (**2002**) 26.

[HCB&02] M. A. Hamon, J. Chen, P. Bhowmik, M. E. Itkis, R. C. Haddon, *Appl. Phys. A.* 74 (**2002**) 333.

[HCH&99] M. A. Hamon, J. Chen, H. Hu, A. M. Rao, P. C. Eklund, R. C. Haddon, *Adv. Mater.* 11 (**1999**) 834.

[HDJ&08] A. P. Hitchcock, J. J. Dynes, G. A. Johansson, J. Wang, G. Botton, G., *Micron* 39 (**2008**) 741.

[HET95] H. Hiura, T. W. Ebbesen, K. Tanigaki, *Adv. Mater.* 7 (**1995**) 275.

[HGD93] B. L. Henke, E. M. Gullikson, J. C. Davis, *At. Data Nucl. Data Tables 54* (**1993**), 181.

[HS03] C. Hébert, P. Schattschneider, *Ultramicroscopy* 96 (**2003**) 463.

[HSO92] N. Hamada, S. Sawada, A. Oshiyama, *Phys. Rev. B* 58 (**1998**) R4266.

[HSY08] X. Hu, Y. Sun, J. Yuan, *Ultramicroscopy* 108 (**2008**) 465.

[HTS&02] T. Hayashi, M. Terrones, C. Scheu, Y. A. Kim, M. Rühle, T. Nakajima, M. Endo, *Nano Lett.* 2 (**2002**) 491.

[HVH&01] M. Holzinger, O. Vostrowsky, A. Hirsch, F. Hennrich, M. Kappes, R. Weiss, F. Jellen, *Angew. Chem. Int. Ed.* 40 (**2001**) 4002.

[IOU&94] F. Ikazaki, S. Ohshima, K. Uchida, Y. Kuriki, H. Hayakawa, M. Yumura, K.

Takahashi, K. Tojima, *Carbon* 32 (**1994**) 1539.

[JWF&00] C. Jacobsen, S. Wirick, G. Flynn, C. J. Zimba, *Microscopy* 197 (**2000**) 173.

[KEA&98] C. Kiang, M. Endo, P. Ajayan, G. Dresselhaus, *Phys. Rev. Lett.* 81 (**1998**) 1869.

[KHO&03] Y. A. Kim, T. Hayashi, K. Osawa, M. S. Dresselhaus, M. Endo, *Chem. Phys. Lett.* 380 (**2003**) 319.

[KKL&07] K.V. Kaznatcheev, C. Karunakaran, U.D. Lanke, S.G. Urquhart, M. Obst, A.P. Hitchcock *Nuclear Instruments and Methods in Physics Research Section A: Accelerators, Spectrometers, Detectors and Associated Equipment* 582, 1, (**2007**) 96.

[KR85] J. Kirz, H. Rarback, *Rev. Sci. Inst.* 56,1 (**1985**) 1.

[KRS&07] C. Kramberger, H. Rauf, H. Shiozawa, M. Knupfer, B. Buchner, T. Pichler, *Phys. Rev. B* 75 (**2007**) 235437.

[KPY&01] A. Kuznetsova, I. Popova, J. T. Yates, M. J. Bronikowski, C. B. Huffman, J. Liu, R. E. Smalley, H. H. Hwu, J. G. Chen, *J. Am. Chem. Soc.* 123 (**2001**) 10699.

[KTS&03] A. L. D. Kilcoyne, T. Tyliszczak, W. F. Steele, S. Fakra, P. Hitchcock, K. Franck, E. Anderson, B. Harteneck, E. G. Rightor, G. E. Mitchell, A. P. Hitchcock, L. Yang, T. Warwick, H. Ade, *J. Synchrotron Rad.* 10 (**2003**)125.

[LCL&03] Y. Lee, T. Cho, B. Lee, J. Rho, K. An, Y. Lee, *J. Fluorine Chem.* 120 (**2003**) 99.

[LFS&83] R. D. Leapman, P. L. Fejes, J. Silcox, *Phys. Rev. B* 28 (**1983**) 2361.

[LHB&03] Y. Lin, D. E. Hill, J. Bentley, L. F. Allard, Y. P. Sun, *J. Phys. Chem.* 107 (**2003**) 10453.

[LHB&03a] Y. Lin, D. Hill, J. Bentley, L. Allard, Y. P. Sun, *Microsc. Microanal.* 9 (**2003**) 9 (Suppl 2): 352.

[LRD&98] J. Liu, A. G. Rinzler, H. Dai, J. H. Hafner, R. K. Bradley, P. J. Boul, A. Lu, T. Iverson, K. Shelimov, C. B. Huffman, F. Rodriguez-Macias, Y. S. Shon, T. R. Lee, D. T. Colbert, R. E. Smalley, *Science* 280 (**1998**) 1253.

[LTY&04] R. G. Lacerda, A. S. Teh, M. H. Yang, K. B. K. Teo, N. L. Rupesinghe, S. H. Dalal, K. Koziol, D. Roy, G. A. Amaratunga, W. I. J. Milne, M. Chhowalla, D. G. Hasko, *Appl. Phys. Lett.* 84 (**2004**) 269.

[MBA&99] I. Musa, M. Baxendale, G. A. J. Amaratunga, W. Eccleston, *Synthetic Metals* 102 (**1999**) 1250.

[MCZ&99] E. T. Mickelson, I. W. Chiang, J. L. Zimmerman, P. J. Boul, J. Lozano, J. Liu, R. E. Smalley, R. H. Hauge, J. L. Margrave, *J. Phys. Chem. B.* 103 (**1999**) 4318.

[MDW92] J. Mintmire, B. Dunlap, C. White, *Phys. Rev. Lett.* 68 (**1992**) 631.

[MHR&98] E. T. Mickelson, C. B. Huffman, A. G. Rinzler, R. E. Smalley, R. H. Hauge, J. L. Margrave, *Chem. Phys. Lett.* 296 (**1998**) 188.

[MK08] Moonoosawmy, K. R.; Kruse, P. *J. Am. Chem. Soc.* **2008**, 130 , 13417.

[MSB&01] M. Monthioux, B. W. Smith, B. Burteaux, A. Claye, J. E. Fischer, D. E. Luzzi, *Carbon* 39 (**2001**) 1251.

[NBB&99] P. Nikiloev, M. J. Bronikowski , R. K. Bradley, F. Rohmund, D. T. Colbert, K. A. Smith, R. E. Smalley, *Chem. Phys. Lett.* 313 (**1999**) 91.

[NDO&08] E. Najafi, D. Hernández Cruz, M. Obst, A. P. Hitchcock, B. Douhard, J. J. Pireaux, A. Felten, *Small* 4,12 (**2008**) 2279.

[NKH&05] E. Najafi, J. Kim, S. H. Han, K. Shin, *Colloids Surf. A* (**2005)** 333.

[OBH03] M. J. O'connell, S. M. Bachilo, C. B. Huffman, V. C. Moore, M. S. Strano, E. H. Haroz, K. L. Rialon, P. J. Boul, W. H. Noon, C. Kittrell, J. Ma, R. H. Hauge, R. B. Weisman, R. E. Smalley, *Science* 297 (**2003**) 503.

[P99] M. J. Pelletier, *Analytical Applications of Raman Spectroscopy*, Blackwell Science Ltd., London, **1999**.

[PFO&04] M. Pereira, J. Figueiredo, J. Orfao, P. Serp, P. Kalck, Y. Kihn, *Carbon* 42 (**2004**) 2807.

[PL06] Y. Peng, H. Liu, *Ind. Eng. Chem. Res. 45* (**2006**) 6483.

[PSJ&01] S. Pekker, J. P. Salvetat, E. Jakab, J. M. Bonard, L. Forro, *J. Phys. Chem. B* 105 (**2001**) 7938.

[PTY&01] H. Postma, T. Teepen, Z. Yao, M. Grifoni, C. Dekker, *Science* 293 (**2001**) 76.

[R68] W. N. Reynolds, *Physical properties of graphite*, Elsevier Pub. Co., Amsterdam , **1968**.

[RBV06]

[RON&95] D. Reznik, C. H. Olk, D. A. Neumann, J. R. D. Copley, *Phys. Rev. B*, 52 (**1995**) 116.

[RS02] B. W. Reed, M. Sarikaya, *J. Elec. Microsc.*, 51 (**2002)** S97.

[RSF&88] H. Rarback, D. Shu, S. C. Feng, H. Ade, J. Kirz, I. McNulty, D. P. Kern, T. H. P. Chang, Y. Vladimirsky, N. Iskander, D. Attwood, K. McQuaid, S. Rothman, S. *Rev. Sci. Inst. 59, 1* (**1988***) 52.*

[S92] J. Stöhr, *NEXAFS Spectroscopy*, Series in Surface Science Vol. 25, Springer,

Berlin, **1992**.

[SAC96] O. Ste´phan, P. M. Ajayan, C. Colliex, F. Cyrot-Lackmann, E. Sandre´, *Phys. Rev. B* 53 (**1996**) 13824.

[SDD93] R. Saito, G. Dresselhaus, M. Dresselhaus, *J. Appl. Phys.* 73 (**1993**) 494.

[SER&98] K. B. Shelmov, R. O. Esenaliev, A. G. Rinzler, C. B. Huffman, R. E. Smalley, *J. Chem. Phys. Lett.* 282 (**1998**) 429.

[SFD&92] R. Saito, M. Fujita, G. Dresselhaus, M. Dresselhaus, *Appl. Phys. Lett.* 60 (**1992**) 2204.

[SKH&01] Y. P. Sun, K. Fu, Y. Lin, W. Huang *Acc. Chem. Res.35, 12* (2002) 1096.

[SKR&03] J. Schiessling, L. Kjeldgaard, F. Rohmund, L. K. L. Falk, E. E. B. Campbell, J. Nordgren, P. A. Bruhwiler, *J. Phys.: Condens. Matter* 15 (**2003**) 6563.

[SLG&03] A. Star, Y. Liu, K. Grant, L. Ridvan, J. F. Stoddart, D. W. Steuerman, M. R. Diehl, A. Boukai, J. R. Heath, *Macromolecules* 36 (**2003**) 553.

[SMT&02] R. Saito, K. Matsushige, K. Tanaka, *Phys. B: Condens. Matter* 323 (**2002**) 280.

[SNK&96] Y. Saito, K. Nishikubo, K. Kawabata, T. Matsumoto, *J. Appl. Phys.* 80 (**1996**) 3062.

[SNB&06] J.M. Simmons, B.M. Nichols, S.E. Baker, Matthew S. Marcus, O.M. Castellini, C.-S. Lee, R.J. Hamers, M.A. Eriksson, *J. Phys. Chem. B* 110 (**2006**) 7113.

[SNT06] K. Saitoh, K. Nagasaka, N. Tanaka *J. Elec. Micros.* 55 (**2006**) 281.

[SPA&98] J. Stohr, H. A. Padmore, S. Anders, T. Stammler, M. R. Scheinfein, *Surf. Rev. Lett.* 5, 6 (**1998**) 1297.

[SRN&80] G. Schmahl, D. Rudolph, B. Niemann, O. Christ *Ultrasoft X-Ray Microscopy: Its Application to Biological and Physical Sciences* 342 (**1980**) 1.

[SSH&02] A. Star, D. W. Steuerman, J. R. Heath, J. F. Stoddart, *Angew. Chem. Int. Ed.* 41 (**2002**) 2508.

[SSN&02] D. W. Steuerman, A. Star, R. Narizaano, H. Choi, R. S. Ries, C. Nicolini, J. F. Stoddart, J.R. Heath, *J. Phys. Chem. B* 106 (**2002**) 3124.

[SSS&01] A. Star, J. F. Stoddart, D. Steuerman, M. Diehl, A. Boukai, E. W. Wang, X. Yang, S. W. Chung, H. Choi, J. R. Heath, *Angew. Chem. Int. Ed.* 40 (**2001**) 1721.

[SY05a] Y. Sun, J. Yuan, *Mats. Sci. Forum* 475-479 (**2005**) 4085.

[SY05b] Y. Sun, J. Yuan, *Phys. Rev. B* 71 (**2005**) 1251091.

[SY&06] V. Shanov, Y. Yeo-Heung Yun, *J. Univ. Chem. Technol. Metallurgy* 41 (**2006**) 377.

[TAA&97] K. Tanaka, H. Aoki, H. Ago, T. Yamabe, K, Okahara, *Carbon* 35 (**1997**) 125.

[TCA&01] K. B. K. Teo, M. Chhowalla, G. A. J. Amaratunga, W. I. Milne, D. G. Hasko, G. Pirio, P. Legagneux, F. Wyczisk, D. Pribat, *Appl. Phys. Lett.* 79 (**2001**) 1534.

[TFP&94] G. H. Taylor, J. D. Fitzgerald, L. Pang, M. A. Wilson, *J. Cryst. Growth* 135 (**1994**) 157.

[TGT&96] K. Tohji, T. Goto, H. Takahashi, Y. Shinoda, N. Shimizu, B. Jeyadevan, I. Matsuoka, Y. Saito, A. Kasuya, T. Ohsuna, H. Hiraga, Y. Nishina, *Nature* 383 (**1996**) 679.

[TTS97] K. Tohji, H. Takahashi, Y. Shinoda, N. Shimizu, B. Jeyadevan, I. Matsuoka, Y. Saito, A. Kasuya, S. Ito, Y. Nishina, *J. Phys. Chem. B.* 101 (**1997**) 1974.

[T99] P C Tiemeijer, *Inst. Phys. Conf. Ser.* 161, 5 (**1999**) 191.

[W08] J. Wang, *Radiation Chemistry by Soft X-ray Spectromicroscopy*, McMaster University, **2008**.

[WA08] Watts, B.; Ade, H.; *J. Electron Spectrosc. Relat. Phenom.* 162 (**2008**), 49.

[WAK&02] T. Warwick, H. Ade, D. Kilcoyne, M. Kritscher, T. Tylisczcak, S. Fakra, A. Hitchcock, P. Hitchcock, *J. Synchrotron Rad.* (**2002**). **9**, 254-257

[WBT04] R. B. Weisman, S. M. Bachilo, D. Tsyboulski, *Appl. Phys. A* 78 (**2004**) 1111.

[WC09] D. B. Williams, C. B. Carter *Transmission Electron Microscopy*, Springer, New York, **2009**.

[WLW&08] S. Wang, R. Liang, B. Wang, Ch. Zhang, *Chem. Phys. Lett.457 (***2008**) 371.

[WPA08] A. Warwick, H. A. Padmore, H. Ade, *Proc. SPIE* 12 (**1998**) 3449.

[WYS08] E. Wenbing, W. Yun, G. Schneider, *Appl Phys A: Mater. Sci. & Process.* (**2008**) 92, 3.

[WZL&04] S. Wang, W. Zhu, D. Liao, C. Ng, C. Au, *Catal. Today* 93-95 (**2004**) 711.

[YYR&93] M. J. Yacaman, M. M. Yoshida, L. Rendon, J. G. Santiesteban, *Appl. Phys. Lett.* 62 (**1993**) 202.

[ZOW&97] X. Zhao, M. Ohkohchi, M. Wang, S. Ijima, T. Ichihashi, Y. Ando, *Carbon* 35 (**1997**) 775.

[ZXV02] N. Zhang, J. Xie, V. K. Varadan, *Smart Mater. Struct.* 11 (**2002**) 962.

[ZGR&08] E. Zschech, H. Geisler, J. Rinderknecht, G. Schneider, R. Spolenak, D. Schmeisser, *Curr. Nanosci.* 4, 3, (**2008**), 256-266.

[ZZV&93] X. F. Zhang, X. B. Zhang, G. Van Tendeloo, S. Amelinckx, M. Op de Beek,

J. Van Landuyt, *J. Cryst. Growth*, 130 (**1993**) 368.

Appendix A

This appendix describes the electronic properties of metallic and semiconducting

SWCNT.

A.1 Electronic properties of SWCNT

SWCNT have diameters smaller than 10 nm, making the quantum effects in them rather significant. Due to their structural similarities, the electronic properties of graphite are used to explain those of the SWCNT. **Figure A.1** shows the Brillouin zone of graphite with the high symmetry points Γ, K, and M and the reciprocal unit vectors

$$\vec{k}_1 = \left(\frac{2\pi}{\sqrt{3}a_0}, \frac{2\pi}{a_0} \right) \text{ and } \vec{k}_2 = \left(\frac{2\pi}{\sqrt{3}a_0}, -\frac{2\pi}{a_0} \right) \text{ at } 120°$$
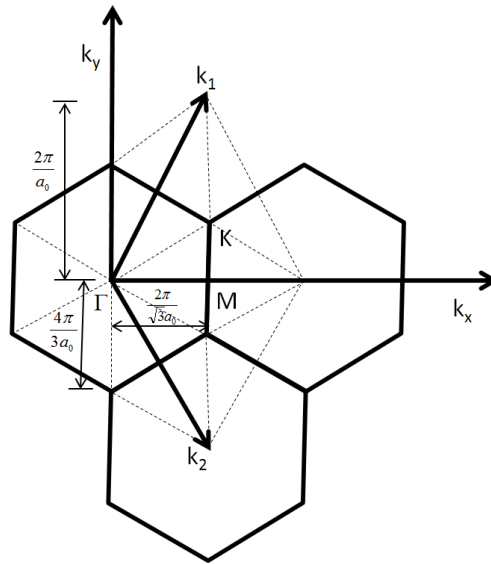

Figure A.1 Brillouin zone of graphene with the high symmetry points Γ, K, and M. k_1 and k_2 are the reciprocal unit vectors at an angle of 120 relative to each other (Adapted from [R68]) .

The unit cell in graphite has two carbon atoms and therefore three σ-bands and one π-band. The binding and antibonding π bands meet at the corner of the Brillouin zone (K); thus at zero Kelvin the bonding π-band is completely occupied and antibonding π-band is completely unoccupied. From tight binding calculations, the energy dispersion for the π electrons in graphite at a point defined by the wavevectors k_x, k_y is given by [R68]:

$$E_{2D}(k_x, k_y) = \pm\gamma_0 \left\{ 1 + 4\cos\left(\frac{\sqrt{3}k_x a}{2}\right)\cos\left(\frac{k_y a}{2}\right) + 4\cos^2\left(\frac{k_y a}{2}\right) \right\}^{1/2}$$

where γ_0 is the nearest-neighbor transfer integral, and a_0 is the in-plane lattice constant. Calculation of the electronic band structure of the 3D graphite shows ~40 meV overlap between the conduction and valence band, making graphite a semi-metal. The 3D diagram of the energy dispersion in 2D graphite is plotted in **Figure A.2**; the valence and conduction bands are degenerate at the *K*-point of the Brillouin zone.
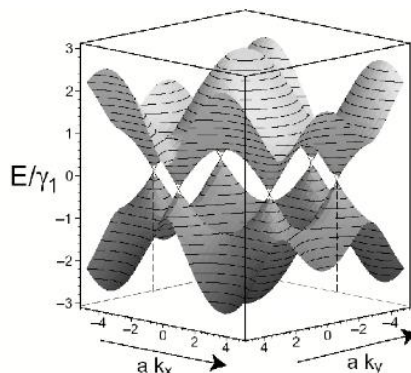

Figure A.2 3D representation of energy dispersion in 2D graphite (Adapted from [R68]).

In graphite, the calculation of the electronic band structure is based on the assumption that the planes are infinitely large. In the SWCNT, this assumption is not valid since the SWCNT are macroscopic along the Z-axis and in atomic scale along the circumference. Therefore, the allowed electronic modes for the wavevectors along the Z-axis (k_z) are large whereas they are quantized around the circumference ($k_\perp$). These wavevectors are determined by the following boundary conditions [DDS95]:

$$\vec{k}_z \cdot \vec{a} = 2\pi \qquad\qquad \vec{k}_z \cdot \vec{c} = 0$$

$$\vec{k}_\perp \cdot \vec{a} = 0 \qquad\qquad \vec{k}_\perp \cdot \vec{c} = 2\pi$$

The substitution results in:

$$\vec{k}_\perp = \frac{2n+m}{qn\Re} k_1 + \frac{n+2m}{qn\Re} k_2$$

$$\vec{k}_z = -\frac{n}{q} k_1 + \frac{m}{q} k_2$$

The Brillouin zone of the (7,7) armchair and (13,0) zigzag SWCNT are showed in **Figure A.3** for $l \in [-n, n]$. The line associated with l=0 passes through the Γ-point of the Brillouin zone; the position of the line associated with l=0 and l=n is the same for all zigzag and armchair SWCNT. The electronic properties of the SWCNT is approximated by cutting the two-dimensional band structure of graphite into q lines with length of $2\pi/a$ and distance of $2/d$ parallel to the direction of the SWCNT's axis. These lines correspond to the Brillouin zone of the SWCNT.
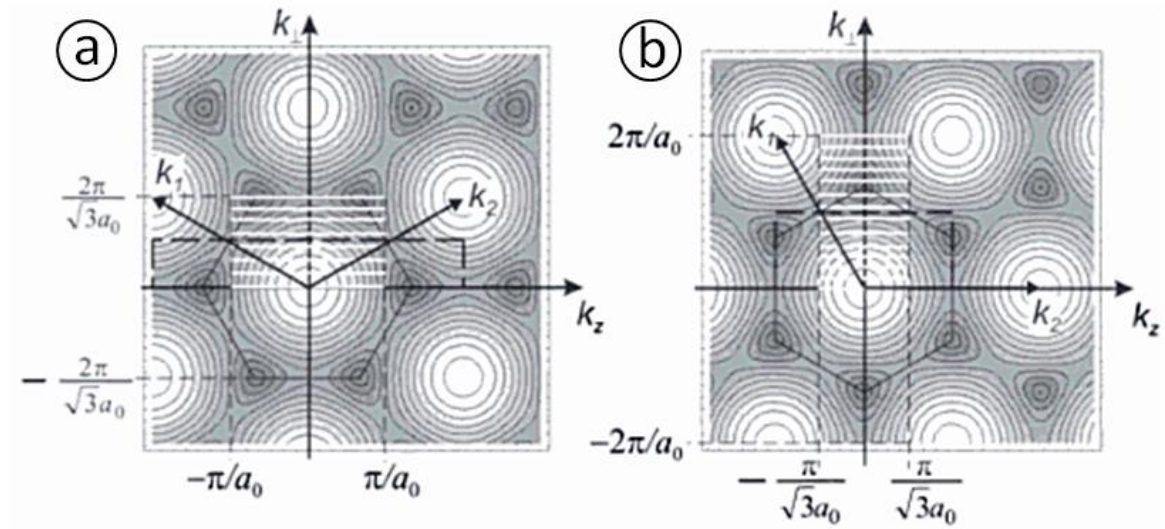
Figure A.3 Calculated Brillouin zone for a) (7,7) armchair and b) (13,0) armchair SWCNT. The contour plot is the band structure of the 2D graphite. The Brillouin zone in the right panel is rotated by 30°. The white lines are the allowed modes for the wavevector along the circumference [SFD&92].

In graphite, the valence and conduction bands are degenerate at the K-point of the Brillouin zone; therefore, if one of the lines include the K-point, the SWCNT becomes metallic. Otherwise, there will be a gap between these two bands and the SWCNT becomes semiconducting.

The energy dispersion relation and Brillouin zone of the (5,5) armchair, (9,0) zigzag and (9,10) zigzag SWCNT are illustrated in **Figure A.4** [DDE96]. For the (5,5) armchair SWCNT, there are five allowed modes for the wavevector around the circumference. Since one of the lines includes the K-point of the Brillouin zone, the SWCNT is metallic; in its corresponding band structure, the valence and conduction

206

bands meet at $\sim \left(\dfrac{2}{3}\right) k/k_{max}$ from the origin (0,0), giving the SWCNT its metallic

conductivity. Calculations indicate that all armchair SWCNT are methallic and have the

same band structure [SFD&92]. In the (9,0) zigzag SWCNT, there are nine allowed

modes for the wavevector, including a line passing through the K-point. The band

structure diagram shows that the valence and conduction bands cross at $k/k_{max} = 0$;

therefore, (9,0) SWCNT is metallic. Zigzag SWCNT are metallic only if n is divisible by

three. For Example, (10,0) SWCNT is semiconducting; none of the allowed lines passes

through the K-point and also in the band structure diagram there is a gap between the

valence and conduction bands. Likewise, chiral SWCNT can be metallic only if the

following relationship holds:

$$n - m = 3q$$

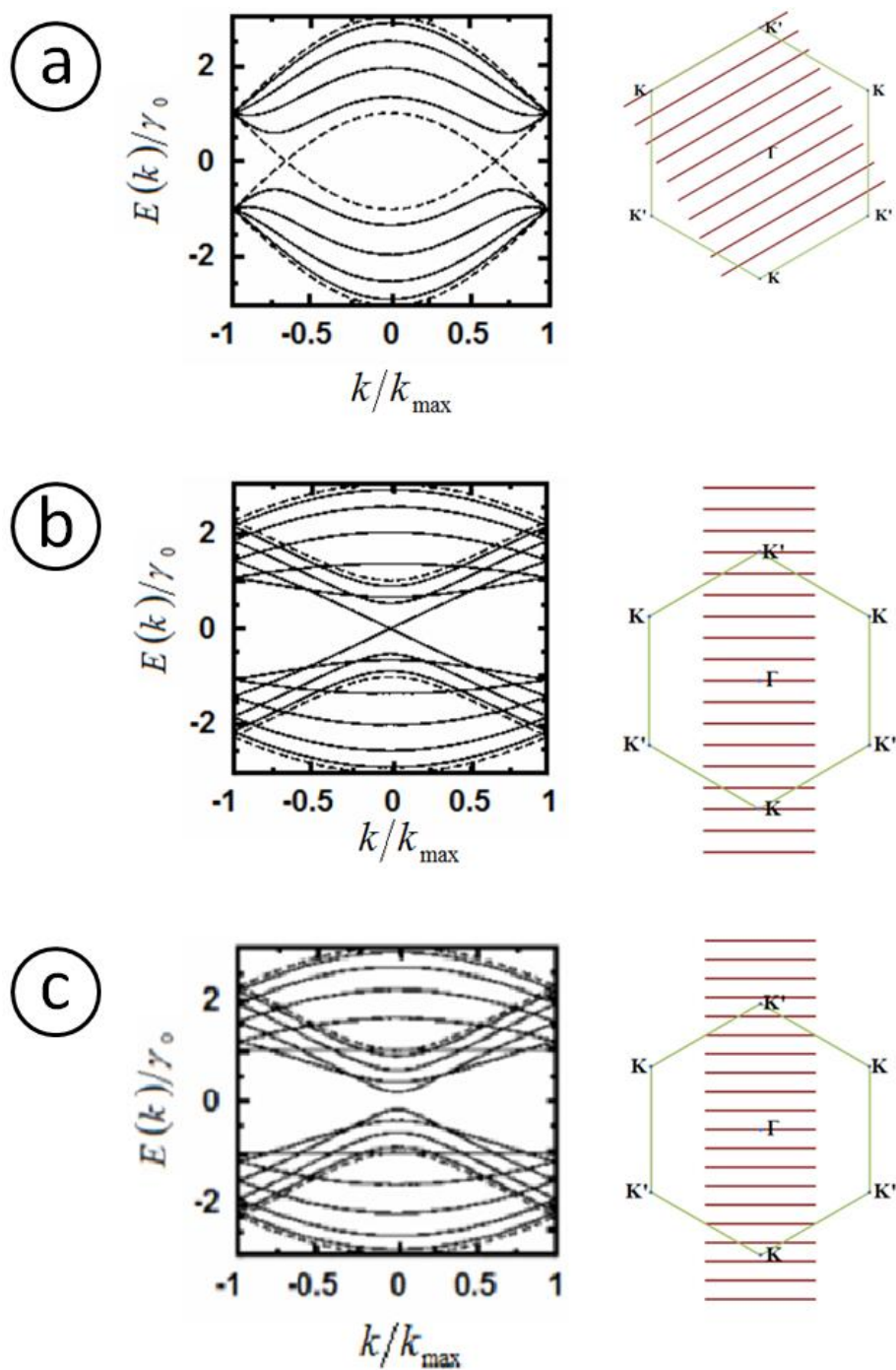where n and m are the SWCNT indices and q is an integer.

Figure A.4 Dispersion relation diagram and Brillouin zone for a) (5,5) armchair; b) (9,0)

zigzag; and c) (10,0) zigzag SWCNT (Adapted from [DDE96]).

Density of states (DOS) is the number of available states for an electron at a given energy range. High DOS for an energy level means that there are many available states for occupation whereas zero DOS means that there are no states to occupy. In 1D crystals such as SWCNT, the DOS is inversely proportional to the square root of energy and rapidly decays between maxima. These kinks in the DOS of 1D crystals are called van Hove singularities (vHS) and occur at the critical points of the Brillouin zone.

The DOS reflects the electronic properties of the SWCNT. The DOS for two zigzag (9,0) and (10,0) SWCNT calculated by Dresselhaus et al. [SFD&92] are plotted in **Figure A.5**. The plots show a finite DOS for the (9,0) metallic SWCNT and essentially zero for the semiconducting (10,0) SWCNT .
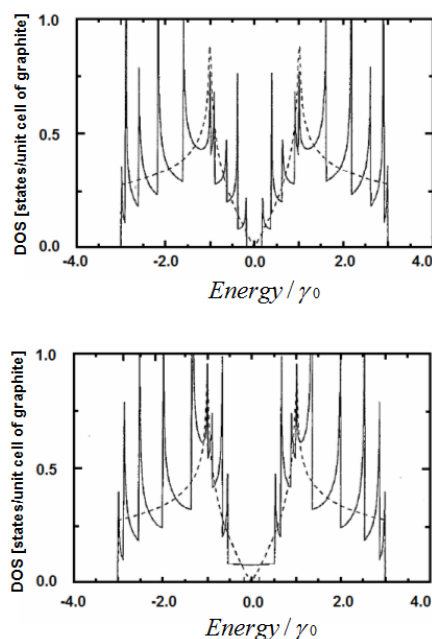

Figure A.5 The density of states for (a) (9,0) conducting SWCNT   and (b) (10,0) semiconducting SWCNT. The dotted line shows the density of states for 2D graphite. (Adapted from [SFD&92])

The electronic properties of MWCNT have been theoretically studied by various groups. Saito et al. [SDD93] suggested that interlayer coupling in the MWCNT is negligible and therefore their electronic properties depend on those of the SWCNT that make them. For instance, if two concentric zigzag SWCNT are metallic, the resulting MWCNT is metallic too. However, Charlier et al. [CM93] showed that the electronic properties of MWCNT also depend on the orientation of the concentric SWCNT such that for two different orientations, the resulting MWCNT can be metallic or semiconducting.

Appendix B

This appendix briefly describes the effects of carbon contamination of the spectromicroscopy beamline (10ID-1) optics at the Canadian Light Source (CLS) on the polarization of the X-rays.

B.1 Carbon contamination of optics

Carbon contamination of optics is a fairly well known issue which results in a dramatic reduction of the X-ray intensity especially in the region of the C 1s edge. While characterizing carbon nanotubes (CNT) by scanning transmission X-ray microscope (STXM) at the spectromicoscopy (SM) beamline at the CLS, I noticed that the polarization of the X-rays is also influenced by carbon contamination. This is probably due to preferential absorption of a specific linearly polarized component by partially oriented graphitic-like carbon layers which results in a partial linear polarization of those X-rays that are not absorbed.

Figure B.1 shows STXM images recorded for bundles of single walled carbon nanotubes (SWCNT) at the C 1s→π* transition at 285.1 eV with left (**Figure B.1a**) and right (**Figure B.1b**) circularly polarized X-rays. In principal, circularly polarized X-rays should remove any dichroic effect in CNT; thus, left and right circularly polarized X-rays should yield the same intensity. However, the comparison of the STXM images show that the optical density of identical regions changes by up to 50%. This indicates that the polarization of the X-rays has deviated from circular polarization to elliptical polarization. In fact, it is estimated that the long axis of the ellipse is roughly twice larger than its short

axis.

This experiment is a caution with respect to naively assuming perfect circular polarization in the C 1s region. It is possible that cleaning the optical surfaces of soft X-ray beamlines could recover the expected purely circularly polarized light at the C 1s edge.
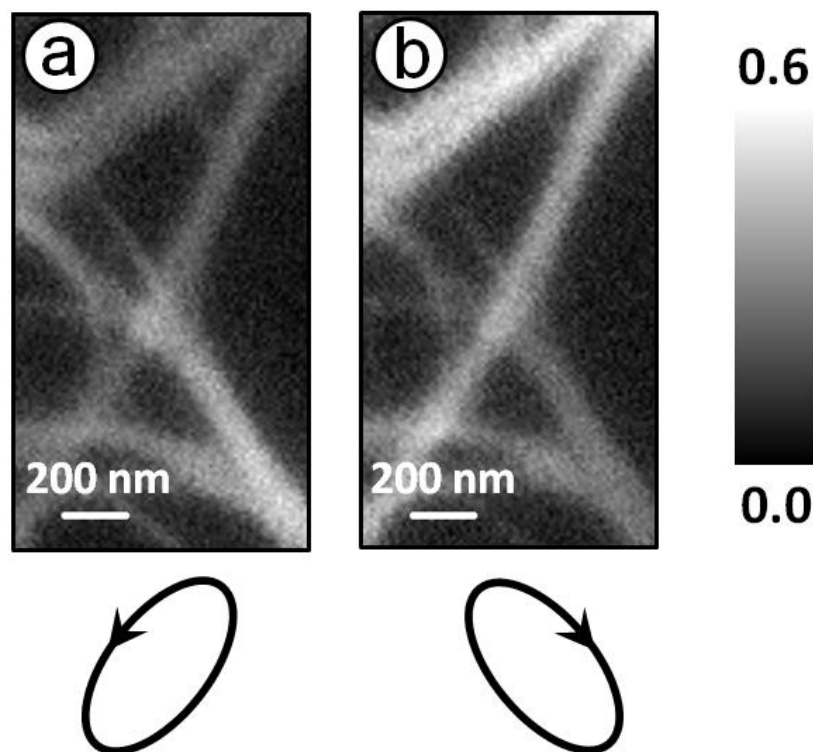

Figure B.1 The STXM images of SWCNT bundles recorded at the C 1s→π* transition at 285.1 eV with left (a) and right (b) circularly polarized X-rays. The illumination of the SWCNT suggests that the polarization of the X-rays has deviated from circular polarization to elliptical polarization.

Appendix C

This appendix lists all the software packages used in this thesis.

C. 1 *aXis2000*

Image, stack and spectral analysis were done by aXis2000; aXis2000 is a freeware program developed in Interactive Data Language (IDL) by Adam Hitchcock. This software is available for downloads at http://unicorn.mcmaster.ca/aXis2000.html.

C.2 *Digital Micrograph*

Digital Micrograph is an image acquisition and processing program produced by Gatan. Digital Micrograph was used to acquire and partially analyze the TEM-EELS data.

C. 3 *Matlab 9.7*

MATLAB (matrix laboratory) is a numerical computing environment developed by MathWorks which allows matrix manipulations, plotting of functions and data, and implementation of algorithms. The processing of STXM and TEM-EELS data was done in algorithms developed in *Matlab 9.7*. For instance, PCA analysis used for removing noises from STXM stacks was performed by using nonlinear iterative partial least squares (NIPALS) algorithm in *Matlab 9.7*:

```
% Calculating five principal components by using NIPALS algorithm
for i = 1:5
  t = rand (n,1);
  p = Main'*t./(t'*t);
  p = p ./ sqrt ( p'*p );
  delt = 1; t1 = 1; p1 = 1;
  Err_val = 10e-10;
  while (delt>Err_val)
    t = (Main*p)./(p'*p);
    t = t./sqrt( t'*t );
    delt=t-t1;
```

```
    t1=t;
    p=Main*t;
     p1=p;
   end;
  P(:,i)=p1;
  T(:,i)=p1;
  E=Main-(t*p');
  Main=E;
 end
```

where Main is the n×m unfolded matrix. NIPALS algorithm is explained step-by-step in

detail in **Table C.1**.

Table C.1- Steps of NIPALS algorithm.

Steps	Mathematical Expression	Explanation
1	$t := rand\ (n,1)$	Generate a random column vector and copy it to the vector $\mathbf{t}$ (n×1)
2	$p := (Main'*t)/(t'*t)$	Project Main onto $\mathbf{t}$ in order to find the corresponding loading $\mathbf{p}$
3	$t := t/|t|$	Normalize the loading vector $\mathbf{p}$ to length 1
4	$t_{old} := t$	Store t into $\mathbf{t_{old}}$
5	$t := (Main*p)/(p'p)$	project the matrix **Main** onto $\mathbf{p}$ in order to find corresponding score vector $\mathbf{t}$
6	$Err\_val := u_{old}\text{-}u$	Check for the convergence If not converged return to step 2.
7	$E := Main - tp'$	Remove the estimated PC from **Main**
8	$Main := E$	To find the other PCs repeat this procedure from step 1 using the matrix **E** as the new **Main**

C.4 *Microsoft Office* (*2000*)

Word and PowerPoint were used to prepare reports and presentations. Excel was used for data manipulation and analysis.

C.5 *NoteTab*

NoteTab is a text and HTML editor which was used to format spectral files in order to use them in various software.

C.6 *PaintShop Pro*

PaintShop Pro was used to prepare images for presentation and publication of spectromicroscopy data. Images were mainly screen saved from aXis2000 and Matlab into PaintShop Pro for editing.

C.7 *Sigma Plot 6.0*

Sigma Plot 6.0 was used to plot spectroscopy data and regression analysis.

C.8 *STXM_Control*

This software was written and developed by Dr. Tolek Tyliszczak and Peter Hitchcock. It controls the beamline (slit sizes and monochromator) and the STXM microscope, and acquires the data at STXM 5.3.2.